UNIVERSITÀ DEGLI STUDI
DI TRENTO

DEPARTMENT OF INFORMATION ENGINEERING AND COMPUTER SCIENCE
ICT International Doctoral School

Microwave and RF system for Industrial and Biomedical Applications

Mohammedhusen Manekiya

Advisor

Prof. Massimo Donelli

Università degli Studi di Trento

October 2020

Acknowledgement

Alhumdulillah! For everything I have earned and to my family and their support. I want to thank **Prof. Massimo Donelli** for continuous support during my PhD. It would not have been possible without the support and freedom to think out of the box. I would kindly thank **Prof. Abhinav Kumar** and **Ashish Yadav** for directing me on a path to research and shape my skill to become a researcher.

I want to thank my friends Trento, *Athar Ali Kazmi, Tahir Ahmad, Haroon Mahmood, Klaudijo Klaser, Valeria Savoca, Sudipan Saha, Nasrullah Sheikh, Priyadarshini Jayashree, Sunil Raghavendra, Abdullah Hamdan, Salek Ali, Shahi Dost, Alma Fabris, Eleonora Grilli.* My friends from IIT Hyderabad, *Pritanjali Kandpal, Ankur Mittal, Aniket Bhosale, Ishaan Goswami, Kedar Otta, Arvind Singh, Ramya Nemana, Ekta Prajapati, Sarika Tyagi, Tarun Kandpal.* Also, I would like to thank all my friends along the way I made.

I would like to thank the University of Trento for this opportunity.

Abstract

Modern smartphone technology has created a myriad of opportunities in the field of RF and Microwave. Specifically, Chipless RFID sensor, compact microwave filter, antenna based on a microstrip structure, and many more. In this thesis, innovative ideas for the industrial and biomedical device has been explored. The work presents the reconfigurable filter design, Switch-beam antenna, Microwave interferometer, X-band Rotman Lens antenna, Ultra-wideband antenna based on SIW resonator, L-band Stepped Frequency Continuous Wave antenna, development of a wireless sensor system for environmental monitoring, Indoor Air Quality monitoring, and Wildfire Monitoring based on the modulated scattering technique (MST). The MST sensor probes are based on the scattering properties of small passive antennas and radiate part of the impinging electromagnetic field generated by an interrogating antenna, which also acquires the backscattered signal as information. The MST probes are able to deliver data without a radio frequency front end. They use a simple circuit that alternatively terminates the antenna probe on suitable loads to generate a low modulation signal on the backscattered electromagnetic wave. The antenna presented in this work has been designed in ADS Software by Keysight Technologies. The designed antenna has been assessed numerically and experimentally. The experimental measurement data demonstrate the effectiveness of the individual system. Simultaneously, the MST sensor system has been proposed to obtain the best performance in communication range, load efficiency, and power harvesting. The MST sensor has been fabricated and assessed in practical scenarios. The proposed prototype, able to provide a communication range of about 15 m, serves as a proof-of-concept. The acquired

measurements of MST demonstrate the accuracy of the data without radio frequency front end or bulky wired connection with the same efficiency of standard wireless sensors such as radio frequency identifier (RFID) or wireless sensor networks (WSN).

Keywords

[Microwave Filter, Ultra-Wide band antenna, Interferometer, Chipless RFID, Modulated Scattering Technique(MST), Microelectromechanical systems (MEMS), Internet of Things(IoT)]

Contents

List of Tables

List of Figures

Chapter 1

Introduction

1.1 State of the Art

More than 100 years have elapsed Heinrich Hertz demonstrated the existence of electromagnetic waves and confirmed Maxwell's electromagnetic theory. The world has seen an era rich in engineering discoveries and innovation within the field of a microwave. The microwave field applications are fascinating and intriguing, how much it had changed the world throughout history. During the Second World War, the Radiowave brought maturity with the superheterodyne concept, later on, Television(TV) and broadcasting. The knowledge of the atmosphere, specifically the ionosphere, revolutionized microwave technology when Radar was created. Indeed, the profound impact was on the RF and microwave industry, which was spearheaded by the Sensor ingenuity in the industry and medical domain. The development of new material and computer-aided design expands the resolution of application in new generation low-cost RF system and Microwave component design. Modern RF communication and Radar systems accommodate a variety of RF components, which opens up the door to the innovative component design [1]. These new designs are cheaper and very practical to use. Thanks to Microtechnology and Nanotechnology's recent progress, offers a more effective and enhanced method to create highly accurate RF component, microwave systems, and sensors that can operate reliably in a wide range of conditions [2, 3]. However, the advances in Modern Telecommunications systems such as mobile smartphones offer multimedia applications and different services that require high reconfigurability despite the devices' limited dimensions. 5G and 4G generation devices offer, in addition to usual voice and other services commonly provided by standard 3G systems, ultra-broadband internet connection, voice-over telephony (VOIP), mobile web access, gaming services, and other exciting multimedia applications (such as high definition television). Advanced

RF techniques such as MIMO antennas, multi-bands antenna and feeding networks, and Carrier Aggregation (CA) could actively improve the performances of standard Radar or radio links. In such a framework, the design of a suitable radiating system and feeding networks can play a vital role in designing a new generation's communication devices. The antenna systems and the related feeding networks for these new devices need to be light, cheap, and able to keep device performances high. That results in RF devices with high complexity and challenging RF requirements, especially on the antenna feeding network [4]. This has forced designers to study methodologies to over exploit the available radio frequency and strongly reduce smartphones and tablets' dimensions. This growing need for miniaturization requires simple, low-cost, and small devices and compact radiators [5].

At the industry level, there are many advance technique has been adapted. Each technique and application is unique and distinct in that it makes the equipment more sophisticated. It had lead to increase in market for the microwave filter [6, 7, 8, 9, 10], wireless sensor networks (WSNs) [11, 12]. Emerging wireless technologies such as tablets, smartphones, or wireless sensor networks (WSNs) [11, 12], require smaller, faster, and more advanced data transmission systems data that require high bandwidth. This led transmitters, receiver's front-end, and all radio frequency circuits to be in close proximity to each other inside devices characterized with strong mechanical constraints and minimal cases. In such a framework, electromagnetic compatibility problems arise, and compact and efficient band-stop filters that can reject incoming interfering signals at specific frequency channels become mandatory. Moreover, modern devices for effectively conveying signals at microwave frequencies make use of planar transmission lines, which are preferred in Microwave Monolithic Integrated Circuits (MMIC) [13, 14, 15, 16]. Microstrip line (MSL) passive structures can facilitate

such integration since they are economical, compact, light, and extremely versatile. Microstrip structures are particularly suitable for the design of almost all passive microwave devices [13, 14] such as filters [17], hybrids and antennas [12, 14, 17, 18, 19, 20] and they can be easily integrated in the next generation devices based on 4G/5G standards. Considering the future cognitive radio and radar systems, it is certain that electronically reconfigurable filters will play an important role in the next wireless systems. The development of an electronically tunable filter could be accomplished by using active semiconductors switches based on pin diodes or MEMs [21, 22] or by using tuning elements such as varactors diode [17]. The switched beam antennas are usually adopted instead of phased arrays using the radiation properties of fully adaptive smart arrays, approximated with a discrete set of radiation pattern configurations available through suitable ports or electronic switches [23, 24, 25]. Several electronically scanning antennas, which employ Butler matrix networks have been proposed to improve the signal to noise ratio of telecommunication systems. The switched beam antennas based on the Butler matrix have multiple input/output ports, each corresponding to different beam directions. By considering the power levels of detected signals, the main beam of the antenna's radiation pattern can be steered to the optimal direction to build or enhance the communication link. Moreover, this kind of antenna can be used with a high degree of effectiveness in multiple-input multiple-output (MIMO) systems.

Different strategies to design smart antenna systems able to remove or strongly reduce interfering signals while maintaining the integrity of the received signals have been developed. Smart antenna systems able to reconfigure the radiation pattern guarantee additional functionalities to wireless systems, such as detecting the direction of arrival (DOA) of incoming signals or for localization applications. Despite the advantages of smart antenna systems with fully adaptive properties such as phased

arrays, their extensive use in commercial applications is strongly limited by their complexity, cost and dimensions.

Furthermore, in the Biomedical fields, the advancement has impacted significantly on our day-to-day life and well-being [26]. In particular, it has affected different aspects, such as faster identification and better disease treatment facility. Simultaneously, the smart sensor system measures the typical physiological parameters such as Body temperature, Heart rate, Respiratory rate, Blood pressure, Gait analysis, spinal posture, Sweat rate, Parkinson's Disease, Stress Monitoring, Arm and limb motion. Different type of technique and system has been developed to deal with the particular situation [26]. The wearable sensor fits with most of the conditions when individual patient monitoring is required. In [27], they have introduced an automated approach to recognize the emotion based on a specific biological signal. Methodology in [27] has been integrated into a tracking system to estimate the emotional state of individuals by classifying features extracted from Blood Volume Pulse(BVP), Heart Rate(HR), Galvanic Skin Response(GSR), and Respiration(RSP). Moreover, research like [28, 29, 30, 31, 32, 33] provides a different and innovative approach as Virtual-Reality-Based Multidimensional Therapy, movement indication, biophysical approach, music therapy approach, and gaming approach, respectively, to detect anxiety. In [27], the technique requires that the patient wear the wearable. However, sometimes patients who are not comfortable with wearable can produce a false result as an increase in blood pressure. The wearable sensor's main objective is to minimize the interaction between the patient and doctor to monitor the patient remotely. To make this wearable sensor highly accurate in nature, the sensor system should collect real-time data with less noise. In [34], developed an integrated SPICE system model of its electrochemical, interconnection, and electronic components. In [35] discussed how Bluetooth compatibility af-

fect the wireless sensor market. There is much progress in the near field radiation and propagation, such as microwave imaging and early detection of a tumor through thermal scanning technique and Microwave interferometer. These techniques are non-invasive in nature, which brings down the cost of equipment installation [36, 37, 38, 39]. Currently, more innovative ideas are emerging to produce a non-invasive system for biomedical. Whereas some research is happening to innovate the active system into the passive and non-invasive technique [38, 39]. The next generation 5G telecommunication system has also opened new doors to the remote medical treatment (telehealth). In coming future, there will be more demand for non-invasive techniques than the active detection system. In this thesis, we have focused more on this kind of non-invasive technique for industrial and biomedical areas, mentioned in the next section.

1.2 Thesis Contribution

In the thesis a tile of methodology as a main and innovative findings are presented as follow.

- A passive reconfigurable filter has been designed using five microstrip spiral resonators to easily integrate the wireless sensor operating at $2.45GHz$ Wi-Fi band. The Wi-Fi channel interference does not affect the designed filter, and it can be activated or deactivated by the PID diode switch. The prototype has been presented with supporting numerical, experimental results.

- Enhanced antenna array system is designed for the wireless sensors which operate at Wi-Fi band $2.45GHz$. The antenna array presented in it is based on a Butler matrix feeding network made from a microstrip structure. The design has been optimized by the Particle Swarm Method. The prototype has been fabricated in the laboratory,

and impedance matching is verified experimentally by the main beam steering capability.

- An X-band Rotman lens antenna has been designed using an Interval analysis method to refine the lens parameters. The prototype antenna has been designed and fabricated in a laboratory. The design has been mathematically formulated according to the interval principle. For the numerical experiment S, C and K band has been considered.

- A proof of conceptMicrowave interferometer has been designed and proposed for the proton beam therapy. The prototype can measure the displacement of the tumor/organ in a real-time environment non-invasively. The state of the art prototype has been assessed experimentally with the supervision proton therapy expert and concerned patient.

- An ultra-wideband antenna structure is proposed. The antenna's geometry consists of 16 surface impedance waveguide(SIW) cavity to improve the antenna's performance. The prototype is fabricated and presented with numerical and experimental assessment data. The prototype has been tested within the frequency range of $3GHz$-$11GHz$.

- An ultra-wideband antenna array structure based on the Orbital Angular Momentum(OAM) technique is designed and tested numerically. The antenna array structure consists of 8 element structure operating at the C band. Each element is arranged circularly. The design of every element is based on a surface impedance waveguide(SIW) cavity.

- A compact Stepped Frequency continuous wave radar has been developed to track the smuggling goods, illegal materials, and weapons at the city's customs check. The developed prototype operates L band

and has a bandwidth of 1GHz-2GHz. The prototype has been assessed numerically and experimentally with the coordination Guardia di Finanza(GdF), the Italian financial police.

- A machine learning post-processing technique has been developed to improve the detection of microstrip reconfigurable filter, RFID sensor, other wireless sensor networks. In specific, the Quantile regression method has been used on RFID sensor signal. The post-processing method has been developed in MATLAB application. The proposed method has been tested on a real-time and numerical result of a chipless RFID signal.

- An RFID sensor based on Modulated Scattering Technique(MST) system has been proposed to sense the environmental parameter. The proposed technique operates on X band,10GHz, and exhibit an alternative to current RFID and Wireless Sensor Network(WSN) architecture. The proposed system has been verified numerically and experimentally in real-time.

- An air quality monitoring system has been presented based on Modulated Scattering Technique(MST). The proposed system is an improvement to the previous system, particularly the sensors. The system operates indoor. The sensor collects the data of Humidity and indoor temperature, compared with real-time data. The system has been experimentally assessed.

- The capability of the MST prob system has been improved to upgrade the performance and improve the system's operating distance. The proposed MST prob is enhanced with an SP3T Microelectromechanical systems (MEMS) switch. The experimental assessment of a proposed prototype has been presented with a mathematical formula-

tion.

- A state of the art Low-Power wildfire detection system has been proposed. The Modulated Scattering Technique(MST) system is improved with a log-periodic antenna. In particular, the antenna of MST tag has been changed. The 2 log-periodic antenna, 12 element, and 20 element, has been designed for the proposed system. The operating frequency of the log-periodic antenna is $600MHz$-$6GHz$. The working of state of the art technology has been presented Mathematically with the antennas' numerical assessment.

1.3 Structure of the Thesis

The thesis is organized mainly into five chapters. The structure is as follows. First, Chapter 1 introduction is a preface of the detailed state of the art and Sensor types. The detailed state of the art is given for the bio-medical and industrial sensors and their use case. It also introduces the thesis's motivation and various antenna design applications based on different bio-medical and industry scenarios.

Chapter 2 focuses explicitly on the antenna design for the industrial and biomedical sector. In particular, the reconfigurable filter based on microstrip spiral resonators is presented with an experimental filter prototype and experimentally assessed. The experimentally assessed compact switch band antenna design introduced for wireless sensors works for Wi-Fi band. For the Proton Beam Therapy, a Microwave Interferometer prototype is given with real-time experimental assessment. Two different Ultra-wideband antenna based on SIW resonator and Orbital angular momentum presented with detailed design and numerical assessment. For the real-time goods control checkpoint, a low-cost High-resolution L band Stepped Frequency Continues wave radar (SFCW) antenna is presented

with numerical results and discussed in detail.

Chapter 3 presents an improvement to the real-time detection capability of the microstrip spiral resonators and RFID systems. This chapter proposes the Quantile regression method, which is part of a machine learning technique. The mathematical system model and numerical assessment on a real-time received RFID signal discussed in detail.

Chapter 4 focuses on the Modulated scattering Technique and its application for RFID sensors, Indoor Air-Quality Monitoring, and Low-Power wildfire detection. All application is discussed detailed with the mathematical formulation and presents with the numerical and experimental assessment. Finally, in Chapter 5, the conclusions are drawn with respective future work.

1.4 Declaration

The work presented in the thesis is an original work. Most of the presented work is published in a scientific journal/conference.

In particular, the work presented in Chapter 2 and Chapter 4 has the hardware prototype experimentally assessed for accuracy. Each section has presented with the individual state of the art and mathematical model. In some cases, the prototype's efficiency has been improved real-time by applying the post-processing technique, as shown in chapter 3.

Moreover, the work of low-power detection using MST has been tested only numerically. It presents the state of the artwork and is supposed to submit in high impact factor journal. Due to the COVID-19 situation, the experimental work has been delayed and not presented in the thesis.

All the thesis work has been done under the guidance of Prof. Massimo Donelli.

Chapter 2

Antenna Design for Industrial and Biomedical Application

In this Chapter different antenna designs are addressed for industrial and biomedical application. In particular, the reconfigurable filter, Switch band antenna, Microwave Interferometer, an Ultra wide band antenna based on SIW resonator and Orbital angular momentum, and High resolution L band Stepped Frequency Continues wave radar antenna. In the following sections, the detailed mathematical formation along with antenna design is reported respectively.

2.1 Reconfigurable Filter

In the last years, there has been growing demand for electronically tunable microwave filters because of their capabilities in improving wireless systems performances [6, 7, 8, 9, 10]. Emerging wireless technologies such as tablets, smartphones or wireless sensor networks (WSNs) [11, 12], requires smaller, faster and more advanced data transmission systems for the data which require high bandwidth. This led transmitters, receivers front-end, and all radio frequency circuits to be in close proximity to each other inside devices characterized with strong mechanical constraints and very small cases.

In such framework, electromagnetic compatibility problems arise and the design of compact and efficient band stop filters able to reject incoming interfering signals at specific frequency channels become mandatory. Moreover, modern devices for effectively conveying signals at microwave frequencies make use of planar transmission lines, which are preferred in Microwave Monolithic Integrated Circuits (MMIC) [13, 14, 15, 16]. In particular microstrip line (MSL) passive structures can facilitate such kind of integration since they are economical, compact, light and extremely versatile. Microstrip structures are particularly suitable for the design of almost all passive microwave devices [13, 14] such as filters [17], hybrids and antennas [14]-[12, 18, 19, 17, 20] and they can be easily integrated in the next generation devices based on 4G/5G standards. Considering the future cognitive radio and radar systems, it is certain that electronically reconfigurable filter will play a key role in next wireless systems. The development of an electronically tunable filter could be accomplished by using active semiconductors switches based on pin diodes or MEMs [21, 22] or by using tuning elements such as varactors diode [17]. This work proposes a reconfigurable filter structure composed of different passive microstrip spiral resonators coupled with the main microstrip line and able to op-

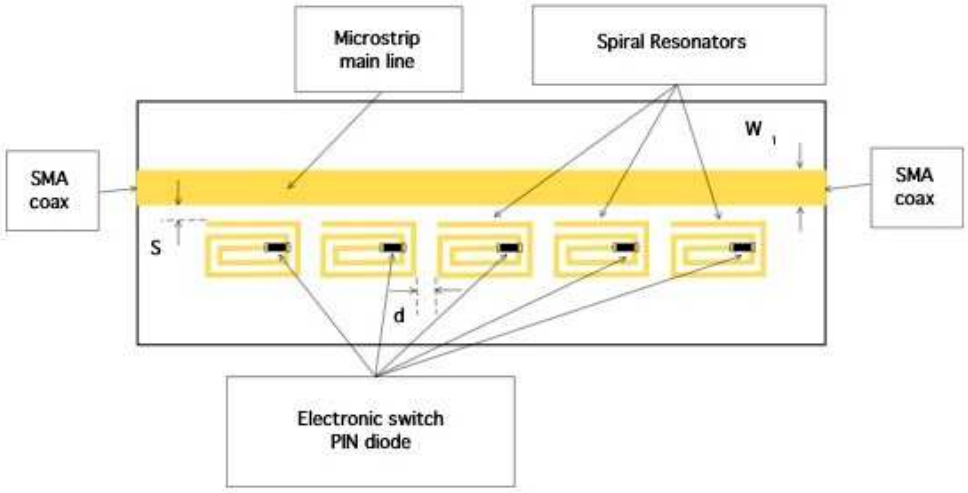

Figure 2.1: Schematic of the proposed reconfigurable filter.

erate at 2.45GHz Wi-Fi channels. The resonators have been designed to reject a given Wi-Fi channel and they could be electronically activated or deactivated by acting of electronic switches based on PIN diodes. An experimental filter prototype consisting of five microstrip spiral resonators operating between $2.40GHz$-$2.50GHz$ has been designed, fabricated and experimentally assessed.

2.1.1 Filter structure

The structure of the proposed microstrip reconfigurable filter is reported in Fig.2.1. It consists of the main microstrip line and a set of spiral resonators [40]. The spiral resonators are placed near to the mainline. Each resonator is equipped with electronic switches made with a positive intrinsic negative

(PIN) diode. The PIN diode is activated by means of a digital signal by acting on a simple bias network consisting of a choke inductors and a by-pass capacitor. When activated the PIN diode acts like a short removing the resonator effects. The coupling between the feeding line and the resonators are obtained with a gap-coupling, which consists in leaving a small gap between the transmission line used for the feeding and the resonator itself [13]. The gap between the resonator and the microstrip feedline can be modeled with a series capacitor [13, 40]. The spiral resonator can be modeled as a series RLC circuit the entire system (resonator plus gap and microstrip feeding line) behaves like a parallel RLC circuit. The equivalent schema of a spiral resonator coupled with microstrip feeding line is shown in Fig. 2.2. Fig.2.2 also reports the geometrical characteristics of the resonator structure. Fig.2.3 shown a photo of a single spiral resonator prototype. The feeding line is provided with two sub-miniature type A (SMA) coaxial connectors to experimentally assess the prototype performances. The geometrical parameters, with reference to Fig.2.2, for the design of a spiral resonator are: the width of the resonator L_s, the number of its sides φ, the width of the spiral turns W_s, the distance between spiral turns G_s and the width of the gap S between resonator and microstrip feedline. The resonance frequency of a microstrip spiral resonator is related to the total length [40, 41] L_{tot} of the spiral:

$$L_{tot} \approx \frac{\lambda_{res}}{2} = \frac{c}{2\sqrt{\varepsilon_e} f_{res}} \tag{2.1}$$

where λ_{res} is the wavelength at the desired resonance frequency, c is the light velocity in the vacuum and ε_e is the permittivity of the dielectric substrate. The total length of the spiral resonator can be estimated with the following relation:

$$L_{tot} = \frac{(\varphi + 1)}{2} \cdot L_s + \frac{(\varphi - 1)}{2} \cdot G_s \tag{2.2}$$

It is worth noticing that φ is odd, the case with φ even is not useful since it cannot permits to have a constant G_s between spiral turns. By considering relations 2.2 and 2.1 it is possible to provide an approximated estimation of the resonant frequency f_{res} vs. the L_s and G_s parameters.

$$f_{res} = \frac{c}{[(\varphi + 1) \cdot L_s + (\varphi - 1) \cdot G_s] \sqrt{\varepsilon_e}} \tag{2.3}$$

The G_s and the S parameter strongly depends on the considered design technology. The guidelines for their values have been found after an intensive simulation campaign. In particular by decreasing the width of the gap S that separates resonator and feeding line, the coupling increases, because the electromagnetic field of the feeding line can better interact with the resonators structure. Coupling phenomena are also increased when the parameter G_s is decreased. A too much coupling could cause an high power adsorption by the resonator at resonance and consequently strong reduction of the device performances. After the simulation campaign, the values of $G_s = 0.3mm$ and $S = 0.1mm$ have been found. Given a resonance frequency f_{res} the length L_s of the resonator is provided by the following approximated relation:

$$L_s \approx \frac{\lambda_{res} - (\varphi - 1) \cdot G_s}{(\varphi + 1)} \tag{2.4}$$

Relation 2.4 provides only a rough approximation of the resonator length L_s . To obtain an accurate resonance frequency a tuning phase, able to take into account the coupling factors due to G_s and S is mandatory. In particular commercial electromagnetic simulators combined with tuning techniques reported in [42, 43, 44, 45] have been considered to take into

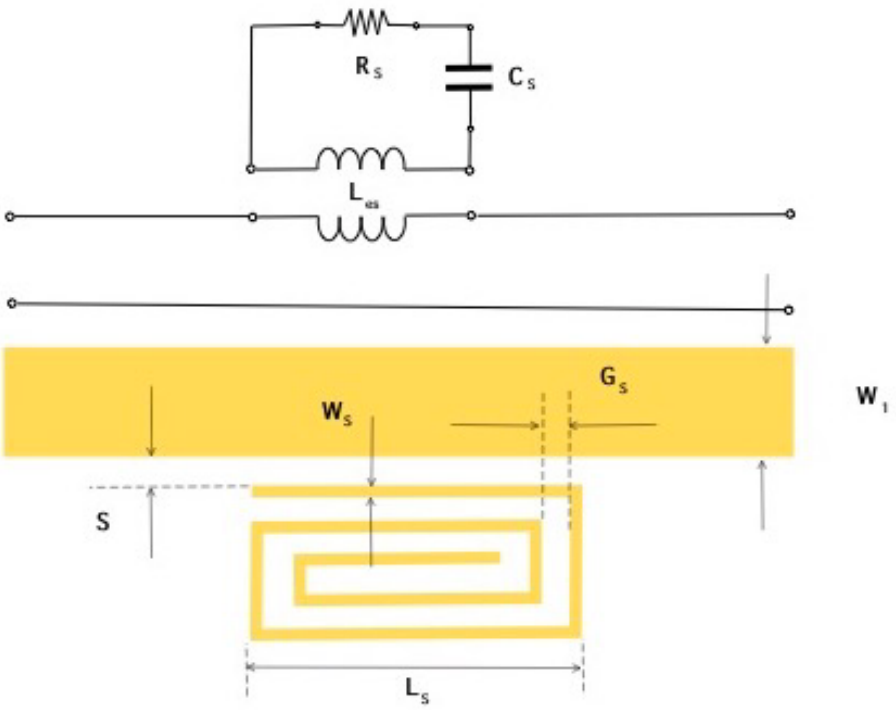

Figure 2.2: Schematic of a single spiral resonator and its circuital model.

account the coupling effects and to obtain a finer tuning of the resonance frequency.

2.1.2 Numerical and Experimental assessment

In this section, a reconfigurable stop band filter prototype based on five spiral resonators is assessed experimentally in details. The filter structure is

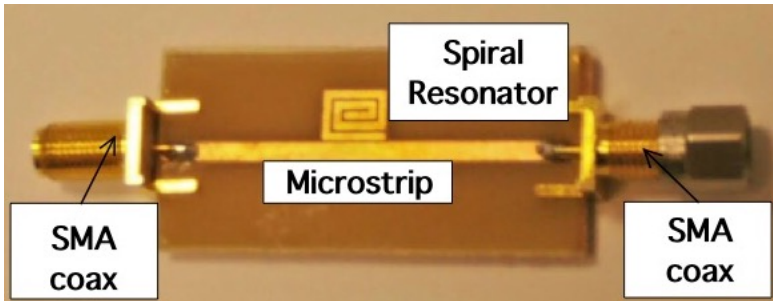

Figure 2.3: Photograph of the single spiral resonator prototype.

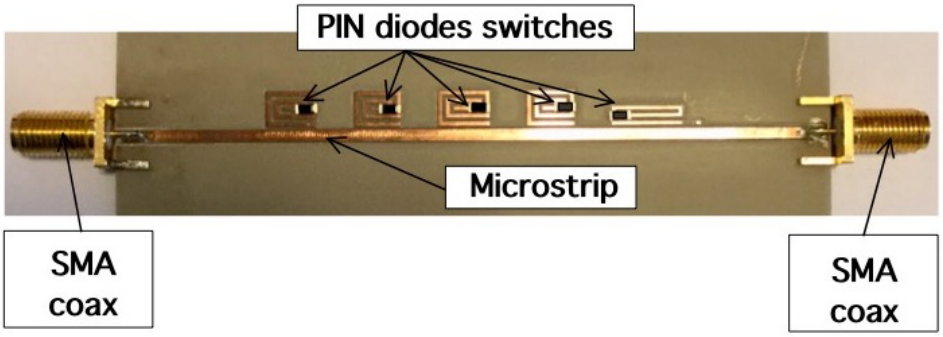

Figure 2.4: Photograph of the reconfigurable filter prototype.

printed on a ceramic dielectric substrate,$\varepsilon_r = 3.38 \pm 0.02$, $tan\,(\delta) = 0.001$ and thickness $t = 0.8mm$. The main microstrip feeding line has been connected with two SMA coaxial connector and designed to have a characteristic impedance $Z_0 = 50\ ohm$. In particular, the length and the width of the main feeding line are $L_{main} = 50mm$ and $W_l = 1.71mm$ respectively, the microstrip width is calculated by using the well known Hammerstad formula [13]. Using equation 2.4 a set of spiral resonators with $\varphi = 9$ sides have been designed and fabricated. In particular, five WiFi channels have been considered, Tab.2.1 reports the five considered channels and the lengths of the spiral resonator estimated with the approximated formula 2.4. The L_s values reported in the third column of Tab.2.1 have been tuned by considering the unsupervised techniques considered in [44, 45]. Concerning the other geometrical parameters (with reference to Fig.2.2) the following dimensions have been considered $S = 0.1mm$, $G_s = 0.3mm$ and $W_s = 0.7mm$. The distance $D_r = 5mm$ between two consecutive resonators has been empirically chosen. The considered separation D_r is a good compromise, which permits to limit the coupling between two adjacent resonators. The obtained values have been found after a set of empirical simulation campaign as reported in the previous section.

To reject a given channel a resonator must be placed near the main feeding line, to deactivate the resonator an electronic switch is placed hor-

Table 2.1: Resonator length $L_s[mm]$ for the five considered WiFi channels.

	$Channel$	$f_{res}[GHz]$	$L_s[mm]$
	CH1	2.412	7.48
	CH2	2.422	7.40
	CH6	2.437	7.35
	CH10	2.457	7.23
	CH14	2.484	7.18

izontally in the middle of the resonator structure. In particular, five PIN diodes have been considered in the proposed filter prototype. Fig.2.4 shows the photo of the reconfigurable five resonators filter prototype. The small rectangular black SMD cases are the PIN diode switches. PIN diodes can be used as efficient and low cost electronic switches considering the direct forward bias characteristic of the diode, in particular the PIN diodes appears to be a very small and a very large impedance under forward and reverse bias respectively. To remove the effect of the resonator the PIN diode must be activated, in particular a single pole single throw switches SPST have been considered. The schema and the control circuit of each switch is quite simple, it consists only of two inductors $L_1 = L_2 = 100nH$, and a bypass capacitor $C_1 = 0.2nF$. The considered PIN diode was a BA5030, from NXP semiconductors, able to operate up to $5GHz$. The filter prototype has been connected to a DDS signal generator (USB-SA44B from Signal Hund company) by mean of coaxial cables equipped with SMA connectors. The return loss $|S_{ii}|\, i = 1, ...2$ and the insertion loss $|S_{12}|$ have been measured by means of a vectorial network analyser (MS2025B -500KHz - 6GHz). In the first test all resonators have been activated (all PIN diode turned off), in this configuration all the five WiFi channels have been rejected. A frequency span of $100MHz$ and a range from $2.40GHz$ up to

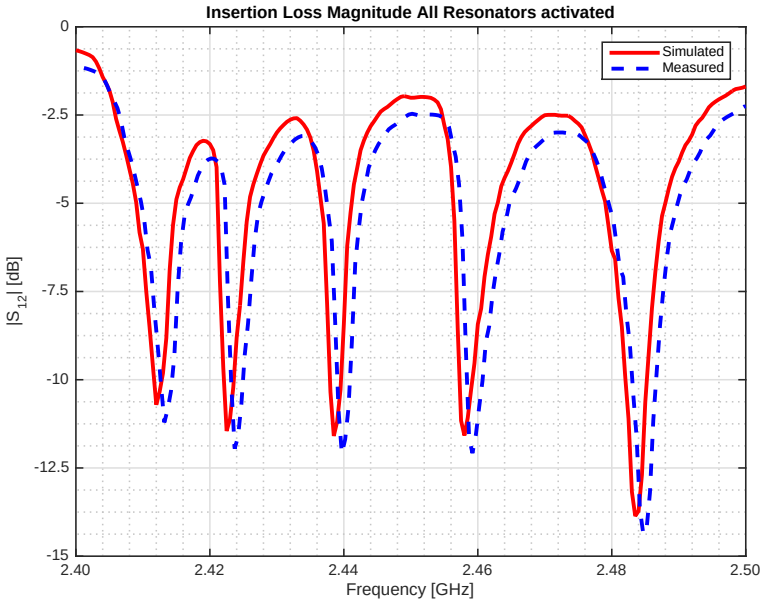

(a)

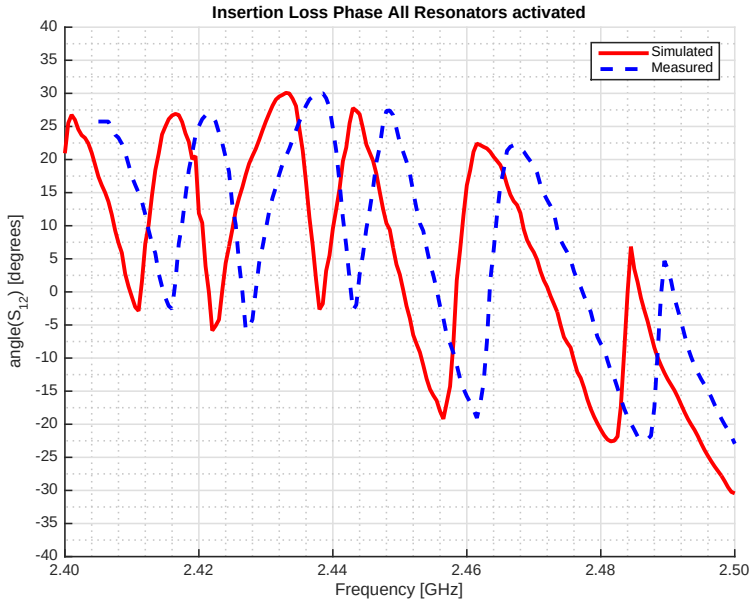

(b)

Figure 2.5: Reconfigurable filter with all the resonators activated. Measured vs. experimental insertion loss S_{12} values (a) magnitude, (b) phase.

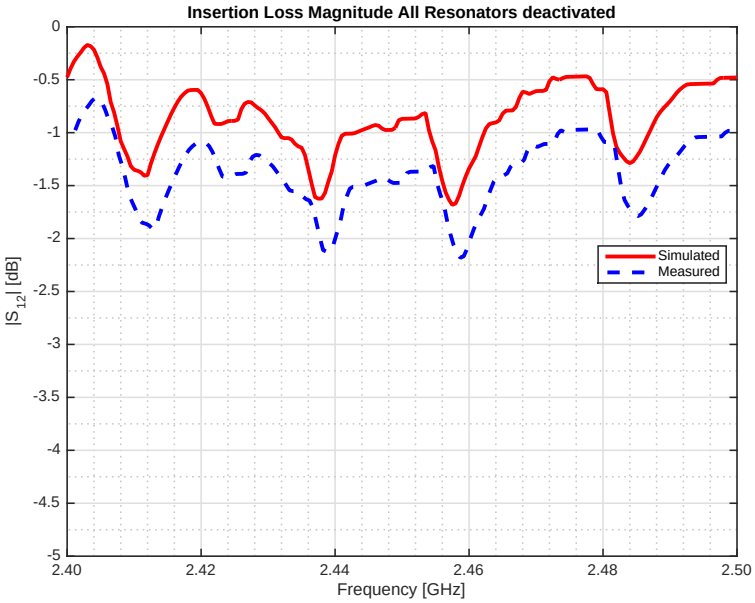

Figure 2.6: Reconfigurable filter with all the resonators deactivated. Measured vs. experimental insertion loss $|S_{12}|$.

$2.50GHz$ has been considered. Figs.2.5 (a) and (b) report the amplitude and phase of the insertion loss $|S_{12}|$. As it can be noticed from the data reported in Fig.2.5 (a) all the five WiFi channels listed in Tab.2.1 are rejected with a frequency band of about $20MHz$. For the sake of comparison the experimental data have been compared with simulated data obtained with a commercial software the ADS simulator from Keysight company. The agreement between simulated and measured data are quite good, only a slight frequency shift, probably due to the dielectric material tolerances can be observed. In the second experimental test all PIN diode switches have been activated and consequently the effects of resonators removed. The results of this test are shown in Fig.2.6 which reports the filter insertion loss with all resonators deactivated. Also in this case the experimental measurements have been compared with numerical results, the presence of activated PIN diode switches have been simulated by inserting a small slab of metallization in the resonator structure. As it can be noticed from the

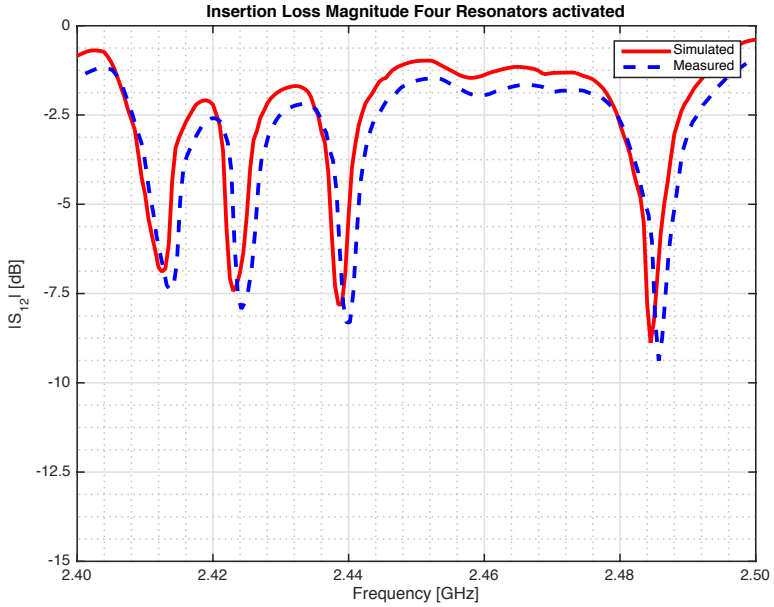

(a)

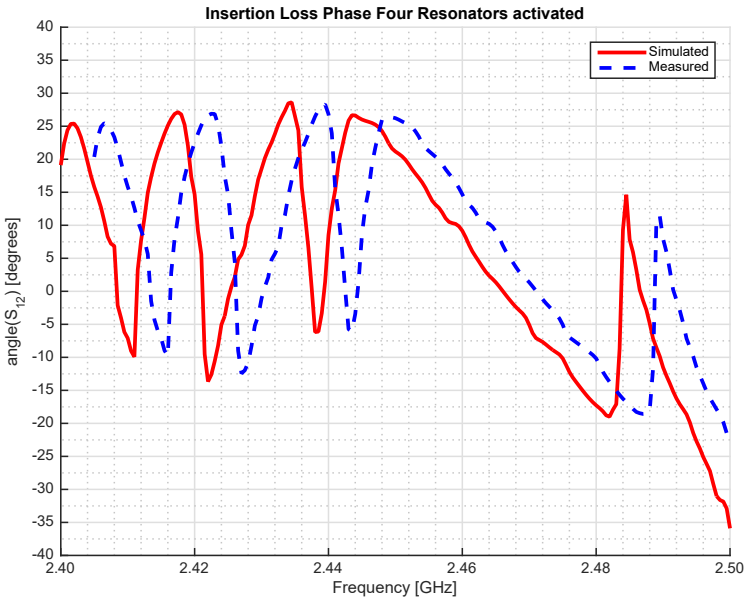

(b)

Figure 2.7: Reconfigurable filter with four resonators activated. Measured vs. experimental insertion loss S_{12} values (a) magnitude, (b) phase.

data of Fig.2.6 the effects of the PIN diode switches are evident and all channels can pass through the filter structure only with a small attenua-

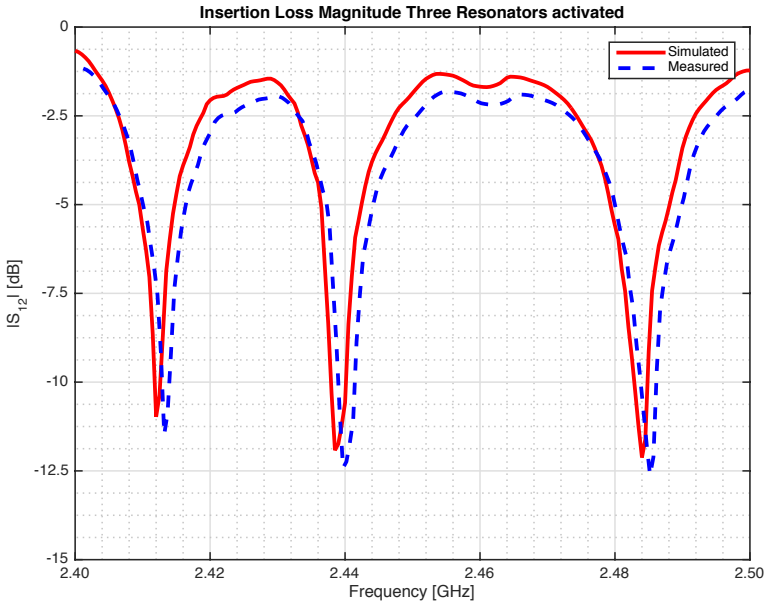

(a)

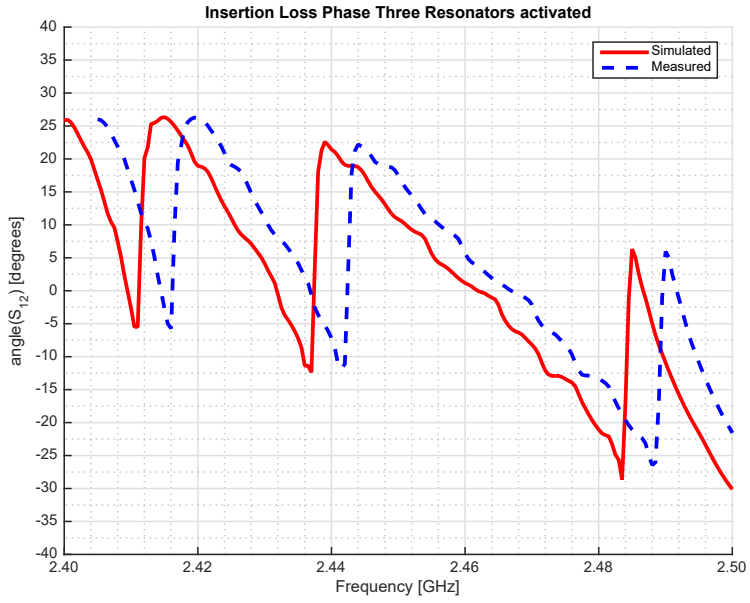

(b)

Figure 2.8: Reconfigurable filter with three resonators activated. Measured vs. experimental insertion loss S_{12} values (a) magnitude, (b) phase.

tion. Also in this case the agreement between numerical and experimental data is good only a slight frequency shift and an amplitude difference of

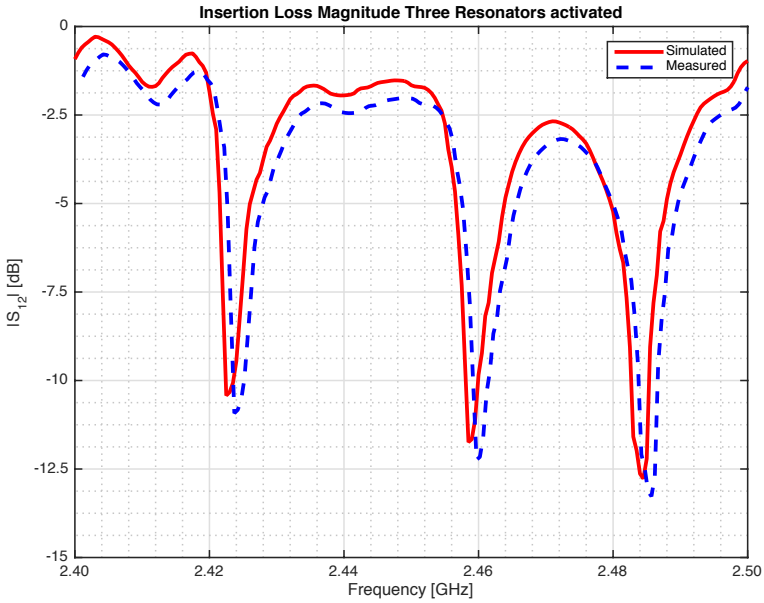

(a)

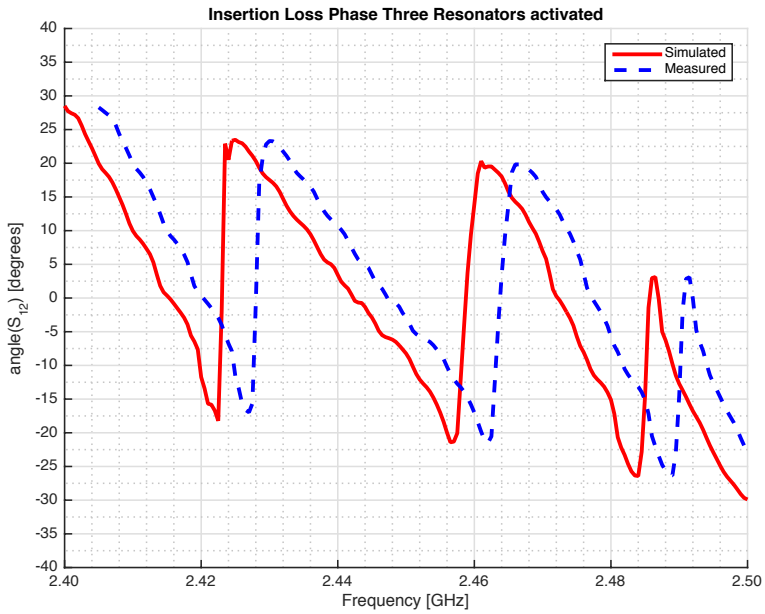

(b)

Figure 2.9: Reconfigurable filter with three resonators activated. Measured vs. experimental insertion loss S_{12} values (a) magnitude, (b) phase.

about $0.5dB$. The following tests are aimed at assess different filter configurations in particular Figs.2.7 (a) and (b) shows the results obtained

considering a filter configuration characterized with CH1, CH3, CH6 and CH14 rejected, only CH10 at $f_{ch10} = 2.457GHz$ is in the pass-band thanks to the deactivation of resonator number four, obtained by activating the correspondent PIN diode switches placed on its structure. The last two experiments consider filter configurations with only three resonator activated. In particular Figs. 2.8 (a) and (b) reports the results concerning filter configuration with channels CH3, CH10 and CH14 rejected, only CH1 and CH6 at $f_{ch1} = 2.412GHz$ and $f_{ch1} = 2.437GHz$ are in the pass-band. The last experiment concerns a configuration characterized by CH6 and CH10 ($f_{ch6} = 2.437GHz$ and $f_{ch10} = 2.457GHz$) in the pass-band and the others channels CH1, CH3 and CH14 stopped. The results of last configuration are reported in Fig.2.9 (a) and (b). The reject capabilities of the filter are quite evident in all the considered configurations.

2.2 Compact Switched-beam planar antenna array for wireless sensors operating at Wi-Fi band

2.2.1 Introduction

This work presents the design of a Wi-Fi a multi-beam antenna array based on a compact planar microstrip structure. The array structure and performances have been tuned by using suitable unsupervised techniques [24] to obtain an efficient and compact structure. In Sec.2.2, an antenna array has been proposed, which is a complex system composed by different passive microstrip microwave components. Conventional microwave design techniques are quite effective for the development of basic microwave active and passive devices [13], but these design techniques are not able to models the interactions between different components of complex system with efficacy. Usually a final tuning phase is required to increase the system performances. This tuning phase requires a lot of computation time and resources due to the design/fabrication cycles, typical of the standard trial and measurement techniques. Recently, unsupervised CAD tools [14, 46], have been proposed for the design of complex microwave systems and the solution of complex electromagnetic problems such as antenna design [42, 43], control [47] as well as other interesting applications [48]. These tool can analyse, design and modify, microwave devices in unsupervised manner. They can not replace an expert microwave engineer but they can offer a valuable help to designers and strongly reduce the time necessary to design a complex microwave system. In these tools the problem is usually recast as an optimization one that can be handled by means of a suitable optimization algorithm and a cost function. This work presents the optimized synthesis of a compact switched beam planar antenna array able to operate in the whole WiFi band. The design and tuning of the

antenna structure is carried out considering a numerical procedure based on a particle swarm optimization (PSO) algorithm [46, 49]. The advantage of the proposed procedure is that it takes into account all the different interactions and coupling phenomena of the different antenna subsystems. At the end of the design procedure this methodology provides, not only the structure of the single antenna components, namely the quadrature hybrids, the microwave cross-overs, the coplanar to microstrip transitions, and the matching transformers, but it provides a complete system where the requirements of each microwave components respect the initial requirements. In Sec.2.2, an experimental array prototype consisting of $2.45GHz$ microchip antennas was designed, fabricated and experimentally assessed.

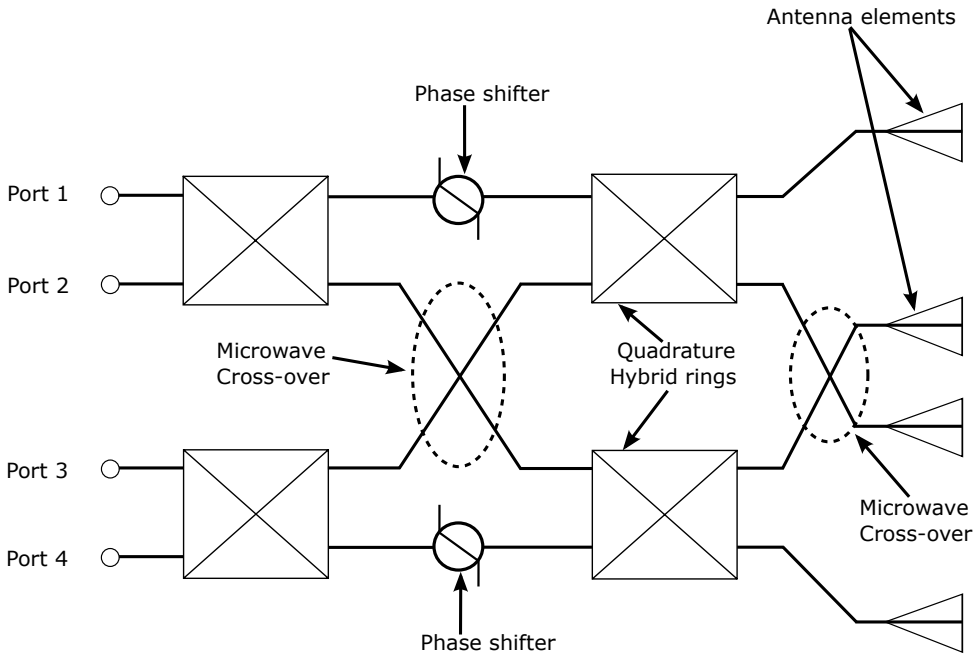

Figure 2.10: A schema of the proposed antenna array feeding network.

2.2.2 Design of the antenna structure

With reference to the feeding network reported in Fig.2.10, it consists of passive planar microwave devices. The feeding network was designed to provide identical magnitude to the array elements. The array elements are equally spaced with distance d and each succeeding element presents a phase progression b relative to the preceding one. The Butler matrix works as a beam forming network when different input ports are excited as shown in Fig.2.10. It provides four output signals with the same power levels and with progressive phases of $+45$, -45, $+135$, and -135, respectively. The feeding network is composed of four quadrature hybrid rings, two phase shifters, and two microwave crossovers. To significantly reduce the antenna dimensions, compact quadrature hybrids based on the methodology described in [15, 16] have been introduced. In particular, to significantly reduce the overall size of the conventional quadrature hybrid rings, the four quarter-wave lines which compose each hybrid ring are periodically loaded with capacitors obtained with open end stub [50]. Moreover, two horizontal quarter-wavelength lines are loaded with two open end stubs while the vertical lines are loaded only with one open end stub. The schematic reported in Fig.2.11 describes the details of the microwave crossover obtained with two compact quadrature hybrids and the structure of the compact hybrids itself. To optimally realize the compact hybrid rings a numerical optimization procedure aimed at optimize a suitable cost function was considered [23, 49, 51]. As a result, the overall reduced hybrid size is more than 80 percent smaller than that of the conventional hybrids. Concerning the design of the two microwave crossover, they are realized considering the chain of two compact quadrature hybrid rings. The structure and the geometrical parameters of the microwave crossovers are detailed in Fig. 2.11. Array elements are commercial surface mount chip antennas (Johanson

Tech. model P/N2450AT43F0100) whose dimensions are $2 \times 6mm^2$. The frequency range and the gain of the chip antennas are $2.4 - 2.5GHz$ and $10dBi$, respectively while the input impedance is 50Ω. The four surface mount chip antennas require a coplanar microstrip waveguide feeding line (50Ω) and an LC matching transformer to better tune the antenna resonance frequency. The LC matching network is composed of two surface mount reactive elements (a capacitor of $0.8pF$ and an inductor of $5.6nH$). Since the most critical component is the capacitor, due to it's low value, a surface mount device (SMD) capacitor from Murata company, devices case code C0402, characterized by a value C=0.8pF and a tolerance +/- 0.05pF. It has to be observed that it is mandatory to obtain a return loss below $S_{11} < -25dB$ as indicated in the antenna data sheet. To connect the coplanar waveguide and consequently the surface mount chip antennas a coplanar to microstrip transition is mandatory. In particular the transition proposed in [50] offers a good compromise in terms of compactness, simplicity, performances. It can be easily optimized to guarantee a good match between the coplanar waveguide and the output lines of the hybrids. At the end of the design procedure, a compact array of dimensions $35 \times 80mm^2$ has been obtained.

The schematic as shown in Fig.2.11 describes the detail of a microwave crossover obtained with two compact quadrature hybrid and the structure of the compact hybrids itself. To optimally realize the compact hybrid rings a numerical optimization procedure aimed at a suitable optimize cost function was considered [23, 49, 51]. As a result, the overall reduced hybrid size is more than 80 % smaller than that the conventional hybrids. Concerning the design of the two microwave crossover, they are realized considering the chain of two compact quadrature hybrid ring. The structure and the geometrical parameters of the microwave crossovers are given in Fig. 2.11. Array elements are commercial surface mount chip antennas (Johanson

Tech. model P/N2450AT43F0100) whose dimensions are $2 \times 6\ mm^2$. The frequency range and the gain of the chip antennas are $2.4 - 2.5\ GHz$ and 10 dBi, respectively, While the input impedance is 50 Ω. The four surface mount chip antennas are required for a coplanar microstrip waveguide feeding line (50 Ω) and an LC matching transformer to tune the antenna resonance frequency. The matching network is composed of two surfaces mount reactive elements (a capacitor of 0.8 pF and an inductor of 5.6 nH). It has to be observed that it is mandatory to obtain a return loss below $S_{11} < -25\ dB$ as indicated in the antenna data sheet. To connect the coplanar waveguide and consequently the surface mount chip antennas a coplanar to microstrip transition is mandatory. In particular, the transition proposed in [50] offers a good compromise in terms of compactness, simplicity, performances. It can be easily optimized to guarantee a good match between the coplanar waveguide and the output lines of the hybrids. At the end of the design procedure, a compact array of dimensions $35 \times 80\ mm^2$ has been obtained.

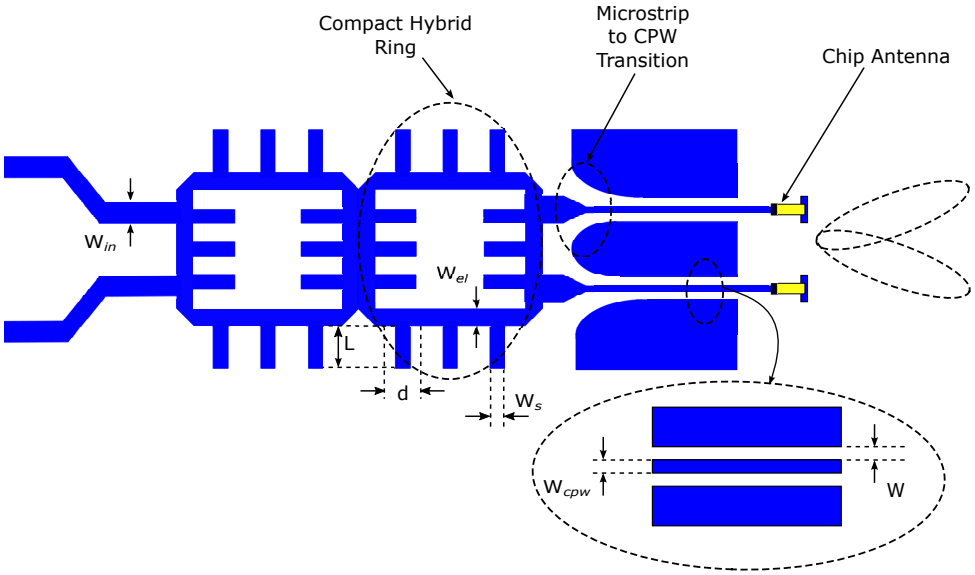

Figure 2.11: Details of the microstrip cross-over, coplanar to microstrip transition, and compact quadrature hybrid ring geometries.

2.2.3 The Particle swarm optimization (PSO) based design method

The PSO is a computational method that optimizes a problem by iteratively trying to improve the solution with regards to given quality measures. It was developed by Kennedy and Eberhart [52] in the nineties and it has been successfully used to solve complex electromagnetic problems and antennas design [47]-[51]. The standard PSO implementation considers a swarm of trial solutions (called particles) explores the solution space by improving its position according to suitable updating equations. In particular each particle moves on the basis of information collected by the particles previous best performance (called cognitive knowledge) and the best previous performances of its neighbours (called social knowledge). With respect to other evolutionary algorithms such as genetic algorithm GAs and different evolution DE, the PSO shows indisputable advantages. Specifically, the PSO is simpler, both in formulation and computer implementation, with respect to the GA, or DE which consider almost three-genetic operators (the selection, the crossover, and the mutation). PSO considers only one simple operator, called velocity updating equation. Moreover PSO allows an easier calibration of its parameters since it has no critical parameters. For almost all problems and solution space sizes, a standard configuration turns out to be adequate for finding a satisfactory solution with a limited amount of computational resources, thanks to this there is no need to perform a PSO calibration for every design experiment. PSO has a flexible and well-balanced mechanism to enhance the global (i.e., the exploration capability) and the local (i.e., the exploitation capability) exploration of the search space. Such a features allow one to overcome the premature convergence (or stagnation) typical of GAs and it enhances the search capability of the optimizer. The PSO requires a very small population size, which turns out in a reduced computational cost of the overall mini-

mization by allowing a reasonable compromise between the computational burden and the minimization reliability. The considered antenna design has been formulated as an optimization problem fixing suitable constraints in terms of impedance matching at the four input port ($|S_{11}|$ values) and on the steer direction of the main beam. The considered antenna structure is based on microstrip technology. The geometrical parameters that completely define the antenna geometry are reported in Fig.2.10. The antenna structure and the considered geometrical parameters have been studied to simultaneously maximize the performance and minimize the size of the antenna structure. In particular the compact quadrature hybrid rings, the microwave inverters, the microstrip to coplanar transition and the whole geometrical antenna structure is uniquely determined by the following vector $\underline{\psi} = \{W_{in}, L, d, W_s, W_{cpw}, W, W_{el}\}$ which represents all the antenna geometrical parameters. To meet the objectives, a suitable cost function, that represents the difference between the requirements and the performances of a trial antenna geometry, is defined by the following relation aimed at minimizing the return loss at each port and to steer the direction of main beams:

$$\Phi\left\{\underline{\psi}\right\} = \sum_{n=1}^{N} max\left\{0; \frac{|S_{nn}\left(\underline{\psi}\right)| - |S_{nn}|_{max,n}}{|S_{nn}|_{max,n}}\right\} + \frac{|\Theta_n\left(\underline{\psi}\right) - \Theta_n|^2}{|\Theta_n|^2} \quad (2.5)$$

N indicates the port number, $|S_{nn}(\underline{\psi})|$ is the return loss at n^{th} port when the trial geometry defined by the $\underline{\psi}$ vector is considered, and $|S_{nn}|_{max,n}$ represents the return loss requirement in dB. $\Theta_n\left(\underline{\psi}\right), n = 1, ...N$ are the direction of the main beam when the n^{th} port is considered as input, and Θ_n is the required steering main beam direction for the n^{th} port. To minimize 2.5 a suitable version of the PSO has been used with a geometrical generator and a commercial electromagnetic simulator (namely HFSS designer), to estimate the characteristics of the trial antenna geometries.

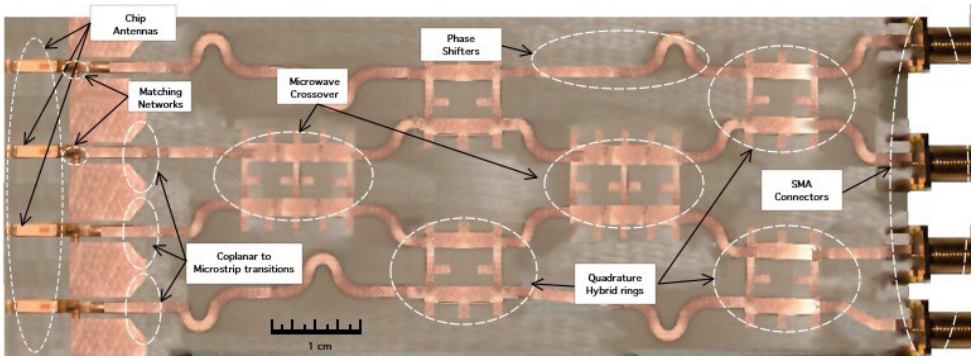

Figure 2.12: Photo of the antenna array prototype.

Especially minimization of 2.5 is obtained by constructing a sequence of trial solutions $\underline{\psi}_s^k$ (s being the trial solution index, and k the iteration index $k = 1, \ldots, K_{max}$) following the strategy of the PSO. The iterative optimization algorithm continues until the stopping criteria are reached, namely when $k = K_{max}$ or $\Phi\left(\underline{\psi}_s^k\right) < \beta$, where K_{max} and β are respectively the maximum number of iterations and a user defined convergence threshold empirically chosen. At the end of the iterative procedure the optimal solution defined as $\underline{\psi}^{opt} = arg\left\{min\left[\Phi\left(\Gamma_k\right)\right]\right\}$ and the obtained antenna geometrical parameters are used to fabricate the prototype.

2.2.4 Numerical and Experimental assessment

After the design methodology explained in the previous section and a numerical validation based on a commercial software (HFSS Designer) a prototype has been fabricated and experimentally assessed. Specifically, the antenna prototype has been printed on a 0.8 mm thick dielectric substrate with $\varepsilon_r = 3.8$ (ARLON 25N), four sub-miniature type A (SMA) coaxial connectors have been connected to the input ports of the array. The photo of the prototype is reported in Fig.2.12. The prototype has been measured in an anechoic chamber for VSWR and radiation pattern assessment. The photo of the experimental set-up is reported in Fig.2.13. The VSWR measurements have been performed at the four ports of the array prototype

with a network analyzer. Figs. 5 shows the VSWR measured in the frequency range 2.3 GHz up to 2.6 GHz for all of the four antenna ports. Figs.2.14 also shows the comparisons between numerical and experimental data, as it can be noticed from Figs.2.14(a-d). The consistency is very good and it demonstrates the capabilities of the design methodology based on evolutionary techniques. The VSWR values turned out to vary between 1.2 and 1.35. Figs.2.15 exhibit the radiation patterns of the antenna array obtained by feeding the different ports of the antenna. As it can observed, the main beam is steered in four different directions corresponding to the four input ports. Especially, the main beam is shown that the measured direction of the beams are slightly different from the theoretical ones due to using real antennas rather than isotropic elements. An error less than

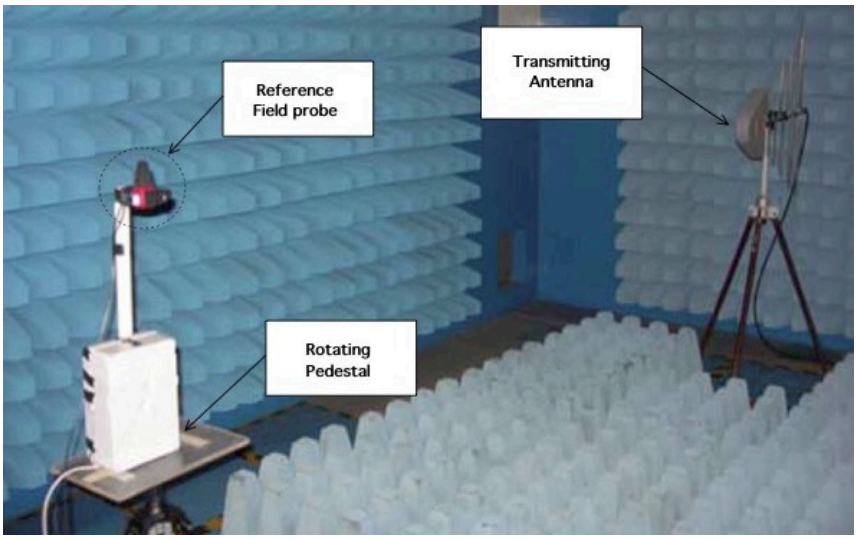

Figure 2.13: Photo of the experimental set-up arranged inside the anechoic chamber.

10° has been observed. Thus, the resulted overall beam pattern has a wide coverage angle from about 30° to 45° with relatively low side lobe levels, as observed in Figs.2.15(a-d). The measured data related to the return loss and the beam pattern are afflicted by noise. As it can be noticed, despite the noise level, the initial antenna requirements are satisfied.

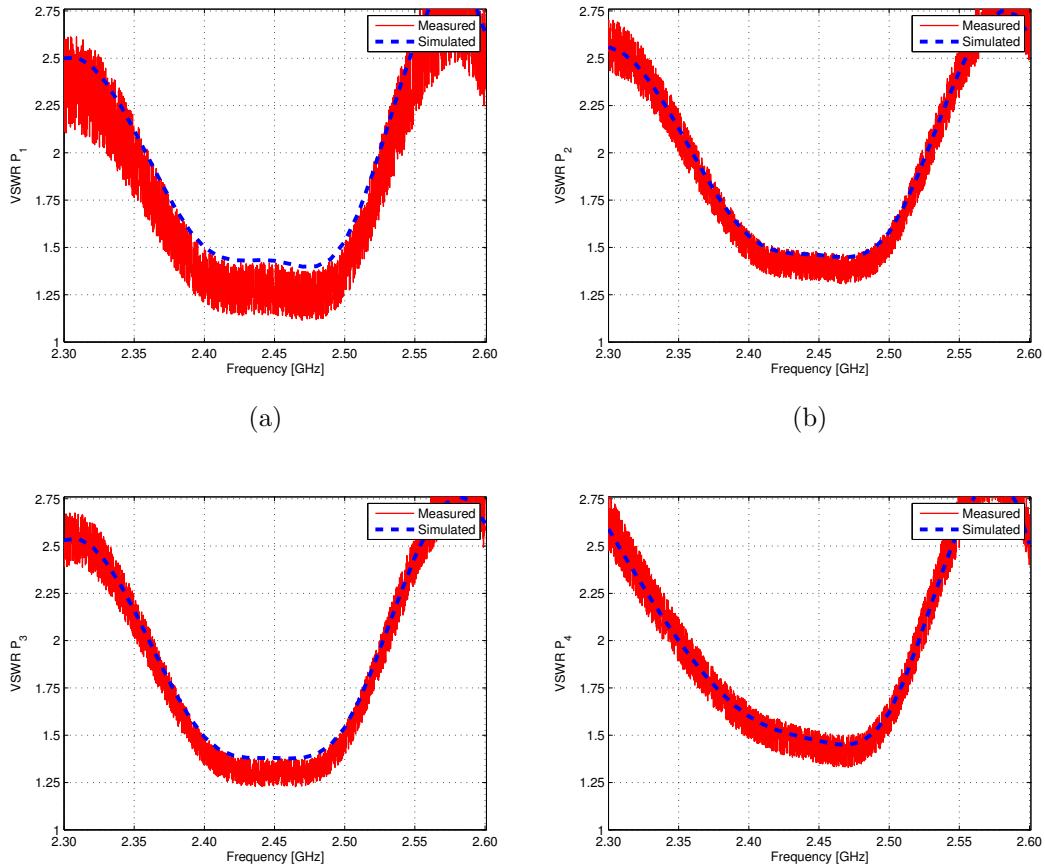

(a) (b)

(c) (d)

Figure 2.14: Measured VSWR values at (a) port 1, (b) port 2, (c) port 3, and (d) port 4.

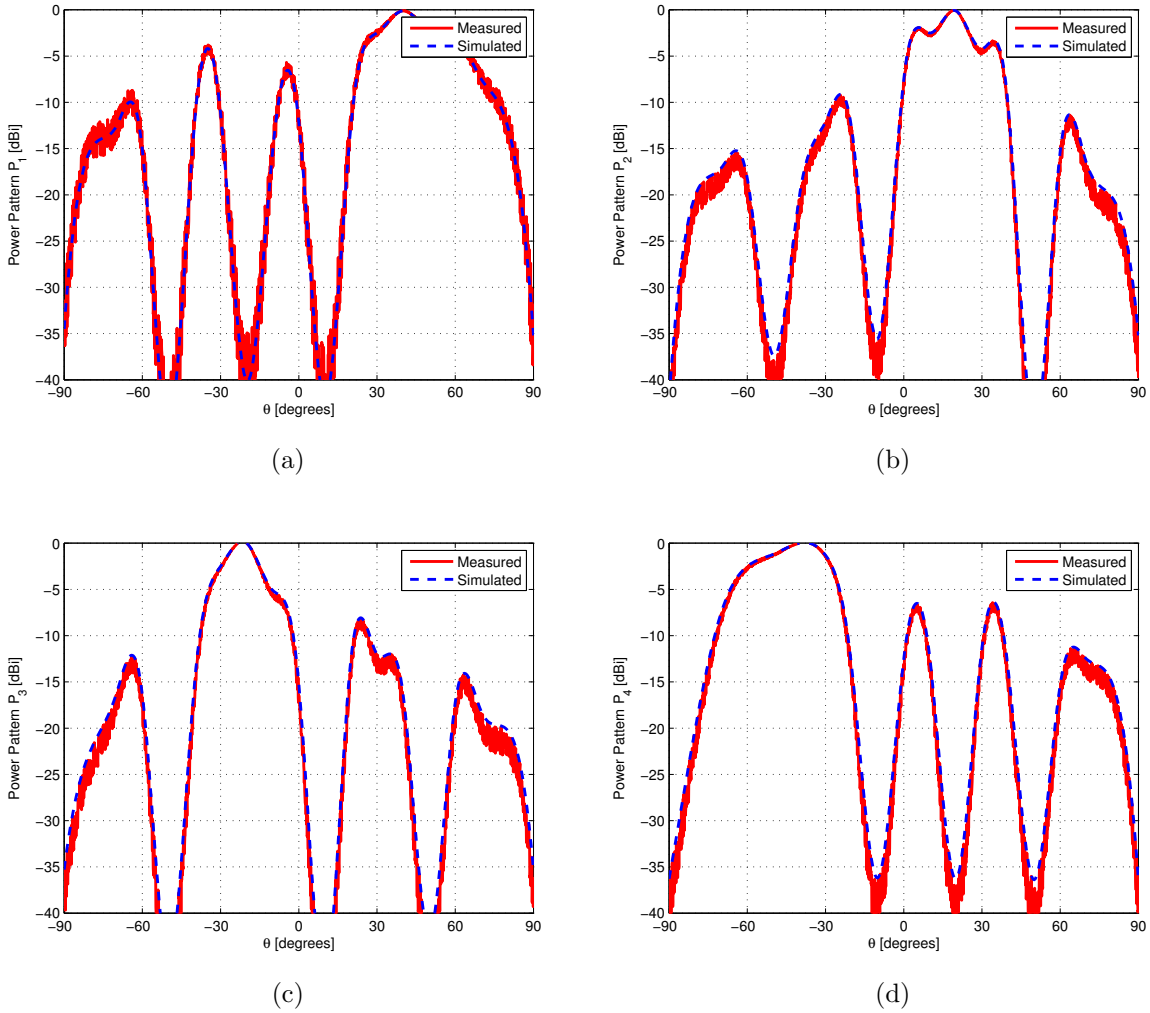

(a) (b)

(c) (d)

Figure 2.15: Measured Power pattern at (a) port 1, (b) port 2, (c) port 3, and (d) port 4.

2.3 Design and Analysis of X-band Rotman Lens using Interval Analysis Technique

2.3.1 Introduction

In the last decades, the use of reconfigurable antennas arrays with fully adaptive properties [53, 54, 55, 56, 57, 58], clearly demonstrated their effectiveness to improve the performances of a telecommunication system dramatically. That kind of antennas, commonly used in several fields such as airport surveillance, missile detection, and tracking, is unfortunately very complex, expensive and bulky to be used for commercial portable devices such as mobile phones, and tablets. Moreover, the introduction of new frequency bands that belong to the millimetric wavelength results in a dramatic increase of the feeding network components such as variable attenuators and phase shifters. For low-cost applications, the use of switched beam antennas is generally adopted instead of adaptive arrays. Recently a new kind of reconfigurable parasitic antennas, able to electronically select different configurations of the radiation patterns [59, 60, 61], have been successfully adopted for various practical applications, such as Wi-Fi systems [62], wireless sensor networks applications and sum-difference radar [63]. These antennas offer a good compromise between fully adaptive arrays and the switched beam solution, but the complexity of the feeding network is still too complex or expensive.

The Rotman lens has proven its capability to be a useful beamformer for designers of electronically scanned arrays [64]-[70]. It is particularly helpful for the design of multi-beams or reconfigurable arrays because it offers a real-time delay phase shift capability that is independent in frequency and removes the need for expensive phase shifters to steer a beam over wide angles. The Rotman lens has a long history in communication

systems ranging from military radar up to standard radio links [5]. The Rotman lens is a planar structure, which can be easily implemented with microstrip technology, and it is used to feed an antenna array to obtain a multi beams behaviour; since it does not require lumped elements or other RF devices, it is simple, cheap, and mechanically robust. Despite the simplicity of the design equations, they are not able to take into account all the real-world effects, such as the material or fabrication tolerances, that can actively reduce the performances of the Rotman lens and require an expensive experimental calibration tuning [71]-[81]. The proposed method in this work is based on the use of the Interval Analysis (IA) and the Interval Arithmetic for the design of the Rotman. IA was initially introduced to bound rounding errors in numeric computations [82], [83], and it has been then extended to the solution of linear and non-linear equations and functional optimisation [84], [85]. Nowadays, interval analysis is widely used in many engineering applications, but its applications to electromagnetics are still limited to few applications mainly concerned with the design of robust antenna [86] or microwave imaging applications [87]-[89]. In this work, the reliability of the IA is used to define an innovative design method where the Rotman lens design formulas are firstly reformulated within the Intervals Arithmetic, and secondly, an IA-based refinement algorithm is to be applied to identify the lens parameters better.

2.3.2 Mathematical Formulation

A Rotman lens is a feeding network made with a parallel plate structure. The shape is carefully chosen to produce a wavefront across the output ports, which connect the array elements, that are phased by the time delay. A standard Rotman lens layout is shown in Fig. 2.16: as it can be noticed it consists of a parallel plate region surrounded by a number N_a of output ports, N_b input ports called beam ports, and a number of N_d dummy ports

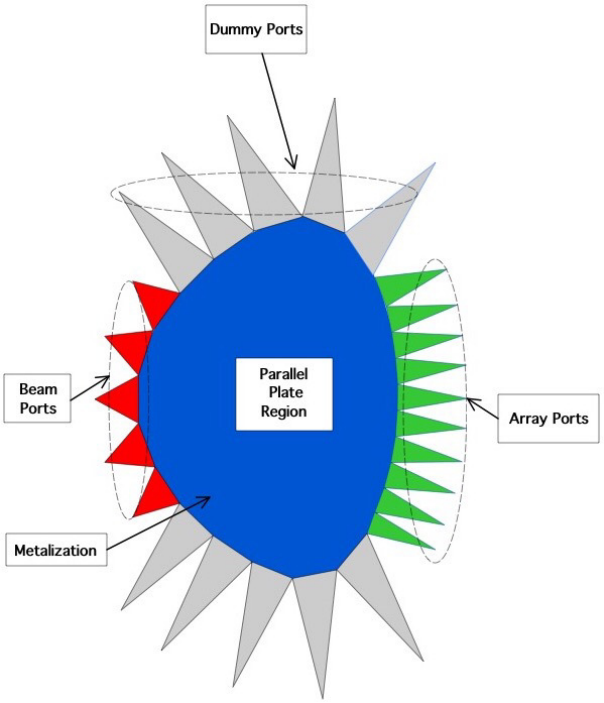

Figure 2.16: Rotman lens geometry.

used to obtain reflectionless termination around the parallel plate region. The design of a Rotman lens starts with the definition of the number of radiating elements (N_a) and their location along the array axis, the number of beams and the required beam steering angles. The other lens parameters are the focal angle α, the focal ratio $\eta = \frac{f_2}{f_1}$, and the expansion factor defined as $\gamma = \frac{sin(\theta)}{sin(\alpha)}$. The length of the transmission lines that connect the array elements located on the array axis must be normalized with respect to the focal length f_1. These parameters are shown in Fig. 2.17, where it can be seen that F_0, F_1, and F_2 are the three foci of the circular beam port arc (in these points there are no phase errors), following the formulation reported in [70] and considering the interval arithmetics rules [82]. The tolerances of the considered ceramic material ARLON25N are $t = 0.5 \pm 0.07[mm]$, thickness of the metalization $t_m = 10 \pm 2[\mu m]$, $\varepsilon_r = 3.28 \pm 0.05$. The mechanical tolerance of the CNC machine for the microstrip

width, lens geometrical characteristics, tapered line structure, transmission lines length, and antenna elements dimensions is $\pm 0.05[mm]$. Considering the above mechanical and electrical tolerances, the lens design formulas have been reformulated. A given interval is represented with a tilde as follow: $\tilde{\varepsilon} = [inf\{\tilde{\varepsilon}\}; sup\{\tilde{\varepsilon}\}]$ where $inf\{\tilde{\varepsilon}\} = \varepsilon - \varepsilon^{(inf)}$ and $sup\{\tilde{\varepsilon}\} = \varepsilon + \varepsilon^{(sup)}$. The array ports phase center locations $\left(\tilde{x}_n^{(ap)}, \tilde{y}_n^{(ap)}\right), n = 1, ..., N_a$ are provided by the following equations:

$$\begin{aligned} \tilde{x}_n^{(ap)} &= 1 - \frac{\frac{1}{2}\tilde{\Upsilon}_n^2 sin^2(\alpha) + \left(1-\tilde{\beta}\right)\tilde{W}}{1-\tilde{\beta}cos(\alpha)} \\ \tilde{y}_n^{(ap)} &= \tilde{\Upsilon}_n \left(1 - \frac{\tilde{W}}{\tilde{\beta}}\right), n = 1, ..., N_a \end{aligned} \tag{2.6}$$

With the knowledge of the array port positions, the solution of the following equation can provide the length of the transmission microstrips connected with the antenna elements (Fig. 2.17 green line):

$$\tilde{a}\tilde{W}^2 + \tilde{b}\tilde{W} + \tilde{c} = 0 \tag{2.7}$$

where $\tilde{W}_n = \frac{\tilde{w}_n}{\tilde{f}_1}, \{n = 1, ..., N_a\}$ are the normalized lengths of the transmissions line connected with the antenna ports and the antenna elements. The coefficients a, b, and c are defined by:

$$\begin{aligned} \tilde{a} &= 1 - \frac{\left(1-\tilde{\beta}\right)^2}{\left(1-\tilde{\beta}cos(\alpha)\right)^2} - \frac{\tilde{\Upsilon}_n^2}{\tilde{\beta}^2}, \\ \tilde{b} &= -2 + \frac{\tilde{\Upsilon}_n^2}{\tilde{\beta}} + \frac{2\left(1-\tilde{\beta}\right)}{1-\tilde{\beta}cos(\alpha)} - \frac{\tilde{\Upsilon}_n^2 sin^2(\alpha)\left(1-\tilde{\beta}\right)}{\left(1-\tilde{\beta}cos(\alpha)\right)^2}, \\ \tilde{c} &= -\tilde{\Upsilon}_n^2 + \frac{\tilde{\Upsilon}_n sin^2(\alpha)}{\left(1-\tilde{\beta}cos(\alpha)\right)} - \frac{\tilde{\Upsilon}_n^4 sin^4(\alpha)}{4\left(1-\tilde{\beta}cos(\alpha)\right)^2} \end{aligned} \tag{2.8}$$

with $\tilde{\Upsilon}_n = \frac{\tilde{y}_n^{(ap)}\gamma}{\tilde{f}_1}$. The solution of equation 2.7 provides the intervals of each transmission line length $\tilde{w}_n, \{n = 1, ..., N_a\}$. The locations of the beam

ports $\left(\tilde{x}_m^{(bp)}, \tilde{y}_n^{(bp)}\right), m = 1, ..., N_b$ aimed at steering the main beam towards $\theta_m, m = 1, ...N_b$ can be estimated considering the following relations:

$$\begin{aligned} \tilde{x}_m^{(bp)} &= \tilde{\vartheta}\left(1 - cos\left(\chi + \tilde{\varphi}\right)\right), \\ \tilde{y}_m^{(bp)} &= \tilde{\vartheta}\left(cos\left(\chi_m + \tilde{\varphi}\right)\right), m = 1, ..., N_b \end{aligned} \tag{2.9}$$

where

$$\begin{aligned} \tilde{\vartheta} &= 1 - \frac{\left(1-\tilde{\beta}^2\right)}{2\left(1-\tilde{\beta}cos(\alpha)\right)}, \\ \chi_m &= sin^{-1}\left(\frac{sin(\theta_m)}{\gamma}\right), \\ \tilde{\varphi} &= sin^{-1}\left(\frac{1-\tilde{\vartheta}}{\tilde{\vartheta}}\right) \end{aligned} \tag{2.10}$$

The above formulas allow to estimate the geometrical layout of the lens, while the following one allows to estimate the coupling terms between the N_b and the N_a beam and array ports:

$$\tilde{S}_{m,n} = \frac{sin\left(\frac{k\tilde{w}_m}{2}sin(\phi_m)\right)}{\frac{k\tilde{w}_m}{2}sin(\phi_m)} \; \frac{sin\left(\frac{k\tilde{w}_n}{2}sin(\phi_n)\right)}{\frac{k\tilde{w}_n}{2}sin(\phi_n)} \times \sqrt{\frac{\tilde{w}_m\tilde{w}_n}{\tilde{\lambda}\tilde{d}}}e^{-j\left(k\tilde{d}+\frac{\pi}{4}\right)} \tag{2.11}$$

where $\tilde{k} = \frac{2\pi}{\tilde{\lambda}}$ is the interval of the wavenumber in the dielectric substrate, $\tilde{d}$ is the interval of inter-element distance between the array elements, $\tilde{w}_n$ and $\tilde{w}_m$ are the intervals of the beam and array widths respectively, ϕ_n and ϕ_m are two angles measured considering the ports boresight direction and the segment connecting the phase centers of the ports m and n. Equation 2.11 provides a prediction of fundamental antenna parameters such as array factor, phase error, and illumination amplitudes. The formulas 1-6 provide all information needed for the geometrical structure of the Rotman lens as intervals, to obtain a better refinement of the intervals estimation the Skelboe Moore algorithm has been used. It is worth noticing that after the

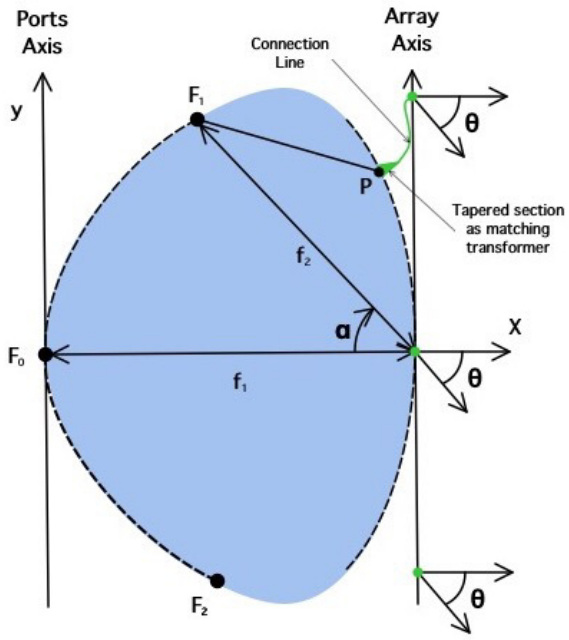

Figure 2.17: Rotman lens design parameters.

design of a Rotman lens, often a manual tuning or an optimization phase is mandatory to obtain the required performances and move towards the fabrication of an experimental prototype. The proposed method based on the interval arithmetics permits to avoid the time-consuming tuning phase and provides the lens geometrical parameters able to take into account the tolerances of materials and to guarantee the initial design requirements.

2.3.3 Numerical and Experimental assessment

The proposed-based design method is assessed by reporting and discussing a selected set of representative results of numerical simulations in the following subsections. All the numerical simulations have been carried on by considering a ceramic substrate ARLON25N of $0.5[mm]$ thickness dielectric permittivity $\varepsilon_r = 3.28$ and $tan\,(\delta) = 10^{-3}$. Starting from the obtained numerical data, an experimental prototype operating in the X band (8-

12GHz) has been designed, fabricated and assessed.

Numerical Assessment

In the first experiment, an S-band (2-4 GHz) Rotman lens has been considered. The lens parameters are: four beam ports with a scan angle of ± 25 [degrees], center frequency $f_c = 2.45GHz$. Ten array ports and four dummy ports. The S-band lens is characterized with a focal length $f_1 = 5.5\lambda$, a focal angle of $\alpha = 25$ [degrees], a focal ratio $\beta = \frac{f_2}{f_1} = 0.9$, and an expansion factor of $\gamma = 1$. The ports impedance is $50[\Omega]$. All ports are connected with tapered transmission lines aligned towards the lens center. The tapered lines length, aimed at guaranteeing a good impedance matching and a phase error reduction, present a length $L_t = 1\lambda$, while the beam and array ports are connected with microstrip lines of length $L_m = 0.5\lambda$. The S-band Rotman lens geometry, obtained after the application of the design formulas 2.8, 2.9, 2.10 and the Skelboe Moore refinement algorithm [82]. In particular, the beam, array, and dummy ports positions are shown Fig.2.18. All the ports positions are reported considering the intervals of confidences provided by the upper and lower limits. The geometry layout of the S band Rotman lens is reported in Fig.2.19.

To assess the S band lens performances the return loss S_{11} at the input beam ports have been estimated. In particular the return loss vs. frequency has been measured in the range between 2.0 GHz and 3.0 GHz. The results are reported in Fig.2.20, as it can be noticed the obtained results are quite satisfactory the return loss is always in the range $-14dB > S_{11} > 18dB$. The isolation between the input ports is estimated in Figs.2.21 (a) and (b), in particular Fig.2.21 (a) reports the isolation between two adjacent ports P_1 and P_2 while Fig. 2.21 (b) reports the isolation between two distant ports P_1 and P_4. As it can be noticed from the data reported in Figs 2.21 the isolation is very good, below $-20dB$ for the adjacent ports P_1 and P_2,

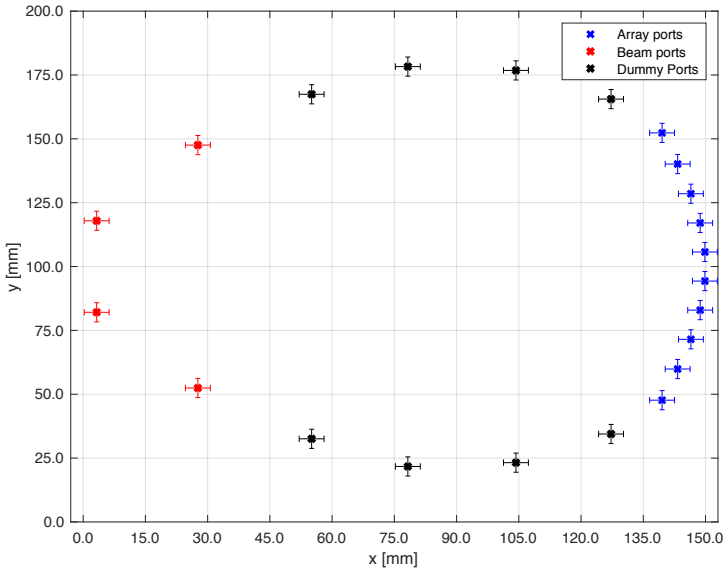

Figure 2.18: S band rotman lens ports positions and positions tolerances after IA interval refinement.

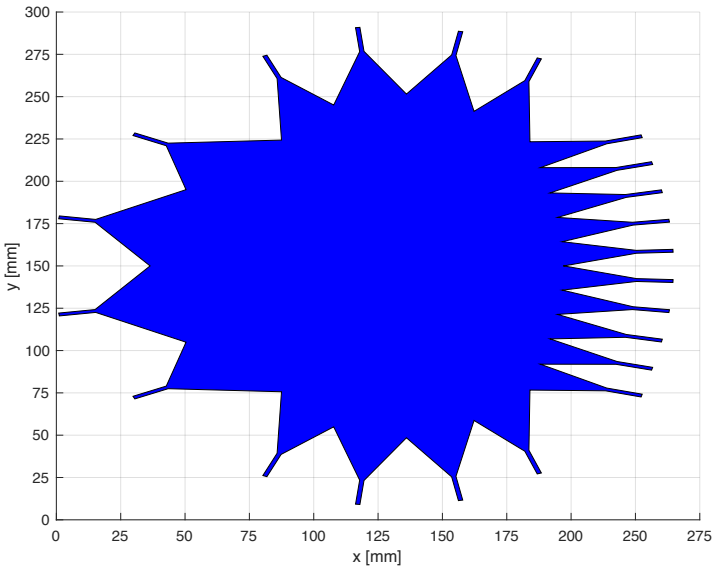

Figure 2.19: S band rotman lens geometry.

and $-30dB$ for the distant ports P_1 and P_4. To show the focusing efficacy of the lens, the surface current flowing from the beam port P_1 to the ten array ports $P_{13}, P_{14}, ...P_{22}$ is reported in Fig.2.22. Finally the phase errors measured at the ten array ports $P_{13}, P_{14}, ...P_{22}$ are reported in Fig. 2.23, as

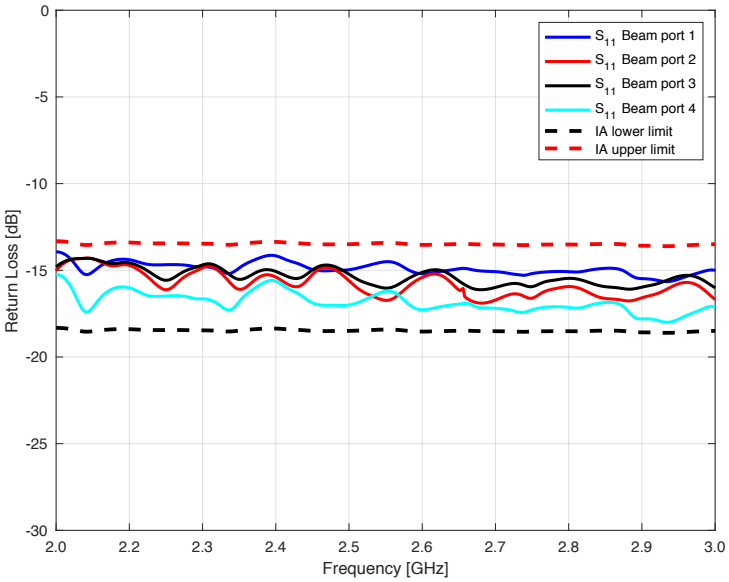

Figure 2.20: S band rotman lens, Return loss at the beam ports.

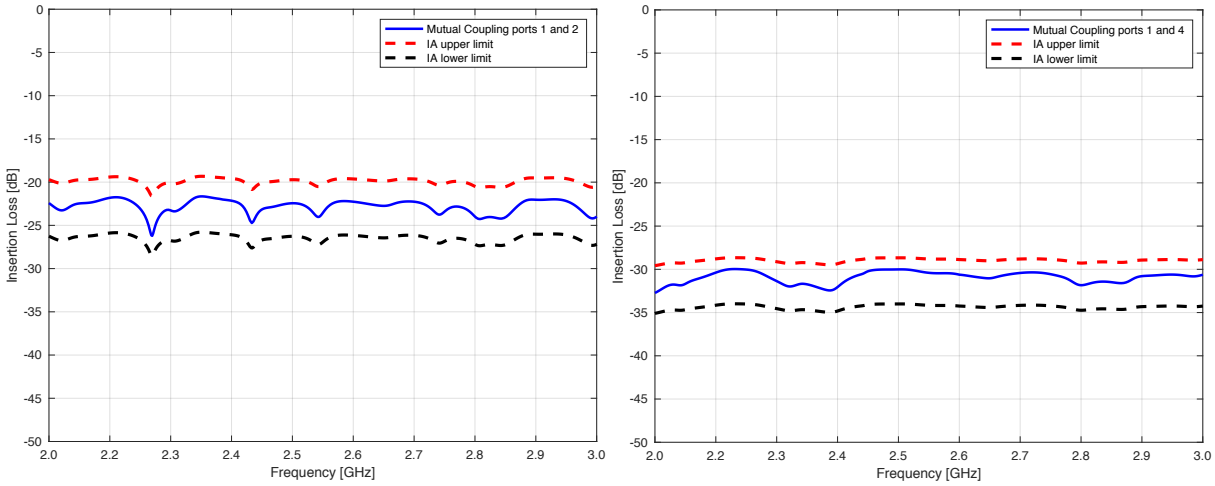

(a) (b)

Figure 2.21: S band rotman lens. Coupling factor vs. frequency between (a) ports 1 and 2 and (b) ports 1 and 4.

expected the maximum phase error is measured at the ports P_{13} and P_{22} placed at the ends of the lens. However the maximum phase error is below 1.5 degrees.

In the next experiment a C-band (5-7 GHz) Rotman lens has been con-

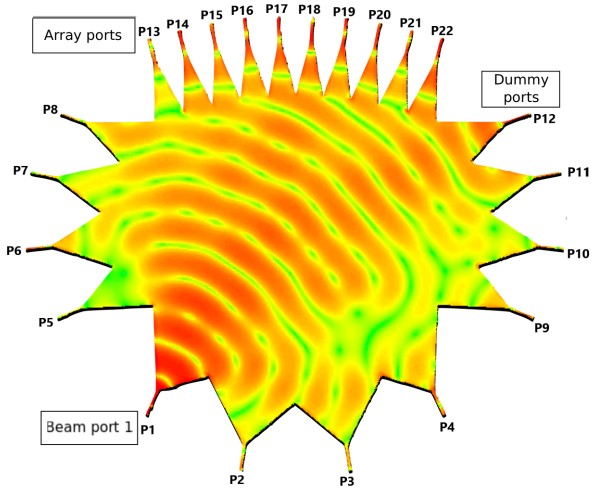

Figure 2.22: S band rotman lens, currents distribution with beam port -2 feeded.

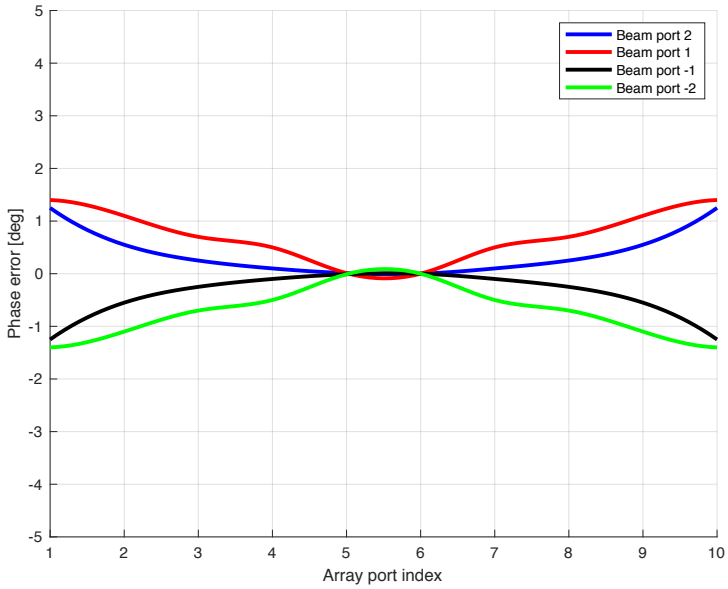

Figure 2.23: S band rotman lens, phase errors at the array ports.

sidered. Also in this experiment four input beams ports with a scan angle of ± 25 [degrees], ten arrays ports and four dummy ports have been considered. Also in this case the port impedance was $50[\Omega]$. The lens center frequency was $f_c = 5.8GHz$. Also the the other C-band geometrical parameters are the same of the previous example in particular: focal length $f_1 = 5.5\lambda$, focal angle of $\alpha = 25$ [degrees], focal ratio $\beta = \frac{f_2}{f_1} = 0.9$, expan-

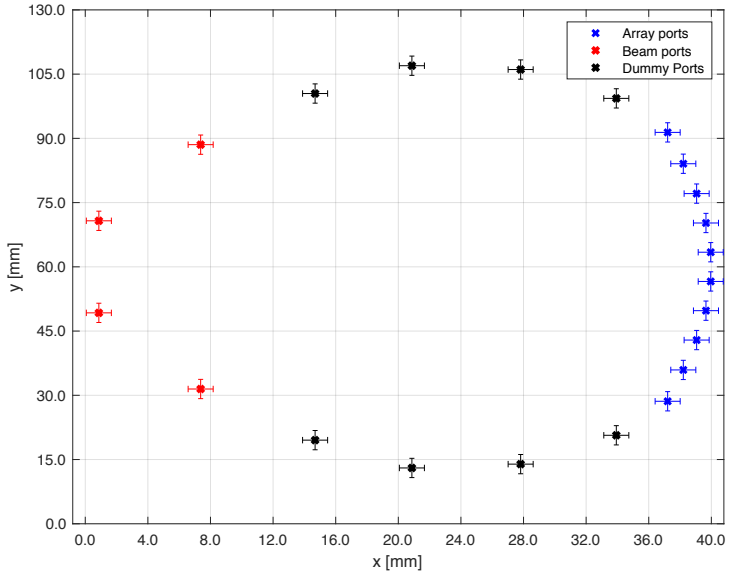

Figure 2.24: C band rotman lens ports positions and positions tolerances after IA interval refinement.

sion factor of $\gamma = 1$. All ports are connected with tapered transmission lines of length $L_t = 1\lambda$, aligned towards the lens center. While the tapered microstrip lines that connect beam and array ports have a length of $L_m = 0.5\lambda$. The lens geometry, and the ports positions have been obtained after the application of the design formulas 2.8, 2.9, 2.10 and the Skelboe Moore refinement algorithm [82]. The ports positions including the upper and lower limits provided by the IA analysis are shown Fig.2.24 while the complete geometry of the C band Rotman lens is reported in Fig.2.25.

The scattering parameters of the C-Band prototype have been estimated, in particular the return loss and the isolations at the input beam ports are reported in Fig.2.26 and Figs.2.27. The obtained results are quite good with a return loss in the range $-12dB > S_{11} > -22dB$, an isolation between two adjacent ports P_1 and P_2 below $-20dB$, and an isolation below $-29dB$ for the more distant ports P_1 and P_4. The current distribution flowing from beam port P_4 toward the ten array ports $P_{13}, P_{14}, ...P_{22}$ is reported in Fig.2.28, the effects of the dummy ports are particularly evident

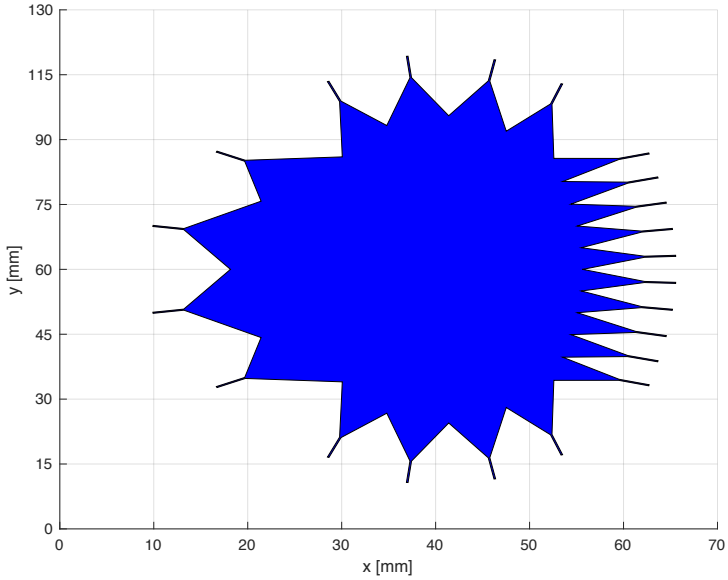

Figure 2.25: C band rotman lens geometry.

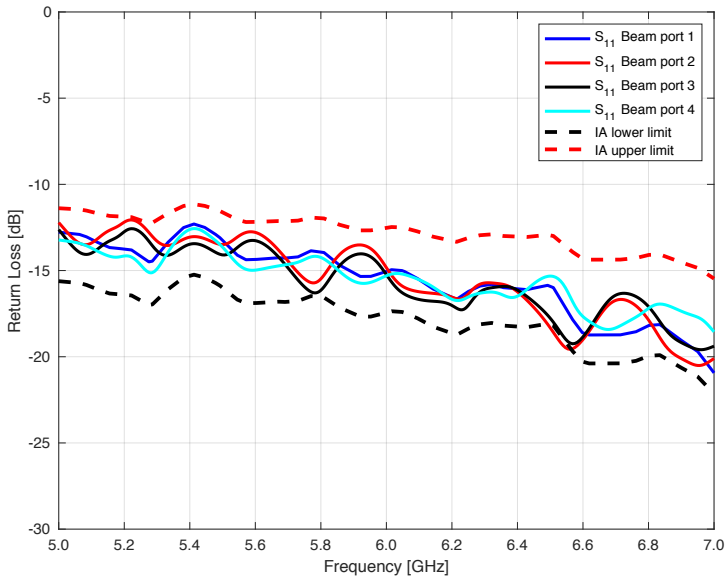

Figure 2.26: C band rotman lens, Return loss at the beam ports.

in the left side of the lens. The phase error is quite satisfactory, from the data reported in Fig.2.29 the phase error is always below 1.5 degrees as in the previous experiment.

In the last experiment a Rotman lens at K band (22 - 26 GHz) has been considered. The considered lens structure is characterized by six input

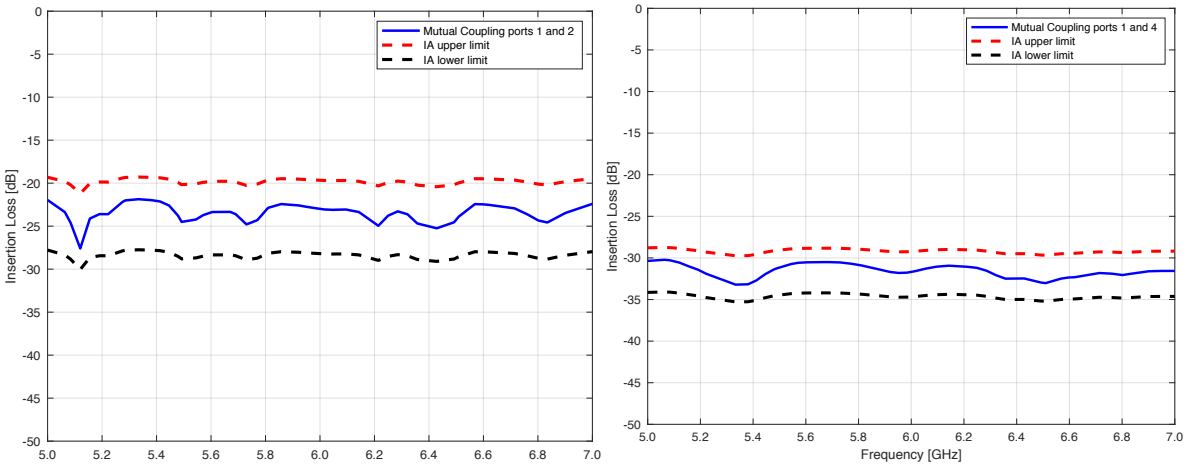

(a) (b)

Figure 2.27: S band rotman lens. Coupling factor vs. frequency between (a) ports 1 and 2 and (b) ports 1 and 4.

beam ports, with a steering angle of 35 degrees, two dummy ports and sixteen output array ports. The considered central frequency was $f_c = 24.0GHz$ and the ports impedance was $50[\Omega]$. The other lens geometrical characteristics are: focal length $f_1 = 5.0\lambda$, focal angle of $\alpha = 35$ [degrees], focal ratio $\beta = \frac{f_2}{f_1} = 0.9$, expansion factor of $\gamma = 1$. Length of the tapered line $L_t = 1\lambda$, lengths of microstrip lines connected with the beam and array ports $L_m = 0.5\lambda$.

The width of the beam, array, and dummy tapered sections are $w_{tb} = 26\,[mm]$, $w_{ta} = 8.5\,[mm]$ and $w_{td} = 25.32\,[mm]$ respectively. The length of the tapered lines and of the $50\,[\Omega]$ transmission lines which connect the ports are 1.5λ and 0.5λ respectively. The ports positions and the geometry of the K band Rotman lens, obtained after the IA procedure and the refinement algorithm, are reported in Fig. 2.30 and Fig.2.31 respectively. The return loss at the six input beam ports P_1 -P_6 is quite satisfactory and always between the limits, $-13dB > S_{11} > -24dB$, predicted by the IA procedure. Also the isolation between the input beam ports is quite good, in particular the nearest ports P_1 and P_2 show an isolation below $-20dB$

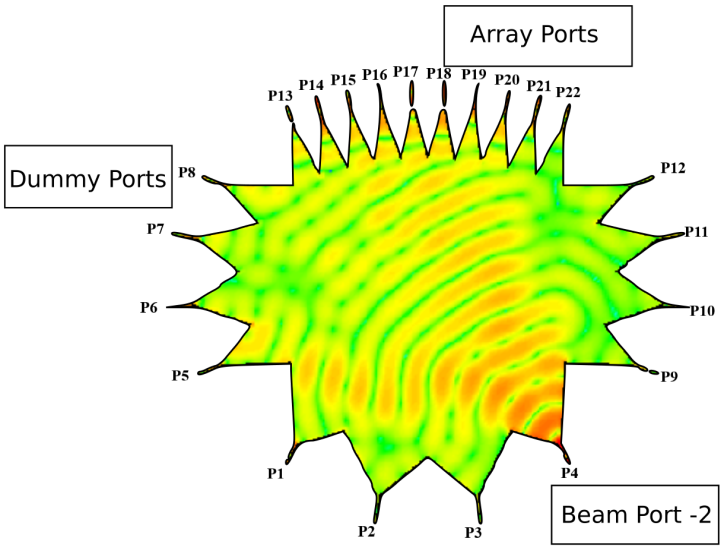

Figure 2.28: C band rotman lens, currents distribution with beam port -2 feeded.

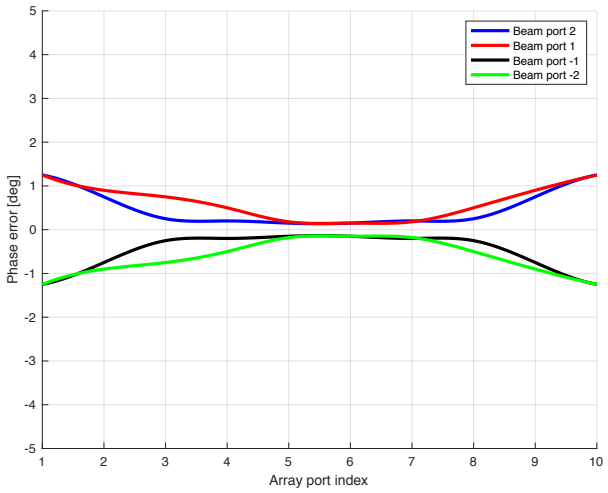

Figure 2.29: C band rotman lens, phase errors at the array ports.

while the isolation of about $-28dB$ is measured between ports P_1 and P_6 as reported in Figs.2.33 (a) and (b). The current distribution between each input beam port and the array ports, are reported in Figs.2.34 (a)-(f). As it can be noticed from the data reported in Figs. 2.34, the focusing effect of the Rotman lens is quite evident. Concerning the phase error at the array ports, the maximum measured phase error at the ports placed far away from the lens center, was below 2.5 degrees, whilst the error at the

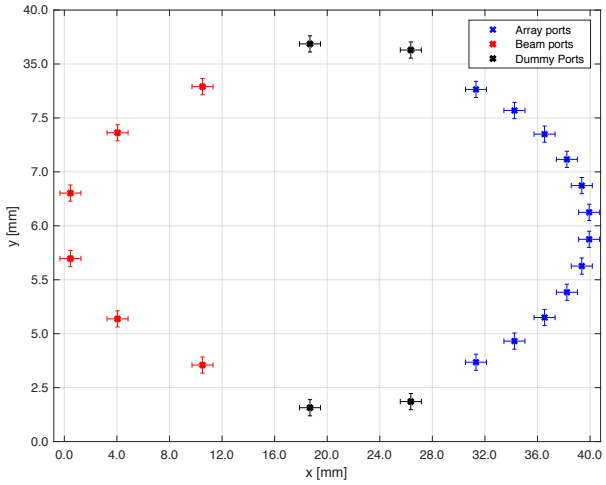

Figure 2.30: K band rotman lens ports positions and positions tolerances after IA interval refinement.

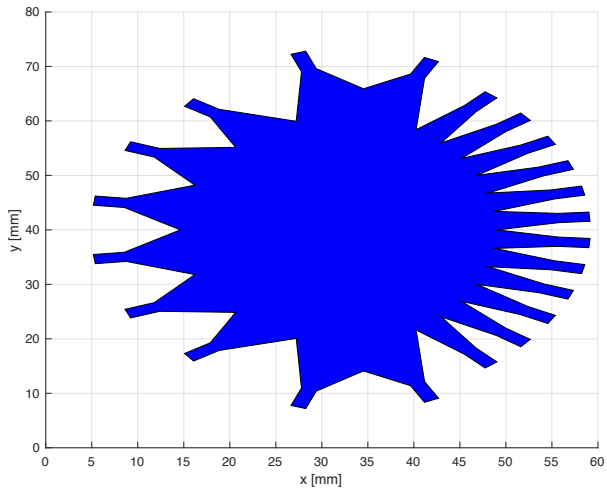

Figure 2.31: K band rotman lens geometry.

mechanical boresight of the lens was below 1.5 degrees. The phase errors is higher with respect to the other lens structures considered in the previous experiments, as expected since the wavelength is lower.

Experimental Assessment

In this subsection an experimental X-band Rotman lens prototype has been designed, fabricated and assessed. The considered Rotman lens parameters

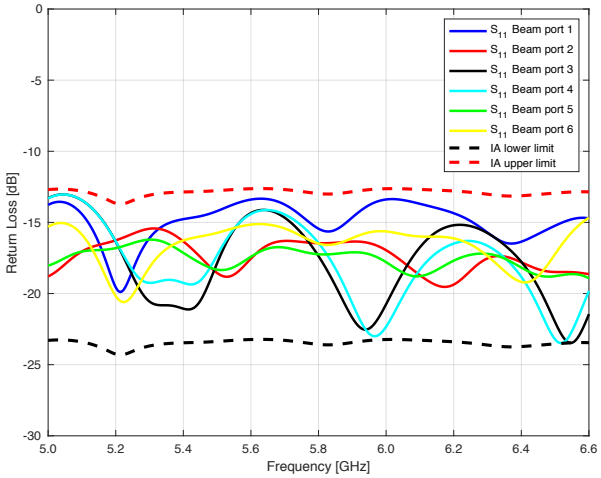

Figure 2.32: K band rotman lens, Return loss at the beam ports.

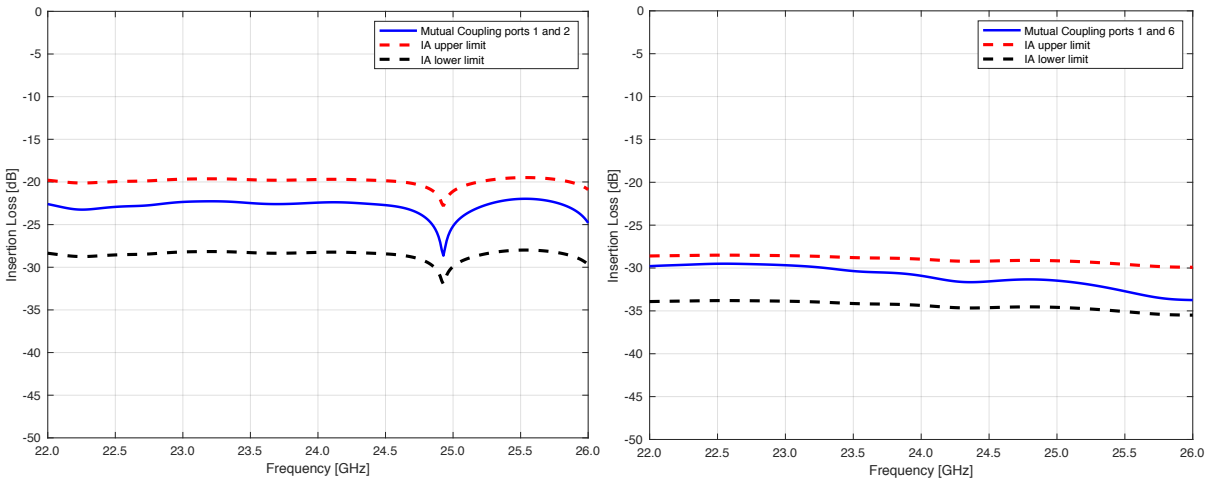

(a) (b)

Figure 2.33: K band rotman lens. Coupling factor vs. frequency between (a) ports 1 and 2 and (b) ports 1 and 6.

are the following: six input beam ports, scan angle ±30[degrees], center frequency of $10GHz$ with a $4GHz$ bandwidth to cover the whole X-band range. The high bandwidth provided by the Rotman lens feeding network is strongly limited to $500MHZ$, by the radiators (rectangular patch antennas equipped with a quarter wavelength matching transformer). Sixteen array ports connected to sixteen antennas with an inter-element spacing of

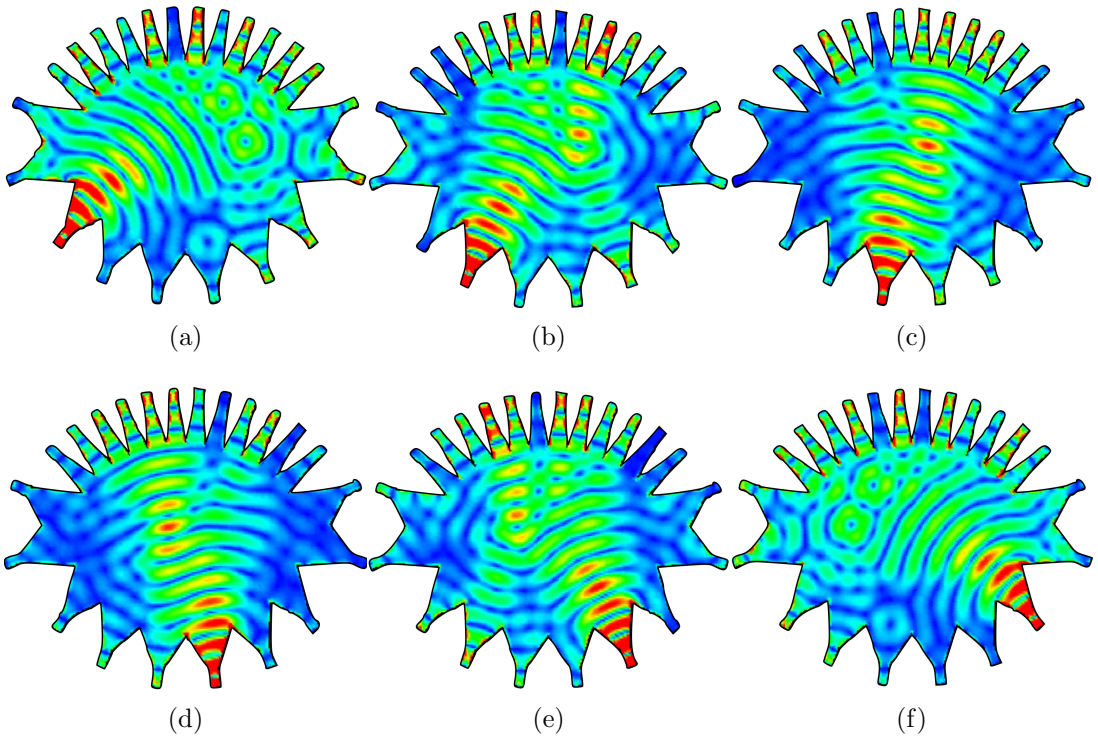

Figure 2.34: K band rotman lens. currents distribution, (a) port 3, (b) ports 2, (c) port 1, (d) port -1, (e) port -2, (f) port -3.

0.4λ. Summarizing the feeding network is characterized by $N_a = 16$ array ports, $N_b = 6$ beam ports, and $N_b = 4$ dummy ports. Concerning the other lens parameters a focal length of $f_1 = 6$, a focal angle of $\alpha = 35$ [degrees], a focal ratio $\beta = \frac{f_2}{f_1} = 0.9$, an expansion factor of $\gamma = 1$ and $50[\Omega]$ for the ports impedance have been considered. The lens is realized considering a ceramic substrate ARLON25N of $0.5[mm]$ thickness dielectric permittivity $\varepsilon_r = 3.28$ and $tan\,(\delta) = 10^{-3}$. A circular curvature lens on the beam and array ports have been considered and four dummy ports aimed at absorbing energy reflections at the top and bottom side of the lens structure. All ports are connected with tapered transmission lines which are aligned towards the lens center, and the tapered lines are aimed at guaranteeing a good impedance matching, good beams, and a phase error reduction. To apply formulas 2.6-2.9 for the geometrical estimation of geometrical

lens parameters with IA the following intervals tolerances have been considered: $\tilde{\varepsilon}_r = \{3.23; 3.33\}$, $\tilde{t} = \{0.43; 0.57\}\,[mm]$, $\tilde{t}_m = \{8; 12\}\,[\mu m]$, and $\tilde{L} = \{L - 0.05; L + 0.05\}\,[mm]$ being L a geometrical parameter indicating a given length. After the application of design formulas and the Skelboe Moore refinement algorithm [82] beam, array and dummy ports positions are estimated. Fig.2.35 shows the ports positions with the intervals of confidences provided by the upper and lower limits. The exact ports coordinates are reported in Tab.2.2, 2.3, and 2.4 which report the positions of the array, beam and dummy ports respectively. The width of the beam, array, and dummy tapered sections are $w_{tb} = 26\,[mm]$, $w_{ta} = 8.5\,[mm]$ and $w_{td} = 25.32\,[mm]$. The length of the tapered lines and of the $50\,[\Omega]$ transmission lines which connect the ports are 1.5λ and 0.5λ respectively. The geometry of the obtained Rotman lens is shown in Fig.2.36. The phase errors at the array ports have been estimated by considering relation 2.11, the results are shown in Fig. 2.37. As expected the higher phase errors can be found where the ports are placed far away from the lens boresight and it can be noticed from the data in Fig.2.37: the maximum phase error is about ± 2 degrees, whilst the amplitude errors at the outer ports is about $1.5dB$. The correspondent computed lens array factor for all the beam ports are reported in Fig. 2.38.

X band prototype description

After the IA design procedure and the preliminary numerical estimation of the lens characteristics, an antenna array prototype, with a Rotman lens as a feeding network, has been fabricated and assessed. In particular, sixteen rectangular patch antennas equipped with a quarter wavelength transformer have been connected to the $N_a = 16$ array ports with sixteen microstrip lines; each length has been estimated by solving equation (2.7). The lens geometrical parameters are retrieved from Table 2.2, 2.3, and 2.4.

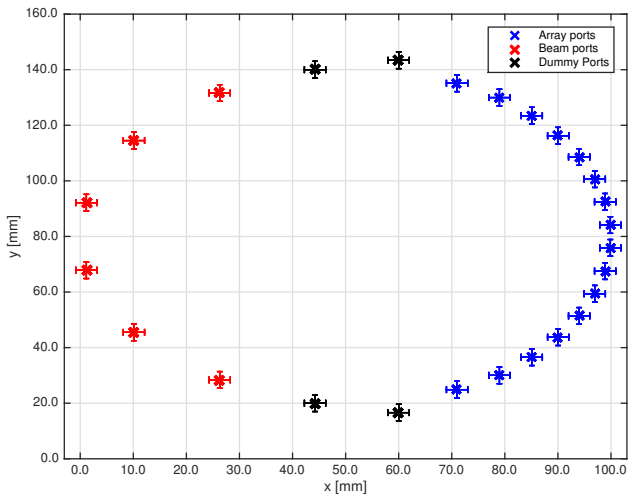

Figure 2.35: X band Rotman lens prototype. Ports positions and positions tolerances after IA interval refinement.

Table 2.2: Array ports positions [mm]

	p_1	p_2	p_3	p_4	p_5	p_6
x_n^{ap}	130.11	138.21	145.05	150.22	153.11	155.32
y_n^{ap}	55.10	58.52	66.01	73.42	81.33	89.00
	p_7	p_8	p_9	p_{10}	p_{11}	p_{12}
x_n^{ap}	157.92	158.51	159.01	158.02	156.32	153.65
y_n^{ap}	97.54	102.11	115.43	124.14	131.02	138.11
	p_{13}	p_{14}	p_{15}	p_{16}		
x_n^{ap}	148.06	143.41	137.42	130.02	-	-
y_n^{ap}	142.71	155.02	162.31	164.21	-	-

Table 2.3: Beam ports positions [mm]

	p_1	p_2	p_3	p_4	p_5	p_6
x_n^{bp}	85.13	70.15	59.12	59.11	70.34	85.31
y_n^{bp}	55.25	76.11	97.24	122.23	145.03	160.14

Table 2.4: Dummy ports positions [mm]

	p_1	p_2	p_3	p_4
x_n^{dp}	102.51	117.11	102.52.12	117.43
y_n^{dp}	44.51	47.12	174.41	177.31

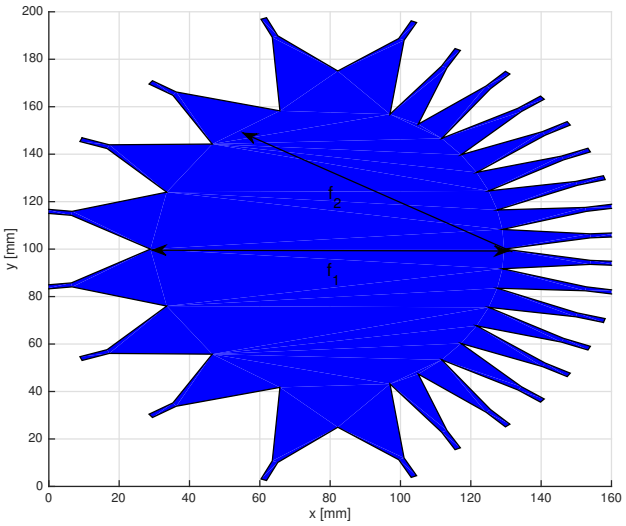

Figure 2.36: Geometry of the X band Rotman lens.

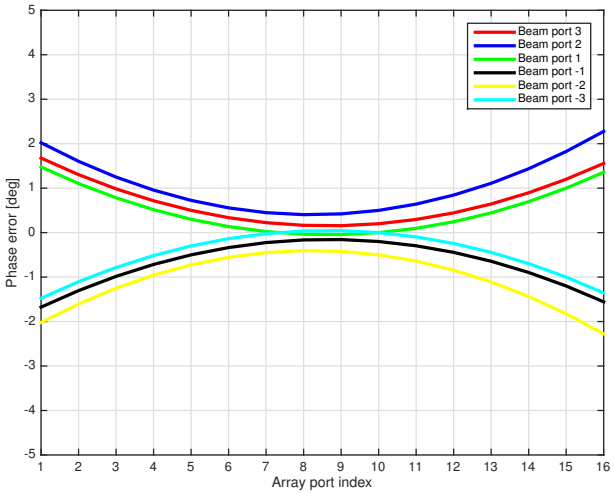

Figure 2.37: Array ports phase errors.

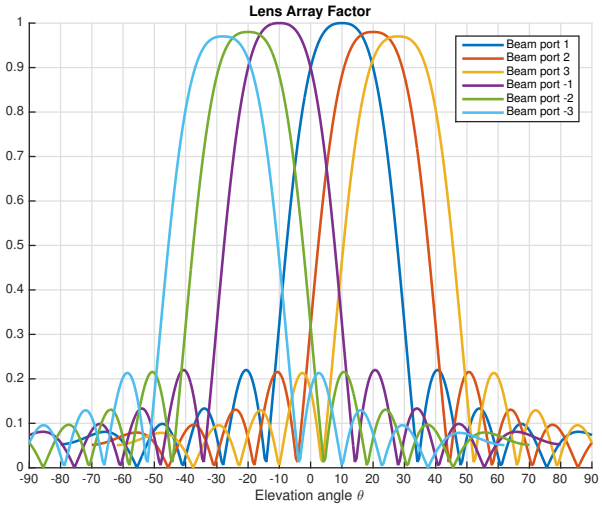

Figure 2.38: Rotman lens array factor rosette.

The prototype has been obtained with a CNC milling machine with a mechanical resolution of 0.05 $[mm]$. The prototype is shown in Fig.2.39: it has been equipped with ten subminiature type A (SMA) coaxial connectors in order to measure the prototype scattering parameters. An experimental setup has been arranged in an anechoic chamber. The first set of measurements concerns the estimation of the return loss at the beam ports. For the sake of comparisons, the measurements have been compared with the simulation obtained with commercial software, namely ADS 2019. In particular, the insertion loss measures are reported in Fig. 2.40, which also reports the synthetic results obtained with ADS and considering the upper and lower limits of the geometrical lens parameters provided by the IA approach. It can be noticed the data from Fig.2.40 the measured insertion loss is quite satisfying: below $-12dB$ for all the considered frequency range. The second set of measures is related to the estimation of the isolation between the beam ports. In particular, the insertion loss parameter has been estimated for each couple of ports. In particular, Figs.2.41 (a) and (b) report the measured insertion loss between two adjacent ports (port 1

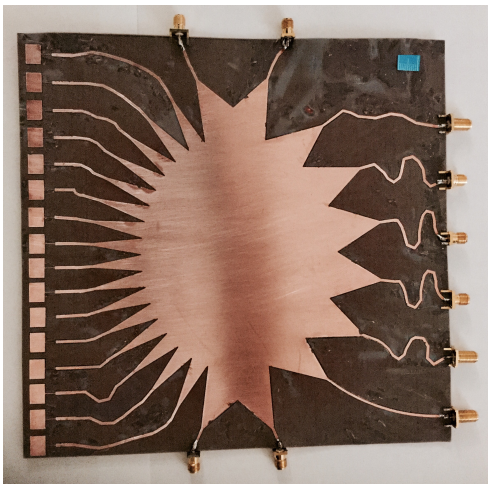

Figure 2.39: Photo of the Rotman lens prototype equipped with SMA coaxial connectors.

and 2) Fig.2.41 (a), and between two distant ports (port 1 and 6). As it can be noticed from the data of Fig.2.41 the isolation between the beam ports is very good, about $-22dB$ and $-32dB$ for the adjacent and distant ports respectively. Also, the measured data have been compared with the simulated ones, and by considering the upper and lower IA limits. The predicted and measured values are very similar. Fig. 2.42 shows the measured array pattern rosettes at $10GHz$ for beams 1-6. Moreover, it can be noticed that the main beam is correctly steered toward the angular direction of the ports. In particular the Table 2.5 reports the required and measured direction of the main beam and its directions. As it can be noticed, the higher measured error is $+3degrees$. The shape of the main beam is quite regular, and the secondary side lobe level (SSL) is satisfactory and comparable with the simulated results obtained with ADS.

Fig.2.43 and 2.44 report the comparisons of predicted and measured beam patterns related to beam ports p_{-1} and p_3 respectively. The numerical values have been obtained considering the upper and lower geometrical parameters provided by the IA rules and the refinement algorithm. It can be noticed that the measured main beam is exactly located between the

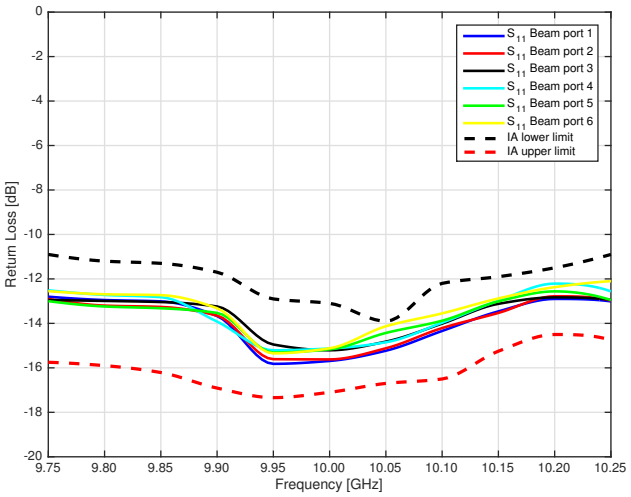

Figure 2.40: Insertion loss measured at the beam ports.

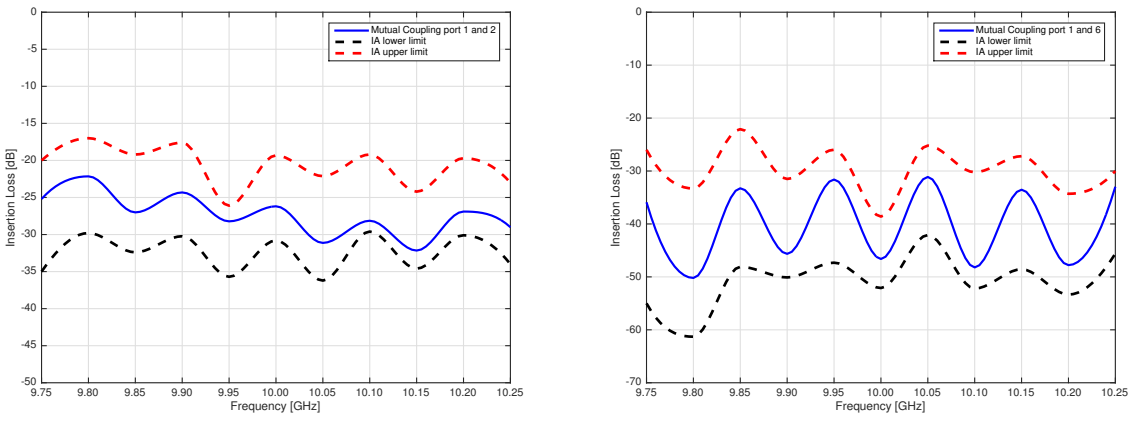

(a) (b)

Figure 2.41: Measurement of the coupling factor between (a) ports 1 and 2 and (b) ports 1 and 6.

beams obtained by considering the upper and lower IA limits demonstrating the effectiveness of the proposed method.

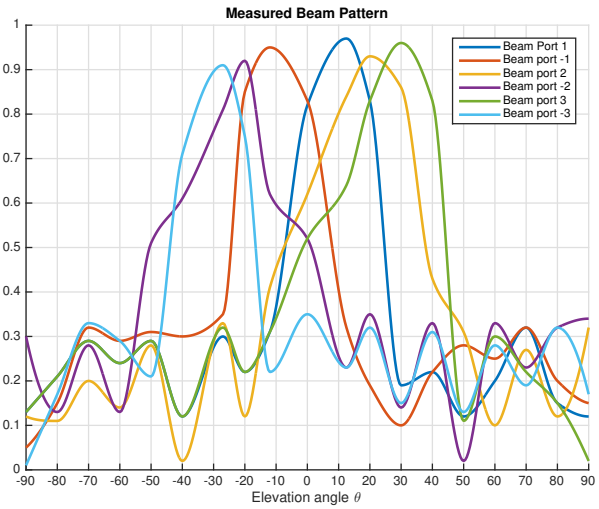

Figure 2.42: Measured beam patterns at the six beam ports.

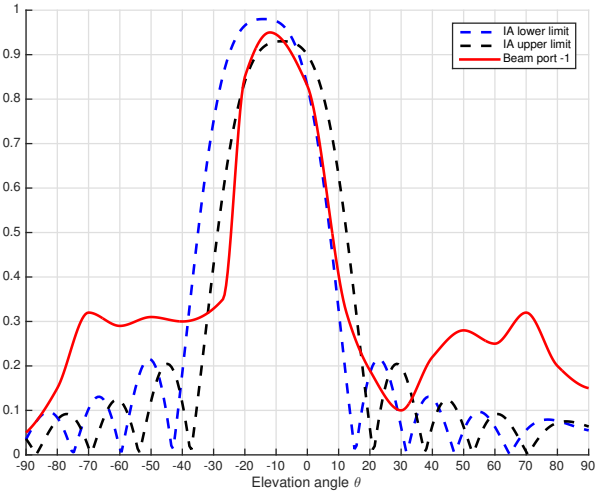

Figure 2.43: Measured versus simulated beam pattern considering the lower and upper IA limits. Beam port -1, beam stearing at -10 degrees.

Table 2.5: Beam steering directions [degrees]

	θ_{req}	θ_{meas}	θ_{err}
p_{-1}^{bp}	-10.0	-12.0	2.0
p_{-2}^{bp}	-20.0	-21.0	1.0
p_{-3}^{bp}	-30	27.0	3.0
p_{1}^{bp}	10.0	12.5	2.5
p_{2}^{bp}	20.0	21.5	1.5
p_{3}^{bp}	30.0	31.5	1.5

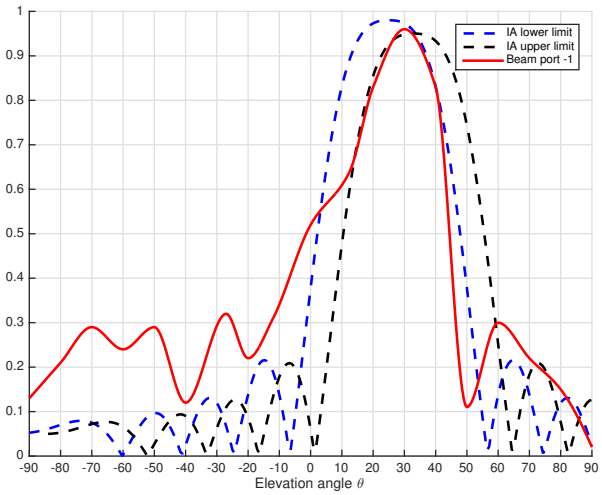

Figure 2.44: Measured versus simulated beam pattern considering the lower and upper IA limits. Beam port 3, beam stearing at +30 degrees.

2.4 Microwave Interferometer

The Proton beam therapy is a particular radiotherapy that uses protons to treat cancer [90]. Proton are positively charged particles that, at an energy between 70MeV and 230MeV, can be used to irradiate tumor cells. This therapy could be used alone or combined with other treatments, such as surgery or chemotherapy. Proton beam therapy is a non-invasive treatment that delivers radiation through the body from a machine outside the body. There is a significant difference between standard radiation treatments based on X rays and the proton beam therapy. The proton therapy is based on the specific behavior of protons to release the greatest quantity of dose in a narrow spatial range (a few millimeters) due to the Bragg peak. Furthermore, the rapid fall off to zero of the dose on the distal side of the peak allows to spare sparing tissues behind it. The advantage of proton beam therapy is that the dose to normal tissues can be considered lowered compared to any other conformal conventional radiotherapy. To create a beam of high energy protons it is necessary to use synchrotrons or cyclotrons which accelerate the protons. Proton energy determines the depth of the Bragg peak: high energy protons travel deeper in the body than low-energy ones. It's possible to release the radiation dose in the tumor by modulating each proton beam in terms of energy, position, and intensity. The proton beam therapy requires accurate patient positioning before the starting of the treatment. During the treatment sessions, patients are placed on a couch (usually called the patient positioning system) often using immobilization devices, to prevent involuntary movements which can significantly alter the desired dose distribution. The problems arise when the tumor is located on a moving organ such as the chest wall, the liver or lungs [91]. In such a scenario the proton beam must be synchronized with the breathing cycle. Usually, piezoelectric belts, video or

IR cameras are used to monitoring the patient movements [92] during the treatment sessions and the operators are to be continuously in contact with patients through of headphones. In this context, a non-invasive, compact and accurate method based on microwave interferometry able to accurately monitoring the surface movements can be proposed as a valid alternative. Microwave systems based on continuous waves CW Doppler radar demonstrated their potentialities for non-invasive monitoring of vital signs such as heartbeat and breathe [93]. In particular, they are able to correctly identify the heartbeat and breathing rate with a good degree of accuracy [94, 95, 96, 97, 98] and they demonstrated their effectiveness in rescue operations or risky scenarios (i.e. biological, chemical and nuclear contamination), but they are not sufficiently accurate to provide the exact displacement of the chest wall [94, 95]. In this work, a simple microwave interferometer able to measure displacements of wavelength fractions [99] is proposed to synchronize the proton beam with the chest movements of patients and therefore offering a good alternative to the standard techniques. The accuracy of the measurement of chest wall displacement, reached by the system was less than 2 millimeters. It is worth noticing that the only way the microwave signal would affect the proton beam it is through the magnetic field but the proton energy is so high (the energy range is between 70MeV and 230MeV) that the proton trajectory is not affected, also considering the low power of microwave signal of about 10 mW. An experimental prototype has been developed and assessed in real environments as a proof of concept.

2.4.1 System Prototype

The schema of the microwave interferometer is shown in Fig.2.45. It consists of a microwave generator operating in the K band at 24GHz. The electromagnetic wave is directed toward a semi-reflecting dielectric

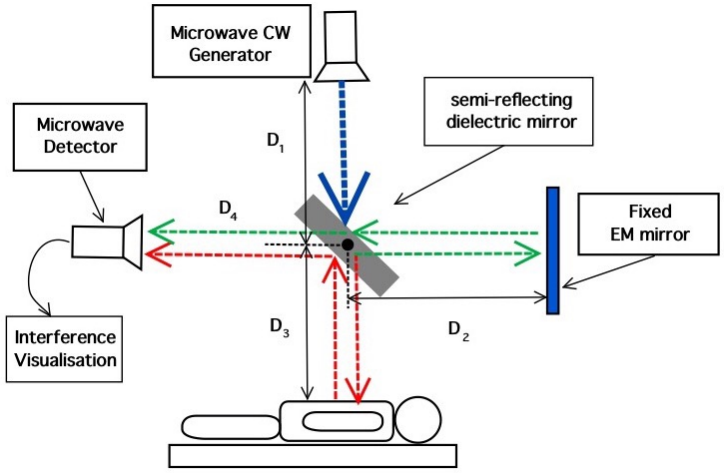

Figure 2.45: Schematic of the proposed microwave interferometer system.

mirror, fabricated with a plate of ceramic material (ARLON 25N, $\varepsilon_r = 3.38, tan\,(\delta) = 0.0001$), thickness t=0.8 mm and dimensions $50 \times 50mm^2$. The semi-reflecting mirror partially reflects and partially transmits the electromagnetic wave. Reflected wave rays travel toward a fixed electromagnetic mirror fabricated with a copper plate of dimensions $50 \times 50mm^2$. The mirror reflects to the semi-reflective mirror the electromagnetic wave. The reflected wave partially passes back through the semi-reflecting mirror and travels to the detector. The detector is composed of a rectangular waveguide (WR42) to coaxial transition and a Schottky detector diode. The detector output is converted through an analogic to digital A/D converter and visualized using a personal computer. The semi-reflecting mirror splits the microwave beam into two different paths which are reunited at the microwave detector. In particular the first beam travels along a distance $L_1 = D_1 + 2D_2 + D_4$ while the second beam travels for a distance $L_2 = D_1 + 2D_3 + D_4$. At the detector the two beams present a path difference $\Delta L = L_1 - L_2 = 2\,(D_2 - D_3)$, in particular the second beam present a phase shift of $\phi = n\left(\frac{2\pi}{\lambda_0}\right) 2\,(D_2 - D_3)$. If the phase difference ϕ produces two in-phase beams at the detector the output signal will be maximum,

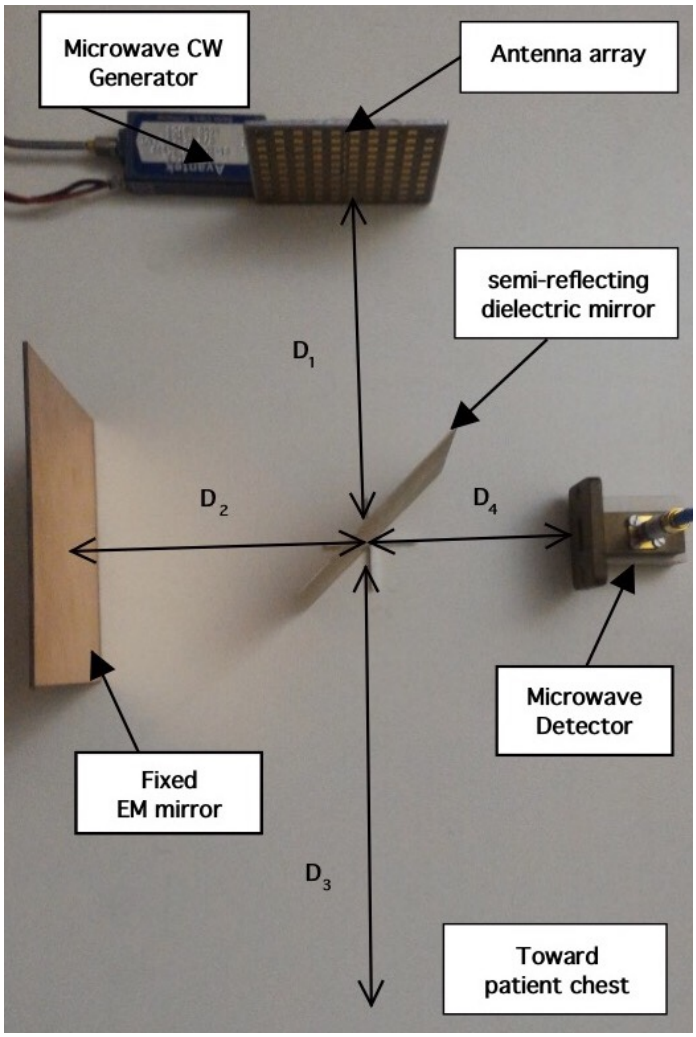

Figure 2.46: Photo of the microwave reflectometer prototype assembled on a plastic support.

otherwise, if the phase difference produces two signals in phase opposition the signal at the detector output will be minimum. In particular, if we assume the two beams with the same polarization the signal power at the detector can be expressed as a function of the phase angle ϕ as follows:

$$P_{det}(t) = A_1^2\left(\frac{1}{2} + \frac{cos(2\omega_0 t)}{2}\right) + A_2^2\left(\frac{1}{2} + \frac{cos(2\omega_0 t + 2\phi)}{2}\right) + \tag{2.12}$$

$$A_1 A_2 cos\,(\phi) = \frac{A_1^2}{2} + \frac{A_2^2}{2} + A_1 A_2 cos\,(\phi)$$

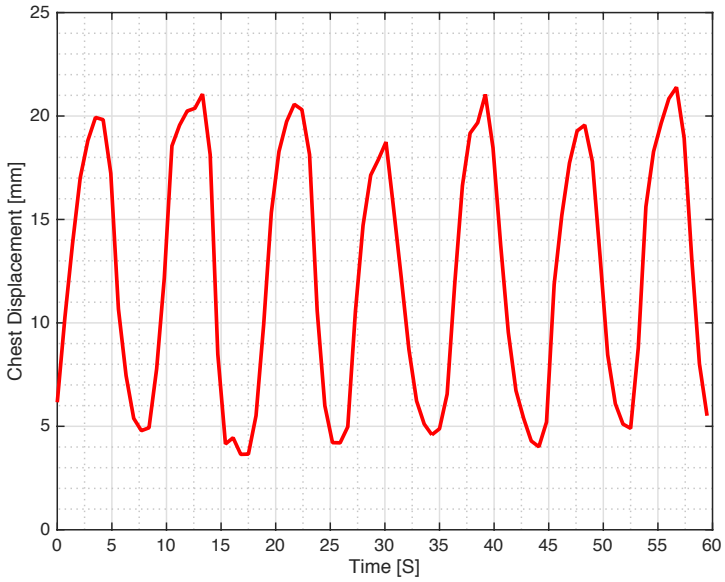

Figure 2.47: Experimental assessment, chest displacement measured with the microwave interferometer on a lying patient.

where ω_0 is the angular frequency, A_1 and A_2 are the amplitude of the two electromagnetic waves split by the semi-reflective mirror respectively, ϕ is the phase difference produced by the patient chest movements. It can be noticed from relation 2.12 the terms with $2\omega_0$ are neglected since they are removed by the detector. A photo of the microwave reflectometer prototype is reported in fig. 2.46.

During the measurement campaign, different subjects have been placed on a medical examination table similar to the proton therapy facility. The reflectometric system has been arranged on a plastic mechanical support and positioned at a distance of $d = 1.5m$ from the patient's chest. For each subject, the data have been recorded for a time interval of $T = 60s$. Fig.2.47 shows the life signals of a relaxed subject. The obtained estimation of the breathing rate has been compared with the measurement of a piezoelectric belt to verify the quality of the experimental results. Fig.2.47 reports the chest movements versus time of a relaxed subject. The measured breathing rate is normal $0.12Hz$ (or 7 breath/minute) which clearly

indicates a relaxed subject. The range of chest movements during the inhale and exhale phases are of about $20mm$. This experiment clearly demonstrated that the proposed system, thanks to its low invasiveness, accuracy, and robustness with respect to video and infrared cameras, could be a valid support tool to synchronize in real-time the proton beam during the proton therapy.

2.5 Design of an Ultra Wide Band Antenna Based on a SIW Resonator

2.5.1 Introduction

In the past decades, wireless systems and handy devices such as mobile phones and tablets were able to provide different services and tools which require high bandwidth and channel capabilities [100, 101]. Moreover, the recent evolution of digital transformation and industry 4.0 lead to a dramatic evolution and diffusion of wireless sensors. One of the critical points of any wireless devices is the antenna since it must be compact, broadband and characterized by a high gain. UWB techniques permit to manage the frequency spectra efficiently and to obtain high spatial resolutions; moreover, UWB antenna structures are well known in scientific literature and simple to fabricate [102, 103, 104, 105, 106]. They have been successfully adopted in different practical applications such as radar systems able to provide fine spatial resolution for range measurements, through the wall applications for homeland security [107], microwave imaging systems, non-invasive monitoring of heartbeat and breath, and other interesting biomedical applications [108]. However, as stated above, the modern wireless system requires a continuous progress in terms of miniaturization, efficiency and band occupation [109, 110, 111]. UWB MIMO antennas permit to obtain high efficiency and optimal use of the wireless channel. However, they usually require different antenna elements, and strong miniaturization which cannot be easily achieved [112, 113]. Attempts to obtain compact antenna structures have been made by considering fractal geometries. Even though the good results in terms of miniaturization are obtained for fractal antenna geometries, they are problematic from the point of view of the fabrication due to mechanical constraints [114]. Recently the use of substrate

impedance waveguide resonators [115, 116, 117, 118, 119, 120, 121] could solve the problem of antenna miniaturization in an easy way. SIW can be easily integrated into a planar structure like microstrip line, rectangular antenna patch as well as into a nonplanar structure like waveguide thus combining the advantages of both structures [122, 123]. Thanks to SIW technique, classical waveguide structures or resonators (characterized by a very high-quality factor) can now be fabricated in microstrip technology by simply using metallized vias or holes in dielectric substrates. The SIW not only contains the advantages of classical microstrip circuit such as low cost, easiness of fabrication and compact size but also provides the high performances, in terms of the quality factor, that up to now can by only offered by waveguides, which are bulky and expensive metallic structures. One of the first integration of passive SIW component was proposed for the design of a microwave filter based on inductive-post, which allows higher quality factor with respect to microstrip technology [124]. Chipless RFID tags based on a set of SIW resonators have been proposed. The obtained experimental results demonstrated the positive effects of the SIW cavity use. The obtained antenna prototype is compact, cheap, and it shows very good performances in the whole considered frequency range.

2.5.2 Design of the antenna structure

The UWB antenna structure is reported in Fig. 2.48. A fork monopole antenna with a microstrip feeding line of width w_0 is proposed, according to [125]. The ground plane is printed on the backside of the dielectric substrate, and it consists of a strip of copper of height and width h_0 and w_0, respectively. The fork monopole is backed with a surface impedance waveguide SIW cavity obtained with a set of metallized vias. The SIW cavity is aimed at improving the antenna performances in terms of return loss of S_{11}. With reference to Fig. 2.48 the SIW cavity consists of sixteen

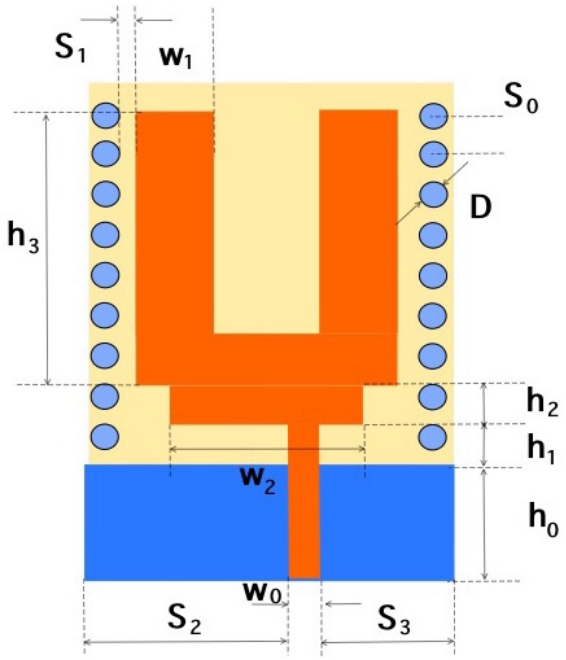

Figure 2.48: Antenna geometry.

metallized holes of diameter D, the inter-element hole space is S_0, and the distance of the two holes rows from the fork monopole arms is S_1. The resonance frequency of the SIW cavity is provided by the following relation:

$$f_{TE_{m0q}} = \frac{C_0}{2\sqrt{\varepsilon_r}} \sqrt{\left(\frac{m}{W_{eff}}\right)^2 + \left(\frac{q}{L_{eff}}\right)^2} \tag{2.13}$$

where ε_r is the dielectric permittivity of the considered dielectric substrate and C_0 is the light velocity, m and q represent the two indexes of the transverse electric propagation mode.

$$L_{eff} = \left(\left(N-1\right) S_0 + D\right) - \frac{D^2}{0.95 S_0} \tag{2.14}$$

$$W_{eff} = 2\left(S_1 + w_1 + \frac{w_2}{2}\right) - \frac{D^2}{0.95S_0} \tag{2.15}$$

where S_0 is the distance between via centres, D is the via diameter, and N is the via number, the term $((N-1)S_0 + D)$ represent the length of the SIW cavity. In the considered structure the SIW resonator is directly excited by the structure of UWB antenna therefore empirical tuning of D, S_0 and w_1 parameters is mandatory. In order to obtain a high performance antenna, all the geometrical parameters reported in Fig. 2.48 must be accurately tuned. In order to accomplish this task, an unsupervised methodology based on an evolutionary algorithm, namely the particle swarm optimizer (PSO) has been considered. The antenna design, based on microstrip technology, has been formulated as an optimization problem [126, 127, 128]. The process goals are fixed with reference to the impedance matching at the antenna input port (S_{11} values). In particular, an $|S_{11}| \leq -10[dB]$ in the frequency range $3GHz \leq f_w \leq 11GHz$ has been considered as objective for the optimization procedure, where f_w is the working frequency. The antenna structure is uniquely identified by considering the following geometrical parameters (with reference to Fig. 2.48) $\underline{X} = \{w_0, w_1, w_2, S_0, S_1, S_2, S_3, h_0, h_1, h_2, D\}$. In order to meet the requirements a suitable cost function reported in the following relation has been defined:

$$\Gamma(\underline{X}) = \Sigma_{m=1}^{M} max\left\{0; \frac{\vartheta(m\Delta f, \underline{X}) - |S_{11}|_{req}}{|S_{11}|_{req}}\right\} \tag{2.16}$$

where Δf is the considered frequency step in the operative range $3GHz \leq f_w \leq 11GHz$, $|S_{11}|_{req}$ represents the return loss constraints expressed in dB. The term $\vartheta(m\Delta f, \underline{X})$ represent the return loss value obtained at frequency $m\Delta f$ when a trial antenna geometry defined by the vector $\underline{X}$ is considered. It is worth noticing that relation (2.16) represents the dif-

ference between the return loss requirements and the performances of a trial antenna geometry. In order to obtain an optimized antenna relation (2.16) has been minimized with a customized version of PSO. To estimate the characteristics of trial antennas, provided by the term $(m\Delta f, \underline{X})$, a suitable geometrical generator combined with a commercial electromagnetic simulator (namely ADS by Keysight) have been considered. The minimization of relation (2.16) is obtained with a set of trial solutions $\underline{X}_j^k$ where $k = 1, ..., K_{max}$ is the iteration number, and J is the trial solution index. The set of trial solutions is constructed following the PSO rules. The optimizer continues to tune the geometrical parameters $\underline{X}_j^k$ until the stopping criteria related to the maximum iteration number $k = K_{max}$ or a threshold on the cost function $\Gamma\left(\underline{X}_m^k\right) \leq \eta$ is reached. When the optimizer reaches a satisfactory solution the optimal geometrical parameters defined as $\underline{X}^{opt} = arg\left\{min\left[\Gamma\left(\underline{X}_k\right)\right]\right\}$ are stored and used to fabricate the antenna. In particular, the optimization procedure based on the PSO optimizer has been initialized with a population of $M = 5$ particles (which are aimed at encoding the trial antenna geometrical parameters) randomly initialized and used as a starting point for the optimizer. Concerning the other specific PSO parameters a threshold on the fitness of $\eta = 10^{-3}$ and a maximum number of iterations $K_{max} = 100$, and a constant inertial weight $I_{weight} = 0.4$ were used. The remaining PSO parameters have been chosen according to the guidelines reported in the reference literature [24]. The antenna geometry has been optimized by using a serial machine equipped with 16 Gigabyte of memory and four processors. Each iteration of the optimization procedure required about 40 seconds and the whole design for about one hour. The optimized geometrical parameters obtained after the design procedure are reported in Tab.2.6. An experimental prototype has been fabricate considering the geometrical parameters reported in Tab.2.6 and a ceramic dielectric substrate namely ARLON 25N, $\varepsilon_r = 3.38$,

Parameter $[mm]$	w_0	w_1	w_2	S_0	S_1	S_2	S_3	h_0	h_1	h_2	D
	1.91	5	9.91	2.5	1.01	16.8	10.09	7.55	0.45	2	1.5

Table 2.6: Geometrical antenna parameters obatined after the optimization procedure. A ceramic dielectric substrate of ARLON 25N, $\varepsilon_r = 3.38$, $tan\,(\delta) = 10^{-3}$, and thickness $t = 0.8mm$ has been considered.

$tan\,(\delta) = 10^{-3}$, and thickness $t = 0.8mm$. The main body of the antenna, consisting in the fork dipole, has been obtained by using a CNC miling machine with an accuracy $\delta = 0.02mm$. The realization process of the SIW cavity is summarized in Fig. 2.49, it requires the creation of metallized vias, covering the internal surface of the holes with copper. In particular, to implement the metallization process, the antenna prototype was covered with a dry film layer on the front side and then heated at $120°C$ for 1 minute to improve the dry film adhesion. After cooling, the dry film protective cover was removed, also removing the dry film above the holes. The antenna prototype was then inserted in an evaporation chamber supported by a 6-inch silicon wafer and firmly attached to it with adhesive Kapton tape. A copper film of a nominal thickness of $1.5\mu m$ was deposited by e-gun evaporation under vacuum at room temperature. The antennas were then detached from the support and immersed in a KOH concentrated (10%) solution in order to remove the dry film and the copper above it by lift-off. The photo of the top and bottom side of the antenna prototype, equipped with a sub-miniature type A (SMA) coaxial connectors, is reported in Fig. 2.50.

2.5.3 Experimental assessment

In order to assess the antenna capabilities in term of return loss and beam pattern, an experimental setup has been arranged inside an anechoic chamber. The antenna $|S_{11}|$ has been measured by means of a Vector Network

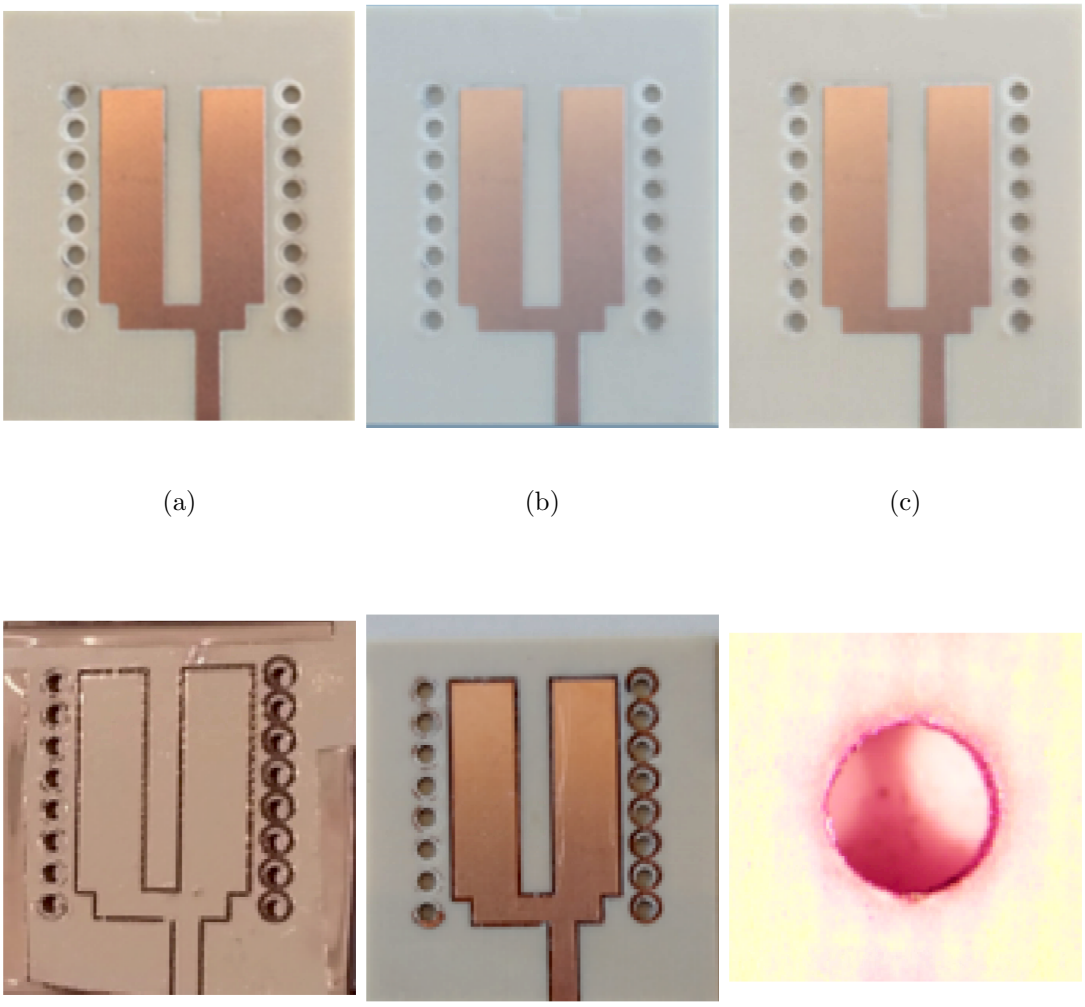

(a) (b) (c)

(d) (e) (f)

Figure 2.49: Copper vias metalization procedure, (a) original antenna fabricated by CNC milling, (b) dry film lamination, (c) process of removal of protective sheet, which removes also the dry film above the holes, (d) after copper evaporation, (e) dry film removal, (f) hole metallization seen from antenna bottomside.

Analyser (VNA). Fig. 2.51 reports the experimental data with those obtained by simulation using ADS software. An antenna prototype without

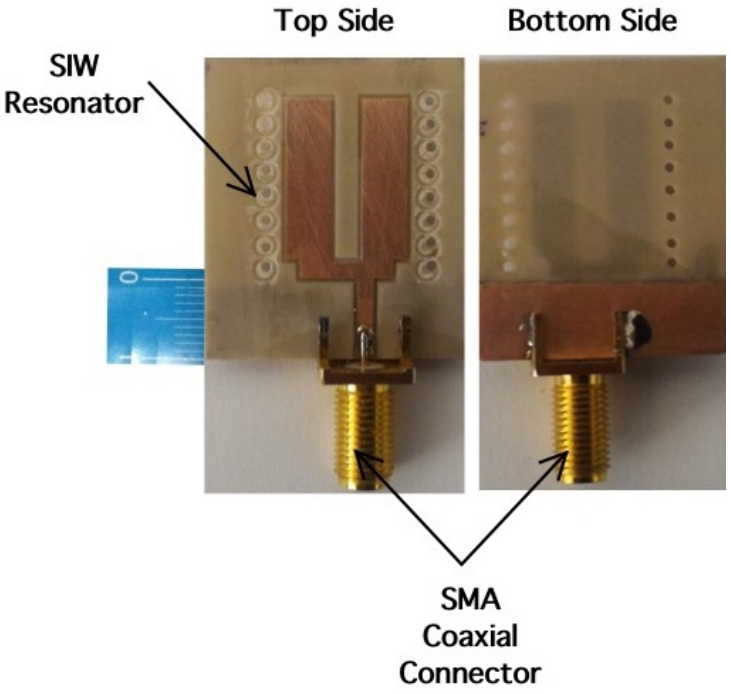

Figure 2.50: Photo of the UWB antenna prototype.

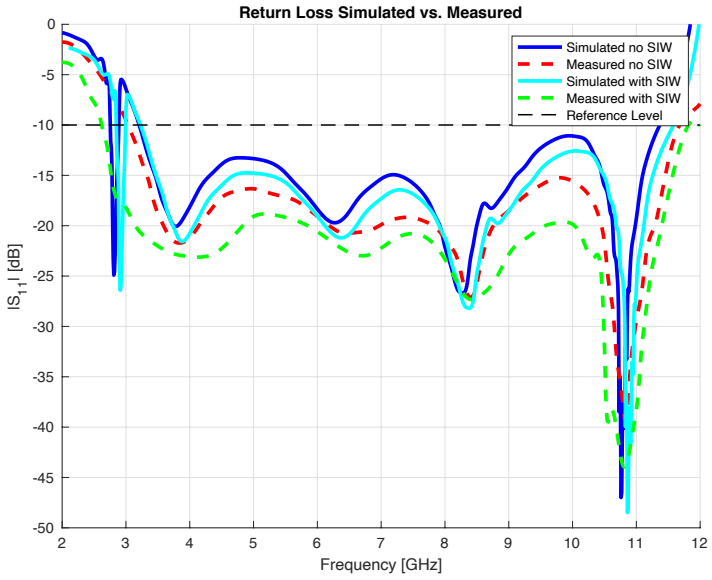

Figure 2.51: Numerical versus measured antenna return loss S_{11}.

the SIW structure has also been measured to evaluate the effect of the SIW cavity. As it can be noticed the $|S_{11}|$ of the prototype equipped with the SIW cavity (green dotted line) meets the initial requirements: in particular the return loss for the whole considered frequency band is found to be well below the initial requirements of about -10 dB. The dotted black line represents the reference level. For the sake of comparisons, the measurements have been compared with numerical data obtained with the ADS commercial software. As it can be noticed from the data reported in Fig. 2.51, the agreement between numerical and experimental data is quite satisfactory. There is only a strange spike in the numerical data located near a frequency of $f = 2.8GHz$, and the spike is not present in the experimental measurements. The measurement obtained without the SIW cavity (red dotted line) shows lower performances compared to the prototype equipped with the SIW cavity. In particular, in the frequency range between 9 *and* $10GHz$ the return loss is higher, and it reaches a value up to $5dB$, for the prototype with the SIW cavity. The antenna beam pattern has been measured both in the E and H-plane for $3GHz$, $4GHz$, $5GHz$, $6GHz$, $7GHz$, $8GHz$, $9GHz$ and $10GHz$. The antenna prototype has been placed on a mechanical pedestal, and the beam pattern has been estimated by considering an angular step of ten degrees. The measurements have been compared with the numerical results obtained with ADS the data are reported in Figs.2.52 and 2.53. As it can be noticed from the data of Figs.2.52 and 2.53 the agreement between simulated and experimental data is very good.

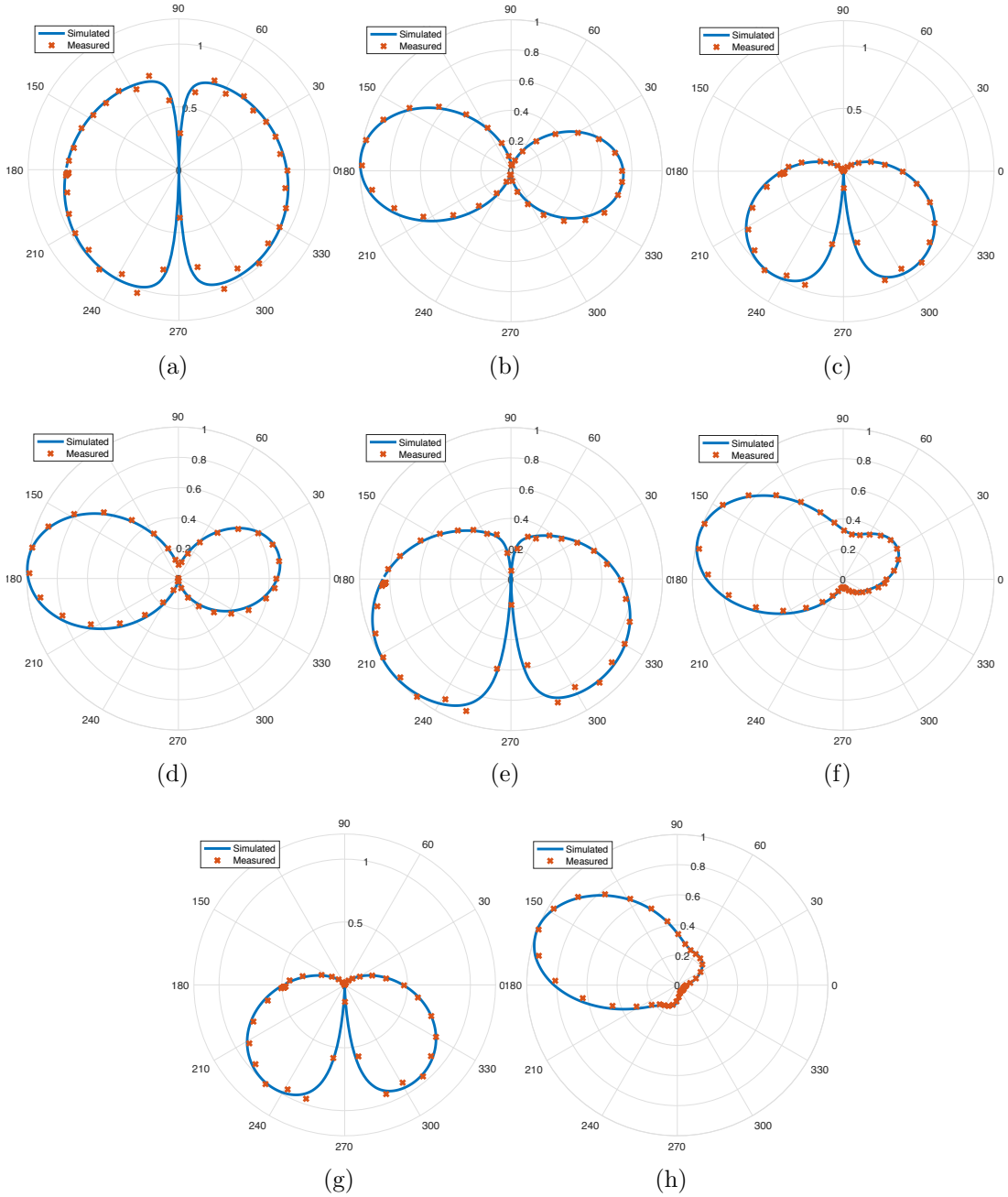

Figure 2.52: Simulated vs. measured antenna beam patterns, (a) E-plane (b) H-plane 3GHz, (c) E-plane (d) H-plane 4GHz, (e) E-plane (f) H-plane 5GHz,(g) E-plane (h) H-plane 6GHz.

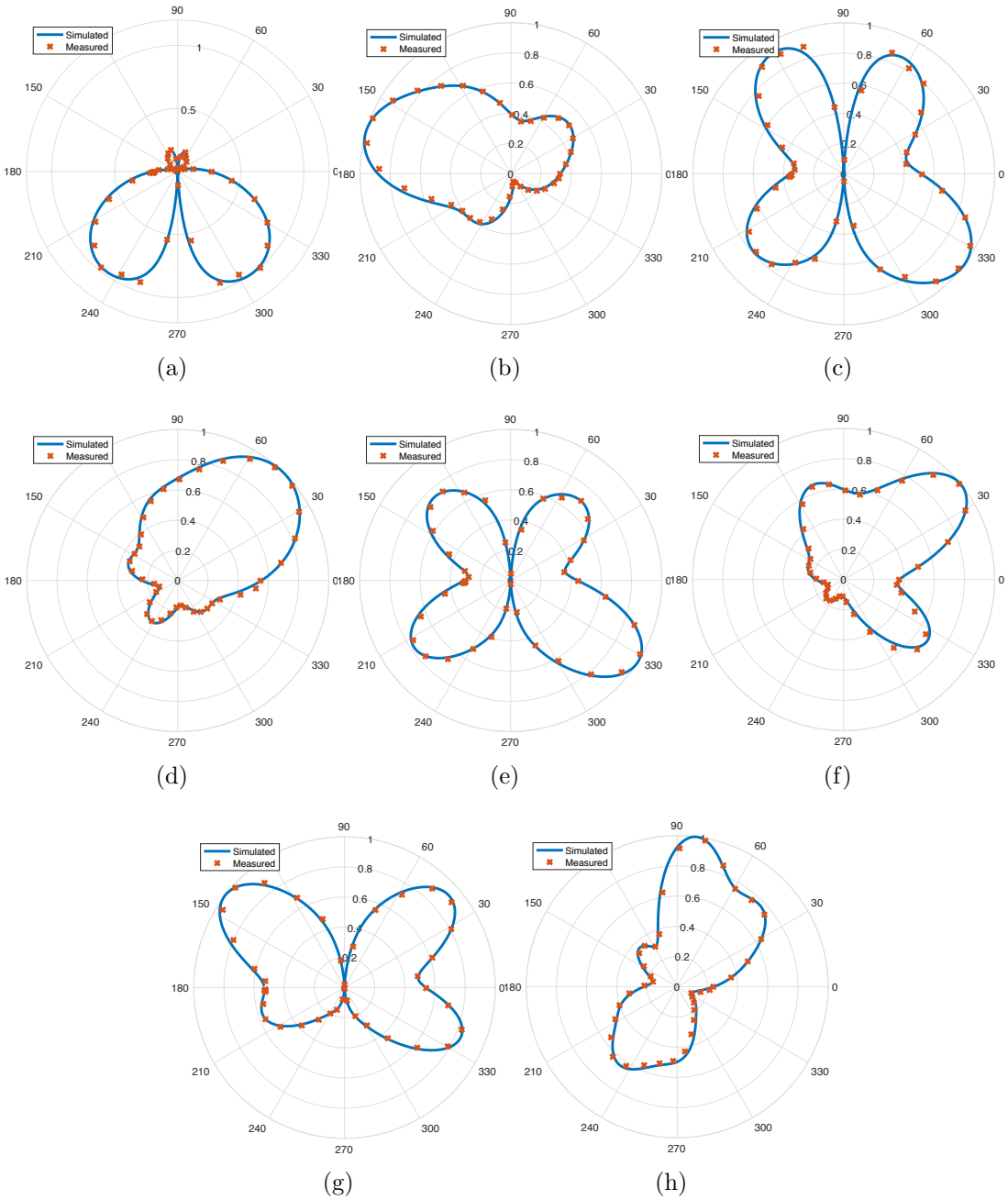

Figure 2.53: Simulated vs. measured antenna beam patterns, (a) E-plane (b) H-plane 7GHz, (c) E-plane (d) H-plane 8GHz, (e) E-plane (f) H-plane 9GHz,(g) E-plane (h) H-plane 10GHz.

2.6 Ultra-wideband antenna array based on Orbital Angular Momentum

2.6.1 Introduction

In the last decade there has been a widespread presence of wireless services and systems which lead to an huge demand of high speed, large bandwidth and good efficiency wireless channels. Increase channel capacity and data transfer is mandatory for the future wireless applications, unfortunately the available frequency bands are overcrowded and it turns out to be quite difficult to obtain further bandwidth extensions for wireless systems to overcome this problem. Recently a technique called electromagnetic vortex beam orbital angular momentum (OAM) has opened a new dimension for the research in wireless communication systems. The OAM technique creates electromagnetic waves called OAM modes, orthogonal each other. Thanks to this unique multi-mode transmission it is possible to transmit on the same channel different data within the same frequency band and the same carrier on the same channel. Different studies have been conducted on OAM using different antenna structure. A reflect array has been proposed for generating wide band circular polarized OAM antenna with mode l=1 at $10GHz$ in [129]. In [130], studies have proposed a reconfigurable OAM array antenna that can generate multiple OAM modes in a frequency range of 5.5-6.1GHz and 5.65-6.1GHz. This mode can be electrically controlled by using a reconfigurable feeding network consisting of multiple PIN diodes as a reconfigurable switch. To enhance the directivity of a dual-band OAM antenna a parabolic reflector has been proposed in [131] to coincide the center of feed array of dual-band. The OAM has provided more degree of freedom to the researcher. Studies like [132] has shown that the OAM based communication systems has more or equal number of de-

grees of freedoms and channel capacity than the multiple-input-multiple-output (MIMO) based communication system. However, further studies are mandatory. In this work an ultra wide-band OAM antenna array consisting of 8 antenna elements and able to operate in the whole C band has been designed, fabricated and assessed. The array elements are circularly arranged, and each element consists of a cavity backed UWB antenna. In particular the cavity is fabricated with a surface impedance waveguide SIW to increase the quality factor and to reduce the array dimensions and weight. The correct phase shift between adjacent elements, mandatory to obtain the OAMs modes, has been obtained with reconfigurable phase shifters based on two quadrature hybrids and a sets of PIN diodes. The obtained numerical and experimental results demonstrated the effectiveness and potentialities of the proposed antenna array.

2.6.2 Antenna array description

The schema of the proposed UWB-OAM antenna array shown in Fig.2.54. It is composed by eight microstrip SIW cavity backed UWB antennas. The array has been designed to operate in the C band. The array elements are circularly arranged. A feeding network consisting of reconfigurable phase shifters and T-junctions power splitters, provides the specific phase shift to each antenna element mandatory to obtain the OAM modes. The reconfigurable phase shifters are reflection type, composed by a quadrature hybrid ring and a couple of PIN diodes and they are able to provide the correct phase shift to each array element in the whole frequency band. In particular the phase of each antenna elements is provided by the following relation:

$$\phi_m^n = \phi_0 + m \times \frac{2 \cdot \pi \cdot n}{M}, \;\; m = 1, 2, \cdots, M \tag{2.17}$$

Where n is the OAM mode, ϕ_0 is the phase reference of the first antenna element, and M is the number of array elements. The phase can be incre-

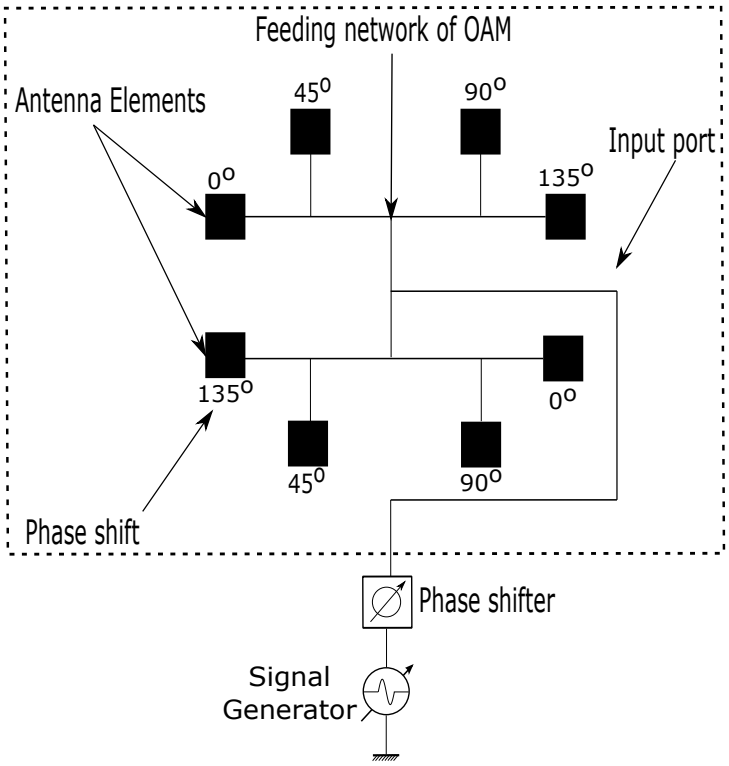

Figure 2.54: Schema of the UWB-OAM antenna array

mented in one geomerical rotation by 2πn radians. The array elements consist of microstrip UWB antennas, backed with SIW resonators. The SIW cavities have been obatined with a set of metallized vias and they strongly improve the performances of the UWB antennas in term of return loss. In particular the resonance of a SIW resonator feeded by a microstip, is given by the following relation:

$$f_{TE_{m0q}} = \frac{C_0}{2\sqrt{\varepsilon_r}} \sqrt{\left(\frac{m}{W_{eff}}\right)^2 + \left(\frac{q}{L_{eff}}\right)^2} \tag{2.18}$$

where ε_r is the dielectric permittivity of the considered dielectric substrate and C_0 is the ligth velocity

$$L_{eff} = L - \frac{D^2}{0.95b} \tag{2.19}$$

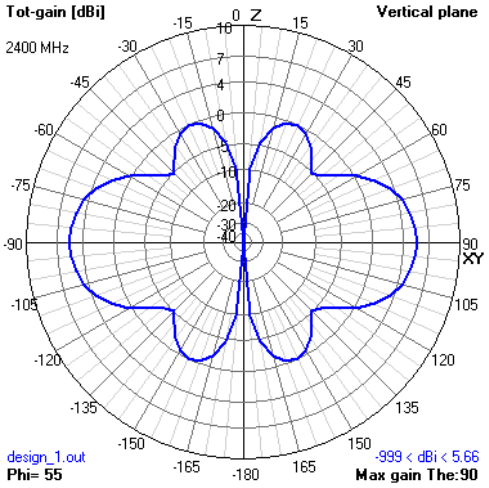

Figure 2.55: Far-field radiation pattern of the UWB-OAM array at 2.4GHz. One OAM propagation mode has been considered.

$$W_{eff} = W - \frac{D^2}{0.95b} \tag{2.20}$$

where b is the distance between vias centes, D is the vias diameter, W is the width of the microstrip, and L is the length of the SIW resonator. In the considered structure the SIW resonator is directly excited by the UWB antenna therefore an empirical tuning of D and b parameters is mandatory. The single element UWB antenna structure is reported in Fig. 2.48.

Then an array consisting in eight UWB elements has been fabricated considering a ceramic dielectric substrate, namely ARLON 25N $\varepsilon_r = 3.38$, $tan(\delta) = 0.001$, thickness $h = 0.8mm$. A microcontroller provides to properly set the correct phase shift to each array elements by acting on the reflective phase shifters.

Fig. 2.48 reports the beam pattern of the UWB-OAM array in the vertical plane, for a central frequency $f_w = 2.45$ GHz and considering only $n = 1$ OAM modes. As described in relation 2.17 the elements have been fed by using the same signal with an incremental phase shift step of $+45^o$ between adjacent antenna elements.

2.7 High-resolution L-band stepped frequency continuous wave radar

2.7.1 Introduction

In the recent years thanks to the globalization there has been a sharp increase in smuggling of goods and illegal materials such as drugs, tobacco and weapons. In order to contrast smuggling Guardia di Finanza (GdF), the italian financial police increase the controls at customs and ports, check the contents of thousands containers or vehicles requires a lots of time human resources, and money. The development of specific technological tools able to help or facilitate the GdF work is mandatory to obtain an effective smuggling contrast. In such a scenario radar technologies and in particular ground penetration (GPR) and through the wall radars (TTR) could represent effective tools for GdF. A scan-A (1D) analysis of a container can provide accurate information concerning the contents, presence of false bottoms or hidden humans without the need to empty the container or vehicle saving time, money and resources. In order to be useful for these operations it is necessary reach an high resolution of about tens centimeters and an unambiguous range less than ten meters. These performances can be easily obtained with a SFCW radar [133]. Due to their complexity and the high cost of microwave components, stepped frequency continuous wave radar have not been a large diffusion for through the wall and ground penetration radar applications with respect to pulsed radar [134]. However in the last decade microwave components strongly improve their performances, reduce their dimensions and cost making more feasible the realization of compact (SFCWR). Recently SWCW radars have been successfully adopted for GPR applications [135, 136], landmine detection [137], surveillance [138], through the wall inspection [139], the monitoring

of the structural integrity of engineering structures [140, 141, 142] or for biomedical applications such as the monitoring of human or animal life signals [143, 144], in particular the last application can be very useful fot police operation since it can be used to detect fugitives hidden inside improvised hiding places such as bunkers and wall false bottoms or human traffic. The capabilities of SFCW radar to characterize the electric properties of materials as in [142] can be very useful to identify hidden goods, such as tobacco, drugs and hidden weapons. To improve the radar performances, such as resolution, detection capabilities, clean the clutter and reduce the background noise suitable post processing algorithms can be applied [145, 146, 147, 148, 149].

In this work the implementation of a versatile low cost SFCW radar for support the GdF work is discussed and numerically assessed in realistic scenarios. The device operates over a bandwidth from 1GHz to 2GHz (L band) and it is capable of taking a single scan-A deep profile measurements using 300 frequency steps in less than 2 seconds with a resolution less than 0.15 m. However the frequency band of the system can be extended up to 12.5GHz. The proposed system is easily reconfigurable and it can be used for GPR as well as TTW inspections. The obtained preliminary results related to realistic scenarios, directly provided by the GdF, demonstrated the potentialities of the proposed system.

2.7.2 Mathematical Formulation

The schema of a the stepped frequency continuous wave radar is shown in Fig.2.56. It consists of a programmable digital signal generator (DDS) namely tha TG124A (Signal Hund company) with a frequency range from 100KHz up to 12.5GHz. The DDS is directly connected with a wideband directive antenna a log-periodic able to work in the L band. The receiving section is composed by a SA124B (Signal Hund company) receiver able

to receive the backscattered electromagnetic wave and to provide the I/Q that can be directly processed by the control system. In particular the received base band I/Q signals, are combined into a complex number as follows:

$$\Gamma_m = I_m + jQ_m = A_i e^{j\phi_m} \tag{2.21}$$

where $\phi_m = -2\pi f_m \tau$ where f_m is the m-th frequency step and τ is the propagation delay, $I_i = A_i cos(\phi_i)$, and $Q_i = A_i sin(\phi_i)$.

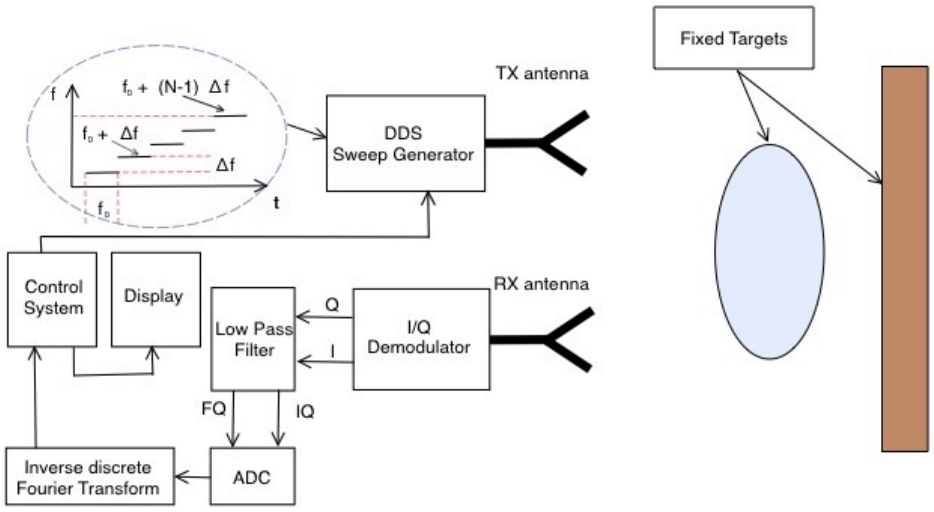

Figure 2.56: Schema of the SFCW radar.

The DDS generates a sequences of M frequencies and the receiver collect all the I_m/Q_m baseband signals and the complex vector $\hat{\Gamma} = [\Gamma_0, \ldots, \Gamma_{M-1}]$. The inverse discrete Fourier transformer is applied to the $\hat{\Gamma}$ vector in order to obtain the time domain of the echoes.

$$T_m = \frac{1}{M}\sum_{m=0}^{M-1}\Gamma_m = \frac{1}{M}\sum_{m=0}^{M-1} A_m e^{j\left(\frac{2\pi m_i}{M} - 2\pi\Delta f\frac{2R_t}{v}\right)} \tag{2.22}$$

The radar range resolution is provided by the following:

$$\Delta R = \frac{v}{2M\Delta f} \tag{2.23}$$

where v is the electromagnetic wave propagation velocity in the medium. The unambiguous range can be estimated by

$$R_{max} = \left(\frac{M}{2} - 1\right) \Delta R \tag{2.24}$$

By processing the received signal for a given fixed position of the RX nd TX antennas, the range profile representing a the A-scan (1D) for the scenario under investigation. Repeating the procedure for different antenna positions will permit to obtain a B-scan (2D) representation.

2.7.3 Numerical Assessment

This section is aimed at the numerical assessment of the SFCW radar in realistic operative scenarios suggested by the GdF, in particular the contents of containers equipped with false bottom are checked with a fast scan-A (1D) analysis. The radar system as well as the antenna and related scenarios are accurately simulated with a customized numerical time domain electromagnetic engine (FDTD), all the simulations have been performed with quad-cores personal computer, 16 GByte RAM. A gaussian white noise has been added to the original data in order to better simulate a realistic scenario, the signal to noise ratio in this experiment was $SNR = 5dB$. Different SNR ratio have been tested in controlled environment, a noise above 5 dB produced very low effects on the simulations demonstrating the robustness of the proposed system. With reference to Figs.2.57, 2.59, 2.61, and 2.64, the blue color represents the metallic walls of the container, gray color in Fig.2.57 represents air filled, brown color in Fig.2.59 relates to a homogeneous content of woods or granite blocks. The small gray lines in Fig.2.61 represents empty space between wood blocks. The light pink color in Fig.2.64 represents an homogeneous block of tobacco. With reference to ground penetration radar scenario reported in

Fig.2.66, the dark blue represents the buried wood coffer, the brown color refers to the soil.

Empty container with false bottom at different distance

Containers transported by ships arriving in ports may have been modified by inserting a false bottom inside them to hide various smuggled material. In the first experiment an empty standard container of length 6.058 m, width 2.438 m, and height 2.591 is analysed. The container doors are opened and the radar pointed exactly in the meddle of the aperture at position $x_r = 1.219m$, $y = 1.2945m$. Figure2.57 shows the container section equipped with false metallic bottom placed at different distances.

The radar parameters are the following: $f_{min} = 1.0GHz$, $f_{max} = 2.071GHz$, $M = 120$, $\Delta f = 90MHz$, bandwidth $B = 1071GHz$. With these parameters an unambiguous range $R_{max} = 16.8m$ and a resolution of $\Delta R = 0.14m$. The post processed I/Q data converted into scan-A time domain diagrams are reported in Figures2.58.

The following Table2.7, summarize the obtained results, as it can be noticed from the data reported in Table I the false bottom has been correctly identified with an error less than half centimeter for every false position.

Table 2.7: Radar response for different false bottom positions, (a) 0.353 m, (b) 0.453 m, (c) 0.554 m, (d) 0.653 m, and (e) 0.754 m.

Scenario	**Range**	**Error**
A	*5.705 m*	*0.0050 m*
B	*5.6049 m*	*0.0049 m*
C	*5.5039 m*	*0.0039 m*
D	*5.4043 m*	*0.0043 m*
E	*5.3033 m*	*0.0033 m*

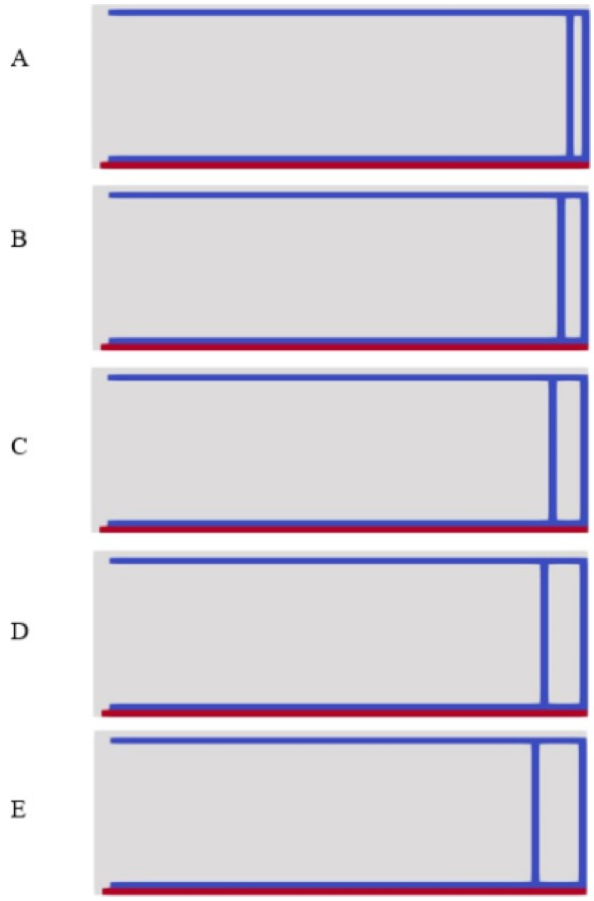

Figure 2.57: Empty container equipped with a metallic false bottom placed at different distances, A 0.353 m, B 0.453 m, C 0.554 m, D 0.653 m, and E 0.754 m.

Container with a false bottom homogeneously filled with different materials.

In the second experiment a container is homogeneously filled with different materials in particular two scenarios have been considered: case A where the container carries wood, with a dielectric constant equal to $\varepsilon_r = 2.0$, and case B where the container transports blocks of granite with a dielectric constant equal to $\varepsilon_r = 7.0$. The container dimensions are the same as in the previous experiment as well as the radar parameters and position. A metallic false bottom was placed at a distance of $50cm$ from the container wall.

In this experiment it is assumed the knowledge of container content in

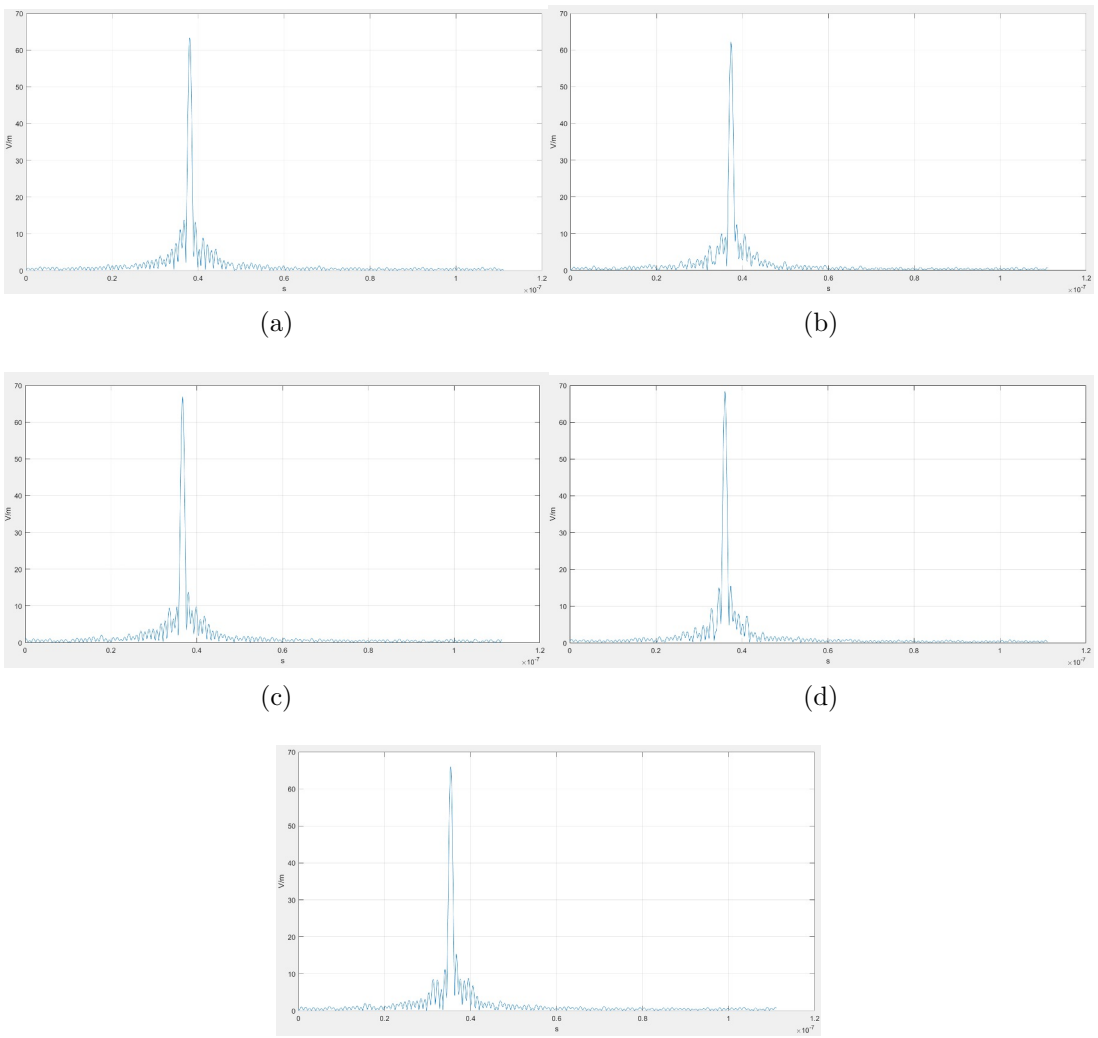

Figure 2.58: Scan-A (1D) time domain radar response for different false bottom positions, (a) 0.353 m, (b) 0.453 m, (c) 0.554 m, (d) 0.653 m, and (e) 0.754 m.

order to correctly estimate the propagation velocity and consequently the correct position of the false bottom. Figure2.60 reports the Scan-A radar response, for the sake of readability the time scale has been converted into a distance multiplying the time of fly for the propagation velocity $v = \frac{c}{f\sqrt{\varepsilon_r}}$. In particular Figure2.60 (a) and (b) reports the radar response for a container filled with wood and blocks of granite respectively. As it can be noticed from the peaks reported in Figures2.60 the false bottom is

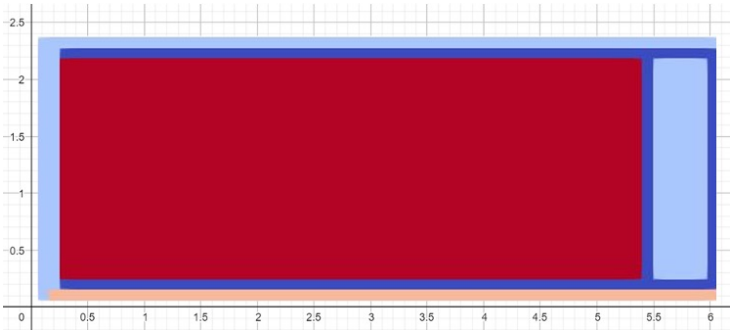

Figure 2.59: Container with a metallic false bottom homogeneously filled with woods and granite blocks.

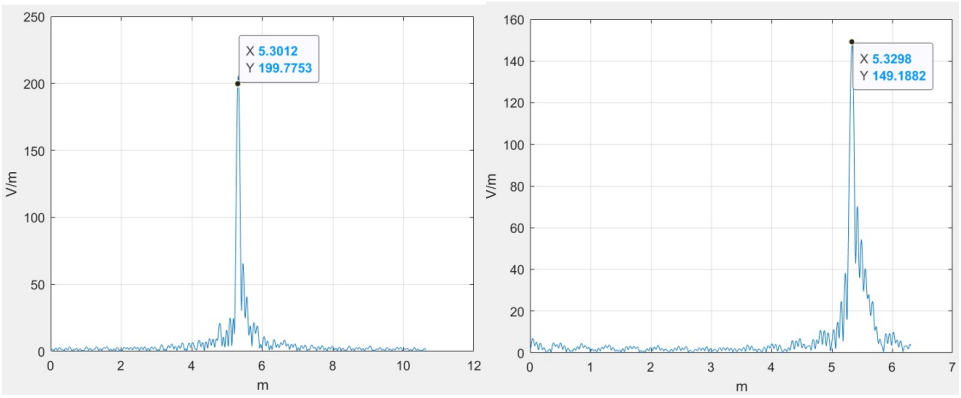

(a) (b)

Figure 2.60: Homogeneously filled container with a metallic false bottom placed at 5.3 m from the aperture. Scan-A (1D) time domain radar response for different material, (a) wood, (b) blocks of granite.

correctly retrieved in both scenarios with a very limited error, these results demonstrated the radar potentialities.

Container with a false bottom filled with woods separated by empty spaces.

This experiment is intended to assess, whether it is possible, to detect the presence of a false bottom of a container carrying material with a relative dielectric constant equal to 2.0, such as wood. Differently from the previous cases the container content is not homogeneous, it consists of several blocks separated by a space. The scenario examined in this

simulation is shown in Figure2.61. In particular the content is composed by six different wood blocks ($\varepsilon_r = 2.0$) separated by five empty space of ten centimeters ($\varepsilon_r = 1.0$). The time domain radar response is reported in Figure2.61, the main peak represents the reflection due to the metallic false bottom, despite the presence of empty space the position of false bottom is retrieved with an high accuracy, the localization error is about $25cm$.

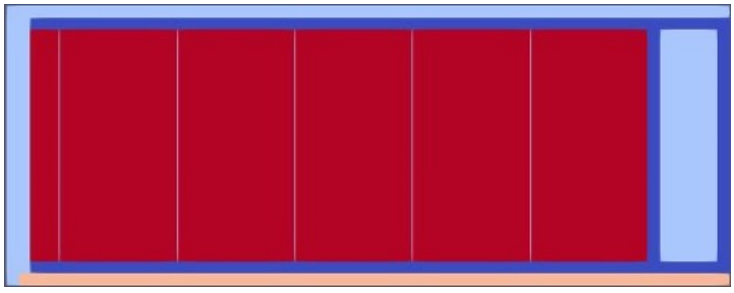

Figure 2.61: Container with a metallic false bottom inhomogeneous filled with woods.

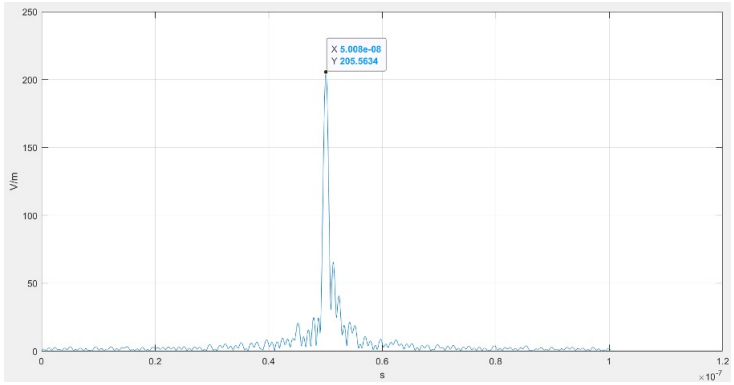

Figure 2.62: Container with metallic false bottom inhomogeneous filled with woods. Scan-A (1D) time domain radar response.

Container with a dielectric false bottom.

In the previous experiments false bottoms are made with metal. Metals are perfect reflectors and they can be easily detected with electromagnetic waves. The following experiment is aimed to assess if it is possible to

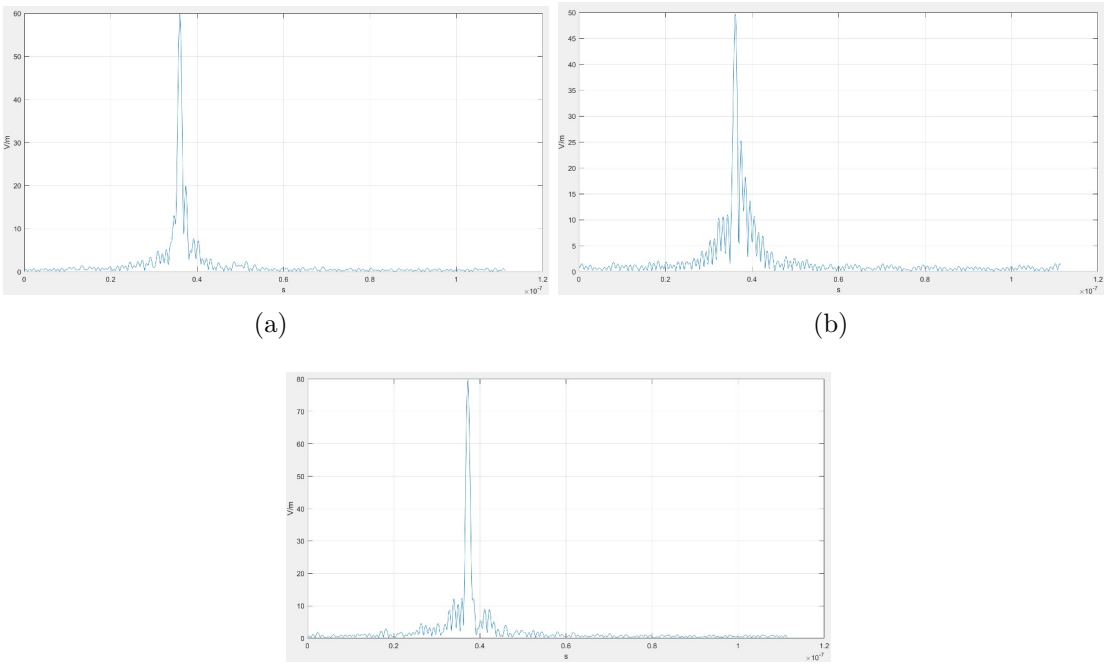

(a) (b)

(c)

Figure 2.63: Detection of false bottoms of different dielectric material, (a) dry wood, (b) plexiglas, and (c) Pressed board wood.

detect a container false bottom made with materials characterized by a low dielectric constant so that the reflected waves are not so evident.

Table 2.8: Dielectric characteristics of materials used to fabricate the container false bottom.

Material	ε_r
Dry Wood	*4.5*
Plexiglas	*3.5*
Pressed Board wood	*2.0*

Also in this experiment the radar parameters and the position are the same of the previous experiments. The results are reported in Figures2.63 (a), (b) and (c) which report the time domain response scan-A (1D) radar diagram for the three kind of dielectric false bottom. In particular Figure2.63

(a) reports the radar response for the false bottom made of dry wood, Figure2.63 (b) with plexiglas and Figure2.63 (c) the pressed board wood false bottom. As it can be observed in all the considered scenarios the false bottom has been correctly revealed with an high degree of accuracy. The localization error *gamma* was quite satisfactory $3mm$ for the dry wood, $7mm$ for the plexiglas, and 161 for the pressed board wood false bottom. As expected the higher error is related to the pressed board wood that present a very low dielectric permittivity contrast with respect to the background.

Container with a dielectric false bottom filled with tobacco.

In this experiment a more complicated scenario has been considered. A container with a dielectric false bottom made of dry wood ($\varepsilon_r = 4.5$), positioned at 5.5 m from the aperture. The container is filled with tobacco ($\varepsilon_r = 1.6$, humidity of 20%) The contrast between the background ant the false bottom is not so high moreover the tobacco humidity produce a strong attenuation on the impinging electromagnetic wave making the detection of false bottom quite difficult. For manage this scenario the radar parameter have been changed, in particular $f_{min} = 1.105GHz$, $f_{max} = 1.99GHz$, $M = 60$, $\Delta f = 15MHz$, bandwidth $B = 885MHz$. With these parameters an unambiguous range $R_{max} = 7.3m$ and a resolution of $\Delta R = 0.12m$. The considered scenario and the scan-A time domain diagrams are reported in Figures2.64 and 2.65 respectively. As expected the data obtained in this experiment are more noisy with respect the previous experiments this is due to the low dielectric contrast and to the attenuation introduced by the tobacco humidity. However thanks to a suitable post process algorithm (MUSIC) the main peak is identify and the false bottom position estimated with a good localization error of about $\gamma = 0.04m$

Figure 2.64: Container with a dielectric false bottom filled with tobacco.

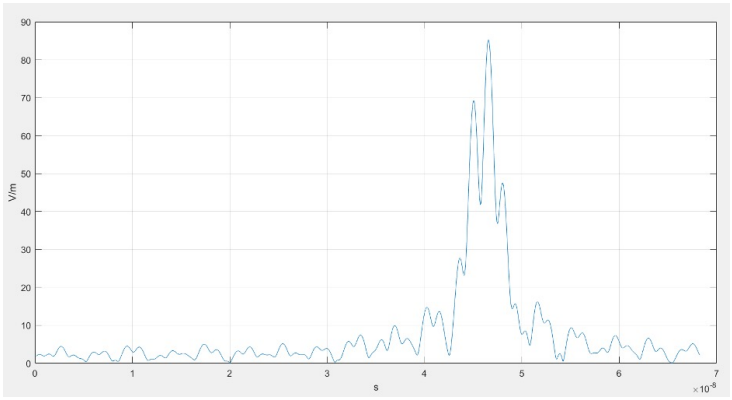

Figure 2.65: Container with a dielectric false bottom filled with tobacco. Scan-A (1D) time domain radar response.

Buried coffer.

In the last experiment a GPR scenario has been considered. In particular a wood coffer ($\varepsilon = 4.5$) has been buried in a background soil characterized by $\varepsilon_r = 6$. The coffer is placed at a depth $d = 1.50m$ and its dimension are $1.0 \times 0.5 \times 0.2m^3$. The dielectric contrast with respect to the background is quite low 1.5. The considered scenario is reported in Figure2.66.

A scan-B (2D) radar response has been obtained considering 100 different radar positions. In particular the TX/RX antennas have been moved with a step of $X_{step} = 0.02m$ along the whole investigation domain of dimension $2.0 \times 2.0m^2$. Concerning the radar parameters a $f_{min} = 1.0GHz$, $f_{max} = 2.048GHz$, $M = 75$, $\Delta f = 20MHz$, and bandwidth $B = 1.48GHz$ have been considered. The 100 tracks are composed to-

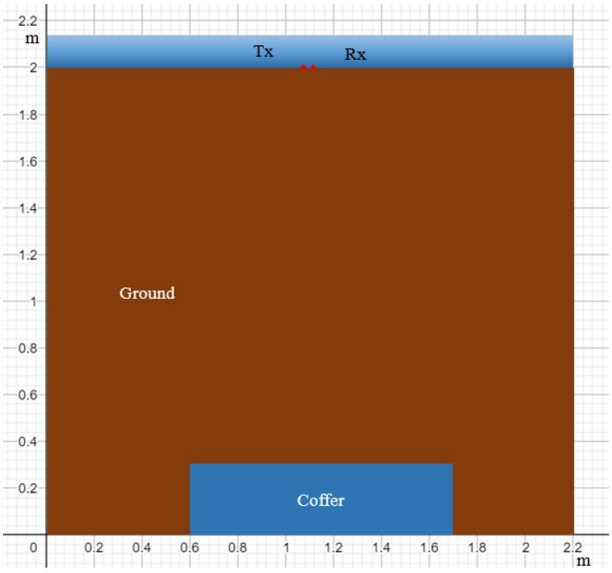

Figure 2.66: GPR scenario a buried wood coffer.

gether to obtain a typical scan-B radar, output reported in Figure2.67. The data of Figure2.67 has been post processed, in particular the reflection due to the soil air interface has been removed and a gaussian filter has been aplied to each track in order to reduce the background noise. The wood coffin position is localized at track 50 which present the higher peak value as it can be observed in Figure2.68 which reports the scan-A radar response for different tracks.

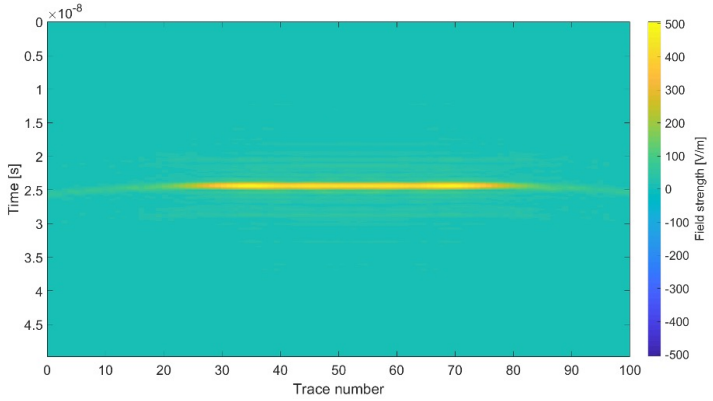

Figure 2.67: Buried wood coffer scenario. Scan-B (2D) radar response.

From the time domain data of track 50, reported in Figure2.68, the

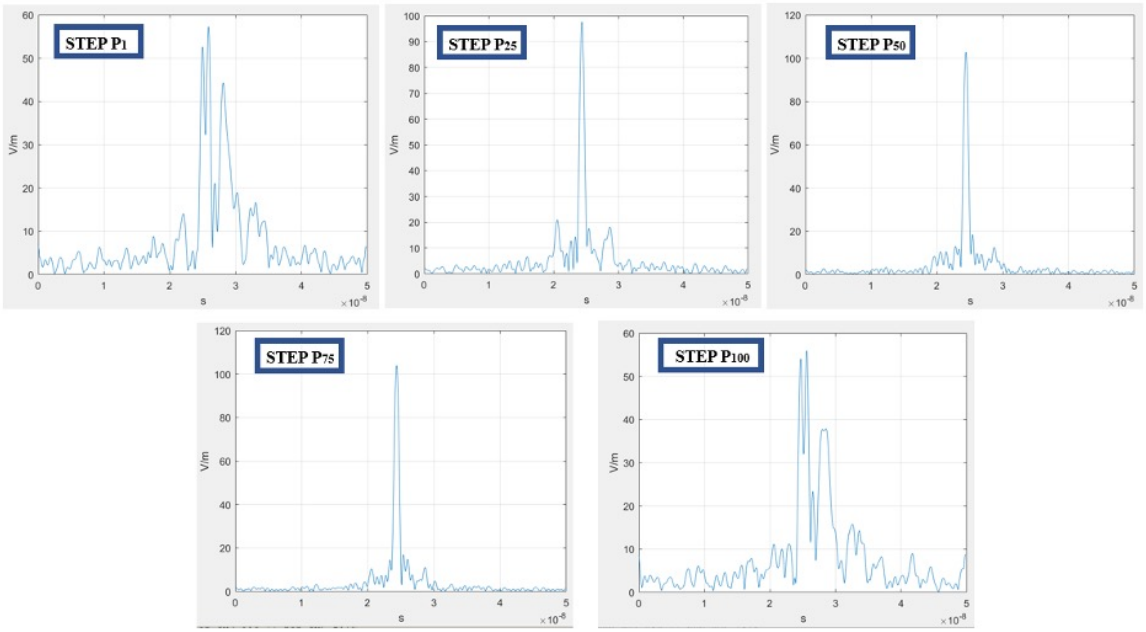

Figure 2.68: Buried wood coffer scenario. Scan-A (1D) radar response for different tracks.

coffer depth is estimated with a good degree of accuracy, the localization error is $\gamma = 0.01m$.

Chapter 3

Detection Technique for a Chipless RFID System Using Quantile Regression

In this chapter, an improvement to the detection capabilities of the chipless RFID system based on quantile regression method is proposed. The following Section describes the chipless RFID system and provides guidelines for the design of a chipless tag on spiral resonators. Later, the quantile regression model is explained in detail as a detection method. Moreover, the numerical assessment and an experimental assessment has discussed with reference to proposed experimental chipless RFID system.

3.1 Introduction

Radio Frequency Identification (RFID) has been one of the most influential inventions in the last decades. Over these years, this technology has become mature enough to be used in various applications, such as health monitoring, supermarket food and goods tracking systems, libraries in book tracking systems, environmental sensing [150], and for Internet of Things (IoT) applications. The current research as regards chipless RFID focuses on cost and a compactness [151]. The RFID technique that eliminates the use of the chip is called chipless RFID [152]. The chipless RFID techniques can be divided into two groups based on the encoding mechanisms: time-domain (TD) or frequency-domain (FD), as in Reference [153]. In order to overcome the issue of cost, different types of approaches have been taken. In References [154, 155], high-density compact chipless RFID tags for item-level tagging and switch controlled RFID employing a external laser light source are presented, respectively. Whereas, References [156, 157] focus on low manufacturing cost, compactness, flexibility, and efficient bandwidth utilization for IoT based sensing applications. In Reference [152, 160, 158, 159, 153, 161, 162, 163, 164, 165, 166, 167, 168, 169], various shapes of resonators are proposed to increase the compactness and flexibility. Nevertheless, some researchers [170, 171, 172, 173, 174, 175, 176, 177] have discussed various ways to increase the range of the RFID. Wherein, References [153, 163] have also proposed a way to increase the data capacity and coding capacity of RFID tag, respectively. In Reference [160], a novel approach for a chipless RFID sensor tag design integrating dipole resonators as the ID encoders and a circular microstrip patch antenna (CMPA) resonator as the crack sensor for metal crack detection are proposed. In detection, reading, and identification of the tag, various studies have been presented [178, 179, 180, 181]. In Reference [182],

the resonances in spectral encoded chipless RFIDs were performed. This method uses the second-order derivative of the phase of the signal instead of its amplitude and does not require a reference signal. However, research from Reference [183] draws attention towards the security of IoT devices against the attacks such as Denial of Service (DoS), tag/reader anonymity, and tag impersonation.

An implemented measurement campaign was performed considering different tag considering different tag configurations by using copper tap tape. The tag was placed at 10 cm from the reader, the power of the transmitter was $-12dBm$. However, it is possible to increase the operative range by increasing the power of the generator or antenna gain. Moreover, the noise was added (with the resistive loads). The measured insertion losses $y(\beta)$ collected with the SA124B receiver were processed with the quantile regression tool in order to correctly identify the tag's bits. An accuracy of 95% was obtained with the experimental data demonstrating the accuracy of the quantile post-processing tool of the proposed system.

3.2 System Description

In this section, the description of a chipless RFID system is presented. Figure 3.1 shows the schematic of the system. With reference to Figure 3.1, the reader contains a sweep signal generator, a power splitter, a circulator, a mixer, a low pass filter, and an analog to digital converter. The mixer down-converts the detected RF signal, and a low pass filter removes the high-frequency components. This mixer with the lowpass filter implements a homodyne detector mandatory to retrieve the signal correctly. A tag section comprises two main elements, spiral resonators, and two antennas. Here, we have used multiple resonators in our experiment. As shown in Figure 3.1, all the resonators are in cascade form, and they are con-

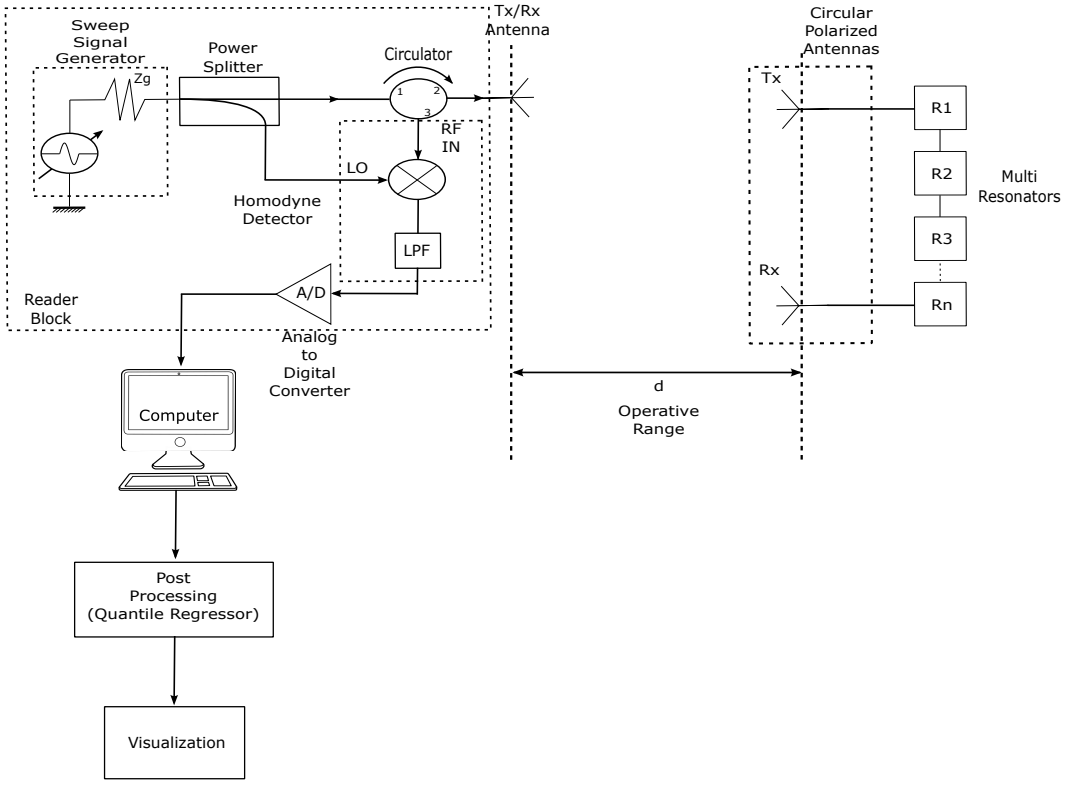

Figure 3.1: Chipless Radio Frequency Identification (RFID) system schematic.

nected with circular polarized antennas. The distance between the reader and tag is defined as the operative range at which information is correctly retrieved from the tag by the reader. When the RF signal impinges on the receiving (Rx) tag antenna and propagates further towards the resonating circuit, cascaded spiral resonators produce phase frequency jumps at particular frequencies of the spectrum, which encode the data bits. Later, when the signal has been passed through the resonating cascade resonators, the unique spectral signature of the tag is transmitted back by means of the transmitter antenna (Tx) tag. This re-transmitted encoded signal is detected and presented to the reader. This digital signal is obtained on a computer system for the post-processing. As a post-processor, we used a quantile regressor. A detailed description of the quantile model is described later in the next sections.

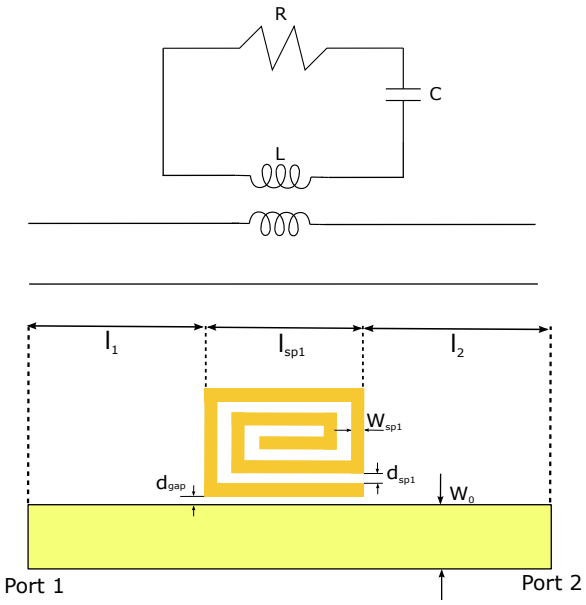

Figure 3.2: Layout of the spiral resonator and the equivalent shunt resonator circuit.

3.2.1 Tag Description

This section provides the guidelines for the design of chipless tags based on spiral resonators. In addition, The tag structure is given in Figure 3.2, it consists of the main microstrip feeding line and a set of spiral resonators [184], which encode the data into bits.

Spiral resonators provide better performance on thin laminates because the resonators are fabricated in microstrip or coplanar waveguide technology. Spiral resonators are a better alternative to the simple stub resonator, since they provide a satisfactory quality factor (Q) with respect to a simple stub resonator. As shown in Figure3.2, the resonators are coupled to a microstrip line and modeled using distributed elements. The design parameters and the layout calculation of the microstrip spiral resonator are defined as follows.

The width of the microstrip line is W_0, d_{gap} is the gap between the resonator and feeding line, and the width of the spiral conductor is W_{sp1}. The separation between the spiral conductors is d_{sp1}, the length and width of

the spiral resonator is l_{sp1}. l_1 and l_2 are the distance between the resonator and ports. The total length has been represented by $l_{sp,tot}$, Ψ is number of the spiral resonators sides, λ_m is the wavelength, c_0 is the light velocity, and ϵ_e is the permittivity of the dielectric substrate, respectively. A small gap between the feeding line is used for activating the resonators [13].

$$l_{sp,tot} = \frac{\Psi + 1}{2} l_{sp} + \frac{\Psi - 1}{2} d_{sp} \quad (\Psi \ odd) \tag{3.1}$$

$$l_{sp} \approx \frac{\lambda_m - (\Psi - 1) d_{sp}}{\Psi + 1} \tag{3.2}$$

$$f_{res} = \frac{c_0}{[(\Psi + 1) l_{sp} + (\Psi - 1) d_{sp}] \sqrt{\epsilon_e}}. \tag{3.3}$$

The total length of the spiral resonator has been estimated using Equation 3.1. The length of the resonator l_{sp} at the resonance wavelength λ_m can be calculated using the following Equations 3.2 and 3.3, respectively. It is worth noticing that Equation 3.2 provides only a rough approximation of the resonator length l_{sp}. Please note that the above formulas are approximated and a tuning phase frequency aimed at refining the resonator geometrical parameters is mandatory to obtain an accurate resonance.

3.3 Quantile Regression

This section is aimed at explaining the quantile regression model used to improve the detection capabilities of the chipless RFID system. Quantile regression, which was introduced by Koenker and Bassett (1978) [185], seeks the estimation of conditional quantile functions. As given in Reference [186], this model quantiles the conditional distribution of a response variable and expressed as a functions of independent variables. Other linear regression models have the relationship between one or more independent

variables and the conditional mean of a response variable; in contrast, quantile regression intends to find out the influence of independent variable(s) on a response variable in terms of range variation and conditional distribution.

Therefore, quantile regression has the capacity to provide a whole picture of distribution characteristics and a more complete statistical analysis [187]. In addition, quantile regression is more robust to outliers relative to least squares regression when estimating parameters [188]. Furthermore, the quantile regression model does not require any dataset for the training of a model like in the classification model. The main difference between quantile regression with linear and other regression models is that a quantile regression does not require any specific distribution like the others. In the past decade, quantile regression has become very useful in comprehensive statistical analysis methods applied in various fields such as economics, medicine, environmental science, survival analysis, botany, and zoology in the form of linear or non-linear models [189].

Here, the quantile regression model has been adapted to predict the frequency shift and amplitude variations of peaks of the resonators, which encode the data. A quantile regression is commonly applied to solve parametric, non-parametric, and semi-parametric regression problems in statistics and economics [190]. Quantile regression turns out to be particularly useful when the distribution formation cannot be defined and the other regression models are not applicable or require too much customization. It is worth noticing that depending on the problem at hand, there are different regression models characterized by unique structure and responses depending on a measurement scale and distribution. This is the situation of chipless RFID system where the peaks, which represent the information, could present a frequency shift and different depths values due to noise, material tolerances, and fabrication defects. The peak depth and

frequency shift are difficult to predict and model. As described in Figure 3.1, when the RF signal is transmitted back with the unique spectral signature, the signal is recovered at the reader. In particular, the encoded data can be observed in the insertion loss y signal. The behavior of the y signal shows that at a particular frequency, the signal gives a phase frequency jump which is recorded as peaks and represents the encoded bit value. In post-processing, the phase frequency, observed in the signal behavior, is detected, and the decoded data bits from the signal are retrieved by means of the quantile regression model. The mathematical model for the quantile has been described as follows.

The $y(m), m \in 1, 2, ..., M$, is the detected signal at the reader signal and $\beta(m), m \in 1, 2, ..., M$, are the frequencies at which resonators perform, where $M \, \epsilon \, \mathbb{N}$ represents the number of samples. The signal collected by the Rx antenna shows that the y signal does not follow any particular distribution form. Therefore, in order to detect the peak, we have applied quantile regression on the given data as a post-processor. As described earlier, the quantile method is very useful when the signals distribution function is unknown. The theoretical quantiles of a random variable are commonly and implicitly defined by its probability values. In which, through its observed probability values it calculates the weighting function. The weighting function commonly gives the quantile of the given data [190].

$$\hat{\mu} = argmin_{\mu \, \epsilon \, \mathbb{R}} \sum_{m=1}^{M} (y(m) - \mu)^2 \tag{3.4}$$

$$f(\beta_m / Pr(y(m))) = \begin{cases} 0 \;\; ; \;\; Pr \geq \hat{\mu}, \\ Pr \;\; ; \;\; Pr < \hat{\mu}. \end{cases} \forall \; m = 1, ..., M \; \epsilon \; \mathbb{N} \tag{3.5}$$

As per the model shown in references [190, 191], the mean $\mu(y(m))$,unconditional mean $\hat{\mu}(y(m)) \; \forall \; m \in 1, 2, ..., M$, and the variance $\sigma(y(m))$ of the sig-

nal y have been calculated. The knowledge of mean value $\mu(y(m))$ provide the unconditional mean $\hat{\mu}$ and probability $Pr(y)$ of the signal y at a sample of the signal y. Equation (3.4) is the unconditional mean for all $\{m = 1, 2, ..., M\}$. It provides the mean value at a particular sample $\{m = 1, 2, ..., M\}$ of signal y. The following weight function (3.5) calculates the weight of the function using the unconditional mean $\hat{\mu}$ and the probability Pr of the signal $y(m)$. Equation (3.5) provides the peak of the signal as shown in numerical assessment. However, the above mathematical model works only in ideal condition where there is no noise. For all the samples, the weight of the function $f(\beta_m/Pr(y(m)))$ detects the location of the peak at the given frequency range but in the case of frequency shift, Equation (3.5) fails. In addition, when we considered the noise, the noise produces the frequency and amplitude shift as we have shown in numerical assessment.

$$f(\beta_m/y(m)) = \begin{cases} 0 \;\; ; \;\; y(m) \geq \hat{\mu}, \\ y(m) \;\; ; \;\; y(m) < \hat{\mu}. \end{cases} \forall\ m = 1, ..., M \in \mathbb{N}\ and\ \forall \in [\beta_{min} : \beta_{max}] \tag{3.6}$$

$$\beta_{min} = \beta + j * d\delta(n)\ , \quad d\delta(n) \in [0 : 1],\ j \in \mathbb{N} \tag{3.7}$$

$$\beta_{max} = \beta_{min} + d\delta(n)\ ,\ d\delta \in [0 : 1]. \tag{3.8}$$

In order to overcome the issue of the frequency and amplitude shift, and the noise, we implemented a new weighting function (3.6). The advantage of this function is that instead of calculating a quantile of the whole signal $y(m)$, this function calculates the quantile for the conditional mean value for a given frequency step size $[\beta_{min},\ \beta_{max}]$, where β_{min} and β_{max} are the lower and the higher frequency values of the signal y. We have calculated

the bandwidth $BW = \beta_{min} - \beta_{max}$ of the given signal y, which also represents the frequency range of the signal y. Equations (3.7) and (3.8) have been used to calculate the percentage quantile range value (starting from 10% to 100%) for each frequency step size $d\delta$. In References (3.7) and (3.8), a frequency step size is represented by $d\delta \in [0 : 1]$ which gives the quantile percentage value. In Equation (3.7), the value of $j \in \mathbb{N}$ decides the range of the β_{min} and β_{max} by giving length of $d\delta$. For simplification, we have chosen the quantile percentage value $d\delta$ as $\{0.1, 0.2, 0.3, ...1\}$ so that the length of $d\delta$ is $j = 10$.

Moreover, for all the possible values of $d\delta$ in Equations (3.7) and (3.8), the weight of the function is calculated from Equation (3.6). In Equation (3.6), instead of the probability $pr(y(m))$ we have changed the parameter to the signal $y(m)$. The Equation (3.6) estimates the peak more accurately than the Equation (3.5) because Equations (3.7) and (3.8) work like a moving window for the considered frequency range. The movement of the windows is defined by the frequency step size $d\delta$. Here, $d\delta$ has been verified over all the possible range of $\{0.1, 0.2, 0.3, ...1\}$. The possible range value of a $d\delta$ decides the window size. Equation (3.6) detects the frequency shift and phase magnitude shift of the signal for a smaller window size as shown in the numerical assessment. However, in an experimental assessment, we have noticed that Equation (3.6) detects false peaks for the smaller window size. Further explanation on this matter is given in the Section of experimental validation. The experimental assessment proved that even in a real-time environment where noise is high, our proposed algorithm is able to detect the peak. Equations (3.5)-(3.8) provide all the information needed to calculate the peak at a given frequency range. It is worth noticing that after the proposed weighting function, we get satisfactory performance and accuracy of peak detection.

3.4 Numerical Assessment

This section is aimed at numerically assessing the proposed methodology. In particular, a tag, composed of five resonators, able to encode 5-bit data with $N = 2^5$ combinations is considered. The tag structure was modeled and simulated by means of a commercial software namely ADS2017 by Keysight Technologies (Keysight Technologies Inc., Santa Rosa, CA, USA). The tag was designed to operate in the Wi-Fi frequency band at the central frequency of $2.45GHz$. The considered dielectric substrate was ARLON25N, $\epsilon_r = 3.38$, thickness t= $0.8mm$, $tan(\delta) = 10^{-3}$. The geometrical details of the considered five resonators are reported in Table 3.1 with the correspondent resonating frequencies. Concerning the other geometrical parameters, they are $W_0 = 1.61mm$ (microstrip width) and $d_{gap} = 0.2mm$ (the coupling gap between microstrip and resonators). To simulate the different tag combinations, a given resonator can be short-circuited by means of a vertical metallic slab. In particular, a short-circuited resonator represents a "0", while a resonator without a metallic slab encode a "1". For almost all tag configurations, a simulation with ADS2017 was performed in order to simulate the signal received by the reader $y(\beta)$ in the frequency range from $2.4GHz$ to $3GHz$. Figure 3.3 represents the simulated received 5-bit signal at the reader for a tag configuration of 11111 (all the resonators activated). It is worth noticing that we have used a 5-bit tag configuration only to provide a proof of concept system and to numerically and experimentally assess it. Theoretically, the quantile regression method can be applied to detect data of any length and certainly longer than 5 bits. As it can be noticed from the data reported in Figure 3.3, the peaks of resonance which identify the bit "1" are clearly evident even if not so deep. For all the numerical experiments, the post-processing tool based on the quantile regressor (implemented in MATLAB) was applied to

Table 3.1: Design parameters of the five spiral resonators.

n^o	f_{res} [GHz]	λ_m [mm]	Ψ	L_{sp} [mm]	W_{sp} [mm]	D_{sp} [mm]	D_{gap} [mm]
1	2.4	80.1	9	7.48	0.7	0.3	0.1
2	2.5	76.5	9	7.18	0.7	0.3	0.1
3	2.6	73.5	9	6.9	0.7	0.3	0.1
4	2.7	71	9	6.65	0.7	0.3	0.1
5	3	66.3	9	5.95	0.7	0.3	0.1

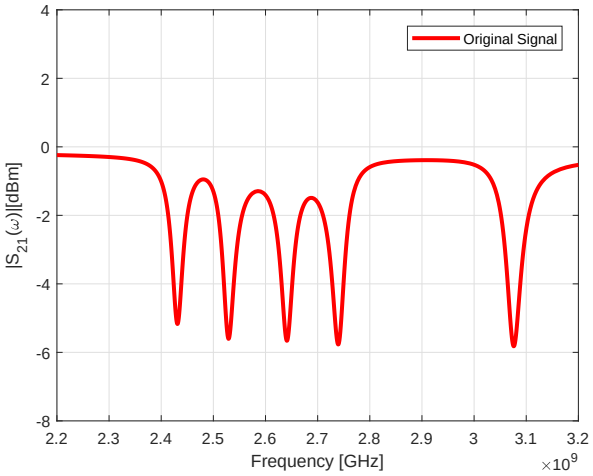

Figure 3.3: Received 5-bit signal for the tag configuration of 11111.

the signal $y(\beta)$ obtained with the ADS.

Figure 3.4 reports the peak detection obtained with the regression method reported in Section 3.3 for the a tag characterized by three active resonators (tag configuration "10110"). The data have been numerically generated with a peak depth and frequency shift variations of 10%. As it can be noticed from the data in Figure 3.4, the peaks are correctly identified, the blue dots identify the frequency range of each resonator. The process of peak identification obtained by considering the quantile regression reported in section 3 which consider the new weighting function (3.6) is reported

in Figure 3.5. In addition, the data reported in Figure 3.5 were numerically generated and corrupted by random amplitude and frequency range variations for each peak. The received signal is reported in Figure 3.5a. Figure 3.5b–d shows the detection of peaks located between 2.4–2.5 GHz (b), 2.6–2.7 GHz (c), and 3.1–3.2 GHz (d), respectively. The data reported in Figure 3.6 refer to the tag configuration 00101, where two resonators are active and three short-circuited. Furthermore, in this case, the data were numerically generated, Figure 3.6 (a) reports the simulated data received at the reader and corrupted with a random error on the peak amplitude depth of ±3 dB and a random frequency shift error of ±5 % of the active resonators. Additionally, in this experiment, all the peaks (corresponding to bit "1" in the tag) are correctly identified. In particular, Figure 3.6 b–d clearly show the different identification steps of the quantile regressor. To better simulate realistic scenarios, different kinds of noise scenario was added to the obtained synthesized signal $y(\beta)$. In particular, a strong additive white Gaussian noise (AWGN) as well as random frequency shifts and amplitude peak changes were added to corrupt the $y(\beta)$ simulated data. In particular, Figure 3.7 reports an example of data corrupted both by 10dB AWGN noise, a random amplitude variation, and a frequency shift of 10%. Furthermore, in presence of a high noise level, the quantile regressor is able to identify the peaks with a high degrees of accuracy. Particularly, Figure 3.8b–d clearly show the different identification steps of the quantile regressor. It is worth noticing that only a selected set of results has been reported in this section to demonstrate the potentialities of the method. The quantile regressor was tested on several combinations and considering different scenarios with different noise levels, frequency shifts, and peak depth variations. Notably, the numerical assessment was performed by considering more than 200 different configurations obtained by adding noise to the original 2^5 sequences; the method based on quantile

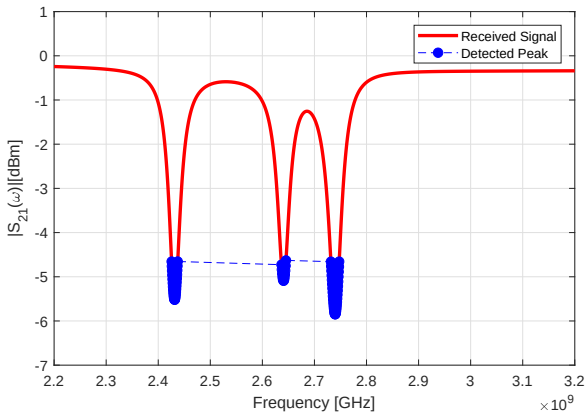

Figure 3.4: Numerical assessment. Peak detected with the quantile regression, tag configuration 10110.

regressor demonstrated its potentialities showing a success rate of about 95%.

3.5 Experimental Validation

In order to assess the capabilities of the proposed system, an experimental system prototype (acting as proof of concept) with different tags was fabricated and assessed. The reader is a monostatic continuous wave radar (CW) composed of a sweep signal generator (TG124A, 100 KHz–12.5 GHz from Signal Hound USB-TG124A, La Center, WA, USA), a circulator (RE83CR1004, 2 GHz–4 GHz from Pasternack, Huntington, CA, USA), a broadband circular polarized antenna [192]. The receiver is a SA124B spectrum analyzer (100 KHz–12.5 GHz from Signal Hound, La Center, WA, USA). The schema of the reader is reported in Figure 3.1. Concerning the tags, they are fabricated with two kind of dielectric materials, the ARLON25 (h = 0.8 mm, $\epsilon_r = 3.28$, $\tan\delta = 0.001$) and FR4 (h = 1.0 mm, $\epsilon_r = 4.2$, $\tan\delta = 0.001$). In particular, tags with five spiral resonators tuned considering Table 3.1 were considered. In order to compare the experimental measurements with the simulations reported in Section 3.4, the

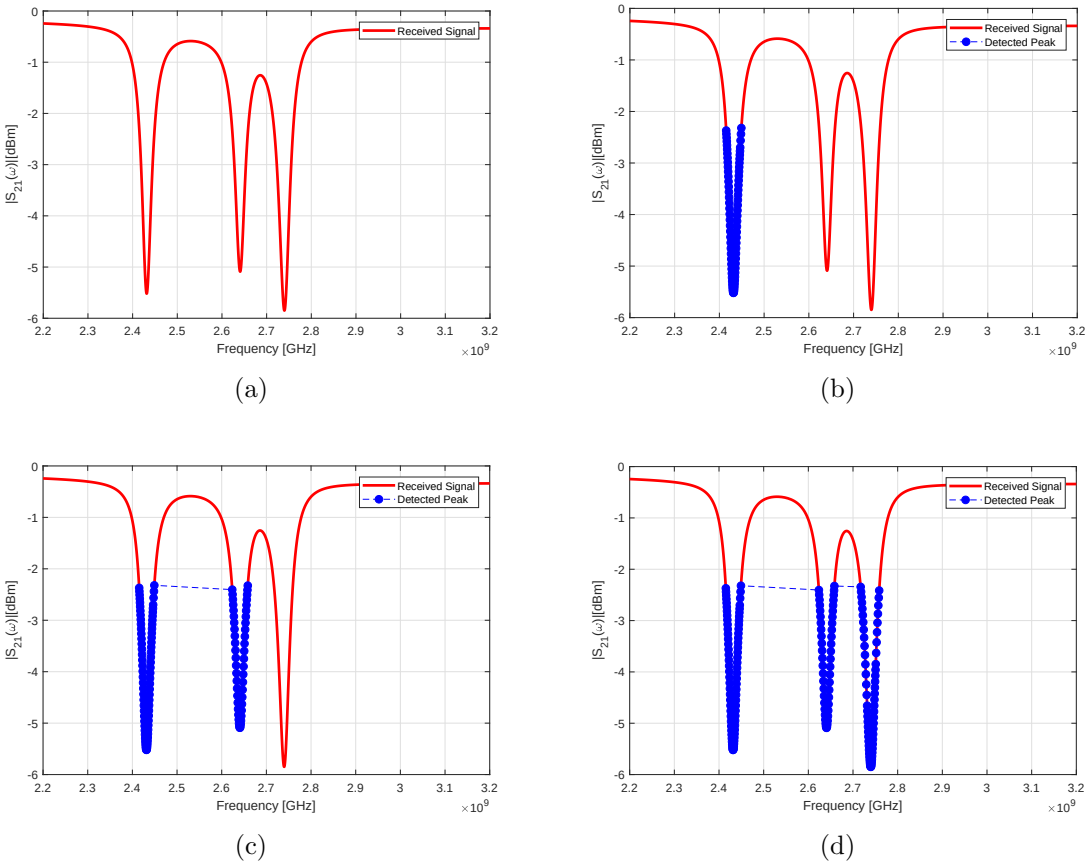

Figure 3.5: Peak detected for the tag configuration of 10110, (**a**) original detected signal, peaks between the frequency range of (**b**) 2.4–2.5 GHz, (**c**) 2.6–2.7 GHz, (**d**) 3.1–3.2 GHz.

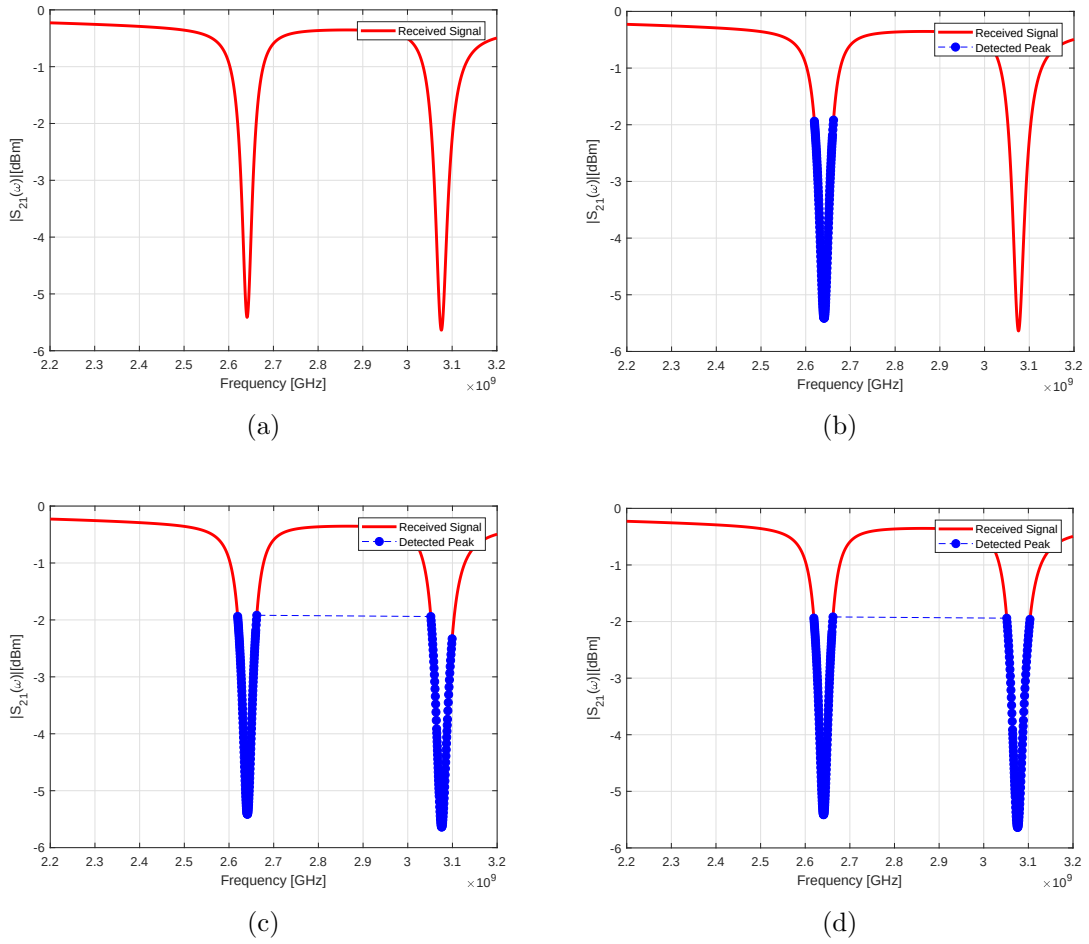

Figure 3.6: Peak detected for the tag configuration of 00101, (**a**) original detected signal, between the frequency range of (**b**) 2.6–2.7 GHz, (**c**) 3.0–3.1 GHz, and (**d**) 2.2–3.2 GHz with a frequency shift at 3.1–3.2 GHz.

resonators were excited by means of a microstrip line, and fed by the two antennas (a Tx and Rx one) connected to the tag using two sub-miniature type A (SMA) coaxial connectors. To obtain one of the 2^5 different tag combinations, a copper tape was used to short-circuit the resonators (and exclude them) to obtain "0". Figure 3.9 reports a photo of the tag prototype (a proof of concept) with five resonators and the two broad band circularly polarized antennas connected. To increase the number of possible combinations and further increase perturbation/noise in the measured

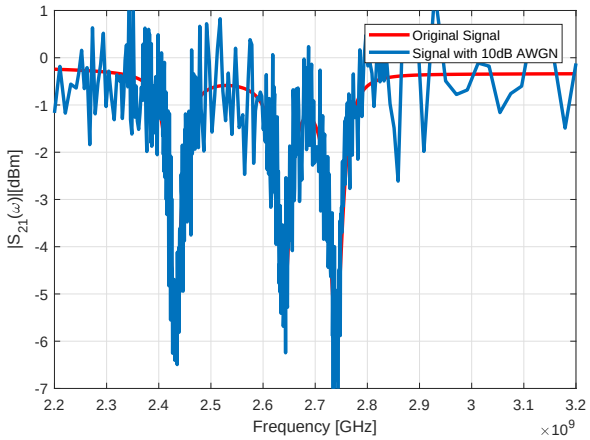

Figure 3.7: Numerical assessment. Signal corrupted by additive white Gaussian noise (AWGN), frequency shift and peak amplitude random variations. Tag configuration 10110.

data set $y(\beta)$, different surface mount device (SMD) resistive loads were soldered at the end of spiral resonators. The resistive loads are usually inserted to provide sensing capability to the chipless tag. In this work, the resistive loads were used to simulate frequency shifts and resonating amplitude variations. An example of the effects of the resistive loads on the resonator response is reported in Figure 3.10. The loads were connected to the last resonator designed to resonate at $3GHz$ as indicated in Table 3.1. The use of resistive loads permitted us to increase the experimental data set, their effects being quite evident as shown in Figure 3.10.

The prototype demonstrator is, shown in Figure 3.9, was tested considering different tag configurations. A copper tape was used to insert a short circuit on a given resonator and to obtain a "0". Figure 3.11a reports the experimental data obtained for the tag configuration 11110, the last resonator was short circuited by means of a small slab of copper tape. The different steps of the quantile regressor post-processing process are reported in Figure 3.11b–e, respectively. As can be seen from the data reported in Figure 3.11, the peaks which encode a "1" are correctly detected

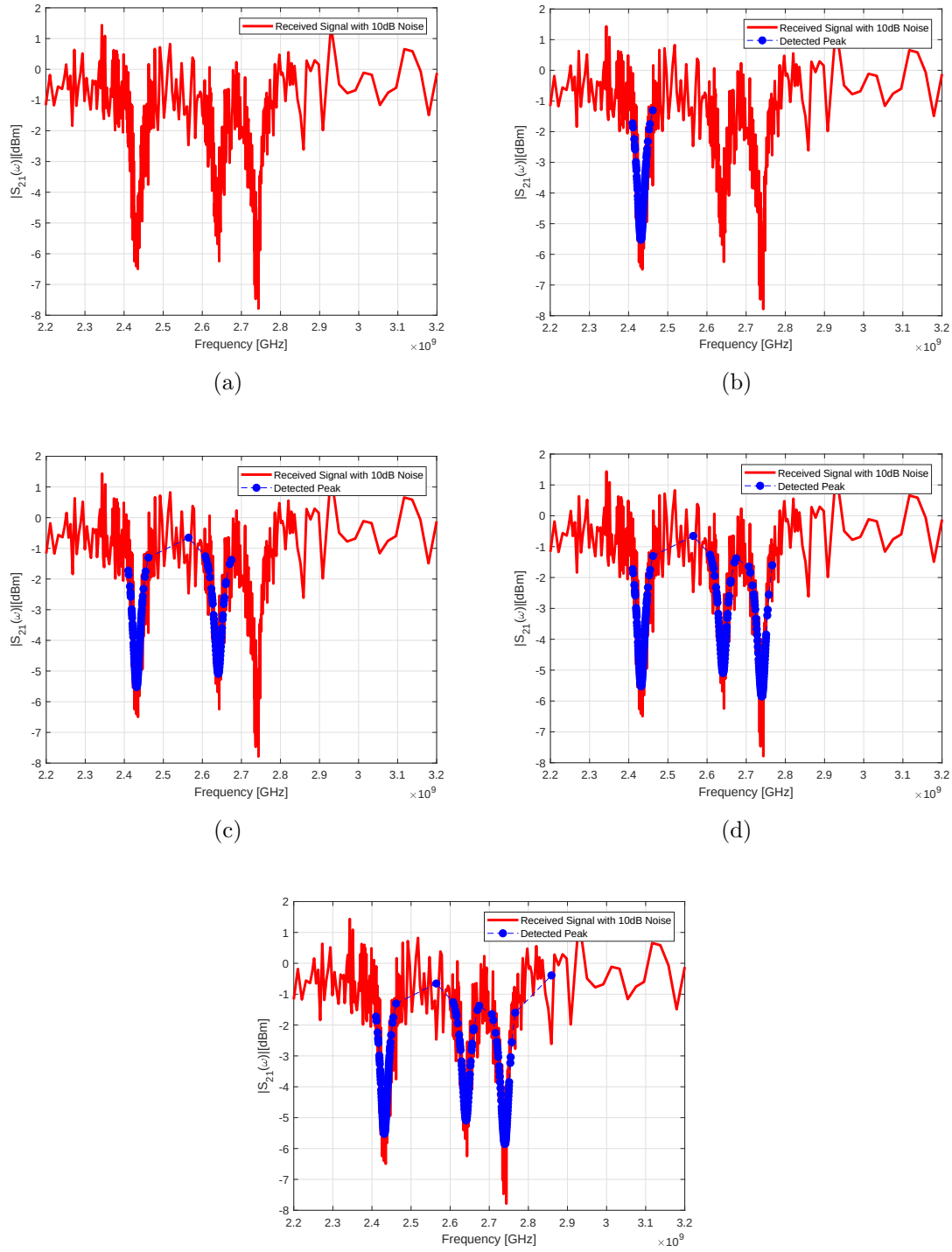

(a) (b) (c) (d) (e)

Figure 3.8: Numerical assessment, noisy scenario. Peaks detected for the tag configuration of 10110, (**a**) original detected signal, peaks between the frequency range of (**b**) 2.6–2.7 GHz, (**c**) 3.0–3.1 GHz, (**d**) 3.1–3.2 GHz with frequency shift at 3.1–3.2 GHz, and (**e**) final step.

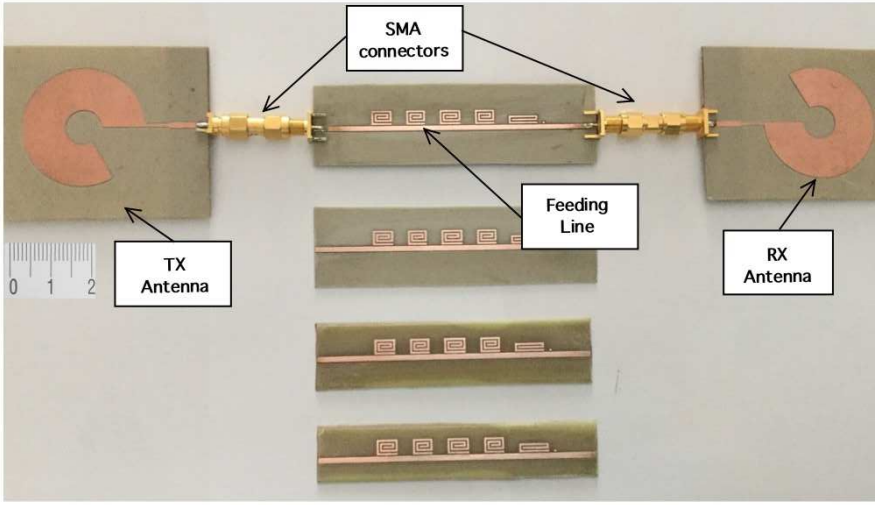

Figure 3.9: A photo of the tag prototype demonstrator with five resonators and two broadband circularly polarized antennas.

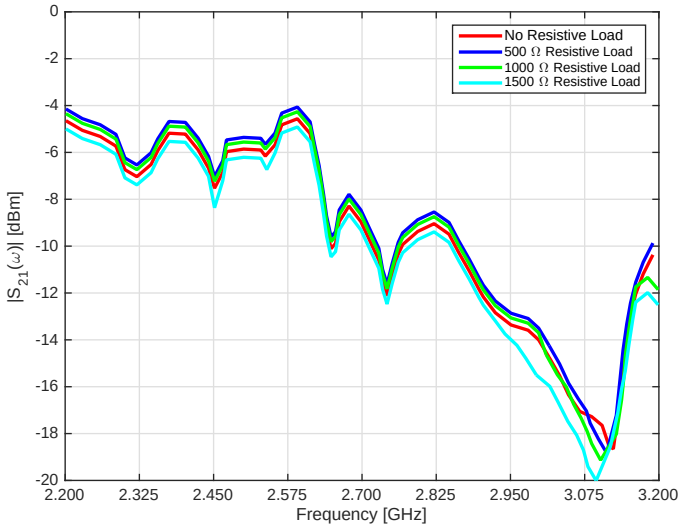

Figure 3.10: The effects of resistive loads on the resonator response.

despite the noise level and the different amplitude level of the first two resonators with respect to the others. As well as for the numerical validation, the experimental assessment section presents only a selected set of results. For the sake of completeness, experiments with different tag configurations were carried out. In addition, with experimental data, the quantile regressor method demonstrated its potential showing a success rate of about 94%. The number of tag configurations was improved by loading the five resonators with resistive loads (soldering surface mounted SMD components). Additionally, in this case, the number of tag configurations was extended from 2^5 to 200. The last experiment reveals the limitations of the proposed methodology based on the quantile regressor method. Problems arise when the peak depth is too perturbed. A typical scenario is reported in Figure 3.12a, which shows the signal retrieved at the reader for a tag with all five resonators activated (tag configuration 11111). As can be seen, the quantile regressor procedure is able to correctly identify only the last three peaks (Figure 3.12a–e). The first two resonances were not correctly identified. This is certainly due to the high difference between the peak depths. It was observed that when the peak amplitude difference between the resonances is greater than 10 dB, some peaks can be lost. The scenario reported in Figure 3.12 presents a depth difference of about $11dB$ between the first two resonances, located in the frequency range from 2.2 and $2.5GHz$, and the last peak located between 3.0 and $3.1GHz$. This condition occurs only when the resonators present too much difference in quality factor. In the last experiment, a high peak perturbation was deliberately introduced by using a resistive load $R_s = 1500\ \Omega$ on the last resonator to assess the robustness of the proposed methodology.

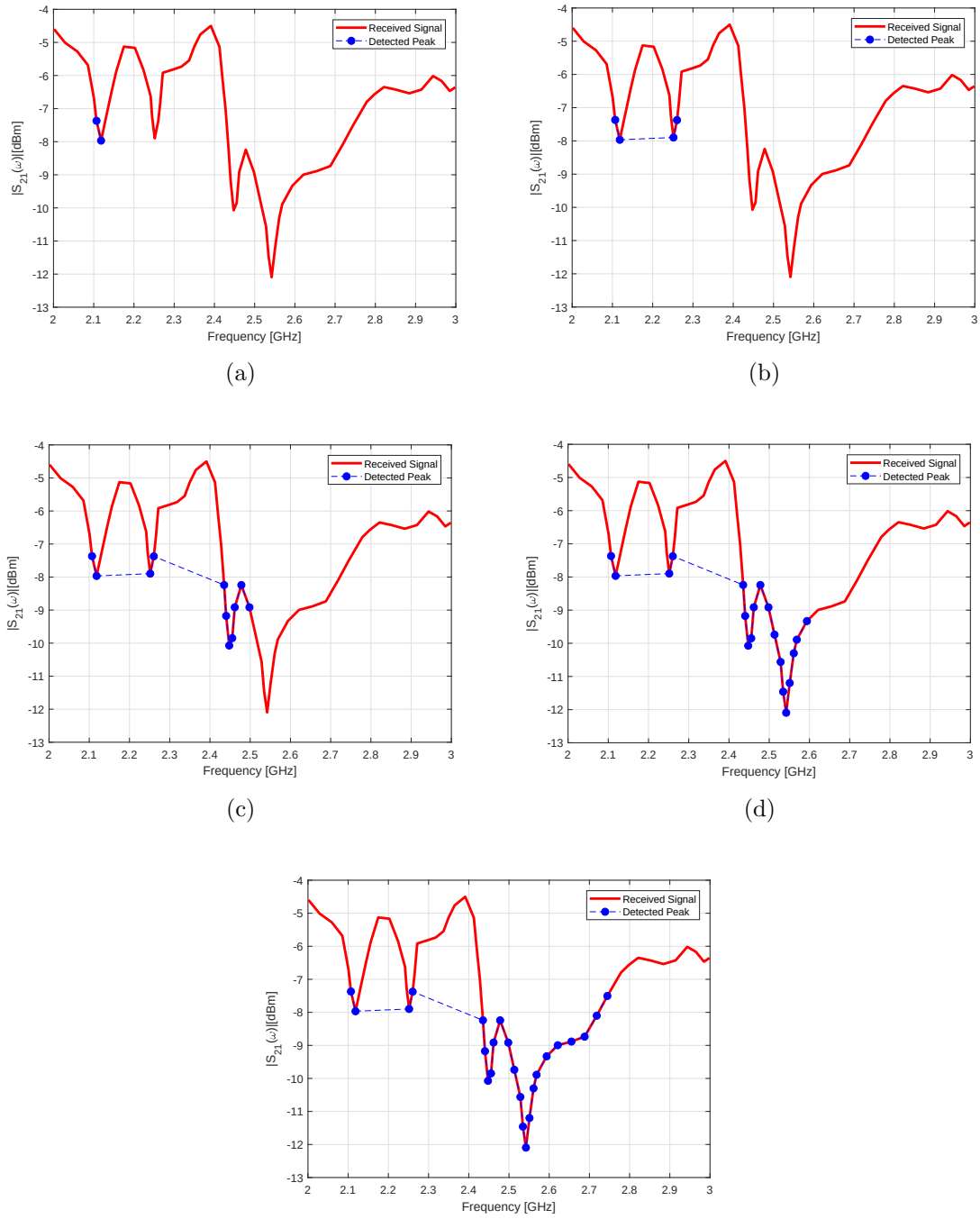

Figure 3.11: Peak detection for the received real-time signal with the tag configuration of 11110 using the newly proposed method. (**a**) step 1, (**b**) step 2, (**c**) step 3,(**d**) step 4, and (**e**) final step.

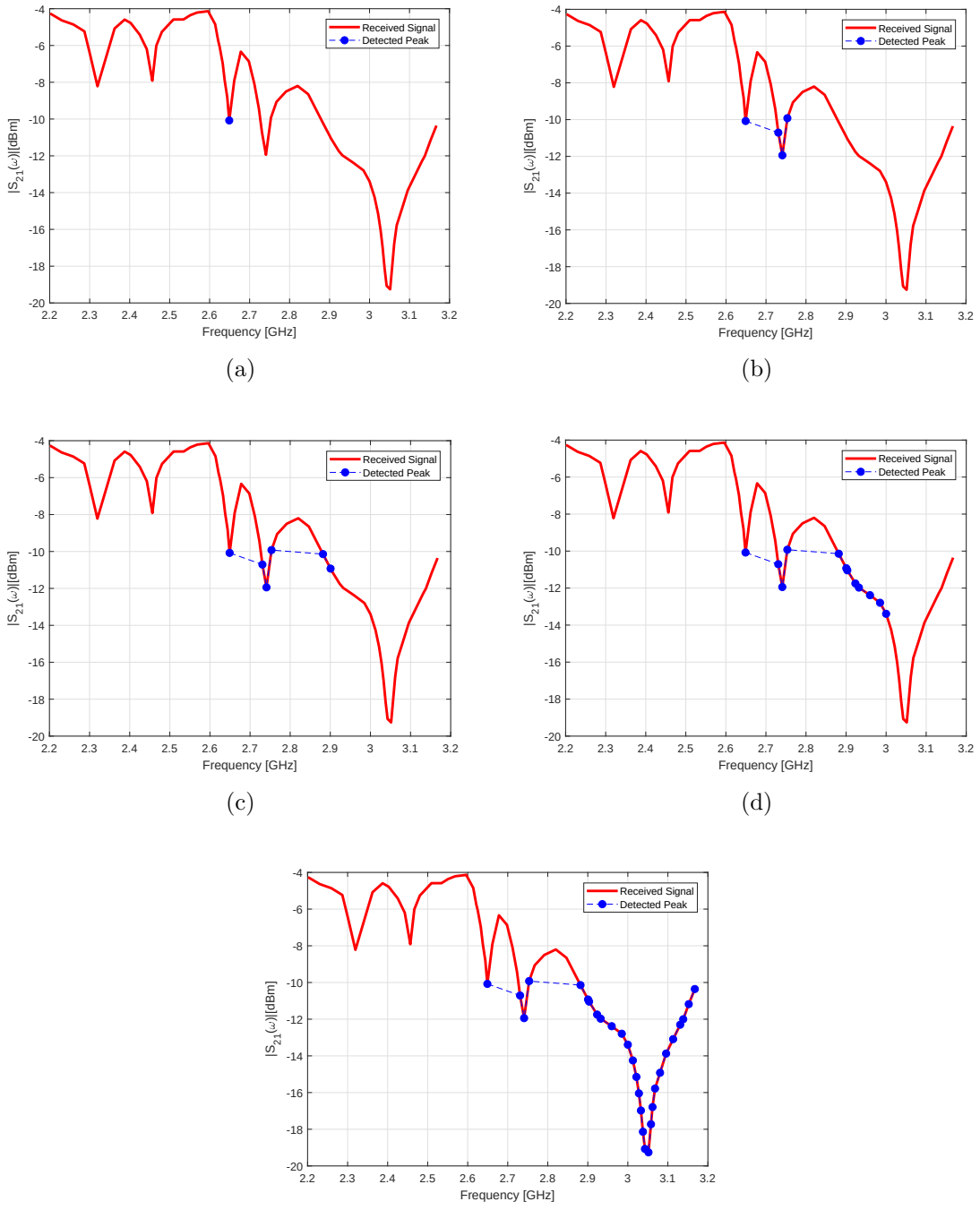

Figure 3.12: Peak detection for the received real-time signal with the tag configuration of 11111 using the newly proposed method. (**a**) step 1, (**b**) step 2, (**c**) step 3,(**d**) step 4, and (**e**) final step.

Chapter 4

Modulated Scattering Technique (MST)

In this chapter, various Modulated Scattering applications have been discussed with the mathematical system model and supported with Numerical/Experimental assessment respective to each application.

4.1 Environmental RFID Sensors Based on the Modulated Scattering Technique (MST)

4.1.1 Introduction

In the past few years, the demand for sensors that are low cost and have the capability to work in multi-function wireless environments has grown. The data collected from the sensors must be elaborated and transmitted related to a given environmental parameter [193]. The advantage of this sensor is evident especially in critical scenarios such as after natural disasters with restricted or dangerous areas [194].

Furthermore, they are very beneficial for practical purposes like homeland security [195], rescue operation and law enforcement services. Wireless sensor networks [196, 197] (WSNs) have been successfully adopted for the advancement of long-range estimation systems, but they use dense frequency bands and require maintenance and complex communication protocols. Radio frequency identification systems (RFID) [198, 199] are another type of wireless system that have been successfully used to track foods and goods. Now, they are widely used in many practical scenarios such as supermarkets and stores [122, 200, 201, 202, 203, 204, 205, 206, 207, 208, 209, 210, 211, 212, 213, 214, 215, 216]. The main benefit of adopting an RFID system is the long life and low cost, but it requires a close proximity between the reader and tag. Therefore, for a long-range communication system, it would not be suitable. Another drawback of RFID is the difficulty in providing environmental probes directly on the RFID tags. To overcome this kind of issue, in [217, 218, 219], the modulated scattering technique (MST) was defined. The MST provides an alternative solution to the WSN and RFID technologies' disadvantages. The MST probes use the scattering properties of small passive antennas as in [220, 221], and because

of this, they do not require a physical connection with the measurement system. MST systems do not rely on the sensitivity of the antenna tag, nor its load with respect to the relevant quantity to be sensed, like standard RFID sensors. The signal is delivered toward the MST reader, and it is insensitive to propagation effects. On the contrary, RFID sensors' performances are strongly sensitive to propagation effects, since they are impedance-based devices.

In particular for RFID systems, as in [222], electromagnetic propagation problems like reflections, interferences, propagation losses and collision problems [223, 224] are more important. Furthermore, the RFID is able to demodulate the signal accurately and give the answer only if examined correctly. For this reason, a local oscillator, an antenna driver, a demodulator and a data encoder are required in a standard RFID transceiver. The MST tag sends the information by modulating the impinging electromagnetic wave, without doing any operations like demodulation. Therefore, in complex scenarios, the RFID-based system would not work accurately. Moreover, RFID systems work in a very short range, while MST systems can work in free space, near-field, as well as far-field scenarios, and the operative range r can be evaluated simply by considering the radar equation, as in [225]. In particular, the MST probe antenna has different loads. These loads change by means of a suitable electronic switch. The change of antenna impedance in an MST reader introduces a low-frequency modulation signal in a backscattered electromagnetic wave, as in [218, 221], and also, it reads the backscattered field.

The information is retrieved from the low-frequency modulation signal provided by the tag to the backscattered wave. A radio frequency front end is not required for the MST tags. After interactions with the MST tag reader, it generates an electromagnetic wave, which carries the information. The absence of RF front end makes the tag less expensive

and suitable for a small probe to reduce perturbations and noise measurements. The MST probes have been used successfully in applications like, microwave imaging [226, 227], measurements in near-field electromagnetics [228, 229, 230, 231, 232, 233], characterization of materials [234, 235] and other applications, as given in [128, 236, 237]. In this work, an X band wireless MST monitoring system is proposed for environmental monitoring. The prototype requires only a limited amount of power and ensures a good communication range of about 15 m. It represents a good alternative to standard WSN- or RFID-based architecture. The proposed wireless sensor tag presents the following innovations: the operative frequency located in the X band at 10 GHz permits strongly reducing the tag and reader antenna dimensions. Higher frequency bands can be used to further reduce the sensor size and improve the signal bandwidth. Most of the state of the art long-range RFID tag systems work on crowed frequency bands such as WiFi at 2.45 GHz, and most of them are not passive devices, since they make use of the WiFi module [238]. The proposed system does not need RF or microwave front-ends; moreover, with respect to the other commercial or experimental devices, it is theoretically able to reach distances up to kilometers [218, 239]. Thanks to these characteristics, these sensors are particularly suitable to monitoring environmental parameters during natural disasters, such as earthquakes or avalanches. A three-month measurement campaign has been carried out to evaluate the proposed MST environmental monitoring systems. In particular, meteorological quantities, namely the temperature variations and humidity, were measured during the summer season in Northern Italy.

4.1.2 Mathematical Formulation

The schema of a mono-static MST measurement system is shown in Figure 4.1. It consists of a reader aimed at communicating with a remote tag

placed far away from the reader at a distance r called the communication range. The tag could be equipped with different environmental probes. The reader is composed of a sinusoidal signal generator, a microwave low noise amplifier, a homodyne detector, a circulator and a high gain antenna. The circulator is used to consider only one high gain antenna, acting both as transmitter and receiver. The reader not only generates the electromagnetic wave, which impinges on the MST tag, but it also collects the back-scattered electromagnetic wave, which carries the information reflected by the tag. The homodyne detector is mandatory to correctly retrieve the information from the backscattered electromagnetic wave [240, 241]. In particular, the high-frequency signal is converted to the baseband, and a suitable elaboration system is aimed at collecting, processing and storing the information from the low modulation signal of the backscattered wave [218]. On the left side of Figure 4.1 is shown the tag structure. The MST tag is composed of a small receiving antenna, an electronic switch, a set of loads, an elaboration unit, power units and a set of environmental probes. The elaboration unit reads the measured quantities from the probe. The elaboration units also act on the electronic switch; it permits connecting the antenna tag toward two different loads. The variation of impedance, connected with the antenna tag, produces a low-frequency modulation on the back-scattered electromagnetic wave. The low-frequency modulation carries the information, and it can be easily read by the reader. A good MST system design permits maximizing the communication range r [221]. This goal can be accomplished by considering the well-known radar equation reported in the following relation [225, 242] (under the hypothesis of free space and far-field conditions):

$$r = \frac{1}{2}\left(\frac{P_{tx} \cdot G_{tx} \cdot \lambda^2 \cdot A_{tag} \cdot G_{tag} \cdot ME\left(Z_1, Z_2\right)}{\left(4\pi\right)^2 \cdot P_{rx}}\right)^{\frac{1}{4}} \tag{4.1}$$

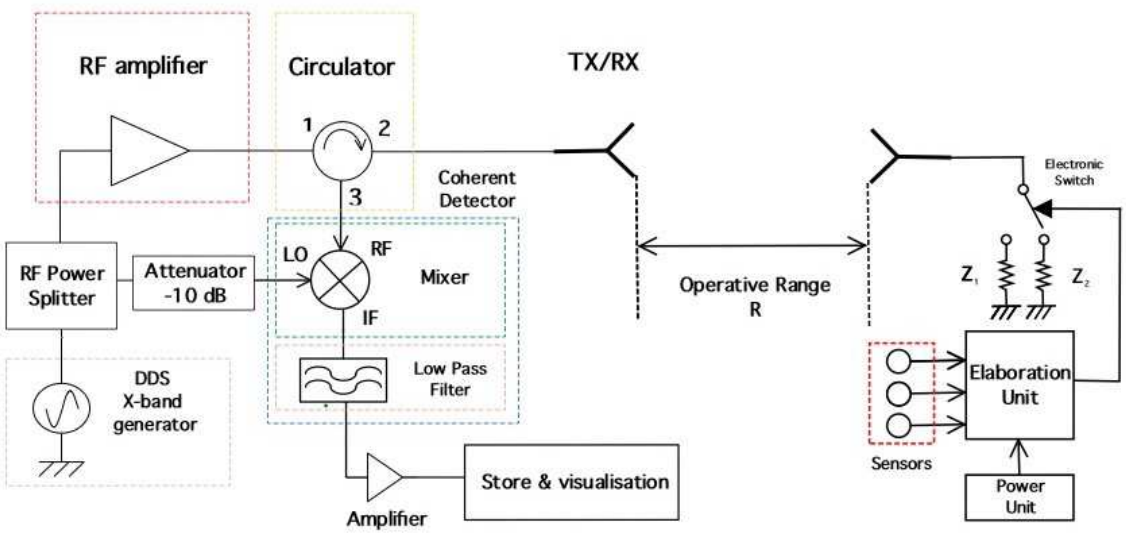

Figure 4.1: Schematic of a mono-static modulated scattering technique (MST)-based measurement system.

where P_{tx} and G_{tx} are the power of the sinusoidal generator and the reader receiving antenna gain, respectively. P_{rx} is the minimum detectable power, and it depends on the receiver sensibility. A_{tag} and G_{tag} are the antenna tag aperture cross-section and gain, and λ is the wavelength of the sinusoidal signal generated by the reader. The quantity of ME, called the modulation efficiency, is reported in the following relation:

$$ME\left(Z_1, Z_2\right) = \frac{4Re\left\{Z_{tag}\right\}\left|Z_2 - Z_1\right|^2}{\left|Z_{tag} - Z_1\right|^2 \cdot \left|Z_{tag} - Z_2\right|^2} \tag{4.2}$$

where Z_{tag} is the antenna tag impedance and Z_1 and Z_2 are the two loads connected to the electronic switch. As can be noticed from Equation (4.2), the modulation efficiency ranges between $0 \geq ME$ and $ME \leq 4$. Considering Equation4.1, it is quite evident that the only way to improve the communication range r is to act on the values of the two loads Z_1 and Z_2 or to modify the antenna tag impedance Z_{tag}. The other parameters are fixed quantities. To obtain the maximization of the ME, the best values

for the two loads are $Z_1 = 0$ and $Z_2 = Z_{tag}^*$. Z_2 is called the adsorbing load, and it is used to obtain a perfect match.

4.1.3 Description of the MST Environmental System

The following sub-sections are aimed at the description of the reader, MST tag structure and transmission protocol.

Reader Description

In Figure4.2, the picture of the MST reader's working prototype is shown. The prototype consists of a ferrite circulator, an X band microwave Gunn generator of $P_{tx} = 50$ mW, a lens antenna characterized with a gain of $G_{tx} = 17$ dBi and two low-frequency amplifiers with a total gain of $G_{amp} = 20$ dB. As can be noticed from Figure4.2, the reader is a classical mono-static structure (characterized by only one antenna, which acts as a receiver and transmitter at the same time). The reader is quite compact and mechanically robust. The ferrite circulator output is connected to the homodyne receiver. The receiver is composed of an unequal splitter aimed at providing the reference to the mixer, a low-cost monolithic microwave integrated circuit mixer (an anadigics AKD12000). The signal at the mixer output is then filtered by means of a low pass seven order equal ripple $0.5dB$ filter. The low modulation signal is extracted from the high frequency backscattered wave using a coherent detector. Further, the two low noise amplifiers are used to amplify the obtained baseband signal, where the amplifier has a total gain of $G_{rx} = 20dB$. The least detectable power is about $P_{rx} = -100dBm$ at the reader output.

MST Tag Description

To illustrate the abilities of the MST method-based wireless sensors, the development of a wireless sensor tag is described in this section. To develop

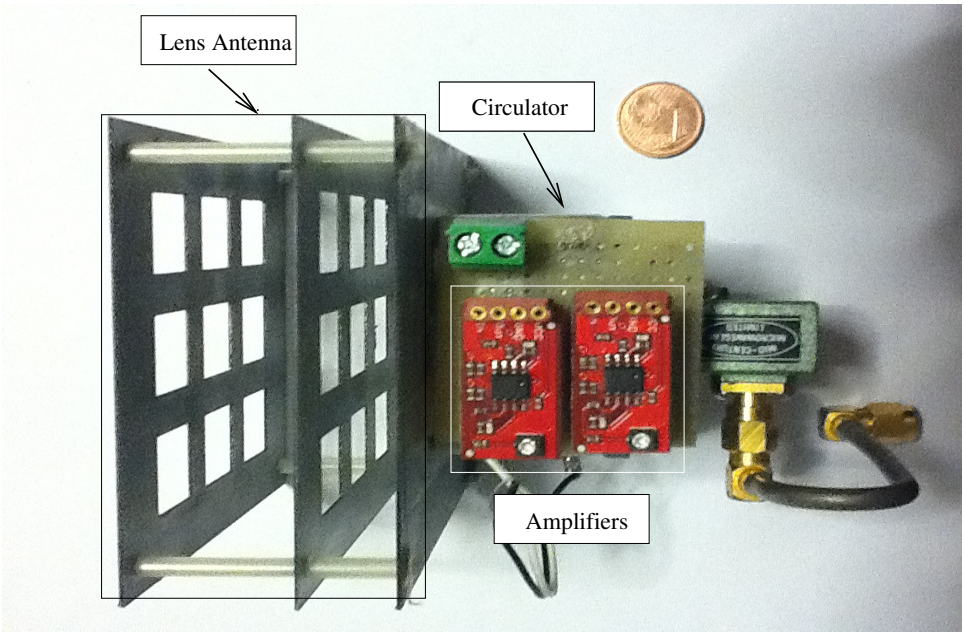

Figure 4.2: Photograph of the compact MST reader.

an MST sensor tag, the first step is to choose the electronic switch properly by considering the guidelines followed in [221]. MOSFET-based switches offer the best performances, which could lead to nearly the maximum theoretical upper limit for the ME. The MOSFET switch developed in Section III D of [221] was chosen for the considered MST tag prototype because it offers the best performances with respect to the communication range. The PIC18F876A microchip, a low-cost microcontroller, was chosen as the elaboration unit, to acquire, convert and send the proper modulation signal to the driven modulation circuit.This microcontroller is equipped with A/D channels to connect a different kind of sensor. Moreover, it is equipped with a low power wake-up module. To reduce the power consumption, the microprocessor is kept in stand-by mode, and it is activated by means of a suitable interrupt only to perform the measurement.

A switching step down voltage regulator, the MAX1044 (Maxim company), was used to reduce the power consumption. The elaboration and the switching sub-units were assembled into a compact two-layer structure

of dimensions $50 \times 35 \times 25$ mm^3. As can be seen from the photo in Figure 4.3, the prototype is quite compact. However, the dimensions could be further reduced since the elaboration unit was assembled with standard components and not with surface-mounted devices (SMD). To obtain a wireless temperature/humidity probe, the two A/D channels out of the four were connected to a precision temperature sensor LM35DZ and the humidity sensor HR202. The humidity and temperature sensors have been calibrated in a controlled environment. In particular, a climatic chamber (ANGELATONI DY1200 with a temperature and humidity range of $-40°C < T < 180°C$ and $10\% < H < 98\%$) was been kindly provided by the EMC company, Genoa Italy. Figure 4.4a,b reports the calibration graph for the temperature and humidity sensor, respectively. As can be observed from the graph of Figure 4.4, the agreement is quite good. The working of the MST tag is as follows: The microcontroller collects the data for the temperature and humidity from the sensors continuously and converts them into bits using the 12-bit AD converter. Then the data are transmitted by changing the loads of the tag antenna using the MOSFET switch. To transmit the data, the modulation frequency is considered as 2 kHz. Furthermore, the modulation protocol is the same as for the RFID systems in [223, 224]. In detail, as a protocol, EM4102, and for the modulation, the Manchester modulation were used. In the Manchester modulation, a low to high transition is represented by a logical one state, and a high to low transition is represented by a logical zero state. The EM4102 protocol allows immediate integration with commercial and RFID systems, databases and other RFID resources. The data organized in the EM4102 are as follows: the first nine bits of the data represent a logical one state. These first nine bits signify the start of the data string as a marker sequence. Then, the remaining string is followed by 10 groups of four data bits and one even parity bit. Finally, four bits of a column parity

(even) and a stop bit (zero) are used. The MST tag performs tasks like read, convert and transmit the string data and represents the measured temperature perfectly as long as it has power. Furthermore, the length of each bit in the tag is defined in terms of clock cycles. Any bit length can be used from 64, 32 to 16 clock cycles in the EM4102 protocol. For this preliminary experiment, a 32-bit length and a reference frequency clock of 100 kHz has been used. An example of data sequence, transmitted by the tag and measured at the reader, output with a digital storage oscilloscope (DSO) is reported in Figure 4.5a. The tag has been placed at an operative distance $r = 15$ m from the reader. Figure 4.5b reports the reader output when the tag is not activated. As can be seen from the waveform reported in Figure 4.5a, the data are clearly detected. Concerning the measurement of the MST tag prototype's power consumption, it was carried out using suitable checkpoints introduced in the driving circuit of the modulation and microcontroller section. The MST tag was tested under different realistic operative conditions. In particular, in standby, with the modulation driven circuit turned off, the microcontroller required $3V$ and $I_s = 3.5\mu A$; while during the measurement phase, the current required by the microcontroller was about $I_o = 8\mu$A, considering that the modulation circuit required about $I_m = 2mA$. The total current required by the MST tag in normal working conditions was about $I_t = 2\mu$A. The power supply was provided by two standard rechargeable (1.2 V, $I = 1400mA$) batteries, which can ensure a measured lifetime of the MST tag of about 12 h of continuous operation.

The prototype was also equipped with a small solar panel ($V = 3$ and $I = 10mA$), able to guarantee not only the correct working conditions during the day, but also to recharge the two batteries, aimed at providing the necessary current during the night.

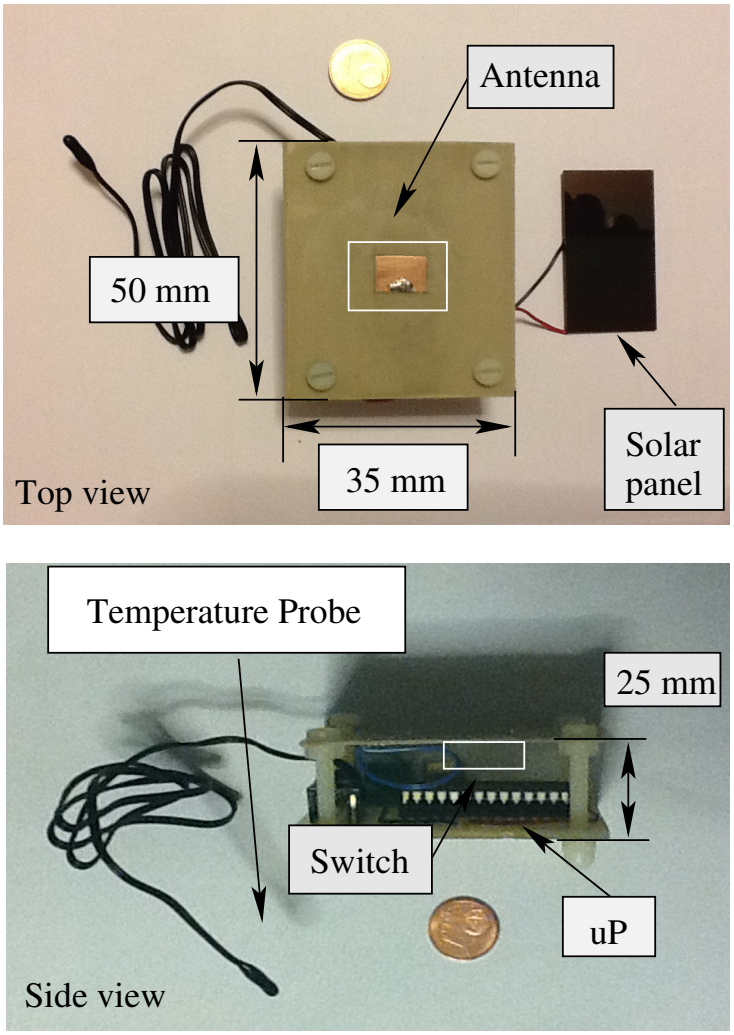

Figure 4.3: Photo of the MST tag equipped with temperature and humidity probes and a solar panel.

Experimental Setup and Measurement Campaign

Before starting the measurement campaign, the theory described in Section 4.1.2 was assessed in a controlled environment. In particular, the operative range versus the transmitted power was measured. The operative range was considered valid when the transmitted tag sequence was correctly received a hundred times. Concerning the other system parameter $G_{tx} = 17dBi$, $G_{tag} = 6dBi$ are the reader and tag antenna gains. respectively, and $P_{rx} = -110$ dBm is the minimum detectable power at the

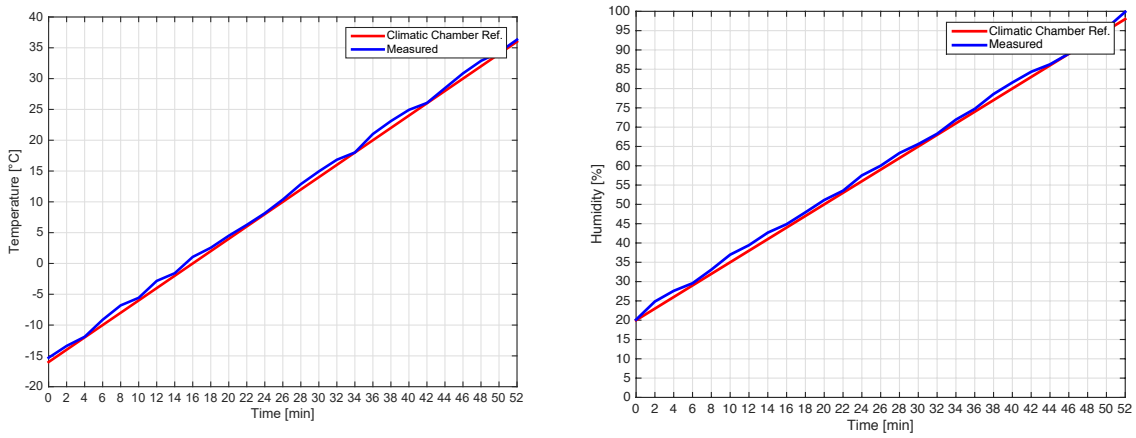

(a) (b)

Figure 4.4: Temperature and humidity calibration curves obtained with a climatic chamber: (**a**) temperature and (**b**) humidity.

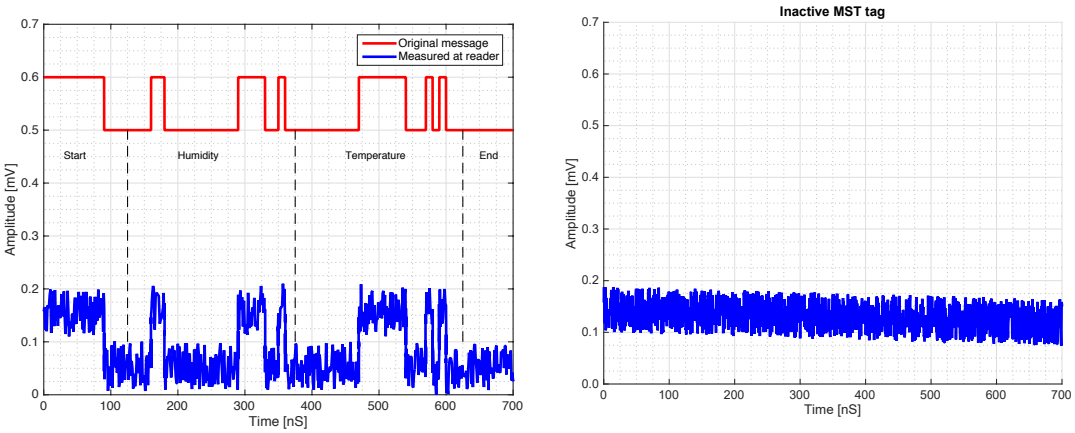

(a) (b)

Figure 4.5: Example of the data structure received at the reader output (**a**). Signal detected with an inactive tag (**b**).

receiver, $P_{tx} = -17dBm$. The obtained modulation efficiency $ME = 3.2$ was very close to the upper theoretical limit. For the the transmitter a direct digital synthesis (DDS) generator is able to modify its power in the range of 1 mW $< P_{rx} < 20mW$ with a step of $1mW$. The results reported in Figure 4.6 show a good agreement between theoretical and experimental

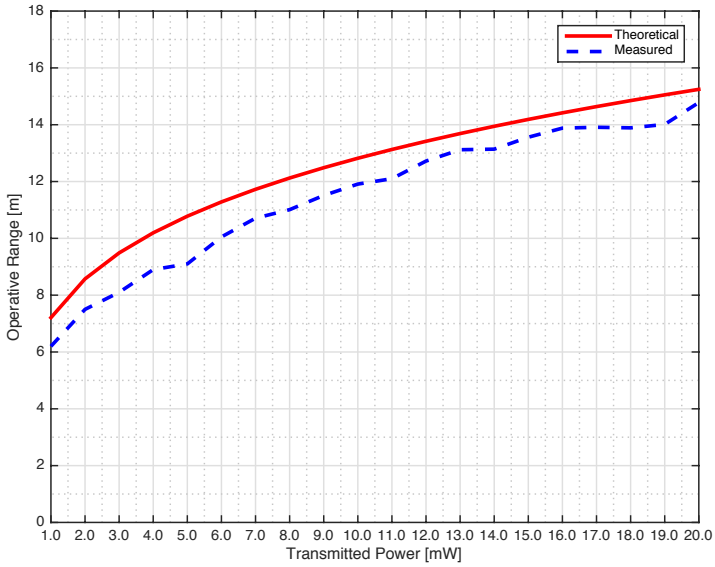

Figure 4.6: Operative range vs. transmitted power. Continuous red line, theoretical; dotted blue line, experimental.

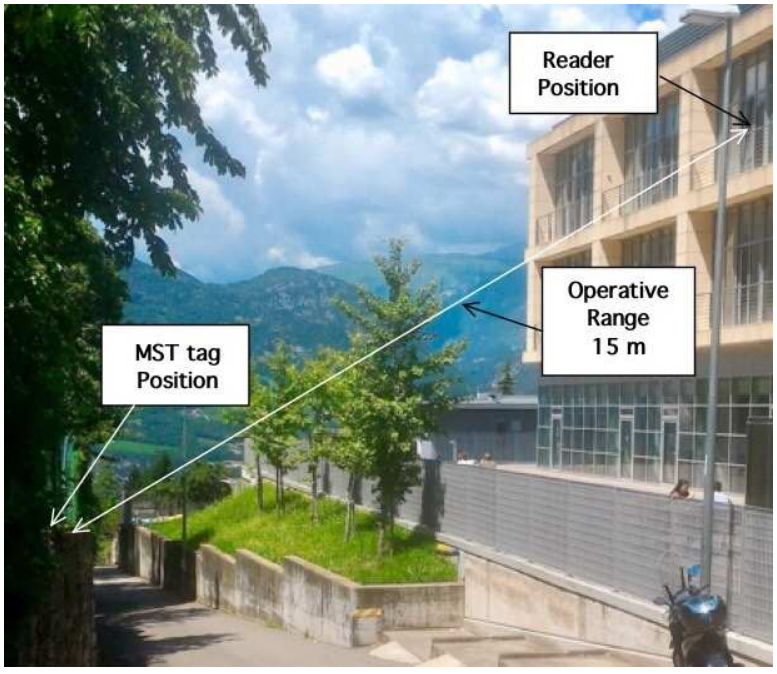

Figure 4.7: Photo of the experimental setup.

data.

To assess the capabilities of the MST sensor, it was placed in a line of sight at a distance $r = 15m$ from the reader. The data at the reader output

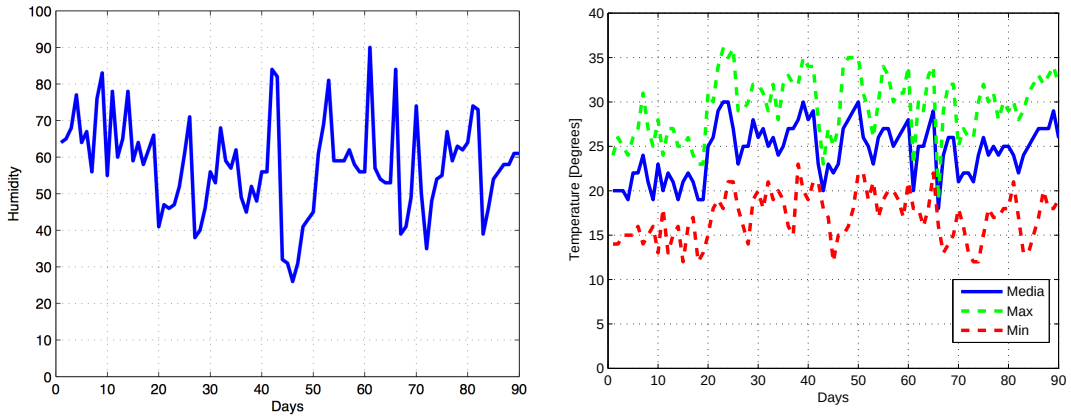

(a) (b)

Figure 4.8: Three-month measurement campaign data.(**a**) humidity (**b**) temperature

were elaborated by means of a laptop provided with an A/D board, and a monitoring campaign of three months was carried out. In particular, the MST sensor was placed outdoors, exposed to the weather and used to monitor the temperature and humidity during the summer season. The photo of the considered measurement scenario is reported in Figure 4.7. The reader has been placed beyond a window of the laboratory, and the MST tag was placed on a small wall outside the building and exposed to meteorological phenomena. The distance between the reader and the tag was measured by using a commercial laser telemeter (the Bosh PLR40C with an accuracy of $\pm 2mm$). The microcontroller was connected to the MST reader, and it was programmed to take a measurement every half an hour. In these operating conditions, the lifetime of the MST tag was more than 12 h. Figures 4.8 show the humidity and temperature values recorded during the three-month campaign. As can be noticed from the data in Figure 4.8, the maximum and minimum temperature values recorded were $T_{max} = 37$ and $T_{min} = 12$, respectively (typical temperature values of the summer in Northern Italy). These data were compared and confirmed by the official meteorological reports. This is a further demonstration of the MST-based

Table 4.1: State of the art RFID system performance comparisons.

Freq. (GHz)	**TX Power (W)**	**Range (m)**
0.915	0.5	9.25[53]
2.450	0.007	3.30[54]
2.450	4.0	10.00[55]
10.0	0.002	15.00

systems' potentialities as wireless sensors for real-time environmental monitoring applications. For the sake of comparison, the performances of other state of the art RFID systems were compared with the proposed prototype. The data are reported in Table 4.1, and as can be noticed, the proposed MST system is able to reach a higher operative range with a lower transmitting power with respect to the other considered systems.

4.2 Air Quality Monitoring System based on the Modulated Scattering Technique (MST)

4.2.1 Introduction

An air pollution state the biggest environmental impact to human health. In 2012, one out of every nine deaths was due to the result of air pollution conditions. Of those deaths, around 3 million are attributable solely to ambient (outdoor) air pollution. The air pollution effects on all regions, settings, socio-economic groups, and all age groups. All the people living in a given area breathe from the same air. Nevertheless, there are some important geographical differences in exposure to air pollution. Places like Africa, Asia and the Middle East have air pollution levels which are several times higher than the safe air quality consideration by the World Health Organization (WHO) Air quality guidelines [243]. At the present time, air pollution is highly featured agenda of a global economy. According to the Global Health Observatory (GHO) data says that 194 members of WHO states had adopted a resolution to respond to the effects of air pollution on the health. The road map for an enhanced global response outlines goals and approaches for monitoring and reporting of air pollution, as well as enhancing systems, structures and processes to support the monitoring. The reporting on health trends are associated with air pollution sources [244].

Academic researchers, scientists and international organizations around the world have combined their efforts to develop comprehensive and reliable models for air pollution, which can estimate the impact of air pollution on a human health. Our motive in this work is to contribute in their efforts. There are two types have been considered when it comes to monitoring the air pollution, 1) Outdoor (Urban) and 2) Indoor air

quality. In both types, air quality can be demonstrated by pollutants concentration such as carbon monoxide (CO), carbon dioxide (CO_2), tobacco smoke, perfume, sulphur dioxide (SO_2), nitrogen dioxide (NO_2), and ozone (O_3). Some of these pollutants can be created by indoor activities such as smoking and cooking [245]. Air quality as an indoor quality monitoring in industries and houses are most prominent in consumer application, especially in countries like China and India [246]. Over the last few years, many sensor-array instruments have been proposed and employed to detect and diagnose the odorants in many applications like, environment, and agriculture monitoring, food manufacturing, fragrance, pharmaceuticals, and medical diagnosis. Most of the published work has been based on solid-state sensors as reported in [247], like metal oxide semiconductor (MOS), metal oxide semi-conductor field effect transistor (MOSFET), and conducting polymer (CP) arrays. In [246], The Karlsruhe Micronose (Karlsruher mikronasev[KAMINA]) based microarray gas sensor has been proposed and practically tested for an indoor air quality monitoring for the fire prevention and air quality analysis in air conditioned room. Similarly in [245, 248, 249], to perceived car-cabin air quality a low power MOS, and field asymmetric ion mobility spectrometry and photoionization detection based sensor has been presented, respectively. Furthermore research presented in [250, 251, 252, 253, 254, 255] reports air quality assessment data analysing and processing is equally important as acquiring the data. To analyse and process the data [252, 254, 255] have presented a principal components multinomial logistic regression classifier ,an anomaly detection framework, and deep learning based technique, respectively. In [247], a state-of-the-art for low-cost air pollution sensors has been presented to identify their major error sources. However, a survey of wireless sensor network based air pollution monitoring systems [256] gives the insight of different standard of pollutants, pollutants health effect, monitoring equip-

ments, and equipments accuracy, price and range. Although, there are many other factors which are considered and discussed in [256] but here in this work we are focusing on important factor like, price, range of the sensor, accuracy and power consumption.

In this work, we have presented a real-time carbon dioxide (CO_2) monitoring system for an indoor environment. The system is implemented through a MST. Each reader is placed at particular distance has high gain antenna to transmit and receive the data from the MST tag.

4.2.2 Mathematical Formulation

The schema of a mono-static MST measurement system is shown in figure 4.9. It consists of a reader aimed at communicating with a remote tag placed far away from the reader at a distance r called communication range. The tag could be equipped with different environmental probes. The reader is composed by a sinusoidal signal generator, a microwave low noise amplifier, a homodyne detector, a circulator, and a high gain antenna. The circulator is used to consider only one high gain antenna, acting both as transmitter and receiver. The reader not only generates the electromagnetic wave which impinges on the MST tag, but it also collects the backscattered electromagnetic wave, which carries the information, reflected by the tag. The homodyne detector is mandatory to correctly retrieve the information from the backscattered electromagnetic wave [240, 241]. In particular, the high-frequency signal is converted in the baseband and a suitable elaboration system is aimed at collect, process and store the information from the low modulation signal of the backscattered wave [218]. On the left side of figure 4.9 is shown the tag structure. The MST tag is composed by a small receiving antenna, an electronic switch, a set of loads, an elaboration unit, power units and a set of environmental probes. The elaboration unit reads the measured quantities from the probe. The

elaboration units also act on the electronic switch, it permits to connect the antenna tag toward two different loads. The variation of impedance, connected with the antenna tag, produces a low-frequency modulation on the back-scattered electromagnetic wave. The low-frequency modulation carries the information and it can be easily read by the reader. A good MST system design permits to maximize the communication range r [221]. This goal can be accomplished by considering the well-known radar equation reported in the following relation [225, 242] (under the hypothesis of free space and far field conditions):

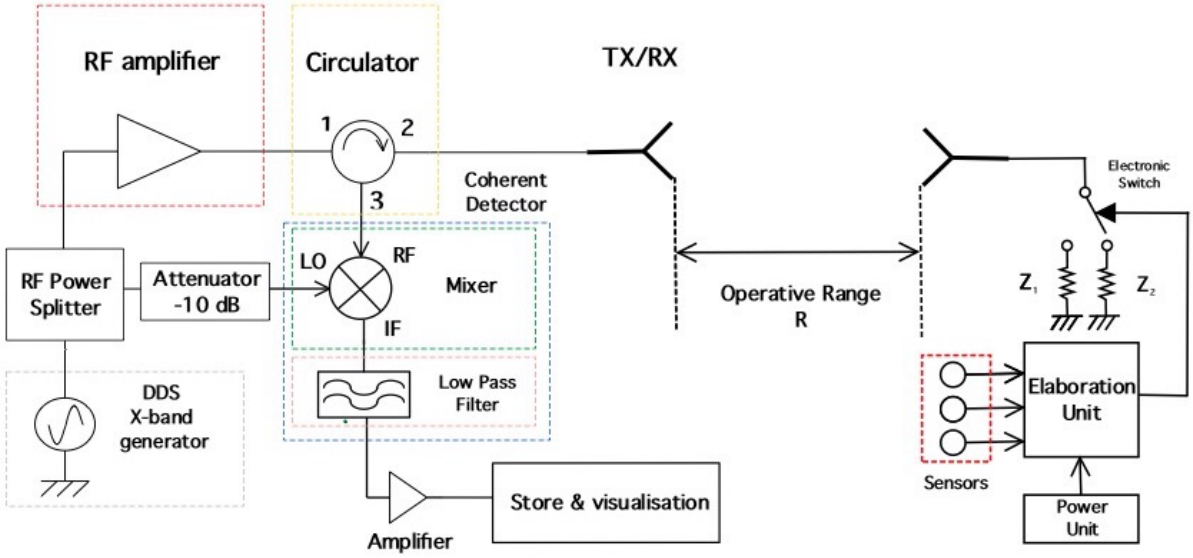

Figure 4.9: Schematic of a mono-static MST based measurement system.

$$r = \frac{1}{2}\left(\frac{P_{tx} \cdot G_{tx} \cdot \lambda^2 \cdot A_{tag} \cdot G_{tag} \cdot ME\left(Z_1, Z_2\right)}{\left(4\pi\right)^2 \cdot P_{rx}}\right)^{\frac{1}{4}} \tag{4.3}$$

where P_{tx} and G_{tx} are the power of the sinusoidal generator and the reader receiving antenna gain respectively. P_{rx} it is the minimum detectable power and it depends on the receiver sensibility. A_{tag} and G_{tag} are the antenna tag aperture cross section and gain, λ is the wavelength of the sinusoidal signal generated by the reader. The quantity of ME, called modulation efficiency is reported in the following relation:

$$ME\left(Z_1, Z_2\right) = \frac{4Re\left\{Z_{tag}\right\}\left|Z_2 - Z_1\right|^2}{\left|Z_{tag} - Z_1\right|^2 \cdot \left|Z_{tag} - Z_2\right|^2} \tag{4.4}$$

where Z_{tag} is the antenna tag impedance, Z_1 and Z_2 are the two loads connected to the electronic switch. As it can be noticed from Equation4.4, the modulation efficiency ranges from $0 \geq ME$ and $ME \leq 4$. Considering Equation4.3 it is quite evident that the only way to improve the communication range r is to act on the values of the two loads Z_1 and Z_2 or modify the antenna tag impedance Z_{tag}. The other parameters are fixed quantities. To obtain the maximization of the ME the best values for the two loads are $Z_1 = 0$ and $Z_2 = Z_{tag}^*$. Z_2 is called adsorbing load and it is used to obtain a perfect match.

4.2.3 Description of the MST environmental system

The following sub-sections are aimed at the description of the reader, MST tag structure, and transmission protocol.

Reader Description

In figure 4.2, The picture of the MST reader's working prototype is shown. The prototype consists of a ferrite circulator, an X-band microwave Gunn generator of a $P_{tx} = 50mW$, a lens antenna characterized with a gain of $G_{tx} = 17dBi$, and two low-frequency amplifiers with a total gain of $G_{amp} = 20dB$. As it can be noticed from figure 4.2 the reader is a classical

mono-static structure (characterized by only one antenna which acts as a receiver and transmitter at the same time). The reader is quite compact and mechanically robust. The ferrite circulator output is connected to the homodyne receiver. The receiver is composed by an unequal splitter aimed at providing the reference to the mixer, a low-cost monolithic microwave integrated circuit mixer (an anadigics AKD12000). The signal at the mixer output is then filtered by mean of a low pass seven order equal ripple $0.5dB$ filter. The low modulation signal is extracted from the high frequency backscattered wave using coherent detector. Further, the two low noise amplifiers were used to amplify the obtained baseband signal, where amplifier has a total gain of $G_{rx} = 20dB$. The least detectable power is about $P_{rx} = -100dBm$ at the reader output.

MST Tag description

To illustrates the abilities of the MST method based wireless sensors, the development of a wireless sensor tag is described in this section. To develop an MST sensor tag, the first step is to choose the electronic switch properly by considering the guidelines followed in [221]. The MOSFET based switches offer the best performances, which could lead nearly the maximum theoretical upper limit for the ME. The MOSFET switch developed in this Section of [221] was chosen for the considered MST tag prototype The PIC18F876A microchip, a low-cost microcontroller, was chosen as elaboration unit, to acquire, convert, and send the proper modulation signal to the driven modulation circuit. This microcontroller is equipped with an A/D channels to connect a different kind of sensors. Moreover, it is equipped with a low power wake-up module. To reduce the power consumption the microprocessor is keep in stand-by mode and it is activated by means of a suitable interrupt only to perform the measure. A switching step down voltage regulator, the MAX1044 (Maxim company) was used to reduce

the power consumption. An elaboration and the switching sub-units were assembled into a compact two-layer structure of dimensions $50 \times 35 \times 25$ mm^3. As can be seen from the photo in figure 4.10, the prototype is quite compact. However, the dimensions could be further reduced since the elaboration unit was assembled with standard components and not with surface mount devices (SMD). To obtain a wireless temperature/humidity probe the two A/D channels out of the four were connected to a precision temperature sensor LM35DZ and the humidity sensor HR202. The humidity and temperature sensors have been calibrated in a controlled enviroment. In particular a climatic chamber (ANGELATONI DY1200 with a temperature and humidity range of $-40C < T < 180C$ and $10\% < H < 98\%$) the climatic chamber has been kindly provided by the EMC company, Genoa Italy. Figs 4.11 (a) and (b) report the calibration graph for the temperature and humidity sensor respectively. As it can be observed the from the graph of Figs 4.11 the agreement is quite good. The working of the MST tag is as follows: The microcontroller collects the data of the temperature and humidity from the sensors continuously and converts them into bits using the 12 bits AD converter. Then the data is transmitted by changing loads of the tag antenna using the MOSFET switch. To transmit the data the modulation frequency is considered as $2KHz$. Also, the modulation protocol is same as RFID systems, in [223, 224]. In detail, as a protocol the EM4102, and for the modulation, the Manchester modulation were used. In Manchester modulation, a low to high transition is represented by a logical 1 state, and a high to low transition is represented by a logical 0 state. The EM4102 protocol allows immediate integration with commercial and the RFID systems, databases, and other RFID resources. The data organized in the EM4102 is as followed: the first 9 bits of the data represent a logical 1 state. These first 9 bits signifies the starting of the data string as a marker sequence. Then the remaining string is followed by 10 groups

of 4 data bits and 1 even parity bit. Finally, 4 bits of a column parity (even) and a stop bit (0) are at last. The MST tag perform the tasks like to read, convert, transmit the string data and representing the measured temperature perfectly as long as it has power. Furthermore, The length of each bit in the tag is defined in terms of clock cycles. Any bit length can be used from the 64, 32, or 16 clock cycles in the EM4102 protocol. For this preliminary experiment, a 32-bit length and a reference frequency clock of $100KHz$ has been used. An example of data sequence, transmitted by tag and measured art the reader output with a digital storage oscilloscope DSO is reported in Fig. 4.12 (a). The tag has been placed at an operative distance $r = 15m$ from the reader. Fig. 4.12 (b) reports the reader output when the tag is not activated. As it can be seen from the waveform reported in Fig. 4.12 (a) the data are clearly detected. Concerning the measurement of the MST tag prototype's power consumption, it was carried out using suitable checkpoints introduced in the driving circuit of the modulation and microcontroller section. The MST tag was tested under different realistic operative conditions. In particular, in standby, with the modulation driven circuit turned off, the microcontroller requires $3V$ and $I_s = 3.5$ μA. While during the measurement phase, the current required by the microcontroller is about $I_o = 8\mu A$, considering that the modulation circuit requires about $I_m = 2mA$. The total current required by the MST tag in normal working conditions is about $I_t = 2\mu A$. The power supply is provided by two standard rechargeable (1.2 V, $I = 1400$mA) batteries, which can ensure a measured lifetime of the MST tag of about 12 hours of continuous operation.

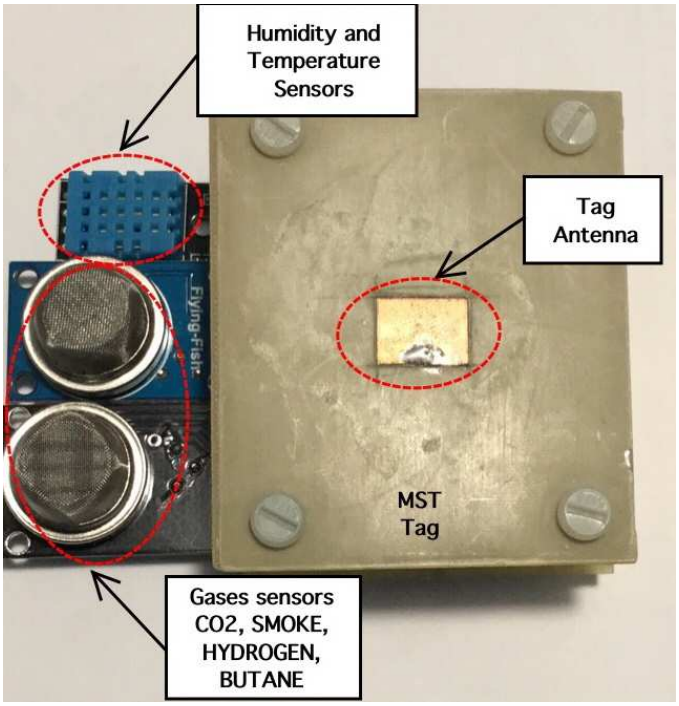

Figure 4.10: Photo of the MST tag equipped with a temperature and humidity probes and a solar panel.

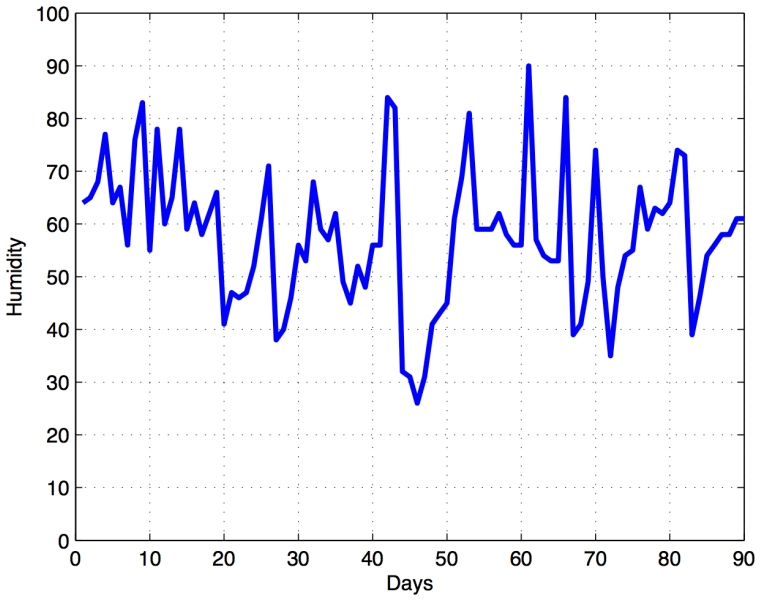

(a)

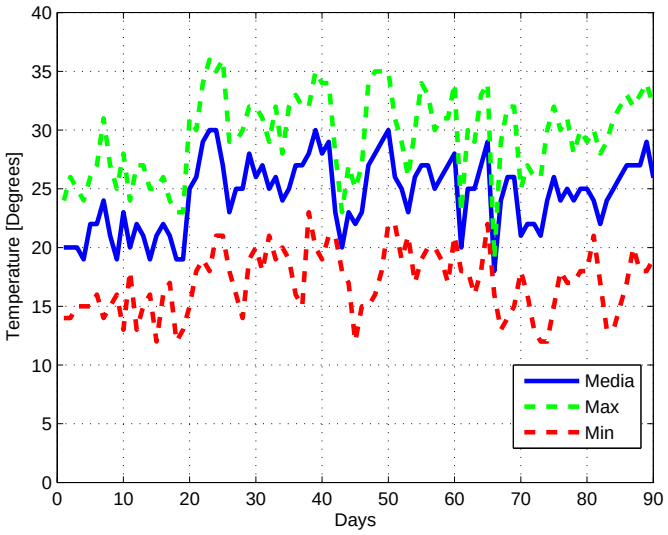

(b)

Figure 4.11: Temperature and humidity calibration curves obtained with a climatic chamber (a) temperature, (b) humidity.

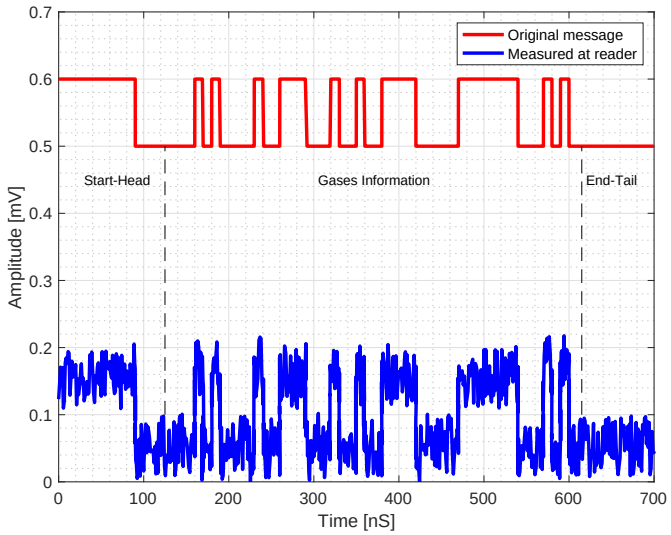

(a)

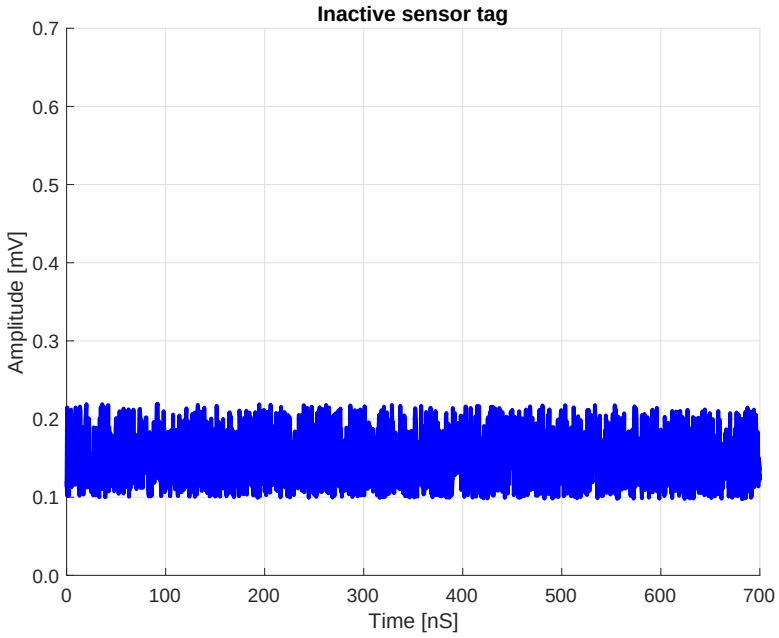

(b)

Figure 4.12: Example of data structure received at the reader output (**a**) Observed Signal with an active tag (**b**) Signal with an inactive tag

4.3 Microelectromechanical systems (MEMS) based Modulated Scattering Technique (MST)

4.3.1 Introduction

In the last years modulated scattering technique (MST) probes [217, 239] demonstrated to be an attractive alternative to standard monitoring systems such as RFID or wireless sensor networks WSNs. The MST sensors are flexible, low cost, present an high communication range, and low invasive since they are not physically connected with the measurement system. They can be easily integrated with limited Hardware (HW) modifications in an existing monitoring system based on RFID or doppler radar. Moreover, multi-ports MST sensors recently demonstrated their potentialities to sense the electrical properties of materials when the power of the interrogating electromagnetic wave is very low or when the sensors are embedded in different material or used in very complex scenarios [126, 235, 257]. The MST probes are usually composed by a micro-controller, an electronic switch, a set of loads, a transmitting/receiving antenna and a rectifying unit aimed to provide the power supply. The MST antenna can be switched on different loads by using a suitable electronic switch. The impedance changes at the antenna tag produce variations on the backscattered waves that can be detected by the reader and deliver the information. The main drawback of MST probes is the electronic switch especially if broadband behaviour is required. In such a framework, microelectromechanical systems (MEMS) switches [258, 259, 260] have recently successfully adopted in a broadband MST probe demostrating superior performances in terms of reflection coefficient and insertion loss. In this work the capabilities of the MST probe reported in [126] has been strongly improved, thanks to an enhanced version of a SP3T MEMS switch able to connect the MST

antenna probe with three different loads. A tag prototype has been designed, fabricated and experimentally assessed. The MST probe equipped with the SP3T MEMS switch is able to retrieve the electric characteristics of the surrounding media and it can be used to detect materials anomalies or contaminations. The obtained experimental results are quite promising and they demonstrated the potentialities of MST probes as sensing devices.

4.3.2 Mathematical Formulation

The schema of an MST probe able to retrieve information concerning the electric characteristic of the surrounding media is reported in Fig. 4.13. It consists of a transmitting/receiving antenna, a power splitter, an electronic switch connected with three loads Z_1, Z_2, and Z_3, a power unit able to convert the incoming radio frequency signal into a DC current, an elaboration unit, and a set of sensors. When an interrogating electromagnetic wave reaches the antenna probe, a portion of the signal is delivered to the power unit and used to activate the elaboration unit. The elaboration unit provides to collect the signals from the sensors and to encode them into a set of bits. Then it sequentially activates the switch in order to connect the antenna tag with the three loads. The changes of impedance provide a modulation on the backscattered wave which leads the information toward the reader. The electronic switch is the core of the system and it is the most critical component [221]. In this work a MEMS switch has been used to obtain optimal performances in terms of operative ranges and power consuming. The layout of the considered MEMS switch is reported in Fig. 4.14, the device dimensions are $8.3 \times 3.6mm^2$. It shows very good performances in terms of isolation and return loss in the frequency range $0 - 20GHz$.

Thanks to the presence of three different loads, optimized to obtain the maximum communication range following the guidelines [221], the probe

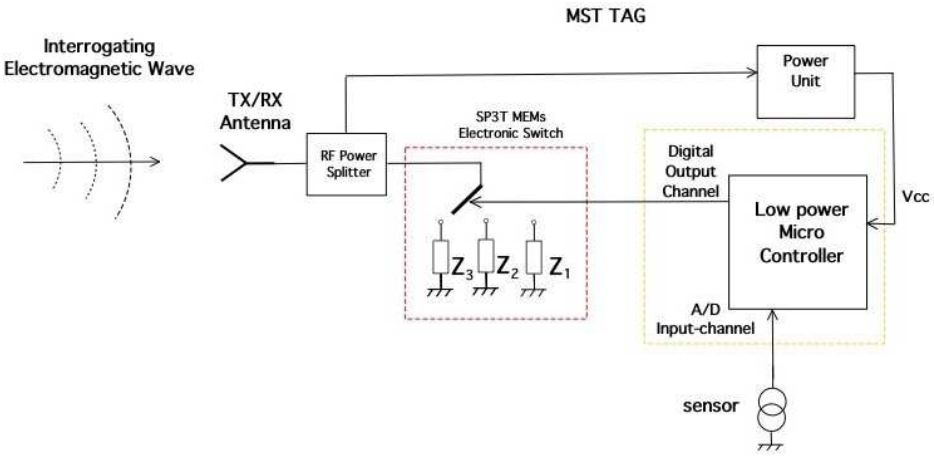

Figure 4.13: MST tag schema.

not only delivers the information provided by the sensors but also the electric characteristic of the media which surrounds the antenna tag. In particular the following system of equations summarizes the method to extract the electric characteristic of the surrounding media from the backscattered signal at the reader:

$$\begin{bmatrix} 1 & Z_1 & -\Gamma_1 \\ 1 & Z_2 & -\Gamma_2 \\ 1 & Z_3 & -\Gamma_3 \end{bmatrix} \cdot \begin{bmatrix} \varepsilon_m + Z_{ant} \cdot \Gamma_0 \\ \Gamma_{und} \\ Z_{ant} \end{bmatrix} = \begin{bmatrix} Z_1 \cdot \Gamma_1 \\ Z_2 \cdot \Gamma_2 \\ Z_3 \cdot \Gamma_3 \end{bmatrix} \tag{4.5}$$

where Z_i, $i = 1, 2, 3$ and Z_{ant} are the three loads and the antenna tag impedance respectively, and they are known quantities. Γ_i, $i = 1, 2, 3$ estimate the amplitude of the backscattered wave with respect to the impinging wave, they are quantities which can be easily measured at the reader output. Γ_{und} is given by the following relation [235]:

$$\Gamma_{und} = S_{11} + \frac{S_{scatt} + S_{struct}}{P_{inc}} \tag{4.6}$$

where S_{struct} is the antenna structural term, a quantity which can be neglected, P_{inc} is the power of the generator, S_{11} is the return loss at the

reader port, and S_{scatt} is the contribute due to the reflections of the environment. The goal is to invert the system of equations (4.5) and retrieve ε_m the impedance of the surrounding media.

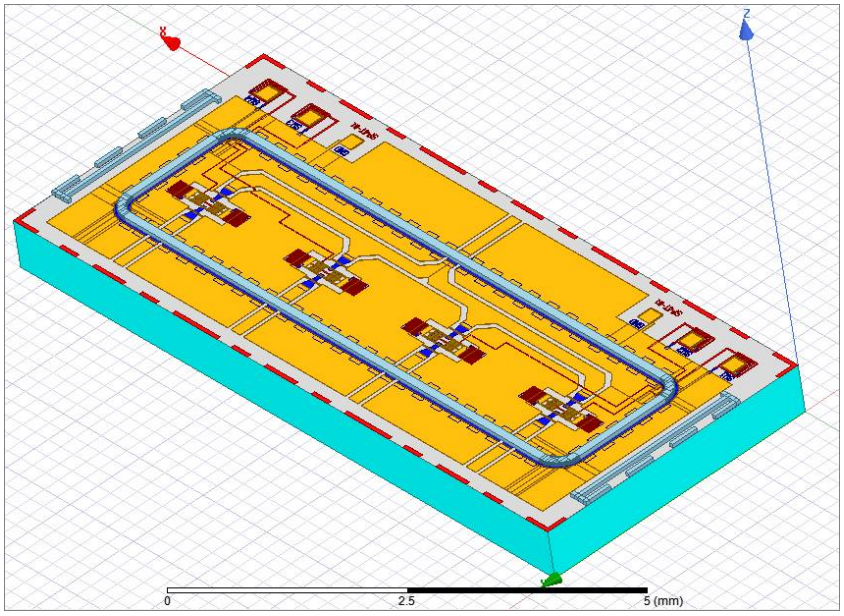

Figure 4.14: Example of SP4T RF-MEMs switch.

4.3.3 Experimental assessment

In order to assess the capabilities of the MST tag, a prototype equipped with the RF-MEMS switch reported in Fig. 4.14 has been fabricated and experimentally assessed. In particular the MST tag has been designed to operate in the whole X band 8-13 GHz. When an impinging electromagnetic wave provided by the reader reaches the antenna tag, the microcontroller is immediately activated. Successively, the SP3T MEMS switch is also activated, with a low-frequency (100 kHz) square wave signal. In particular the microcontroller connects the antenna tag with three different combinations of loads every 100 nS. The changes of impedances provide the modulation to the backscattered electromagnetic wave and transmit

back the information toward the reader with the goal to retrieve ε_m. The response of the MST tag for an impinging wave with a $f = 10GHz$ is shown in Fig. 4.15. The distance between the reader and the MST tag is r = 0.5 m. As it can be noticed from the data of Fig. 4.15, the tag response (changing every 100 ns) is quite clear and stable for all the three loads combinations.

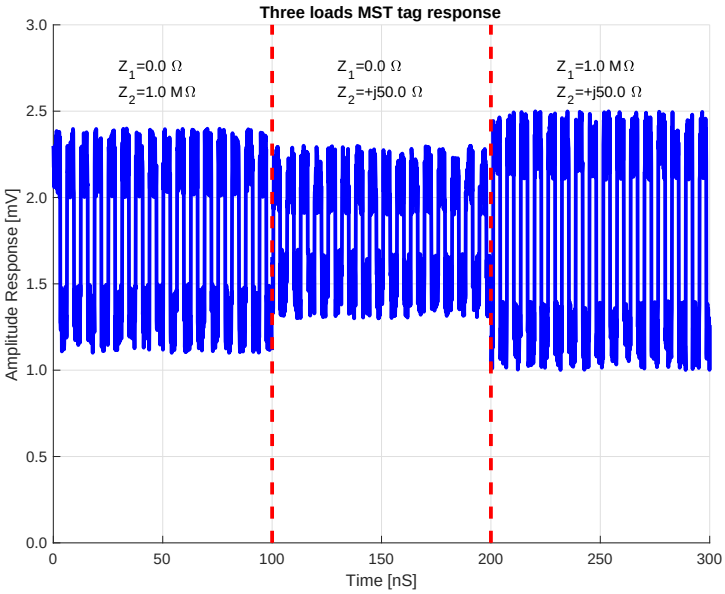

Figure 4.15: Response of a three loads MST MEMs based tag. Distance between reader and tag $r = 1.5m$

4.4 Low-Power Wildfire Detection

4.4.1 Introduction

The earth climate has been changed quickly over since 1950. We have seen many changes as we evolved technologically. In that process, we have contributed much harm to our climate, while protecting the human and their needs. Most of these harm to climate change contributes to variation in the Earth's atmosphere that controls the total amount of solar energy our planet receives from the Sun. In [261], Scientists have observed that since 1950 the carbon dioxide level has been increased drastically because of the emission of the coal and petrochemical products. These cause the rapid changes in Earth's atmosphere and the results we are noticing as Global temperature rise, Extreme weather events, Oceans warming, Shrinking ice glacier, Sea-level rise and many more to see. In particular, the rise in global temperature can cause extreme weather change like extreme summer/winter/rain. These extreme events can damage the forest area, especially in summer. Very recently we have seen a catastrophic disaster of Australia's wildfire due to the extreme heat of summer. In [262] report it was reported that in Australia's raging wildfire more than 12.8 million acres have been burned, nearly 1 billion of animals have been killed and above all, it has pumped out more emissions than 100 nation combined. Many ideas have been proposed over the year to prevent wildfire in the forest and build the smart forest. There were different types of technology that has been proposed to detect the early stage wildfire such as IoT based sensor networks [263],[264], Wide Area Network [265], infrared sensor [266], Open DeviceNet control system [267], remote sensing satellite-based early warning system [268], [269], [270], [271], [272], Unmanned Airborne Vehicle (UAV) [273],[274], Video camera-based [275],[276], [277], and thermal imaging [266, 277]. While some researcher have worked to make

post-processing faster and quicker by using data mining(artificial neural network)[278], image data mining [279], improving routing protocol [280], and wildfire simulation-based synthetic image optimization [281]. Most of the IoT based sensor presented was using a Zigbee and raspberry pi based system because the system works on very low power, and it is very efficient to connect many sensors. But the system provides a very short range. On the other side, remote sensing satellite imagery can cover a wide area of forest and provide good results, but the fire is not visible until it reaches some hight so it can be visible in the satellite image. By the time the fire reaches a certain amount of hight, it is challenging to control and stopped the fire in the forest. In this kind of challenging scenario, Unmanned Airborne Vehicle (UAV), a video camera and thermal imaging-based device can come very useful although we can not cover the whole forest with these devices since they are costly, especially UAV.

When we consider the communication system in the forest, the propagation of the radio wave is not similar to the regular plane surface. Many factors have to take into consideration. It has been recognized long ago that communicating through radio wave hampered by the transmission losses because of the presence of vegetation. Experimental investigation in a forest for propagation condition revealed that transmission losses had been characterized on the following reasons given by [282]:

1. Hight of an antenna; for constant hight of antenna received field caries inversely to the distance squared.

2. Vegetation Factor; the presence of vegetation contribute a constant loss which is independent of the distance.

3. Height gain effect of the receiving/transmitting antenna; Transmission loss can be reduced by increasing hight of receiving or transmitter antenna. In dB, the variation is roughly linear or logarithmic with

antenna height.

4. Received field may depolarize relative to the orientation of the transmitter antenna.

Experimental data confirmed that these characteristics are for the frequency range 1-100 MHz over 30 miles distance and the depolarization effect has been observed at 50-100MHz over 4 miles distance. These effects can be understood in terms of scattering by the vegetation. However, this is the situation for normal radio wave propagation in the forest. When fire outrage in the forest, the scenario becomes bit different. We need to consider more parameters like ionization and attenuation due to plasma. In [283] it has presented a radio experiment with fire and the calculation of attenuation due to fire for the different frequency range. The results in [283] show a significant effect on radio propagation due to wildfire. Moreover, [283] suggests that VHF and UHF bands did not interact with ionized electrons presented in the fire, which are causing attenuation.

In this work, we have presented a unique and state of the art technology to detect wildfire at a very early stage. The state of the art prototype consists of a Transmitter/Reciever antenna and RF- micro-electro-mechanical systems (MEMS) switch. This state of the art prototype does not require any external power source, and it is an entirely passive device. The state of the art prototype is very cheap in comparison to other solution available for wildfire detection. The state of the art device works on broadband behaviour, and it has been designed and numerically assessed. The prototype was equipped with an SP3T MEMS switch and combined with MST probe to retrieve the signal characteristics due to variation in the surrounding media in case of fire. The obtained results are promising, and they demonstrated the potentialities as a sensing device.

4.4.2 Design and configuration

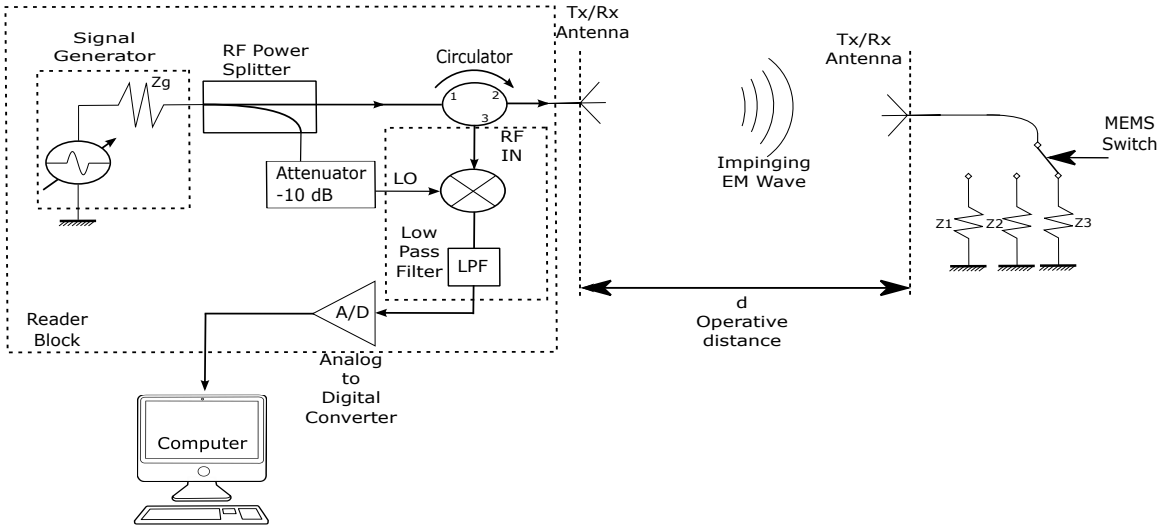

Figure 4.16: Schema of the device.

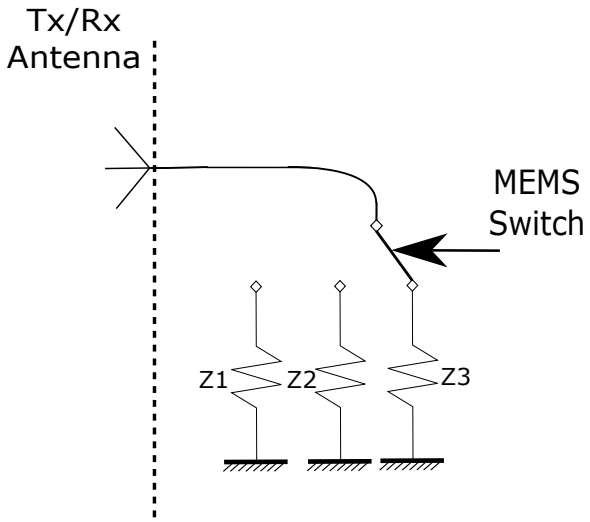

Figure 4.17: Schema of prototype sensing tag.

In this section, the design of the prototype has been explained in details. The schema of state of the art device able to detect the change of impedance of surrounding has been shown in Fig. 4.16 and Fig. 4.17. The device has been divided in two-part. 1) Central elaboration Unit and 2)

Sensing tag. Central elaboration Unit sends the signal to sensing tag, and It comprises a signal generator, RF power splitter, circulator,10 dB attenuator. Here, in attenuator power comes from one of the outputs of RF power splitter and another output was given to circulator. Following to circulator a transmitting/receiving antenna has connected to transmit the impinging wave towards sensing tag. A sensing tag has very simple structure consist a transmitting/receiving dipole antenna and an electronic switch connected with three loads Z_1, Z_2, and Z_3. Here, an electronic switch uses the power of the impinging signal directly into a DC current. When an electromagnetic signal wave reaches the Tx antenna probe, a part of the electromagnetic signal activates the switch senses the change of surrounding media impedance with the three loads. The changes in impedance provide a modulation on the backscattered EM wave, which carries the sensing information toward the central elaboration unit. The electronic MEMS switch is the heart of the system and most critical component of state of the art sensing tag [221]. In this work, a MEMS switch has obtained optimal performances in operative ranges and power consumption. The design layout of the considered MEMS switch has been presented in Fig. 4.14, the dimensions of MEMS switch are $8.3 \times 3.6mm^2$. It displays very good performances in terms of isolation and returns loss for the frequency range of $0 - 20GHz$. Three different loads are optimized to obtain the best communication range by the guidelines following in [221]. The sensing tag probe delivers the information provided the electric characteristic of the media surrounded by the antenna tag. The following equations summarize the method to extract the electric characteristic of the surrounding media from the backscattered EM signal at the central elaboration unit, also known as a reader.

$$\begin{bmatrix} 1 & Z_1 & -\Gamma_1 \\ 1 & Z_2 & -\Gamma_2 \\ 1 & Z_3 & -\Gamma_3 \end{bmatrix} \cdot \begin{bmatrix} \varepsilon_m + Z_{ant} \cdot \Gamma_0 \\ \Gamma_{und} \\ Z_{ant} \end{bmatrix} = \begin{bmatrix} Z_1 \cdot \Gamma_1 \\ Z_2 \cdot \Gamma_2 \\ Z_3 \cdot \Gamma_3 \end{bmatrix} \tag{4.7}$$

where $Z_i,\ i = 1, 2, 3$ are the three loads and Z_{ant} is the antenna tag impedance. $\Gamma_i,\ i = 1, 2, 3$ measures the amplitude of the backscattered EM wave for the impinging wave; these quantities can be measured at the elaboration unit output. The following relation gives the value of Γ_{und} :

$$\Gamma_{und} = S_{11} + \frac{S_{scatt} + S_{struct}}{P_{inc}} \tag{4.8}$$

where, S_{struct} is the antenna structural term, which can be neglected. P_{inc} represent the power of the generator, S_{11} denote the return loss at the reader port, and S_{scatt} is the scattering due to the reflections of the environment. By inverting the system of equations(4.7) we can retrieve ε_m the impedance of the surrounding media.

4.4.3 Mathematical Formulation

Previous studies of propagation in forest environment have considered electromagnetic properties due to vegetation in a plain terrain and experimental data has been lead us to the physical understanding of the wave propagation mechanism. First time presence of vegetation has been taken account made by Pounds and LaGrone, who recommended a forest can be viewed as a dissipative dielectric slab. The concept of the slab came into practice by Lippman. The slab concept was adopted to consider the forest, and it's propagation as an equivalent circuit which was considered by Taylor. Taylor had assumed that the field in the forest was due to sky-wave reflection from the ionosphere. Later, Sachs has dismissed the sky-wave and considered a lateral wave instead. Sachs work has been recognizing the importance of "tree-top" mode propagation and pointed out

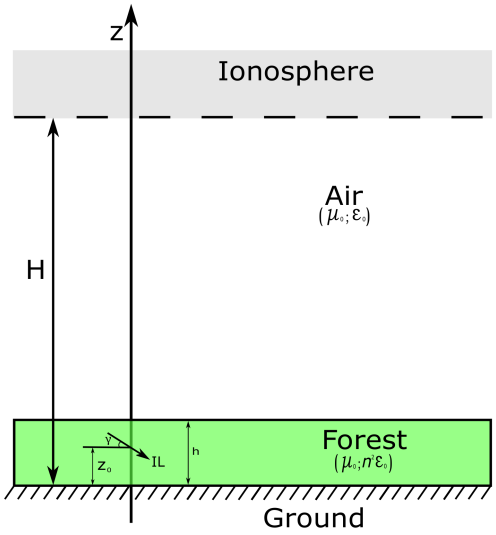

Figure 4.18: Propagation model geometry of Forest.

that many of the experimental results matched with the lateral-wave mechanism. In [282] has presented an absolute study of wave propagation for the frequency range of 1-100 MHz by considering the transmitting and receiving antenna are in the vegetation. This study has examined a forest can be represented in terms of a conducting dielectric layer bounded by the ground below and air region. The model involves three interfaces: 1) ground-forest, 2) forest-air, and 3) air-ionosphere. However, in the absence of vegetation, the interface between ground and forest plays a minor role when the forest is sufficiently dense. Most important interfaces are forest-air and air-ionosphere, which has strong field contributions in the form of a lateral and a sky-wave, respectively. The sky-wave consists of the single-hop reflection from the ionosphere, which occurs only for the lower frequencies. On the other hand, the lateral wave is presented at all frequencies and travels via air region by skimming over the tree-tops. The study in [282] shows that the lateral waves are stronger than the sky-wave, except for lower frequencies and large distance. In this section, the lateral

waves mathematical expression has been given in detail, which enables us to determine path loss, attenuation and other essential quantities concerns to propagation properties. Considering the basic slap geometry as given in Fig. 4.18, where the conductive slab represents a forest with an average tree height h. The plane geometry is satisfactory even for the larger distances $\rho = (x^2 + y^2)$, since both the sky-wave and the lateral wave are affected slightly by small amounts of curvature. The transmitter has been placed at z_o height above the ground and pretended to have a small-current element of moment Il inclined at an angle of y to the x-axis. The complex refractive index (n) of the forest given by:

$$n^2 = \epsilon_1 - j * \frac{\sigma_1}{\omega \varepsilon_0} = \varepsilon - j60\sigma_1\lambda_0 \tag{4.9}$$

where ϵ_1 signifies the average relative permittivity and μ_1 shows the average conductivity of the forest medium; ϵ_0 and λ_0 are the absolute permittivity and the wavelength in the air (vacuum) of a wave with frequency f. For all the possible circumstances a coverage ranges considered as in [282].

$$1.01 \leq \epsilon_1 \leq 1.5 \;\; and \;\; 10^{-3} \geq \sigma_1 \geq 10^{-5} mho/m \tag{4.10}$$

The relation between ionosphere height H and the height of the effective reflection plane at any given frequency f is

$$h << \rho < H \tag{4.11}$$

Equation(4.9) has been used frequently throughout the following discussion. As discussed earlier in the forest, many factors have to consider for radio propagation model. Here, in a forest model of the primarily the form of a lateral wave has been considered. In particular, the intensity of this field can be characterized [282] by the following equation, which yields a

magnitude.

$$|E_L| = \frac{60Il}{|n^2 - 1|} \frac{e^{-\alpha_L s}}{\rho^2} \tag{4.12}$$

where,

$$\alpha_L = \frac{2\pi}{\lambda_0} Im(\sqrt{n^2 - 1}) \tag{4.13}$$

and α_L indicates the exponential attenuation factor by the presence of vegetation. The effect of vegetation factor affects E_L and is given as follow:

$$F_v = \left|n^2 - 1\right| e^{\alpha_L s} \tag{4.14}$$

The result for E_L has been expressed in terms of a fixed- current moment Il and by considering power quantities derives the path loss L_b. The available power from a small-dipole antenna located in the forest is given by [282]:

$$P_r = \frac{|E_L|^2 \lambda_0^2}{320} \cdot \frac{1}{Re(n)} \tag{4.15}$$

where the real part of n accounts for the medium surrounding the antenna. By substituting equation(4.14) into equation(4.12) and(4.15) we get,

$$P_r = \frac{45}{4\pi} \left(\frac{Il\lambda_0}{\rho^2}\right)^2 \cdot \frac{1}{|F_v|^2 Re(n)} \tag{4.16}$$

The transmitted power is given by:

$$P_t = 80\pi^2 \left(\frac{Il}{\lambda_0}\right)^2 \cdot Re(n) \tag{4.17}$$

Equation(4.16) and (4.17) yield a basic path loss L_b,

$$L_b = \left(\frac{3}{2}\right)^2 * \frac{P_t}{P_r} \left[4\pi^2 \mid F_v \mid Re(n) \left(\frac{\rho}{\lambda_0}\right)^2\right]^2 \tag{4.18}$$

Where the factor $\left(\frac{3}{2}\right)^2$ considers for the gain of the two antennas. If both the receiving and transmitting antenna are close to the tree-tops, then equation(4.18) reduces to

$$L_{b0} = 1570 \left[\left|n^2 - 1\right| Re(n)\right]^2 \left(\frac{\rho}{\lambda_0}\right)^4 \tag{4.19}$$

Where L_{b0} denotes the value of L_a at $s = 0$. The basic path loss L_b increases strongly with the frequency f if both antennas are close to the tree-tops. The situation may change if any of the antennas (or both) are sufficient above the vegetation canopy. In such a case, propagation occurs by the refraction or the line of sight rather than a lateral wave.

Moreover, the situation becomes complex in the presence of the wildfire. In particular wildfire scenario, the fire can easily become very intense due to vegetation, and it can reach maximum flame temperatures up to 1900^oC. The excited particulates (A(g)) may shed their outer electrons when it strikes with other energized flame particle to become ion follow the given reaction equation:

$$A(g) \Leftrightarrow A^+(g) + e^- \tag{4.20}$$

Similarly, for the chemical ionization process, CH atom reacts with oxygen atoms in the flame and produce CHO^+ hydrocarbon and electron as given in the following reaction equation:

$$CH^* + O \Leftrightarrow CHO^+ + e^- \tag{4.21}$$

Due to the high vegetation of forest and high-temperature of fire environment thermally induces the flame particles to an unstable state. These thermal and the chemical-ionization process creates a weakly ionized environment in the wildfire zone. The complex relative dielectric permittivity $\widetilde{\epsilon_r}$ for a fire is given as follow by [284]:

$$\widetilde{\epsilon_r} = 1 - \frac{N \cdot e^2}{m\epsilon_0 \left(\omega^2 + \varphi_{eff}^2\right)} - i\frac{N \cdot e^2}{m\omega\epsilon_0 \left(\omega^2 + \varphi_{eff}^2\right)} \tag{4.22}$$

where, N is the density of electron in the fire medium, ω and ϵ_0 are angular propagation frequency and a free space dielectric permittivity, respectively. In equation(4.22) φ_{eff} implies momentum transfer electronneutral particle collision frequency, m and e refer to electron mass and charge, respectively. The presence of free electrons in fire reduced the value of dielectric constant(real part of $\widetilde{\epsilon_r}$ (equation(4.22)). For instance, if we are to considering a lightly ionized gas with an electron density of $1 * 10^{17}$ $m3$ and collision frequency of $1 * 10^{11}$ $s1$, its dielectric constant value is 0.9683 for traversing electromagnetic wave at a $900MHz$ frequency. The complex dielectric permittivity ($\widetilde{\epsilon_r}$) is related to the propagation constant (γ) for the weakly ionized fire medium by the following relation:

$$\gamma = i\frac{\omega}{c}\left\{\widetilde{\epsilon_r}\right\}^{1/2} = \alpha_f + i\beta_f \tag{4.23}$$

where α_f *and* β_f are the attenuation and phase coefficients for the fire, respectively. The attenuation coefficient for the fire can be given from the equation given by [284] as:

$$\alpha_f = \frac{\pi \left(2\ \widetilde{\epsilon}_{real}\right)^{1/2}}{\lambda_0}\left\{\sqrt{1 + (tan\delta)^2} - 1\right\}^{1/2} \tag{4.24}$$

where $tan(\delta) = \widetilde{\epsilon}_{imag}/\widetilde{\epsilon}_{real}$ is the loss tangent of the flame medium. $\widetilde{\epsilon}_{imag}$ and $\widetilde{\epsilon}_{real}$ are imaginary and real components of complex dielectric permittivity.

4.4.4 Numerical assessment

In this section, the numerical assessment of the state of the art prototype is presented. As explained in 4.4.2 the prototype consists of two sections

1) Central elaboration Unit and 2) MST sensing Tag. Our Proposed system equipped with an SP3T RF MEMS switch and a printed log-periodic antenna as shown in 4.20. The capability of the prototype antenna and MST tag has been assessed separately.

The MST tag reported in Sec.4.4.2 Fig. 4.16 and 4.17 has been fabricated and experimentally assessed. In particular, the operating frequency of the MST tag has been designed at $600MHz$-$6GHz$. When an impinging electromagnetic wave provided by the reader reaches the antenna tag, the micro-controller is immediately activated. Successively, the SP3T MEMS switch is also activated, with a low-frequency ($100kHz$) square wave signal. In particular, the microcontroller connects the antenna tag with three different combinations of loads every 100 nS. The changes of impedances provide the modulation to the backscattered electromagnetic wave and transmit back the information toward the reader with the goal to retrieve ε_m. The MST tag's response for an impinging wave with a $f = 600MHz$-$6GHz$ is shown in Fig. 4.15. The distance between the reader and the MST tag is $r = 0.5m$. As it can be noticed from the data of Fig. 4.15, the tag response (changing every $100ns$) is quite clear and stable for all the three loads combinations.

There are two printed log-periodic antenna has been designed, shown in Fig. 4.20 and 4.21. Both antennae have been modeled and simulated by commercial software, namely ADS2020 by Keysight Technologies. Both log periodic antenna is designed to operate at the frequency $f = 600MHz$-$6GHz$. The ARLON25N dielectric substrate has been considered for the design of the antenna with the parameter of, $\epsilon_r = 3.38$, thickness t= 0.8 mm, $tan(\delta) = 10^{-3}$. Antenna presents in Fig. 4.20 has 12 dipole element and the dimension of antenna is $92mm * 87mm$. Whereas antenna shown in Fig. 4.21 contains 20 dipole element with the dimension of $162mm * 179mm$. However, the dielectric constant of ARLON25N has

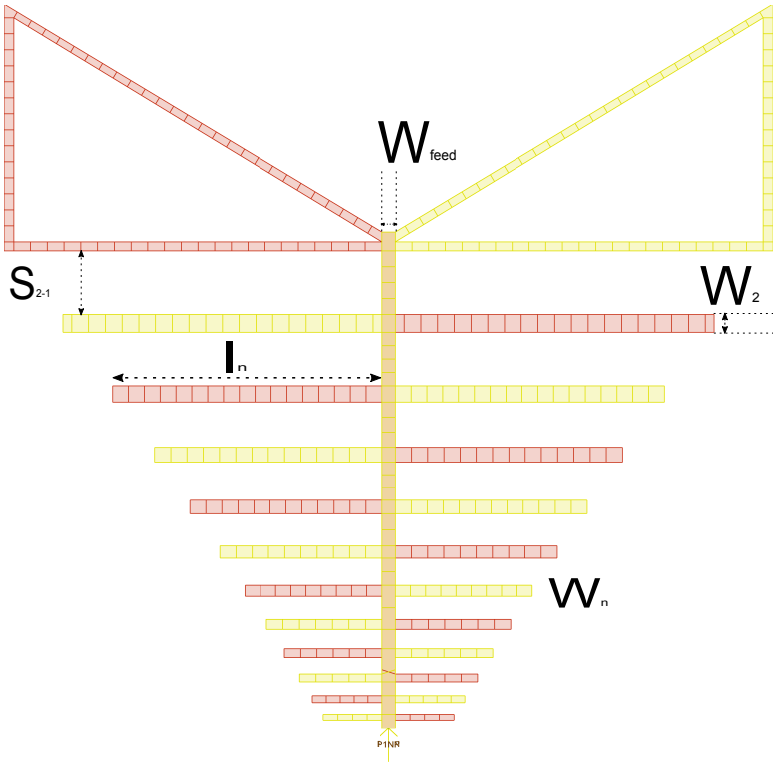

Figure 4.19: Basic Geometry of proposed 12 element $92mm * 87mm$ Log Periodic antenna

been taken into account while designing the LDAP antenna. The dimension of proposed antenna structure is reported in the following Table 4.2 and Table4.3. The detailed geometry of designed antennas is calculated as in [285]. The length of the dipole element $\bar{l}_n$, width of the dipole element $\overline{w}_n$, spacing between the dipole element $\overline{S}_{n-1} - \overline{S}_n$, and width of the feed line is denoted as $\overline{w}_{feed} = 1.6mm$. The basic design structure of 12 element antenna has been shown in Fig. 4.19. As reported in Fig. 4.24 the return loss $|S_{11}|$ is below $-10dB$ for most of the frequency except the spike at $1.3GHz$. The designed antenna is operating after $900MHz$. Below $900MHz$ does not operate at all, and the reported gain in Fig. 4.23 of the antenna support that the antenna performance below $900MHz$ is very low. Even after the frequency of $1GHz$ the antenna gain fluctuates around $5[dBi]$. Whereas the 20 elements $162mm * 179mm$ antenna's results show

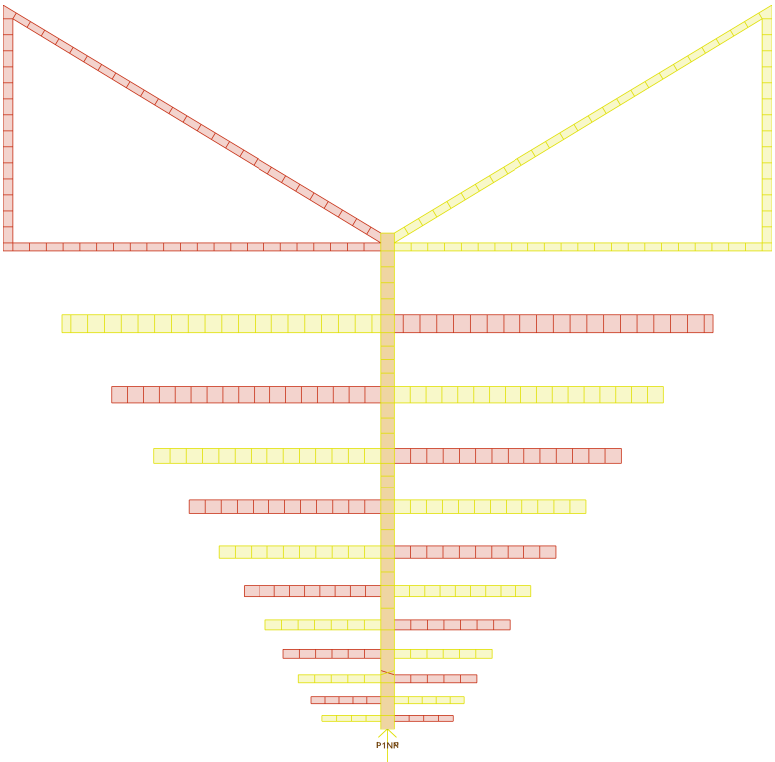

Figure 4.20: Layout of proposed 12 element $92mm * 87mm$ Log Periodic antenna in ADS.

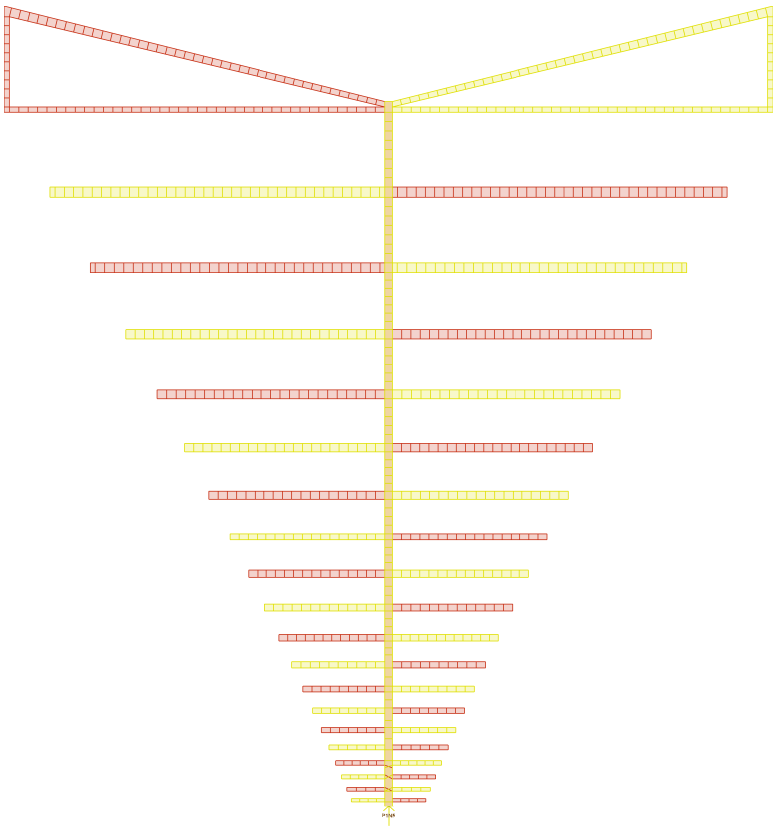

Figure 4.21: Layout of proposed 20 element $162mm * 179mm$ Log Periodic antenna in ADS.

Table 4.2: Geometry of proposed 12 element $92mm * 87mm$ LDPA antenna design.

Dipole Element $\bar{l}_n$	Length of Dipole in $\bar{l}_n$ [mm]	Width of Dipoles $\overline{w}_n$ [mm]	Spacing $\overline{S}_{n-1} - \overline{S}_n$ [mm]
1	45.8	1.1658	-
2	38.7968	2.1305	7.5497
3	32.8836	1.9433	6.3748
4	27.8905	1.7693	5.3827
5	23.6748	1.6074	4.5451
6	20.1147	1.4566	3.8377
7	17.1088	1.3159	3.2405
8	14.5708	1.1858	2.7362
9	12.4277	1.0606	2.3104
10	10.6181	0.9432	1.9509
11	9.0902	0.829	1.6472
12	7.8	0.7	1.3909

that the antenna performs $800MHz$. The return loss $|S_{11}|$ and gain of the 20 element antenna is presented in Fig. 4.24 and Fig. 4.25, respectively. In Fig. 4.25 it can be seen that the gain of the antenna is around $6[dBi]$ for the frequency range of $800MHz$ to $6GHz$. This constant gain and $|S11|$ of 20 element antenna confirm efficient working with the proposed MST tag. Comparatively, 20 element antenna performs better than 12 elements. However, the experimental assessment will provide a better insight into working in a practical scenario. Because of the current Covid-19 situation, the experimental design and assessment have been on hold. However, the numerically assessed result confirms our state of the art system.

Table 4.3: Geometry of proposed 20 element $162mm * 179mm$ LDPA antenna design.

Dipole Element $\bar{l}_n$	Length of Dipole in $\bar{l}_n$ [mm]	Width of Dipoles $\overline{w}_n$ [mm]	Spacing $\overline{S}_{n-1} - \overline{S}_n$ [mm]
1	80.8	1.1249	-
2	71.173	2.1477	15.6311
3	62.7045	2.049	13.75
4	55.2551	1.9534	12.0954
5	48.7021	1.8609	10.6399
6	42.9377	1.7714	9.3595
7	37.867	1.6847	8.2332
8	33.4064	1.6006	7.2424
9	29.4827	1.5191	6.3709
10	26.0311	1.44	5.6043
11	22.9948	1.3632	4.9298
12	20.324	1.2885	4.3366
13	17.9745	1.2157	3.8147
14	15.9078	1.1446	3.3557
15	14.0898	1.0748	2.9519
16	12.4905	1.0061	2.5967
17	11.0837	0.9377	2.2841
18	9.8462	0.8685	2.0093
19	8.7576	0.7958	1.7675
20	7.8	0.7	1.5548

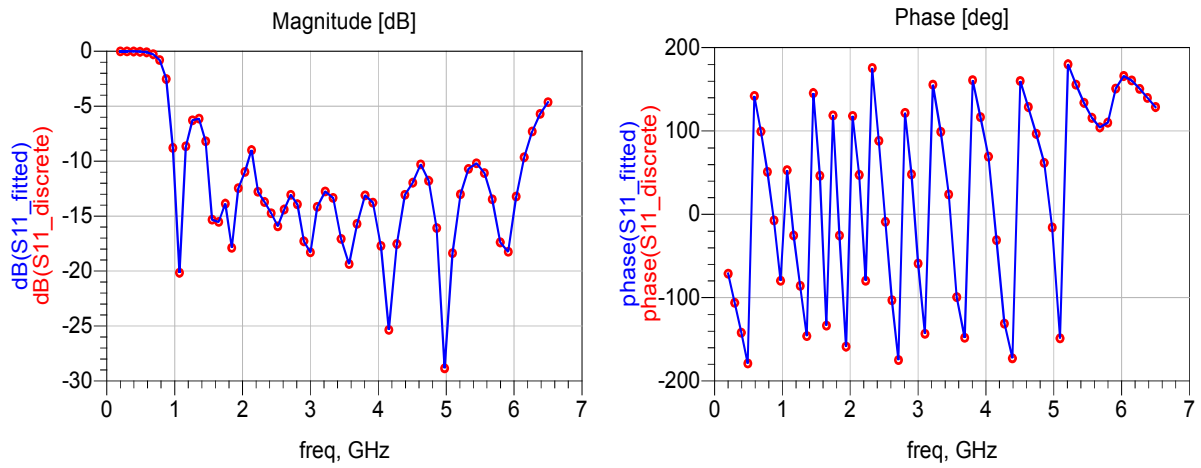

(a) (b)

Figure 4.22: $|S_{11}|$ of proposed 12 element $92mm * 87mm$ LDPA antenna (a) Magnitude $[dB]$ (b) Phase $[deg]$

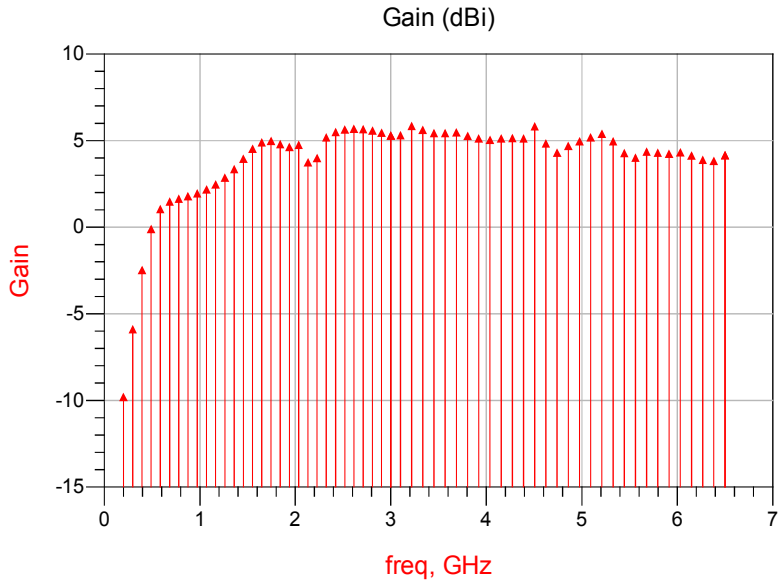

Figure 4.23: Gain $[dBi]$ of proposed 12 element $92mm * 87mm$ LDPA antenna

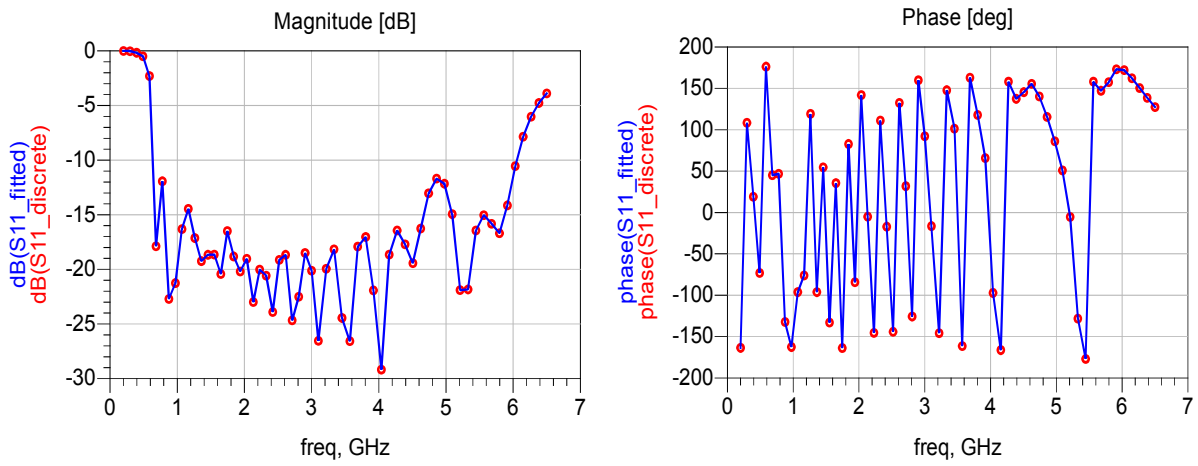

(a) (b)

Figure 4.24: $|S_{11}|$ of proposed 20 element $162mm * 179mm$ LDPA antenna (a) Magnitude $[dB]$ (b) Phase $[deg]$

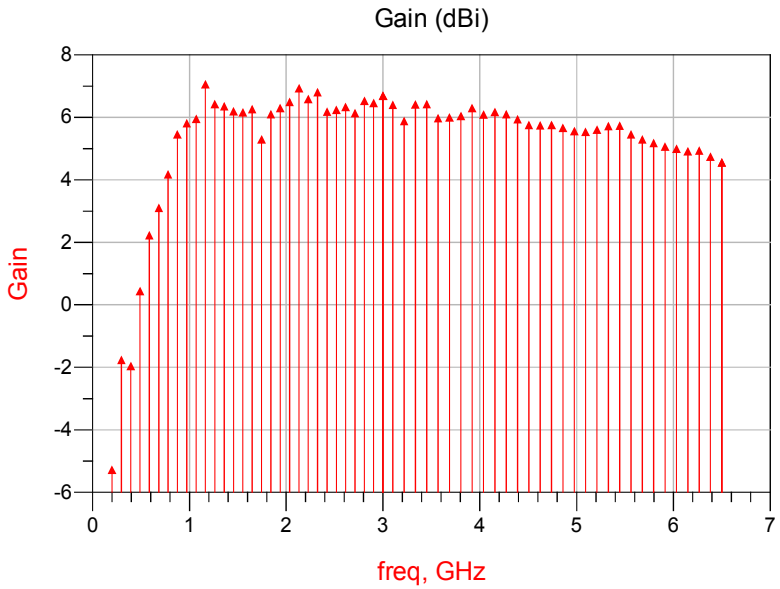

Figure 4.25: Gain $[dBi]$ of proposed 20 element $162mm * 179mm$ LDPA antenna

Chapter 5

Conclusion and Future work

In this thesis following task has been achieved and assessed experimentally in most cases. The findings are concluded as follow:

- In Chapter 2, the proposed antenna design for the industrial and biomedical sector has been assessed. The filter structure has been tuned through a minimization procedure by defining a suitable cost function that has been minimized with a customized evolutionary algorithm. The obtained filter prototype achieved good performance.

- The synthesis of a microstrip switched-beam antenna array with a compact and efficient feeding network was proposed, designed, and experimentally assessed. Each section of the feeding network has been tuned through a minimization procedure by defining a suitable cost function, minimized with a customized evolutionary algorithm. The obtained antenna prototype is able to achieve good radiation and return loss characteristics.

- An innovative approach based on Interval Analysis and the arithmetic of intervals has been proposed to design Rotman lens feeding networks when manufacturing errors are present. The Rotman lens feeding network design problem has been first recast into the IA-based framework

by introducing the interval numbers aimed at describing the tolerances on the lens parameters and the arising lens illumination function. The proposed method is able to: manage the uncertainties and the tolerance errors due to the materials and fabrication process; define exact and analytical bounds of the lens parameters and the corresponding illumination function by using the rules of interval arithmetic. The obtained results have shown the potential of the proposed strategy. Further advances will consider the extension of the proposed method to the analysis of waveguide-based Rotman lenses.

- A microwave interferometer for the detection of chest movements has been developed and experimentally assessed in realistic scenarios. The proposed microwave systems are able to detect the small movements of human respiratory activity, and it represents a valid alternative to standard methods based on infrared cameras or piezoelectric belts. The obtained results are promising and demonstrate the prototype's potentialities and accuracy, mainly when the treatment must be provided to non-collaborative o sedated patients.

- A UWB antenna design based on a SIW resonator has been designed, fabricated, numerically, and experimentally assessed. The obtained antenna prototype provided good radiation and return loss characteristics and a bandwidth in the range from $3GHz$ to $11GHz$. The agreement between measured and simulated data is very good. The antenna size is very small, confirming that it is a good candidate for modern handheld UWB systems.

- An antenna array based on OAM and SIW cavity-backed UWB antennas has been proposed. Different OAM modes can be generated by properly act on the reconfigurable phase shifters. Thanks to OAM combined with UWB elements, it was possible to effectively extend

the channel capability and exploit the whole considered electromagnetic spectra. The proposed antenna array is compact light, and the obtained results are promising.

- A Stepped Frequency Continuous Wave (SFCW) radar operating in the L band, suitable for fast inspection of foods and goods stored in metallic containers, has been proposed and numerically assessed in realistic scenarios. In particular, the proposed SFCW radar can estimate the dielectric characteristics of materials contained in a container and easily detect metallic or dielectric false bottoms commonly used for smuggling. A numerical assessment campaign, carried on considering different materials and simulating realistic scenarios, demonstrated the effectiveness and potentialities of the proposed system as a useful tool for the contrast of smuggling.

- a method for improving the detection capabilities or a chipless RFID system is proposed. The method is based on a quantile regression algorithm able to retrieve the tag information under different noise conditions correctly. The method was numerically and experimentally assessed using a tag prototype (a tag demonstrator) composed of five spiral resonators. The obtained results are quite promising. However, in the experimental assessment, we observed that the resonator quality factor has to be the same regarding the resonator's design. The difference in quality factor affects the insertion loss, which produces the phase magnitude and frequency shift. This difference also produces false peak detection in noisy environments.

- An X band MST wireless sensor for an environmental system has been designed, fabricated, and tested. The MST system prototype is designed by a monostatic reader section, based on a high gain amplifier, a transmitting antenna, a homodyne detector, and an elab-

oration unit based on a low-cost microcontroller. The MST probe uses a rectangular patch antenna, loaded on two different loads by means of a MOSFET based electronic switch. The system efficiency has been optimized as well as the maximize the communication range r. In particular, a distance of about $r = 15m$ has been reached. The experimental assessment results demonstrated the effectiveness and potentialities of the proposed MST wireless sensor prototype, and it confirms that the MST systems could be an appealing alternative to the standard wireless sensor. Future works will be devoted to the further miniaturization of the MST probe and improving the communication range.

- An MST system for air quality monitoring has been designed, fabricated, and tested. The MST system prototype is a mono-static reader based on a commercial homodyne receiver, a high gain antenna. The MST tag uses a rectangular patch antenna, loaded on two different loads by means of a pin diode SP2T switch. The system efficiency has been optimized as well as maximize the communication ranged. In particular, a distance of more than d = 15 m has been obtained. The experimental assessment results demonstrated the effectiveness and potentialities of the proposed MST wireless sensor prototype, and it confirms that the MST systems could be an appealing alternative to the standard wireless sensor.

- This work is an extension of previous work of the X band MST sensor. Here, we have proposed an alternate switch to increase the efficiency and range of the MST device. The main drawback of MST sensors is the RF switch because of its cost and narrowband behavior. The adoption of suitable RF-MEMS microwave switches is a good opportunity to overcome this problem. This work proposes the design and applica-

tion of an SP3T MEMs switchable to provide good performances up to 20 GHz with reduced dimensions and complexity. An MST sensor prototype able to retrieve the surrounding media's dielectric permittivity has been designed, fabricated, and experimentally assessed. The obtained results were quite promising.

- In this work, we are proposing an innovative and cheaper technique for early-stage wildfire detection. In normal conditions, when the impinging EM signal was sent to receiving antenna from an MST reader, then the signal was reflected the reader by the sensing device. We have used an MST reader device and a designed RF MEMs switch attached with a single dipole antenna. This MEMs switch has a unique ability to detect the sudden changes in the impedance of the surrounding media of an antenna. We have utilized this unique feature into the art device state to detect an early-stage wildfire in the forest. We have assessed the device behavior in the fire condition. Our designed prototype able to retrieve the value of the dielectric permittivity of the surrounding media. The propagation characteristics of electromagnetic waves in a forest environment. At $2.5GHz$ frequency prototype has been examined for the case where both transmitting/receiving points are situated within the vegetation. The variation has been observed over the field with the distance, the height-gain effect, the vegetation factor, the basic path loss, and the ionization effects are separately examined mathematically. The designed and numerically assessed prototype results are promising.

All the designed antenna and sensor system developed in the thesis are compact in size, efficient, low-cost, confirming that it could be a good candidate for modern wireless devices.

Our future work will focus on improving our post-processing method by

using an optimized real-time algorithm to detect peaks in noisy environments and scenarios with different quality factors.

Secondly, experimenting with a real-time scenario of the proposed early-stage wildfire detection. Moreover, we are considering publishing the proposed system in a high-impact factor journal in the future.

Published Journal Paper

1. M. Donelli, T. Moriyama, and M. Manekiya, "A Compact Switched Beam Planar Antenna Array for Wireless Sensors Operating at Wi-Fi Band", *PIER C*, vol. 83, pp. 137145, 2018.

2. M. Donelli and M. Manekiya, "Development of Environmental Long Range RFID Sensors Based on the Modulated Scattering Technique", *Electronics*, vol. 7, no. 7, p. 106, Jul. 2018.

3. M. Manekiya, M. Donelli, A. Kumar, and S. Menon, "A Novel Detection Technique for a Chipless RFID System Using Quantile Regression", *Electronics*, vol. 7, no. 12, p. 409, Dec. 2018.

4. M. Donelli, M. Manekiya, and S. K. Menon, "Compact microstrip reconfigurable filter based on spiral resonators", *Microw Opt Technol Lett*, vol. 61, no. 2, pp. 417424, Feb. 2019.

5. M. Donelli, S. K. Menon, G. Marchi, V. Mulloni, and M. Manekiya, "Design of an Ultra Wide Band Antenna based on a SIW Resonator", *PIER C*, vol. 103, pp. 187197, 2020.

6. M. Donelli and M. H. Manekiya, "Design and Analysis of Antenna Feeding Networks Based on the Rotman Lens Using Interval Analysis (IA)", *International Journal of Antennas and Propagation*, vol. 2020, pp. 118, Mar. 2020.

7. M. Donelli, M. Manekiya, D. Cunial, L. Cristoforetti, and F. Fracchiolla, "A microwave interferometer for human breath monitoring in proton therapy applications", *Microw Opt Technol Lett*, vol. 62, no. 2, pp. 589591, Feb. 2020.

8. M. Manekiya, A. Kumar, A. Yadav, and M. Donelli, "A Survey of Resource Allocation Techniques for Cellular Networks Operation in the Unlicensed Band", *Electronics*, vol. 9, no. 9, p. 1464, Sep. 2020.

9. M. Donelli, M. Manekiya, and J. Iannacci, "Development of a MST sensor probe, based on a SP3T switch, for biomedical applications", *Microw Opt Technol Lett*, vol. 63, no. 1, pp. 8290, Jan. 2021.

10. M. Manekiya and M. Donelli, "Monitoring the Covid-19 Diffusion by Combining Wearable Biosensors and Smartphones", *Progress In Electromagnetics Research M*, vol. 100, pp. 1321, 2021.

Published Conference Paper

1. M. Manekiya, M. Donelli, and M. Donelli, "An Air Quality Monitoring System with Enhanced Coverage Capabilities by Using the Modulated Scattering Technique (MST)", in *2019 PhotonIcs & Electromagnetics Research Symposium - Spring (PIERS-Spring)*, Rome, Italy, Jun. 2019, pp. 22352240.

2. M. Donelli, M. Manekiya, V. Mulloni and G. Marchi, "Ultra-Wideband Antenna Array based on Orbital Angular Momentum", *2019 IEEE International Symposium on Antennas and Propagation and USNC-URSI Radio Science Meeting*, Atlanta, GA, USA, 2019, pp. 1241-1242.

3. M. Donelli, M. Manekiya and J. Iannacci, "Broadband MST sensor probes based on a SP3T MEMs switch", *2019 IEEE International Symposium on Antennas and Propagation and USNC-URSI Radio Science Meeting*, Atlanta, GA, USA, 2019, pp. 649-650.

4. G. Marchi, V. Mulloni, M. Manekiya, M. Donelli and L. Lorenzelli, "A Preliminary Microwave Frequency Characterization of a Nafion-Based Chipless Sensor for Humidity Monitoring", *2020 IEEE SENSORS*, Rotterdam, Netherlands, 2020, pp. 1-4.

5. M. Donelli, M. Manekiya, G. Marchi, I. Maccani and C. Pascucci, "High Resolution L-band Stepped Frequency Continous Wave Radar for Smuggling Contrast", *2020 2nd Global Power, Energy and Communication Conference (GPECOM)*, Izmir, Turkey, 2020, pp. 327-332.

Bibliography

[1] J. R. James, "Magical microwaves: the exploitation of the century," *IEE Proceedings H (Microwaves, Antennas and Propagation)*, vol. 136, no. 1, pp. 112, Feb. 1989, doi: 10.1049/ip-h-2.1989.0001.

[2] Arnaud Vena; Etienne Perret; Smail Tedjini, "Chipless RFID Based on RF Encoding Particle: Realization, Coding and Reading System." *ISTE Press - Elsevier*, 2016.

[3] S. Preradovic and N. C. Karmakar, Multiresonator-Based Chipless RFID. New York, NY: *Springer New York*, 2012.

[4] L. Yang, A. Rida, and M. M. Tentzeris, "Design and Development of Radio Frequency Identification (RFID) and RFID-Enabled Sensors on Flexible Low Cost Substrates," *Synthesis Lectures on RF/Microwaves*, vol. 1, no. 1, pp. 189, Jan. 2009.

[5] D. H. Archer, and M. J. Maybell, "Rotman lens development history at Raytheon electronic warfare systems 1967-1995," *IEEE International Symposium on Antennas and Propagation*, 3-8 Jul. 2005, pp. 31-34.

[6] D. Psychogiou, R. Garcia, and D. Peroluis, "A class of fully-reconfigurable planar multi-band bandstop filters," *IEEE MTT-S International Microwave Symposium, (IMS) 2016*, San Francisco USA, 22-27 May 2016.

[7] L. Kurra, M. P. Abegoankar, A. Basu, S. K. Koul, "Bandwidth reconfigurable bandstop filter using planar EBG structure," *IEEE MTT-S International Microwave and RF Conference, New Delhi*, India, 14-16 Dec. 2013.

[8] R. G. Garcia, M. A. Sanchez-Soriano, K. W. Tam, and Q. Xue, "Flexible FIlters," *IEEE Microwave Magazine*, pp. 43-54, Jul./Aug. 2014.

[9] D. Psychogiou,R. G. Garcia, D. Peroulis, "Fully adaptive multiband bandstop filtering sections and their application to multifunctional components," *IEEE Trans. Microwave Theory and Techniques*, vol. 64, no. 12, pp. 4405-4418 Dec. 2016.

[10] A. B. Alterkawi, F. Gentili, W. Bosh, "Fully reconfigurable filter based on a microstrip patch resonator with low-voltage driving," *International Conference on Broadband communications for next generation networks and multimedia applications (CoBCom)* 2016, Sep. 14-16, 2016, Graz Austria.

[11] Viani F., Lizzi L., Donelli M., Pregnolato D., Oliveri G. and Massa A., "Exploitation of parasitic smart antennas in wireless sensor networks," *Journal of Electromagnetic Waves and Applications*, pp. 993-1003.

[12] Bellofiore S., Balanis C., Foutz J. and Spanias A., "Smart antenna systems for mobile communication networks. Part 1: Overview and antenna design", *IEEE Antennas Propagat. Mag.*, 2002, pp. 145-154.

[13] D. Pozar, Microwave Engineering, John Wiley & Sons, New york, 1998.

[14] K Wincza and S Gruszczynski, "Miniaturized quasi-lunped coupled-line single section and multisection directional couplers," *IEEE Trans-*

action Microwave Theory Techniques, vol. 48, no. 11, pp. 2924-2931, Nov. 2010.

[15] Y. C. Chiang, and C. Y. Chen, "Design of a wideband lumped-element 3-dB quadrature coupler," *IEEE Transaction Microwave Theory Techniques*, vol. 9, pp. 476-479, 2001.

[16] Chun, Y. H. and Hong, J. S. "Compact wide-band branch-line hybrids", *IEEE Trans. Microwave Theory and Techniques*, 2013, 54, pp. 704-709.

[17] J. S. Hong, "Reconfigurable planar filter," *IEEE Microwave Magazine*, pp. 73-83, Oct. 2009.

[18] L. Shaik, B. Pramanick,Y. Siddiqui, "Design of a reconfigurable dual state planar filter using SSRs and MEMS on a coplanar waveguide," *Asia Pacific Microwave Conference (APMC)*, Nanijing, China, 6-9 Dec. 2015.

[19] S. F. Peik, J. Jiang, R. R. Mansour, "Selectivity reconfigurable filters with controlled channel bandwidth," *IEEE MTT-S International Microwave Workshop Series on Advanced Materials and Processes (IMWS-AMP 2017)*, 20-22 September 2017, Pavia, Italy

[20] C. Bohorquez, B. Potelon, C. Person, E. Rius, C. Quendo, G. Tanne, E. Fourn, "Reconfigurable planar SIW cavity resonator and filter," *IEEE MTT-S International Microwave Symposium Digest*, pp. 947-950, 11-16 June, San Francisco, CA, USA, 2006.

[21] M. A. Sanchez-Soriano, R. Gomez-Garcia, G. Torregrosa-Penalva, E. Bronchalo, "Reconfigurable-bandwidth bandpass filter within 10-50%" *IET Microwaves, Antennas & Propagation*, vol. 7, no. 7, pp. 502-509, 2012

[22] F. Gentili, F. Cacciamani, V. Nocella, R. Sorrentino, L. Pelliccia, "RF MEMS Hairpin filter with three reconfigurable bandwidth states," *Proceedings of the 43rd European Microwave Conference*, 7-10 Oct. 2013, Nuremberg, Germany, 2013.

[23] R Azaro, M Donelli, L Fimognari, and A Massa, "A planar electronically reconfigurable Wi-Fi band antenna based on a parasitic microstrip structure," *IEEE Antennas and Wireless Propagation Letters*, 2007, 6, pp. 623-626.

[24] M Donelli and P Febvre, "An inexpensive reconfigurable planar array for Wi-Fi applications," *Progress In Electromagnetics Research C*, 2012, 28, pp. 71-81.

[25] P Rocca, M Donelli, G Oliveri, F Viani, and A Massa, "Reconfigurable sum-difference pattern by means of parasitic elements for forward-looking mono-pulse radar," *IET Radar, Sonar and Navigation*, 2013, 7, pp. 747-754.

[26] S. C. Mukhopadhyay, Ed., Wearable Electronics Sensors: For Safe and Healthy Living, vol. 15. Cham: Springer International Publishing, 2015.

[27] N. S. Katertsidis, C. D. Katsis and D. I. Fotiadis, "INTREPID, a biosignal-based system for the monitoring of patients with anxiety disorders," *2009 9th International Conference on Information Technology and Applications in Biomedicine*, Larnaca, 2009, pp. 1-6.

[28] G. Riva, M. Bacchetta, M. Baruffi and E. Molinari, "Virtual-reality-based multidimensional therapy for the treatment of body image disturbances in binge eating disorders: a preliminary controlled study," in *IEEE Transactions on Information Technology in Biomedicine*, vol. 6, no. 3, pp. 224-234, Sept. 2002.

[29] B. K. Wiederhold, I. T. Miller and M. D. Wiederhold, "Using Virtual Reality to Mobilize Health Care: Mobile Virtual Reality Technology for Attenuation of Anxiety and Pain," in *IEEE Consumer Electronics Magazine*, vol. 7, no. 1, pp. 106-109, Jan. 2018.

[30] E. W. McGinnis et al. "Movements Indicate Threat Response Phases in Children at Risk for Anxiety," in *IEEE Journal of Biomedical and Health Informatics*, vol. 21, no. 5, pp. 1460-1465, Sept. 2017.

[31] A. Foletti and P. Baron, "Biophysical approach to minor anxiety and Depressive Disorders," *2016 Progress in Electromagnetic Research Symposium (PIERS)*, Shanghai, 2016, pp. 1400-1403.

[32] F. Li and Y. Xiong, "Application of Music Therapy Combined with Computer Biofeedback in the Treatment of Anxiety Disorders," *2016 8th International Conference on Information Technology in Medicine and Education (ITME)*, Fuzhou, 2016, pp. 90-93.

[33] V. Costarides, I. Kouris, A. Anastasiou and D. Koutsouris, "An Innovative Gaming Approach to Prevent Anxiety Disorders & amp; Promote Youth Resilience," *2017 IEEE 30th International Symposium on Computer-Based Medical Systems (CBMS)*, Thessaloniki, 2017, pp. 191-192.

[34] C. W. Mundt and H. T. Nagle, "Applications of SPICE for modeling miniaturized biomedical sensor systems," *IEEE Trans. Biomed. Eng.*, vol. 47, no. 2, pp. 149154, Feb. 2000.

[35] M. Phillips, "Reducing the cost of Bluetooth systems," *Electronics & Communication Engineering Journal*, vol. 13, no. 5, pp. 204208, Oct. 2001.

[36] R. Caverly et al., "Advancements at the Lower End: Advances in HF, VHF, and UHF Systems and Technology," *IEEE Microwave*, vol. 16, no. 1, pp. 2849, Feb. 2015.

[37] E. C. Fear, X. Li, S. C. Hagness, and M. A. Stuchly, "Confocal microwave imaging for breast cancer detection: localization of tumors in three dimensions," *IEEE Trans. Biomed. Eng.*, vol. 49, no. 8, pp. 812822, Aug. 2002.

[38] B. Stec, A. Dobrowolski, and W. Susek, "Multifrequency Microwave Thermograph for Biomedical Applications," *IEEE Trans. Biomed. Eng.*, vol. 51, no. 3, pp. 548551, Mar. 2004.

[39] C. R. Farrar, T. W. Darling, A. Migliori, and W. E. Baker, "Microwave Interferometer for Non-Contact Vibration Measurement on Large Structure," *Mechanical Systems and Signal Processing*, vol. 13, no. 2, pp. 241253, Mar. 1999.

[40] Preradovic S. and Karmakar N. C., "Multiresonator-based Chipless RFID - Barcode of the future." Springer, 2012.

[41] Menon, Sreedevi K., and Massimo Donelli, "Compact CPW filter with modified signal line." Applied Electromagnetics Conference (AEMC), 2017 IEEE. IEEE, 2017.

[42] R Azaro, F De Natale, M Donelli, and A Massa, "PSO-based optimization of matching loads for lossy transmission lines," *Microwave and Optical Technology Letters*, vol. 48, no. 8, pp. 1485-1487, 2006.

[43] M Donelli, R Azaro, A Massa, and M Raffetto, "Unsupervised synthesis of microwave components by means of an evolutionary-based tool exploiting distributed computing resources," *Progress in electromagnetics research*, vol. 56, pp. 93-108, 2006.

[44] M Donelli, MD Rukanuzzaman, and C Saavedra, "A methodology for the design of microwave systems and Circuits using an evolutionary algorithm, *Progress in Electromagnetic Research Letters*, vol. 31, p. 129-141, 2013.

[45] M Donelli, MD Rukanuzzaman, and C Saavedra, "Design and Optimization of a broadband X-band bidirectional, *Microwave and Optical Technology Letter*, vol. 55, p. 1730-1735, 2013.

[46] J Robinson, S Sinton, and Y Rahmat-Samii, "Particle swarm, genetic algorithm, and their hybrids: Optimization of a profiled corrugated horn antenna," *in IEEE Antennas Propagat. Soc. Int. Symp. Dig.*, vol. 1, 2002, pp. 314-317.

[47] M Donelli, R Azaro, F De Natale, and A Massa, "An innovative computational approach based on a particle swarm strategy for adaptive phased-arrays control," *IEEE Transactions on Antennas and Propagation*, vol. 54, no. 3, pp. 888-898, Mar. 2006.

[48] M Donelli and A Massa, "A computational approach based on a particle swarm optimizer for microwave imaging of two-dimensional dielectric scatterers," *IEEE Transactions on Microwave Theory and Techniques*, Vol. 53, no. 5, pp. 1761-1776, May 2005.

[49] J Robinson and R Saami, "Particle swarm optimization in electromagnetics," *IEEE Trans. Antennas Propagat.*, 2004, 52, pp. 397-407.

[50] G Zheng, J Papapolymerou, and M Tentzeris, "Wideband coplanar waveguide RF probe pad to microstrip transistions without via holes," *IEEE Microwave and Wireless Components Letters*, 2003, 12, pp. 544-546.

[51] P Rocca, M Benedetti, M Donelli, D Franceschini, and A Massa, "Evolutionary optimization as applied to inverse scattering problems," *Inverse Problems*, 2009, 25, pp. 1-41.

[52] J Kennedy, R C Eberhart, and Y Shi, *Swarm Intelligence*. San Francisco: Morgan Kaufmann, 2001.

[53] R. L. Haupt, "Phase-only adaptive nulling with a genetic algorithm," *IEEE Trans. Antennas Propagat.*, vol. 45, pp. 10091015, June 1997.

[54] D. S.Weile and E. Michielssen, "The control of adaptive antenna arrays with genetic algorithms using dominance and diploidy," *IEEE Trans. Antennas Propagat.*, vol. 49, pp. 14241433, Oct. 2001.

[55] S. Caorsi, M. Donelli, A. Lommi, and A. Massa, "A new GA-based strategy for adaptive antenna array control," *in Proc. JINA2002, Nice, France*, Nov. 1214, 2002, pp. 447450.

[56] C. Sacchi, F. De Natale, M. Donelli, A. Lommi, and A. Massa, "Adaptive antenna array control in presence of interfering signals with stochastic arrivalsassessment of a GA-based procedure," *IEEE Trans. Wireless Communications*, vol. 3, pp. 10311036, July 2004.

[57] A. A. Salih, Z. N. Chen, and K. Mouthaan, "Characteristic mode analysis and metasurface based suppression of higher order modes of a closely spaced phased array," *IEEE Trans. on Antenna and Propagation,* vol. 65, nop. 3, pp. 1141-1150, 2017.

[58] D. Gesbert, M. Shafi, D. Shiu, P.J. Smith, and A. Naquib, "From theory to practice: an overview of MIMO space-time coded wireless systems," *IEEE Journal on Selec. Areas in Comm*, Vol. 21, No. 3, pp. 281302, April 2003.

[59] K. Gyoda and T. Ohira, "Design of electronically steearable passive array radiator (ESPAR) antennas," *Proc. Antennas and Propagation Soc. Int. Symp.*, vol. 2, Jul. 16-21, 2000, pp. 922-925.

[60] M. D. Migliore, D. Pinchera, and Fulvio Schettino, "A simple and robust adaptive parasitic antenna," *IEEE Trans Antennas Propagat.*, vol. 53, no. 10, pp. 3262-3272, Oct. 2005.

[61] P. de Maagt, R. Gonzalo, Y. C. Vardaxoglou, and J. M. Baracco, "Electromagnetic bandgap antennas and components for microwave and (sub)millimeter wave applications," *IEEE Trans. Antennas Propagat.*, vol. 51, no. 10, pp. 2667-2677, Oct. 2003.

[62] R. Azaro, M. Donelli, L. Fimognari, and A. Massa, "A planar electronically reconfigurable Wi-Fi band antenna based on parasitic microstrip structures," *IEEE Antennas and Wireless Propagat. Letters*, vol. 6, pp. 623-626, 2007.

[63] P. Rocca, M. Donelli, A. Massa, F. Viani, and G. Oliveri, "Reconfigurable sum-difference pattern by means of parasitic elements for forward-looking monopulse radar," *IET Radar & Sonar Navigation*, vol. 7, no. 7, pp. 747-754, 2013

[64] W. Rotman, and R. F. Turner, "Wide-angle microwave lens for line source applications," *Report AFCRL-62-18 AF Cambridge Research Laboratories*, Bedford, MA, January 1962.

[65] W. Rotman and R. F. Turner, "Wide angle microwave lens for line source applications," *IEEE Trans. Antennas Propag.* AP-11, pp. 623632, Nov. 1963.

[66] M. J. Maybell, "Printed Rotman lens-fed array having wide bandwidth, low sidelobes, constant beamwidth, and synthesized radiation

patern," *IEEE AP Symposium Digest*, May 1983, Houston, pp.373-376.

[67] T. K. Mano, and S. Sato, "An improved design method of Rotman lens antennas," *IEEE Trans. On Antenna and Porpagation*, vol. 32, pp. 524-527, 1984.

[68] K. K. Chan, and S. K. Rao, "Design of a Rotman lens feed network to generate a hexagonal lattice of multiple beams," *IEEE Trans. on Antennas and Propagation,* vol. 50, no. 8, pp. 1099-1108, Aug. 2002.

[69] L. Hall, D. Abbott, and H. Hansen, "Rotman lens for mm-wavelengths," *Proceedings of SPIE - The International Society for Optical Engineering (SPIE2002)*, pp. 215-221, 2002.

[70] P. S. Simon, "Analysis and synthesis of Rotman lenses," 22^nd *AIAA International Communications Satellite Systems Conference & Exhibit*, 9-10 May 2004, pp. 1-11.

[71] C. W. Penney, "Rotman lens design and simulation in software," *IEEE Microwave Magazine*, pp. 1-11, Dec. 2008.

[72] R. P. S. Kushwah, and P. K. Singhal, "Modified design of bootlace lens for multiple beam forming," *Journal of Electrical and Electronics Engineering Research*, vol. 2, pp. 14-24, Feb. 2010.

[73] Y. Zhang, S. Christie, V. Fusco, R. Cahill, G. Goussetis, and D. Linton, "Reconfigurable beam forming using phase-aligned Rotman lens," *IET Microwaves, Antennas & Propagation*, vol. 6, no. 3, pp. 326-330, Nov. 2012.

[74] J. Hasch, E. Topak, R. Schnabel, T. Zwick, R. Weigel, and C. Waldschmidt, "Millimeter-Wave Technology for Automotive Radar Sensors

in the 77GHz Frequency Band," *IEEE Trans. Microwave Theory and Techniques*, vol. 60, no. 3, Mar. 2012.

[75] X. Zou, C. Tong, J. Bao, and W. Pang, "SIW-Fed Yagi Antenna and Its Application on Monopulse Antenna," *IEEE Antennas Propag. Lett.*, vol. 13, 2014.

[76] A. Darvazehban, O. Manoochehri, M. A. Salari, P. Dehkhoda, and A. Tavakoli, "Ultra-Wideband scanning antenna array with rotman lens," *IEEE Trans. Microwave Theory and Techniques*, Jan. 2017.

[77] Chou, Hsi-Tseng, e Chen-Yi Chang, "Application of Rotman Lens Beamformer for Relatively Flexible Multibeam Coverage From Electrically Large-Phased Arrays of Antennas," *IEEE Transactions on Antennas and Propagation*, vol. 67, n. 5, maggio 2019, pagg. 3058-66.

[78] Kou, Na, et al. "One-Dimensional Beam Scanning Transmitarray Lens Antenna Fed by Microstrip Linear Array," *IEEE Access*, vol. 7, 2019, pagg. 90731-40.

[79] Liu, Yi, et al. "Circumferentially Conformal Slot Array Antenna and Its Ka-Band Multibeam Applications," *IET Microwaves, Antennas & Propagation*, vol. 12, n. 15, dicembre 2018, pagg. 2307-12.

[80] Mujammami, Essa H., et al. "Optimum Wideband High Gain Analog Beamforming Network for 5G Applications," *IEEE Access*, vol. 7, 2019, pagg. 52226-37.

[81] Wang, Xiaoyi, et al. "Flexible-Resolution, Arbitrary-Input, and Tunable Rotman Lens Spectrum Decomposer," *IEEE Transactions on Antennas and Propagation*, vol. 66, n. 8, 2018, pagg. 3936-47.

[82] R. Moore, *Interval Analysis*. Prentice-Hall, 1966.

[83] G. Alefeld and J. Herzberger, *Introduction to Interval Computations.* Academic Press, 1983.

[84] L. V. Kolev, *Interval Methods for circuit analysis*, World Scientific, Singapore, 1993.

[85] J. Michel, and F. Schwartz, "Analogue circuit sizing method using interval analysis," *Proc. 6th International IEEE Northeast Workshop on Circuits and Systems and TAISA Conference (NEWCAS-TAISA 2008)*, 22-25 Jun, pp. 331-334.

[86] N. Anselmi, L. Manica, P. Rocca, and A. Massa, "Tolerance analysis of antenna arrays through interval arithmetic," *IEEE Trans. on Antennas and Propagation,* vol. 61, no. 11, nov. 2013.

[87] P. Rocca, M. Carlin, and A. Massa, "Imaging weak scatterers by means of an innovative inverse scattering technique based on the interval analysis," *Proc. 6th European Conf. Antennas Propag. (EUCAP 2012)*, Prague, Czech Republic, 26-30 Mar. 2012, pp. 1139-1140.

[88] M. Carlin, P. Rocca, G. Oliveri, and A.Massa, "Interval analysis as applied to inverse scattering, *Proc. Int. Symp. Antennas Propag. (APS-URSI 2012)*, Chicago, Illinois (USA), 8-14 Jul. 2012, pp. 1-2.

[89] L. Manica, P. Rocca, M. Salucci, M. Carlin, and A. Massa, "Scattering data inversion through interval analysis under rytov approximation," *Proc. 7th European Conf. Antennas Propag. (EUCAP 2013)*, Gothenburg, Sweden, 8-11 Apr. 2013, pp. 82-85.

[90] H. Paganetti, "Proton Therapy Physics," CRC Press - Taylor & Francis Group, Boca Raton, London, New York, 2012.

[91] C. Bert, M. Durante, "Motion in Radiotherapy: particle therapy,' *Phys Med Biol*, Vol. 56, No. 16, R113-R144, 2011.

[92] F. Pfanner, J. Maier, T. Allmendinger, T. Flohr, and M. Kachelrieβ "Monitoring internal organ motion with continuous wave radar in CT," *Med Phys* Vol. 40, No. 9, 091915, 2013.

[93] C. Wu, and Z. Y. Huang, "Using the phase change of a reflected microwave to detect a human subject behind a barrier," *IEEE Trans. Biomed. Eng.*, Vol. 55, No. 1, pp. 267-272, 2008.

[94] Donelli, M , "A rescue radar system for the detection of victims trapped under rubble based on the independent component analysis," *Progress In Electromagnetics Research M*, 2011, 28, pp. 173-181.

[95] M. Donelli, and F. Viani, "Life signals detection system based on a continuous-wave X-band radar," *Electronic Letters*, vol. 52, 23, pp. 1903-1904, 2016.

[96] Z. Park, C. Li, J. Lin, "A broadband microstrip antenna with improved gain noncontact vital sign radar detection," *IEEE Antennas and Wireless Propagation Letters*, vol. 8, pp.939-942, 2018.

[97] Z. Peng, J. M. Munoz-Ferreras, Y. Tang, C. Liu, R. Gomez-Garcia, L. Ran, C- Li, "A Portable FMCW Interferometry Radar With Programmable Low-IF Architecture for Localization, ISAR Imaging, and Vital Sign Tracking," *IEEE Trans. on Microwave Theory and Techniques*, vol. 66, no. 9, pp. 5106-5118, 2018.

[98] C. Tsengm Y. Lin, "24-GHz Self-Injection-Locked Vital-Sign Radar Sensor With CMOS Injection-Locked Frequency Divider Based on PushPush Oscillator Topology," *IEEE Microwave and Wireless Components Letters*, vol. 28, no. 11, pp. 1053-1055, 2018.

[99] C. R. Farrar, T. W. Darling, A. Migliori and W. E. Baker, "Microwave interferometers for non-contact vibration measurements on

structures," *Mechanical Systems and Signal Processing*, vol. 13, 2, pp. 241-253, 1999.

[100] Challita, Frederic, et al. "Massive MIMO Communication Strategy Using Polarization Diversity For Industrial Scenarios," *IEEE Antennas and Wireless Propagation Letters*, pp. 14, 2019.

[101] Jenssen, Rolf Ole Rydeng, et al. "Drone-Mounted Ultrawideband Radar for Retrieval of Snowpack Properties," *IEEE Transactions on Instrumentation and Measurement*, vol. 69, n. 1, pp. 22130, Jan. 2020.

[102] K. Ghaemi, R. Ma, and N. Behdad, "A small-aperture, ultrawideband HF/VHF direction-finding system for unmanned aerial vehicles," *IEEE Trans. on Antennas Propagat.*, vol. 66, no. 10, pp. 5109-5120, Oct. 2018.

[103] W. Li, Y. Hei, P. M. Grubb, X. Shi, and R. T. Chen, "Compact inkjet-printed flexible MIMO antenna for UWB applications," *IEEE Access*, vol. 6, pp. 5290-5298, Aug. 2018.

[104] S. Saxena, B. K. Kanauja, S. Dwari, S. Kumar, and R. Tiwari, "Compact ultra-wideband microstrip antenna with dual polarisation/multi-notch characteristics," *IET Microwave Antennas & Propagation*, vol. 12, no. 9, pp. 1546-1553, 2018.

[105] L. A. Shaik, C. Saha, J. Y. Siddiqui, et al. "Ultra-wideband monopole antenna for multiband and wideband frequency notch and narrowband applications," *IET Microw. Antennas Propag.*, vol. 10, no. 11, pp. 12041211, 2016.

[106] Z. Tang, R. Lian, and Y. Yin, "Differential-fed UWB patch antenna with triple band-notched characteristics," *Electron. Lett.*, vol. 51, no. 22, pp. 17281730, 2015.

[107] Hung, Wei-Ping, et al. "Non-invasive detection of object by UWB radar," *2017 Asia-Pacific International Symposium on Electromagnetic Compatibility (APEMC), IEEE*, 2017, pp. 16971, 2017.

[108] Wu, Shuqiong, et al. "Person-Specific Heart Rate Estimation With Ultra-Wideband Radar Using Convolutional Neural Networks," *IEEE Access*, vol. 7, pp. 16848494, 2019.

[109] M. Shehata, M. S. Said, and H. Mostafa, "Dual Notched Band Quad-Element MIMO Antenna With Multitone Interference Suppression for IR-UWB Wireless Applications," *IEEE Trans. on Antennas Propagat.*, vol. 66, no. 11, nov., pp. 5737-5746, 2018.

[110] Y.-Z. Cai, H.-C. Yang, and L.-Y. Cai, "Wideband monopole antenna with three band-notched characteristics," *IEEE Antennas Wireless Propag. Lett.*, vol. 13, pp. 607610, 2014.

[111] G. S. Reddy, A. Kamma, and J. Mukherjee, "Compact printed monopole UWB antenna loaded with non-concentric open-ended rings for triple band-Notch characteristic," *Proceeding in Proc. APMC, Seoul, South Korea*, Nov. 2013, pp. 221223.

[112] T.-C. Tang and K.-H. Lin, "An ultrawideband MIMO antenna with dual band-notched function," *IEEE Antennas Wirel. Propag. Lett.*, vol. 13, pp. 10761079, 2014.

[113] S. Tripathi, A. Mohan, and S. Yadav, "A compact koch fractal UWB MIMO antenna with WLAN band-rejection," *IEEE Antennas Wireless Propag. Lett.*, vol. 14, pp. 15651568, 2015.

[114] Terki, Abdennour Ben, et al. "Design of Compact UWB Coplanar Waveguide-Fed Modified Sierpinski Carpet Fractal Antenna," *2019*

IEEE International Symposium on Antennas and Propagation and USNC-URSI Radio Science Meeting, IEEE, pp. 109192, 2019.

[115] D. Chaturvedi, A. Kumar, and S. Raghavan, "An Integrated SIW Cavity-Backed Slot Antenna-Triplexer," *IEEE Antennas Wireless Propag. Lett.*, vol. 17, no. 8, pp. 1557-1560, Aug. 2018.

[116] K. Kumar and S. Dwari, "Substrate integrated waveguide cavity-backed self-triplexing slot antenna," *IEEE Antennas Wireless Propag. Lett.*, vol. 16, pp. 32493252, 2017.

[117] F. Xuand, and K. Wu, "Guided-wave and leakage characteristics of substrate integrated waveguide," *IEEE Trans. Microw. Theory Techn.*, vol. 53, no. 1, pp. 6673, Jan. 2005.

[118] J. Wu, Y. J. Cheng, and Y. Fan, "A wideband high-gain high- efficiency hybrid integrated plate array antenna for V-band inter-satellite links," *IEEE Trans. Antennas Propag.*, vol. 63, no. 4, pp. 12251233, Apr. 2015.

[119] X. Li, J. Xiao, Z. Qi, and H. Zhu, "Broadband and High-Gain SIW-Fed Antenna Array for 5G Applications," *IEEE Access*, vol. 6, pp. 5628256289, Oct. 2018.

[120] Z. Chen and Z. Shen, "A compact cavity-backed endfire slot antenna," *IEEE Antennas Wireless Propag. Lett.*, vol. 13, pp. 281284, 2014.

[121] O. Caytan et al. "Half-mode substrate-integrated-waveguide cavity-backed slot antenna on cork substrate," *IEEE Antennas Wireless Propag. Lett.*, vol. 15, pp. 162165, 2016.

[122] M. Donelli, "A chipless RFID system based on substrate impedance waveguide resonators (SIW)," *IEEE-APS Topical Conference on An-*

tennas and Propagation in Wireless Communications (APWC), 2017 , Verona, Italy: IEEE, 2017, p. 29-32. Proceedings of: IEEE-APS, Verona, Italy, 11-15, Settembre, 2017.

[123] M. S. Sorkherizi, A. Dadgarpour, and A. A. Kishk, "Planar high-efficiency antenna array using new printed ridge gap waveguide technology," *IEEE Trans. Antennas Propag.*, vol. 65, no. 7, pp. 37723776, Jul. 2017.

[124] M. Bozzi, A. Georgiadis, and K. Wu, "Review of Substrate Integrated Waveguide (SIW) Circuits and Antennas," *IET Microwave Antennas and Propagation*, Vol. 5, No.8, pp. 909-920, June 2011.

[125] A. H. M. Zahirul Alam, et al. "Design of a Tuning Fork Type UWB Patch Antenna," *International Journal of Electrical, Electronic and Communication Sciences*, vol. 0, n. 8, pp. 1126-1129, Aug. 2007.

[126] M. Donelli, and F. Robol, "Circularly polarized hook antenna for ISM-band systems," *Microwe and Optical Technology Letters*, vol. 60, no. 6, pp. 14521454, 2018.

[127] M. Donelli, and J. Iannacci, "Exploitation of RF-MEMS Switches for the Design of Broadband Modulated Scattering Technique Wireless Sensors," *IEEE Antennas and Wireless Propagation Letters*, vol. 18, no. 1, pp. 4448, 2019.

[128] M. Donelli, "A broadband modulated scattering technique (MST) probe based on a self complementary antenna," *IEEE-APS Topical Conference on Antennas and Propagation in Wireless Communications (APWC), 2017 IEEE-APS, Verona, Italy: IEEE, 2017, p. 25-28.*, Verona, Italy, 11-15, Settembre, 2017.

[129] G. Chen, Y. Jiao, and G. Zhao, "A Reflectarray for Generating Wideband Circularly Polarized Orbital Angular Momentum Vortex Wave", in *IEEE Antennas and Wireless Propagation Letters*, vol. 18, no. 1, pp. 182-186, Jan. 2019.

[130] Y. Wang, Y. Du, L. Qin, and B. Li, "An Electronically Mode Reconfigurable Orbital Angular Momentum Array Antenna," in *IEEE Access*, vol. 6, pp. 64603-64610, 2018.

[131] F. Qin, J. Yi, W. Cheng, Y. Liu, H. Zhang, and S. Gao, "A high-gain shared-aperture dual-band OAM antenna with parabolic reflector," *12th European Conference on Antennas and Propagation (EuCAP 2018)*, London, 2018, pp. 1-4.

[132] H. Jing, W. Cheng, X. Xia, and H. Zhang, "Orbital-Angular-Momentum Versus MIMO: Orthogonality, Degree of Freedom, and Capacity," 2018 IEEE 29th Annual International Symposium on Personal, Indoor and Mobile Radio Communications (PIMRC), Bologna, Italy, 2018, pp. 1-7.

[133] C. Nguyen, J. Park *Stepped-frequency radar sensors.* New York, NY: Springer Berlin Heidelberg, 2016.

[134] G. Tronca, I. Tsalicoalou, S. Lehner, e G. Catanzariti, "Comparison of pulsed and stepped frequency continuous wave (SFCW) GPR systems," in 2018 *17th International Conference on Ground Penetrating Radar (GPR)*, Rapperswil, giu. 2018, pag. 14.

[135] A. Langman e M. R. Inggs, "Pulse versus stepped frequency continuous wave modulation for ground penetrating radar," in IGARSS 2001. *Scanning the Present and Resolving the Future. Proceedings. IEEE 2001 International Geoscience and Remote Sensing Symposium (Cat. No.01CH37217)*, Sydney, NSW, Australia, 2001, vol. 3, pag. 15331535.

[136] G. Gok, Y. K. Alp, e O. Arikan, "A New Method for Specific Emitter Identification With Results on Real Radar Measurements," IEEE Trans.Inform.Forensic Secur., vol. 15, pag. 33353346, 2020.

[137] L. Nicolaescu, P. van Genderen, e K. Palmer, "Calibration procedures of a stepped frequency continuous wave radar for landmines detection," in 2003 *Proceedings of the International Conference on Radar (IEEE Cat. No.03EX695)*, Adelaide, SA, Australia, 2003, pag. 412-417.

[138] A. S. Turk, A. Kizilay, M. Orhan, e A. Caliskan, "High resolution signal processing techniques for millimeter wave short range surveillance radar," in 2016 *17th International Radar Symposium (IRS)*, Krakow, 2016, pag. 14.

[139] Kusmadi e A. Munir, "Simulation design of compact stepped-frequency continuous-wave through-wall radar," in 2015 *International Conference on Electrical Engineering and Informatics (ICEEI)*, Denpasar, Bali, Indonesia, ago. 2015, pag. 332335.

[140] M. Pieraccini, M. Fratini, F. Parrini, G. Macaluso, e C. Atzeni, "High-speed CW step-frequency coherent radar for dynamic monitoring of civil engineering structures," Electron. Lett., vol. 40, n. 14, pag. 907, 2004.

[141] M. Pieraccini, M. Fratini, F. Parrini, e C. Atzeni, "Dynamic Monitoring of Bridges Using a High-Speed Coherent Radar," IEEE Trans. Geosci. Remote Sensing, vol. 44, n. 11, pag. 32843288, nov. 2006.

[142] S. Lambot, E. C. Slob, I. van den Bosch, B. Stockbroeckx, e M. Vanclooster, "Modeling of ground-penetrating Radar for accurate characterization of subsurface electric properties," IEEE Trans. Geosci. Remote Sensing, vol. 42, n. 11, pag. 25552568, nov. 2004.

[143] W.-C. Su, M.-C. Tang, R. E. Arif, T.-S. Horng, e F.-K. Wang, "Stepped-Frequency Continuous-Wave Radar With Self-Injection-Locking Technology for Monitoring Multiple Human Vital Signs," IEEE Trans. Microwave Theory Techn., vol. 67, n. 12, pag. 53965405, dic. 2019.

[144] M. Caruso, M. Bassi, A. Bevilacqua, e A. Neviani, "A 2-16 GHz 65 nm CMOS Stepped-Frequency Radar Transmitter With Harmonic Rejection for High-Resolution Medical Imaging Applications," IEEE Trans. Circuits Syst. I, vol. 62, n. 2, pag. 413422, feb. 2015.

[145] I. Nicolaescu, "Improvement of Stepped-Frequency Continuous Wave Ground-Penetrating Radar Cross-Range Resolution," IEEE Trans. Geosci. Remote Sensing, vol. 51, n. 1, pag. 8592, gen. 2013.

[146] M. Scherhaufl, F. Hammer, M. Pichler-Scheder, C. Kastl, e A. Stelzer, "Radar Distance Measurement With Viterbi Algorithm to Resolve Phase Ambiguity," IEEE Trans. Microwave Theory Techn., pag. 11, 2020.

[147] G. Cui, L. Kong, e X. Yang, "Reconstruction Filter Design for Stepped-Frequency Continuous Wave," IEEE Trans. Signal Process., vol. 60, n. 8, pag. 44214426, ago. 2012.

[148] S. R. J. Axelsson, "Analysis of Random Step Frequency Radar and Comparison With Experiments," IEEE Trans. Geosci. Remote Sensing, vol. 45, n. 4, pag. 890904, apr. 2007.

[149] A. N. Gaikwad, D. Singh, e M. J. Nigam, "Application of clutter reduction techniques for detection of metallic and low dielectric target behind the brick wall by stepped frequency continuous wave radar in ultra-wideband range," IET Radar Sonar Navig., vol. 5, n. 4, pag. 416, 2011.

[150] Costa, F.; Genovesi, S.; Borgese, M.; Dicandia, F.A.; Manara, G.; Tedjini, S.; Perret, E.; Girbau, D.; Lazaro, A.; Villarino, R., "Design of wireless sensors by using chipless RFID technology," In Proceedings of the 2017 Progress In Electromagnetics Research Symposium—Spring (PIERS), St. Petersburg, Russia, 22–25 May 2017; pp. 3309–3313.

[151] Jayakrishnan, M.P.; Vena, A.; Sorli, B.; Perret, E., "Solid-State Conductive-Bridging Reconfigurable RF-Encoding Particle for Chipless RFID Applications," *IEEE Microw Wirel Compon. Lett. 2018* ,28, pp 506–508.

[152] Jiang, T.Y.; Lai, F.P.; Chen, Y.S., "Investigation of the bandwidth of resonators for frequency-coded chipless radio-frequency identification tags," In Proceedings of the 2018 27th Wireless and Optical Communication Conference (WOCC), Hualien, Taiwan, 30 April–1 May 2018; pp. 1–4.

[153] Liu, Y.; Yang, X., "Chipless Radio Frequency Identification Tag Design with Modified Interdigital Hairpin Resonators," In Proceedings of the 2018 International Conference on Intelligent Transportation, Big Data& Smart City (ICITBS), Xiamen, China, 25–26 January 2018; pp. 645–648.

[154] Habib, A.; Anam, H.; Amin, Y.; Tenhunen, H., "High-density compact chipless RFID tag for item-level tagging," In Proceedings of the 2018 International Applied Computational Electromagnetics Society Symposium (ACES), Denver, CO, USA, 25–29 March 2018; pp. 1–2.

[155] Alves, A.A.C.; Spadoti, D.H.; Bravo-Roger, L.L. Bravo-Roger, "Optically Controlled Multiresonator for Passive Chipless Tag," *IEEE Microw Wirel Compon. Lett 2018*, 28, 467–469.

[156] Hester, J.G.D.; Kimionis, J.; Bahr, R.; Su, W.; Tehrani, B.; Tentzeris, M.M., "Radar & additive manufacturing technologies: The future of Internet of Things (IoT)," In Proceedings of the 2018 IEEE Radar Conference (RadarConf18), Oklahoma City, OK, USA, 23–27 April 2018; pp. 0447–0452.

[157] Zeb, S.; Habib, A.; Amin, Y.; Tenhunen, H.; Loo, J., "Green Electronic Based Chipless Humidity Sensor for IoT Applications," In Proceedings of the 2018 IEEE Green Technologies Conference (GreenTech), Austin, TX, USA, 4–6 April 2018; pp. 172–175.

[158] Abbas, H.T.; Abdullah, H.H.; Mohanna, M.A.H.; Mansour, H.A.; Shehata, G.S. , "High RCS compact orientation independent chipless RFID tags based on slot ring resonators (SRR)," In Proceedings of the 2018 35th National Radio Science Conference (NRSC), Cairo, Egypt, 20–22 March 2018; pp. 69–76.

[159] Costa, F.; Gentile, A.; Genovesi, S.; Buoncristiani, L.; Lazaro, A. Villarino, R.; Girbau, D., "A Depolarizing Chipless RF Label for Dielectric Permittivity Sensing," *IEEE Microw. Wirel. Compon. Lett.* 2018, *28*, 371–373.

[160] Marindra, A.M.J.; Tian, G.Y., "Chipless RFID Sensor Tag for Metal Crack Detection and Characterization," *IEEE Trans. Microwave Theory Tech.* 2018, 66, 2452–2462.

[161] Wang, L.; Liu, T.; Sidn, J.; Wang, G., "Design of Chipless RFID Tag by Using Miniaturized Open-Loop Resonators," *IEEE Trans. Antennas Propag.* 2018, 66, 618–626.

[162] Xie, K.; Xue, Y., "A 12 bits chipless RFID tag based on I-shaped slot resonators," In Proceedings of the 2017 6th International Conference

on Computer Science and Network Technology (ICCSNT), Dalian, China, 21–22 October 201; pp. 320–324.

[163] Dey, S.; Karmakar, N.C., "Towards an inexpensive paper based flexible chipless RFID tag with increased data capacity," In Proceedings of the 2017 Eleventh International Conference on Sensing Technology (ICST), Sydney, NSW, Australia, 4–6 December 2017; pp. 1–5.

[164] Song, J.; Li, X.; Zhu, H., "Multiresonator-based chipless RFID system for low-cost application," In Proceedings of the 2017 Progress in Electromagnetics Research Symposium—Fall (PIERS—FALL), Singapore, 19–22 November 2017; pp. 543–547.

[165] Aiswarya, S.; Ranjith, M.; Menon, S.K., "Passive RFID tag with multiple resonators for object tracking," In Proceedings of the 2017 Progress in Electromagnetics Research Symposium—Fall (PIERS—FALL), Singapore, 19–22 November 2017; pp. 742-746.

[166] Su, H.H.; Zhang, J.; Tong, M.S., "Design of chipless RFID tag based on surface acoustic wave," In Proceedings of the 2017 Progress in Electromagnetics Research Symposium—Fall (PIERS—FALL), Singapore, 19–22 November 2017; pp. 2136–2139.

[167] Dey, S.; Karmakar, N.C., "An IoT empowered flexible chipless RFID tag for low cost item identification," In Proceedings of the 2017 IEEE Region 10 Humanitarian Technology Conference (R10-HTC), Dhaka, Bangladesh, 21–23 December 2017; pp. 179–182.

[168] Boussada, A.; Machac, J.; Svanda, M.; Havlicek, J.; Polivka, M., "Erroneous reading of information in chipless RFID tags," In Proceedings of the 2017 Progress In Electromagnetics Research Symposium—Spring (PIERS), St. Petersburg, Russia, 22–25 May 2017; pp. 3304–3308.

[169] Mumtaz, M.; Amber, S.F.; Ejaz, A.; Habib, A.; Jafri, S.I.; Amin, Y., "Design and analysis of C shaped chipless RFID tag," In Proceedings of the 2017 International Symposium on Wireless Systems and Networks (ISWSN), Lahore, Pakistan, 19–22 November 2017; pp. 1–5.

[170] Lazaro, A.; Villarino, R.; Costa, F.; Genovesi, S.; Gentile, A.; Buoncristiani, L.; Girbau, D., "Chipless Dielectric Constant Sensor for Structural Health Testing," *IEEE Sens. J.* 2018, 18, 5576–5585.

[171] Polivka, M.; Svanda, M.; Havlicek, J.; Machac, J., "Detuned dipole array backed by rectangular plate applied as chipless RFID tag," In Proceedings of the 2017 Progress In Electromagnetics Research Symposium—Spring (PIERS), St. Petersburg, Russia, 22–25 May 2017; pp. 3314–3317.

[172] Javed, N.; Habib, A.; Amin, Y.; Tenhunen, H., "Towards Moisture Sensing Using Dual-Polarized Printable Chipless RFID Tag," In Proceedings of the 2017 International Conference on Frontiers of Information Technology (FIT), Islamabad, Pakistan, 18–20 December 2017; pp. 189–193.

[173] Mukherjee, S., "Design of compact Ka- band chipless identification tag using HMSIW cavity resonator," In Proceedings of the 2017 IEEE Asia Pacific Microwave Conference (APMC), Kuala Lumpar, Malaysia, 13–16 November 2017; pp. 694–697.

[174] Chen, C.; Chen, Y.; Li, T.; Yu, Y.; Wu, W., "A chipless RFID system based on polarization characteristics," In Proceedings of the 2017 7th IEEE International Symposium on Microwave, Antenna, Propagation, and EMC Technologies (MAPE), Xi'an, China, 24–27 October 2017; pp. 324–329.

[175] Liu, J., "Joint frequency and time coded chipless UWB-RFID tag for bit data enhancement," In Proceedings of the 2017 7th IEEE International Symposium on Microwave, Antenna, Propagation, and EMC Technologies (MAPE), Xi'an, China, 24–27 October 2017; pp. 74–77.

[176] Sharma, V.; Hashmi, M., "Chipless RFID tag based on open-loop resonator," In Proceedings of the 2017 IEEE Asia Pacific Microwave Conference (APMC), Kuala Lumpar, Malaysia, 13–16 November 2017; pp. 543–546.

[177] Pazmio, E.; Vsquez, J.; Rosero, J.; Pozo, D., "Passive chipless RFID tag using fractals: A design based simulation," In Proceedings of the 2017 IEEE Second Ecuador Technical Chapters Meeting (ETCM), Salinas, Ecuador, 16–20 October 2017; pp. 1–4.

[178] Bibile, M.A.; Karmakar, N.A., "Detection error rate analysis using coloured noise for the movement of chipless RFID tag," In Proceedings of the 2018 Australian Microwave Symposium (AMS), Brisbane, QLD, Australia, 6–7 February 2018; pp. 1–2.

[179] Bibile, M.A.; Karmakar, N.C., "Moving Chipless RFID Tag Detection Using Adaptive Wavelet-Based Detection Algorithm," *IEEE Trans. Antennas Propag.* 2018, 66, 2752–2760.

[180] Herrojo, C.; Mata-Contreras, J.; Paredes, F.; Nez, A.; Ramon, E.; Martn, F., "Near-Field Chipless-RFID System With Erasable/Programmable 40-bit Tags Inkjet Printed on Paper Substrates," *IEEE Microw. Wirel. Compon. Lett.* 2018, 28, 272–274.

[181] Costa, F.; Borgese, M.; Gentile, A.; Buoncristiani, L.; Genovesi, S.; Dicandia, F.A.; Bianchi, D.; Monorchio, A.; Manara, G., "Robust Reading Approach for Moving Chipless RFID Tags by Using ISAR Processing," *IEEE Trans. Microw. Theory Tech.* 2018, 66, 2442–2451.

[182] Dullaert, W.; Reichardt, L.; Rogier, H., "Improved Detection Scheme for Chipless RFIDs Using Prolate Spheroidal Wave Function-Based Noise Filtering," *IEEE Antennas Wirel. Propag. Lett.* 2011, *10*, 472–475.

[183] Sharma, V.; Vithalkar, A.; Hashmi, M., "Lightweight security protocol for chipless RFID in Internet of Things (IoT) applications," In Proceedings of the 2018 10th International Conference on Communication Systems & Networks (COMSNETS), Bengaluru, India, 3–7 January 2018, pp. 468–471.

[184] Preradovic, S.; Karmakar N. C. *Multiresonator-based Chipless RFID-Barcode of the Future*; Springer: Berlin, Germany, 2012.

[185] Koenker, R.; Bassett, G. Regression Quantiles. *Econometrical* 1978, *46*, 33–50.

[186] Han, Y.; Shi, D., "A Case Study on Relationship between Mortgage Payment and Income Using Quantile Regression," In Proceedings of the 2009 First International Workshop on Education Technology and Computer Science, Wuhan, China, 7–8 March 2009; pp. 419–422.

[187] Chen, J.; Ding, J., "A Review of Technologies on Quantile Regression," *Stat Inf Forum, 2008*, 23, 89–96.

[188] Guan, J.; He, Y.; Shi, D., "Using Quantile Regression to Analyze the Trend between the Annual Maximum Sea Level and Southern Oscillation Index," *Periodical Ocean Univ. China*, 2018.

[189] Koenker, R.; dOrey, V., "Computing regression quantiles," *Appl. Stat.* 1987, 36, 383–393.

[190] Fahrmeir, L.; Kneib, T.; Lang, S.; Marx, B. *Regression. Models, Methods and Applications*; Springer: Berlin, Germany, 2013.

[191] Koenker, R.; Hallock, K.F., "Quantile Regression," *J. Econ. Perspect. 2001*, 15, 143–156.

[192] Donelli, M.; Robol, F., "Circularly polarized monopole hook antenna for ISM-band systems," *Microw Opt Technol Lett 2018*, 60, 1452–1454.

[193] D. M. Doolin and N. Sitar, "Wireless sensors for wildfire monitoring," in *Symp. Smart Structures and Materials (NDE 2005)*, San Diego, CA, pp. 6–10, 2005.

[194] M. Rad and L. Shafai, "A wireless embedded sensor for structural health monitoring applications," in *Proc. 13th Int. Symp. Antenna Technol. Appl. Electromagn. Can. Radio Sci. Meeting ANTEM/URSI*, pp. 1–4, 2009.

[195] M. Polivka, M. Svanda, P. Hudec, and S. Zvanovec, "UHF RF identification of people in indoor and open areas," *IEEE Trans. Microw. Theory and Tech.*, vol. 57, no. 5, pp. 1341–1347, May, 2009.

[196] F. Viani, G. Oliveri, P. Rocca, M. Donelli, A. Massa, and L. Lizzi, "WSN-based solutions for security and surveillance," *European Microwave Week 2010, EuMW2010: Connecting the World*, pp. 285–288, 2010.

[197] O. Cayirpurnar, B. Tavli, E. Kadioglu-Urtis, S. Uludag, "Optimal mobility patterns of multiple base stations wireless sensor network lifetime maximization," *IEEE Sensors Journal*, vol. 17, no. 21, pp. 7177-7188, 2017.

[198] D. M. Dobkin, *The RF in RFID: Passive UHF RFID in Practice*, Elsevier, 2006.

[199] K. Finkenzeller, *RFID Handbook, Second Edition*, New York, Wiley, 2004.

[200] A. Rida, V. Lakafosis, R. Vyas, S. Nikolaou, and M. Tentzeris, "Review of technologies for low-cost integrated sensors," *IEEE International Conference on RFID-Technologies and Applictions*, April 12–14, 2011, Orlando, FL USA.

[201] S. Capdevila, L. Jofre, J. Romeu, and J. C. Bolomey, "Passive RFID based sensing," *IEEE International Conference on RFID-Technologies and Applications*, April 12–14, 2011, Orlando, FL USA.

[202] S. Capdevila, L. Jofre, J. Romeu, and J. C. Bolomey, "RFID multiprobe impedance based sensors," *IEEE Trans. Instrumentation Measurement*, vol. 59, no. 12, pp. 3093–3101, Dec. 2010.

[203] F. Fuschini, C. Piersanti, F. Paolazzi, and G. Falciasecca, "Analytical approach to the backscattering from UHF RFID transponder," *IEEE Antennas and Wireless Propagation Letters*, vol. 7, pp. 33–35, 2008.

[204] J. P. Curty, N. Joehl, C. Dehollain, and M. J. Declercq, "Remotely powered addressable UHF RFID integrated system," *IEEE Journal Solid-State Circuits*, vol. 40, no. 11, pp. 2193–2201, Nov. 2005.

[205] D. Girbau, A. Ramos, A. Lazaro, S. Rima, and R. Villarino, "Passive wireless temperature sensor based on time-coded UWB chipless RFID tags," *IEEE Trans. Microw. Theory and Tech.*, to be published, pp. 1–10, 2012.

[206] M. Donelli, "Design of long-range, powerless RFID sensor at 10 GHz," *Electronic Letters*, Vol. 49, no. 7, 1277-1278, 2013.

[207] S. Preradovic and A. Menicanin, "Chipless wireless sensor node," *Proceeding on MIPRO*, May 21–25, 2012 Opatija, Croatia, pp. 179–182.

[208] Aobo Zhao et al. "IQ signal based RFID sensors for defect detection and characterisation," *Sensors and Actuators A. Physical*, vol. 269, pp. 1421, Jan. 2018.

[209] L. Yang, Y. Li, Q. Lin, H. Jia, X.-Y. Li, Y. Liu, "Tagbeat: Sensing Mechanical Vibration Period With COTS RFID Systems," *IEEE/ACM Transactions on Networking*, vol. 25, no. 6, pp. 3823-3835, 2017.

[210] Cristian Herrojo, Javier Mata-Contreras, Alba Nez, Ferran Paredes, Eloi Ramon, Ferran Martn, "Near-Field Chipless-RFID System With High Data Capacity for Security and Authentication Applications," *IEEE Transactions on Microwave Theory and Techniques*, vol. 65, no. 12, pp. 5298-5308, 2017.

[211] M. Garbati, E. Perret, R. Siragusa, C. Halop, "Toward Chipless RFID Reading Systems Independent of Tag Orientation," *IEEE Microwave and Wireless Components Letters*, vol. 27, no. 12, pp. 1158-1160.

[212] S. Grebien, J. Kulmer, F. Galler, M. Goller, E. Leitinger, H. Arthaber, K. Witrisal, "Range Estimation and Performance Limits for UHF-RFID Backscatter Channels," *IEEE Journal of Radio Frequency Identification*, vol. 1, no. 1, pp. 39-50, 2017.

[213] H. Qin, Y. Peng, W. Zhang, "Vehicles on RFID: Error-Cognitive Vehicle Localization in GPS-Less Environments," *IEEE Transactions on Vehicular Technology*, vol. 66, no. 11, pp. 9943-9957, 2017

[214] H. Li, J. Zhu, Y. Yu, "Compact Single-Layer RFID Tag Antenna Tolerant to Background Materials," *IEEE Access*, vol. 5, pp. 21070-21079, 2017.

[215] Po-Jen Chuang; Wei-Ting Tsai, "SwitchTable: An efficient anti-collision algorithm for RFID networks," *IET Communications*, vol. 11, no. 14, pp. 2221-2227, 2017.

[216] Jun Zhang; Zhongxiang Shen, "Compact and High-Gain UHF/UWB RFID Reader Antenna," *IEEE Transactions on Antennas and Propagation*, vol. 65, no. 10, pp. 5002-5010, 2017.

[217] J. C. Bolomey, S. Capdevila, L. Jofre, and J. Romeu, "Multi-loaded modulated scatterer technique for sensing applications," *IEEE Trans. on Instrumentation and Measurement*, vol. 62, no. 4, pp. 794805, Apr. 2013.

[218] J. C. Bolomey and G. Gardiol, *Engineering Applications of the Modulated Scattering Technique*, A. House, Ed. Arthec House, 2001.

[219] R. Bracht, E. K. Miller, and T. Kuckertz, "An impedance modulated reflector system," *IEEE Potentials*, vol. 18, no. 4, pp. 29-33, Nov. 1999.

[220] R. Harrington, "Electromagnetic scattering by antennas," *IEEE Trans. Antennas Propag.*, no. 1, vol. 5, pp. 595–596, Sep. 1963.

[221] M. Donelli, "Guidelines for the design and optimization of wireless sensors based on the modulated scattering techniques," *IEEE Trans. on Instrumentations and Measurements*, vol. 63, no. 7, pp. 1824-1833, 2014.

[222] R. Fletcher, J. P. Marti, and R. Redemske, "Study of UHF RFID signal propagation through complex media," *IEEE Antenna and Propagation Symposium*, Cambridge, MA, pp. 747–750, 2005.

[223] D. Y. Kim, J. G. Yook, H. G. Yoon, and J. Jang, "Interference analysis of UHF RFID systems," *Progress in Electromagnetics Research B*, vol. 4, pp. 115–126, 2008.

[224] S. Leong, J. M. L. Ng, and H. Kole, "The reader collision problem in RFID systems," *2005 IEEE International Symposium on Microwave, Antenna, Propagation and EMC Technologies for Wireless Communication*, pp. 747–750, 2005.

[225] A. Picquenard, *Radiowave Propagation*, MacMillan Bath UK, 1974.

[226] M. Ostradahimi, P. Mojabi, S. Noghanian, L. Shafai, S. Pistorius, and J. Lovetri, "A novel tomography system based on the scattering probe technique," *IEEE Trans. Instrumentation Measurement*, vol. 62, no. 2, pp. 379–390, Feb. 2012.

[227] M. Donelli, M. Pastorino, and S. Caorsi, "A passive antenna system for data acquisition in scattering applications," *IEEE Antennas Wireless Propag. Lett.*, vol. 1, pp. 203–206, 2001.

[228] M. A. Abou-Khousa and R. Zoughi, "Multiple loaded scatterer method for E-field mapping applications," *IEEE Trans. Antennas Propag.*, vol. 58, pp. 900–907, 2010.

[229] R. Bracht, E. K. Miller, and T. Kuckertz, "Using an impedance-modulated reflector for passive communication," *IEEE Antennas and Propagation International Symposium*, 13–18 July 1997, pp. 1070-1073, 1997.

[230] H. M. Tehran, J. Laurin, and R. Kashyap, "Optically modulated probe for precision near-field measurements," *IEEE Trans. Instrumentation Measurement*, vol. 59, no. 10, pp. 2755–2762, Oct. 2010.

[231] S. Vauchamp, M. Lalande, J. Andrieu, B. Jecko, J. L. Lasserre, L. Pcastain, and B. Cadilhon, "Utilization of target scattering to measure high-level electromagnetic field: The MICHELSON method,"

IEEE Trans. Instrumentation Measurement, vol. 59, no. 9, pp. 2405–2413, Oct. 2010.

[232] J. H. Choi, J. I. Moon, and S. O. Park, "Measurement of the modulated scattering microwave fields using dual-phase lock-in amplifier," *IEEE Antennas Wireless Propag. Lett.*, vol. 3, pp. 340–343, 2004.

[233] W. Liang, G. Hygate, J. F. Nye, D. G. Gentle, and R. J. Cook, "A probe for making near-field measurements with minimal disturbance: The optically modulated scatterer," *IEEE Trans. on Antennas Propag.*, vol. 1, pp. 772–780, May, 1997.

[234] J. C. Bolomey, S. Capdevila, L. Jofre, and S. Tedjini, "Sensitivity analysis for wireless dielectric reflectometry with modulated scatterers," *Proc. 15th Int. Symp. Antenna Technol. Appl. Electromagn. Can. Radio Sci. Meeting ANTEM/URSI*, pp. 1–4, 2011.

[235] M. Donelli, and F. Viani, "Remote inspection of the structural integrity of engineering structures and materials with passive MST probes," *IEEE Trans. on Geoscience and Remote Sensing*, vol. 55, no. 12, 2017.

[236] M. Donelli, and F. Viani, "Graphene based antenna for the design of modulated scattering technique (MST) wireless sensors," *IEEE Antennas and Wireless Propagation Letters*, vol. 15, pp. 1561-1564, 2016.

[237] M. Donelli, and D. Franceschini, "Experiments with a modulated scattering system for through-wall identification," *IEEE Antennas Wireless Propag. Lett.*, vol. 9, pp. 20–23, 2010.

[238] Vena, A.; Perret, E.; Tedijini, S. *Chipless RFID Based on RF Encoding Particle*; Elsevier: Exeter, UK, 2016.

[239] M. Donelli, "A 24GHz environmental sensor based on the modulated scattering technique (MST)," *IEEE Conference on Antenna Measurements and Applications CAMA 2014*, Juan Les Pens, France, 16-19 Nov., 2014.

[240] F. Vernon, "Application of the microwave homodyne," *IEEE Trans. Antennas Propagat.*, pp. 110–116, Oct. 1952.

[241] R. J. King, *Microwave Homodyne Systems*, Forest Grove, London, 1978.

[242] M. I. Skolnik, *Radar Handbook*, McGraw-Hill, New York, 1990.

[243] World Health Organization (WHO), "Ambient air pollution: A global assessment of exposure and burden of disease," $https://www.who.int/phe/publications/air-pollution-global-assessment/en/[online]$, 2016.

[244] World Health Organization (WHO), "World Health Statistics 2016: Monitoring health for the SDGs Annex B: tables of health statistics by country, WHO region and globally," $http://who.int/entity/gho/publications/world-health-statistics/2016/en/[online]$, 2016.

[245] P. Spachos and D. Hatzinakos, "Real-Time Indoor Carbon Dioxide Monitoring Through Cognitive Wireless Sensor Networks," in IEEE Sensors Journal, vol. 16, no. 2, pp. 506-514, Jan.15, 2016.

[246] C. Arnold, M. Harms and J. Goschnick, "Air quality monitoring and fire detection with the Karlsruhe electronic micronose KAMINA," in IEEE Sensors Journal, vol. 2, no. 3, pp. 179-188, June 2002. doi: 10.1109/JSEN.2002.800681

[247] B. Maag, Z. Zhou and L. Thiele, "A Survey on Sensor Calibration in Air Pollution Monitoring Deployments," in IEEE Internet of Things Journal, vol. 5, no. 6, pp. 4857-4870, Dec. 2018.

[248] M. Blaschke, T. Tille, P. Robertson, S. Mair, U. Weimar and H. Ulmer, "MEMS Gas-Sensor Array for Monitoring the Perceived Car-Cabin Air Quality," in IEEE Sensors Journal, vol. 6, no. 5, pp. 1298-1308, Oct. 2006.

[249] J. Li et al. "Odor Assessment of Automobile Cabin Air With Field Asymmetric Ion Mobility Spectrometry and Photoionization Detection," in IEEE Sensors Journal, vol. 16, no. 2, pp. 409-417, Jan.15, 2016.

[250] A. Boubrima, W. Bechkit and H. Rivano, "Optimal WSN Deployment Models for Air Pollution Monitoring," in IEEE Transactions on Wireless Communications, vol. 16, no. 5, pp. 2723-2735, May 2017.

[251] A. Kyriacou, S. Timotheou, M. P. Michaelides, C. Panayiotou and M. Polycarpou, "Partitioning of Intelligent Buildings for Distributed Contaminant Detection and Isolation," in IEEE Transactions on Emerging Topics in Computational Intelligence, vol. 1, no. 2, pp. 72-86, April 2017.

[252] U. Jaimini, T. Banerjee, W. Romine, K. Thirunarayan, A. Sheth and M. Kalra, "Investigation of an Indoor Air Quality Sensor for Asthma Management in Children," in IEEE Sensors Letters, vol. 1, no. 2, pp. 1-4, April 2017, Art no. 6000204

[253] A. Kyriacou, M. P. Michaelides, V. Reppa, S. Timotheou, C. G. Panayiotou and M. M. Polycarpou, "Distributed Contaminant Detection and Isolation for Intelligent Buildings," in IEEE Transactions on Control Systems Technology, vol. 26, no. 6, pp. 1925-1941, Nov. 2018.

[254] L. Chen, Y. Ho, H. Hsieh, S. Huang, H. Lee and S. Mahajan, "ADF: An Anomaly Detection Framework for Large-Scale PM2.5 Sensing Systems," in IEEE Internet of Things Journal, vol. 5, no. 2, pp. 559-570, April 2018.

[255] F. Harrou, A. Dairi, Y. Sun and F. Kadri, "Detecting Abnormal Ozone Measurements With a Deep Learning-Based Strategy," in IEEE Sensors Journal, vol. 18, no. 17, pp. 7222-7232, 1 Sept.1, 2018.

[256] Yi WY, Lo KM, Mak T, Leung KS, Leung Y, Meng ML., "A Survey of Wireless Sensor Network Based Air Pollution Monitoring Systems," Sensors (Basel). 2015;15(12):31392-427. Published 2015 Dec 12.

[257] M. Donelli, "An RFID-Based sensor for Masonry crack monitoring," *Sensors,* vol. 18, no. 12, Dec. 2018.

[258] G. M. Rebeiz, *RF MEMS: Theory Design, and Technology, 1st ed.* Hoboken, NJ USA: Wiley, 2003 pp. 1-512.

[259] J. Iannacci, M. Huhn, C. Tschoban, H. Potter, "RF-MEMS Technology for future (5G) mobile and high frequency applications: reconfigurable 8-bit power attenuator tested up to 110 GHz," IEEE EDL, vol. 37, no. 12, pp. 1646-1649, Dec. 2016.

[260] J. Iannacci, A. Faes, F. Mastri, D. Masotti, V. Rizzoli, "A MEMS-Based Wide-Band Multi- State Power Attenuator for Radio Frequency and Microwave Applications," *Proc. of TechConnect World, NSTI-Nanotech 2010*, pp. 328-331, Jun. 2010.

[261] "Climate Change: How Do We Know?," by NASA report, website: *https://climate.nasa.gov/evidence/*

[262] James Temple, "Australias fires have pumped out more emissions than 100 nations combined-Climate change is driv-

ing climate change," MIT Technology review, Jan 10, 2020, site:*https://www.technologyreview.com/s/615035/australias-fires-have-pumped-out-more-emissions-than-100-nations-combined/*

[263] B. Kadri, B. Bouyeddou and D. Moussaoui, "Early Fire Detection System Using Wireless Sensor Networks," 2018 International Conference on Applied Smart Systems (ICASS), Medea, Algeria, 2018, pp. 1-4.

[264] T. Bao, Z. Huang and D. Li, "Data Loss and Reconstruction for Wireless Environmental Sensor Networks," 2017 ieee 3rd international conference on big data security on cloud (bigdatasecurity), ieee international conference on high performance and smart computing (hpsc), and ieee international conference on intelligent data and security (ids), Beijing, 2017, pp. 48-52.

[265] E. A. Kadir, A. Efendi and S. L. Rosa, "Application of LoRa WAN Sensor and IoT for Environmental Monitoring in Riau Province Indonesia," 2018 5th International Conference on Electrical Engineering, Computer Science and Informatics (EECSI), Malang, Indonesia, 2018, pp. 281-285.

[266] M. Antunes, L. M. Ferreira, C. Viegas, A. P. Coimbra and A. T. de Almeida, "Low-Cost System for Early Detection and Deployment of Countermeasures Against Wild Fires," 2019 IEEE 5th World Forum on Internet of Things (WF-IoT), Limerick, Ireland, 2019, pp. 418-423.

[267] S. Kino, "Application and benefits of an open DeviceNet control system in the forest products industry," Conference Record of 1999 Annual Pulp and Paper Industry Technical Conference (Cat. No.99CH36338), Seattle, WA, USA, 1999, pp. 196-203.

[268] W. Halle et al. "Firebird Small Satellites for Wild Fire Assessment," IGARSS 2018 - 2018 IEEE International Geoscience and Remote Sensing Symposium, Valencia, 2018, pp. 8609-8612.

[269] P. Frost and H. Annegarn, "Providing satellite-based early warnings of fires to reduce fire flashovers on south africas transmission lines," 2007 IEEE International Geoscience and Remote Sensing Symposium, Barcelona, 2007, pp. 2443-2446.

[270] B. M. De Vlieger and P. S. Basigos, "Elaboration of a wild fire hazard model for the Eparchy of Pylias (SW-Messinia, Greece) based upon remote sensing and GIS," Proceedings of IGARSS '94 - 1994 IEEE International Geoscience and Remote Sensing Symposium, Pasadena, CA, USA, 1994, pp. 776-778 vol.2.

[271] G. Laneve and E. G. Cadau, "Quality assessment of the fire hazard forecast based on a fire potential index for the Mediterranean area by using a MSG/SEVIRI based fire detection system," 2007 IEEE International Geoscience and Remote Sensing Symposium, Barcelona, 2007, pp. 2447-2450.

[272] S. Jones, B. Hally, K. Reinke, C. Wickramasinghe, L. Wallace and C. Engel, "Next Generation Fire Detection from Geostationary Satellites," IGARSS 2018 - 2018 IEEE International Geoscience and Remote Sensing Symposium, Valencia, 2018, pp. 5465-5468.

[273] V. G. Ambrosia and E. Hinkley, "NASA Science Serving Society: Improving Capabilities for Fire Characterization to Effect Reduction in Disaster Losses," IGARSS 2008 - 2008 IEEE International Geoscience and Remote Sensing Symposium, Boston, MA, 2008, pp. IV - 628-IV - 631.

[274] Y. Zhang, Y. Zhang and Z. Yu, "A Solution for Searching and Monitoring Forest Fires Based on Multiple UAVs," 2019 International Conference on Unmanned Aircraft Systems (ICUAS), Atlanta, GA, USA, 2019, pp. 661-666.

[275] A. Benazza-Benyahia, N. Hamouda, F. Tlili and S. Ouerghi, "Early smoke detection in forest areas from DCT based compressed video," 2012 Proceedings of the 20th European Signal Processing Conference (EUSIPCO), Bucharest, 2012, pp. 2752-2756.

[276] Alkhatib A, "A Review on Forest Fire Detection Techniques." International Journal of Distributed Sensor Networks, 2014.

[277] Fernndez-Berni, Jorge & Carmona-Galan, Ricardo & Carranza-Gonzlez, L., "A vision-based monitoring system for very early automatic detection of forest fires." 161-170.

[278] M. Saoudi, A. Bounceur, R. Euler, T. Kechadi and A. Cuzzocrea, "Energy-Efficient Data Mining Techniques for Emergency Detection in Wireless Sensor Networks," 2016 Intl IEEE Conferences on Ubiquitous Intelligence & Computing, Advanced and Trusted Computing, Scalable Computing and Communications, Cloud and Big Data Computing, Internet of People, and Smart World Congress (UIC/ATC/ScalCom/CBDCom/IoP/SmartWorld), Toulouse, 2016, pp. 766-771.

[279] Divya T.L. and Vijayalakshmi M.N., "Analysis of wild fire behaviour in wild conservation area using image data mining," 2015 IEEE International Conference on Electrical, Computer and Communication Technologies (ICECCT), Coimbatore, 2015, pp. 1-3.

[280] V. Devadevan and S. Suresh, "Energy Efficient Routing Protocol in Forest Fire Detection System," 2016 IEEE 6th International Confer-

ence on Advanced Computing (IACC), Bhimavaram, 2016, pp. 618-622.

[281] J. Mandel et al. "Towards a real-time data driven wild land fire model," 2008 IEEE International Symposium on Parallel and Distributed Processing, Miami, FL, 2008, pp. 1-5.

[282] T. Tamir, "On radio-wave propagation in forest environments," in IEEE Transactions on Antennas and Propagation, vol. 15, no. 6, pp. 806-817, November 1967.

[283] J. Boan, "Radio Experiments With Fire," in IEEE Antennas and Wireless Propagation Letters, vol. 6, pp. 411-414, 2007.

[284] Mphale K. M., D. Letsholathebe, and M. L. Heron., "Effective complex permittivity of a weakly ionized vegetation litter fire at microwave frequencies." Journal of Physics D: applied physics 40.21 (2007): 6651.

[285] C. A. Balanis, Antenna theory: analysis and design, 2nd ed. New York: Wiley, 1997.